ADVANCED METHODOLOGIES FOR THE ASSESSMENT OF THE FATIGUE BEHAVIOUR OF RAILWAY BRIDGES

Carlos Miguel Correia Albuquerque
2015

Dissertation submitted to the Faculty of Engineering of the University of Porto in fulfilment of the requirements for the degree of Doctor in Civil Engineering.

Supervisor: Rui Artur Bártolo Calçada (Full Professor, FEUP)
Co-Supervisor: Paulo Manuel Salgado Tavares de Castro (Full Professor, FEUP)

POPH QUALIFICAR É CRESCER.
QUADRO DE REFERÊNCIA ESTRATÉGICO NACIONAL PORTUGAL 2007.2013
Governo da República Portuguesa
UNIÃO EUROPEIA Fundo Social Europeu

À Diana e
ao Francisco,
à Carolina
e aos meus pais

ABSTRACT

The relevance of railways as a means of transport of passengers and goods has been increasing over the last decades. This reflects in a number of railway projects that are considered as a priority for the European Union. When assessing the economic viability of such projects, in addition to the high initial cost with the infrastructure construction, there are costs deferred over time that must be accounted for, such as inspection, maintenance, retrofitting and renewal of the track and of the Civil Engineering structures, such as bridges. In this context, fatigue arises as one of the main causes of damage during service life of structures. In the case of steel and composite bridges, it is often reported as the main cause of severe damage.

The research presented in this Thesis aimed at providing new numerical and experimental methodologies that allow the accurate and efficient fatigue assessment of railway bridges. These tools would help Infrastructure Managers to optimise bridge inspection, maintenance and retrofitting interventions, in order to minimise their economic impact.

The work starts by performing a brief historical overview encompassing the main milestones in terms of understanding of the fatigue phenomenon. The typical causes for fatigue damage in bridges are enumerated and some case studies of fatigue damage observed in railway bridges, found in literature, are presented. The fatigue damage assessment methodologies present in the main international standards are debated later, with special emphasis put on the Eurocodes. Alternative and more advanced methodologies for the fatigue analysis are also described. Most

of the focus is put on the methodologies based on Fracture Mechanics and fatigue crack propagation laws. In this context, it is highlighted the relevance of the stress intensity factor (SIF) as the parameter governing the stress field at the crack front and, consequently, the crack propagation rate.

The bridge of the new railway crossing of river Sado was used as the case study for the application of the experimental and numerical methods developed. A numerical model of the bridge was built and calibrated based on the results of Ambient Vibration and Load Tests performed in the bridge. A monitoring system was designed and implemented in the structure aiming at characterising traffic and estimating fatigue damage at the critical details identified: the diagonals located in the diaphragms of the deck. Fatigue damage was computed according to linear damage accumulation method present in Eurocode 3. A methodology was developed and incorporated in the monitoring system allowing for the computation of fatigue damage, not only at the directly monitored details (with strain gauges), but also at non-monitored details. The stress state at these non-monitored locations is computed based on the traffic characteristics captured by the monitoring system and on the modal parameters gathered from the calibrated numerical model of the bridge. The results obtained indicate that, for this case study and for the observed traffic volumes, the fatigue damage at the critical locations is very low. Most of the damage is induced by freight trains circulating at low speeds. The contribution of the passenger trains, which typically circulate at speeds above 145 km/h, is almost negligible.

Additionally, a new numerical methodology was developed that allows for the expedite computation of SIF time histories in cracked structures under complex loading. The concept of modal stress intensity factor, required for the application of the proposed methodology, is introduced. The methodology was validated with a simple example, a simply supported beam containing a semi-elliptical crack and subject to dynamic loading. Finally, it was applied to the simulation of a fatigue crack propagation in one of the critical details of the bridge. A local numerical model of the detail, with a finer mesh, was built. Reconciliation with the global model of the bridge was achieved through the implementation of submodelling. A conservative scenario of a pre-existing through-thickness crack, with 15 mm, was considered. The simulation was performed using minimal computational resources. The crack propagation simulation stopped when the maximum simulated SIF achieved the material's toughness. The results obtained under the above mentioned conservative assumptions and for the current traffic volumes, indicate a remaining fatigue life for the detail of approximately 95 years.

RESUMO

A importância da ferrovia como meio de transporte de pessoas e bens tem aumentado ao longo das últimas décadas. Este facto reflete-se no número de projetos ferroviários considerados prioritários para a União Europeia. Na avaliação da viabilidade económica destes projetos, para além do avultado custo inicial com a construção das infraestruturas, há custos diferidos no tempo a contabilizar, tais como a inspeção, manutenção, reparação e renovação da via e das estruturas de Engenharia Civil, como por exemplo as pontes. Neste contexto, a fadiga surge como uma das principais causas de dano durante a fase de serviço das estruturas, sendo até mesmo reportada como a principal causa de dano severo em pontes de aço e mistas.

A investigação apresentada nesta Tese visa fornecer novas metodologias numéricas e experimentais que permitam uma rigorosa e eficiente avaliação da fadiga em pontes ferroviárias. Estas ferramentas poderão ajudar o Gestor das Infraestruturas a otimizar as intervenções de inspeção, manutenção e reparação, de forma a reduzir o seu impacto económico.

Inicialmente apresenta-se uma breve revisão histórica dos principais passos dados em termos da compreensão do fenómeno da fadiga. São enumeradas as causas mais comuns para o dano de fadiga em pontes e são apresentados casos, encontrados na bibliografia, de dano por fadiga em pontes ferroviárias. Posteriormente, são debatidas as metodologias de avaliação do dano por fadiga presentes nos principais códigos internacionais, com especial ênfase nos Eurocódigos. Metodologias alternativas e mais avançadas são também descritas. Maior enfoque é colocado nas

metodologias baseadas na Mecânica da Fratura e em leis de propagação de fendas de fadiga. Neste contexto, é realçada a relevância do fator de intensidade de tensão (FIT) como parâmetro que governa o campo de tensões na frente da fenda e consequentemente a sua taxa de propagação.

A ponte da nova travessia ferroviária do rio Sado foi usada como o caso de estudo para aplicação dos métodos numéricos e experimentais desenvolvidos. Um modelo numérico da ponte foi construído e calibrado com base nos resultados de um Ensaio de Vibração Ambiental e de um Ensaio de Carga realizados na ponte. Um sistema de monitorização foi projetado e implementado na estrutura, visando caracterizar o tráfego e estimar o dano de fadiga em detalhes críticos: as diagonais localizadas nos diafragmas do tabuleiro. O dano por fadiga foi calculado com base no método da acumulação linear de dano preconizada pelo Eurocódigo 3. Uma metodologia foi desenvolvida e incorporada no sistema de monitorização permitindo o cálculo do dano por fadiga, não apenas nos detalhes monitorizados diretamente (com extensómetros), mas também nos detalhes não monitorizados. No último caso, o estado de tensão é calculado com base nas características de tráfego capturadas pelo sistema de monitorização e nos parâmetros modais obtidos com o modelo numérico da ponte. Os resultados obtidos indicam que, para o caso de estudo e para o volume de tráfego observado, o dano por fadiga nos detalhes críticos é muito baixo. A maior parte do dano é provocada por comboios de mercadorias que circulam a baixa velocidade. O contributo dos comboios de passageiros, que circulam, tipicamente, a velocidades superiores a 145 km/h, é quase nulo.

Adicionalmente, foi desenvolvida uma nova metodologia numérica que permite calcular, de forma expedita, o histórico do FIT em estruturas com fendas e sujeitas a carregamento complexo. É introduzido o conceito de fator de intensidade de tensão modal, necessário para a aplicação da metodologia proposta. A metodologia foi validada com um exemplo simples, uma viga simplesmente apoiada contendo uma fenda semielíptica e sujeita a um carregamento dinâmico. Posteriormente, foi aplicada à simulação da propagação de uma fenda de fadiga num dos detalhes críticos da ponte. Foi construído um modelo numérico local do detalhe, com uma malha refinada. A compatibilização com o modelo global da ponte foi feita através de técnicas de submodelação. Foi testado um cenário conservador, em que uma fenda inicial, passante, com 15 mm, estava presente no detalhe. A simulação foi realizada utilizando recursos computacionais reduzidos. A simulação da propagação de fenda terminou quando o máximo FIT simulado atingiu a tenacidade do material. Os resultados obtidos com as considerações conservadoras referidas e para o volume de tráfego atual, indicam que o detalhe tenha uma vida à fadiga de aproximadamente 95 anos.

ACKNOWLEDGEMENTS

This Thesis was only possible with the help, support and guidance of several individuals and institutions to whom I owe much gratitude. To all of them I convey my sincere thanks:

To my Supervisor, Professor Rui Calçada, for all the energy and effort put on providing me the conditions to perform this work. I would like to thank all the teachings that highly contributed to my growth in scientific terms, in particular in the areas of numerical and experimental characterization of the dynamic behaviour of structures. I really appreciate all the friendship and support in the different stages of my work and of my life;

To my Co-Supervisor, Professor Paulo Tavares de Castro, for all the teaching, namely on the areas of fatigue and Fracture Mechanics. I would also like to express all the gratitude for the friendship, availability, willingness to help and incentive words throughout the Thesis;

To Professor Raimundo Delgado, for his example, friendship and always kind words. Also for sparking in me the interest for the dynamic behaviour of structures;

To my friend Diogo Ribeiro, for all the fruitful discussions and always valuable comments and inputs. Also for his example of determination and pragmatism;

To Nuno Pinto, for his generosity and for all the support on the set up and installation of the monitoring system of the bridge of the new railway crossing of river Sado;

To André Paixão, for the sharing of ideas and interests resulting in thriving friendship. Also for the collaboration in the experimental work performed in the bridge;

To my friends Joana Delgado, Joel and Pedro Montenegro;

To Diogo Ribeiro, Joel Malveiro, João Francisco Rocha, João Rocha, Nuno Pinto and Nuno Ribeiro for the companionship during the experimental campaigns in the bridge, including the thousands of km driven between Porto and Alcácer do Sal;

To André Paixão, Carlos da Conceição and Carlos Sousa, for the careful review of this Thesis;

To my friends and colleagues from our department and research group, for contributing to a very pleasant work environment, where discussion and sharing of experiences benefit each ones work;

To Professor Abílio de Jesus and Luís Silva, for the help, guidance and fruitful collaboration in the last phases of the work. Also for kindly welcoming me at UTAD premises, in Vila Real;

To Professor Álvaro Cunha, for the collaboration in the context of the FADLESS project, for the teaching in the area of experimental methods on structural dynamics and for the several words of esteem and consideration over these years;

To Fernando Marques, for the interesting discussions and collaboration in the context of the FADLESS project;

To Professors Joaquim Gabriel and Teresa Restivo, for the lessons on Instrumentation for Data Measurement, Acquisition and Transmission;

To Professor Miguel Figueiredo, Roberto Miranda and Valentin Richter-Trummer for the fundamental role on the execution of fatigue crack propagation tests;

To the Portuguese Foundation for Science and Technology (FCT), for the funding of the work presented in this Thesis through the scholarship SFRH/BD/47545/2008 and the Research Project "Advanced methodologies for the assessment of the dynamic behaviour of high speed railway bridges" (FCOMP-01-0124-FEDER-007195);

To the European Commission, which funded this same work in the context of the Research Project "FADLESS - Fatigue damage control and assessment for railway bridges" (RFSR-CT-2009-00027);

To REFER, in particular to Eng. Ana Isabel Silva, Eng. Fernando Martins and Eng. Hugo Patrício, for providing all the conditions for the installation of the monitoring system and execution of the experimental tests in the bridge;

To Eng. António Reis, designer of the bridge of the new railway crossing of river Sado, for the information provided concerning the design of the structure;

To Teixeira Duarte, S.A., in particular to Eng. Henrique Nicolau, for permitting multiple visits to the bridge during its construction, therefore allowing a better planning of the experimental work performed. Moreover, it was also highly appreciated the availability to provide samples of the steel and welds used on the construction of the critical details of the bridge, which enriched the work performed in this Thesis. In the case of the weld samples, their execution by AMAL is also acknowledged;

To LNEC, in particular to Eng. Luís Oliveira Santos and Eng. João Santos, for the opportunity to perform measurements on the bridge during the load tests performed at the commissioning phase. It is also appreciated the sharing of the results obtained by LNEC during those tests;

To Walter Waes, from Galp Energia, for supporting me in the final stages of this Thesis, seeking its conclusion;

To Professor António Arêde, for the support from the Structural and Seismic Engineering Laboratory, both in terms of personnel and equipment for the experimental campaigns;

To Sr. Valdemar and André for the help on the preparation of the experimental work;

To Marta Poinhas and Joana Rodrigues for their always kind and prompt assistance;

Finally, to my family. To my parents, Francisca and José, who always taught me, through words and example, the value of hard work. I'm forever grateful for their effort, understanding and love and for the way they always encouraged me on pursuing this work. To my sister, Carolina, for always being able to make me laugh. Also for her understanding in all the situations where, during this work, I was not as present as I should. To my beloved wife, Diana, for her permanent joy, love, support and patience. Finally, to Francisco, who, without even knowing it, was the final and definitive inspiration to conclude this work.

CONTENTS

LIST OF FIGURES

LIST OF TABLES

Chapter 1

INTRODUCTION

1.1 CONTEXT

The relevance of railways as a mean of transport of passengers and goods has been increasing over the last decades. This is due to some advantages of railways when compared to alternative means of transport, such as roadway and airway. Those advantages are economic, environmental and safety related: lower costs of transport; lower energy consumption and CO_2 emissions; very low number of incidents and accidents reported. Also, as the speed of railway traffic increases, it becomes competitive for a wider range of distances. In the case of passenger traffic, in particular, this is boosted by the increased comfort provided by railways and by the development of high-speed railways, with speeds higher than 250 km/h (Figure 1.1). In the case of freight traffic, the development of dedicated freight routes also contributes for the reduction of the time of transportation.

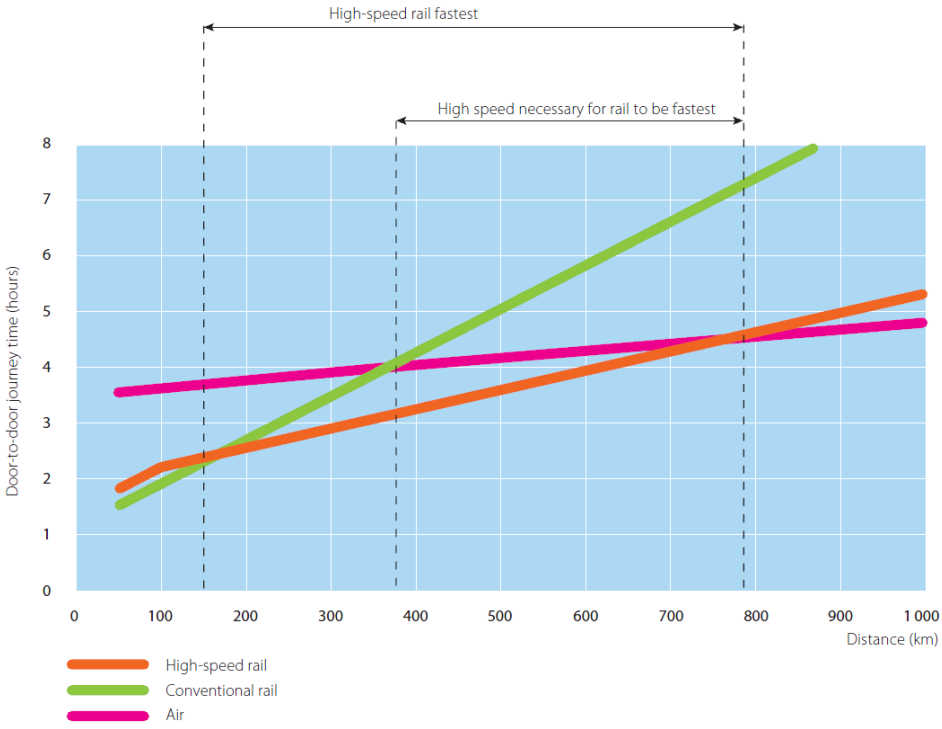

Figure 1.1 – Passenger journey times vs. distance: rail vs air transport (EC, 2010).

The above mentioned advantages have been reflecting in: i) increasing volume of passengers and goods transported per year; ii) increasing share of railway traffic when compared to other types of transport systems; iii) increasing loads per train and per train's axle; iv) expansion of railway networks in many different countries.

In the context of the European Union, the benefits of railways in terms of cost reduction and economic and social cohesion across national boundaries are also acknowledged. The railway sector is expected to take on a larger share of transport demand in the next decades. That intention is reflected in the number of railway projects that are considered as a priority, in the Trans-European Transport Network project (EC, 2013).

Portugal is also to be included in the Trans-European Transport Network. It will connect to the rest of Europe through the Atlantic corridor (in yellow in Figure 1.2).

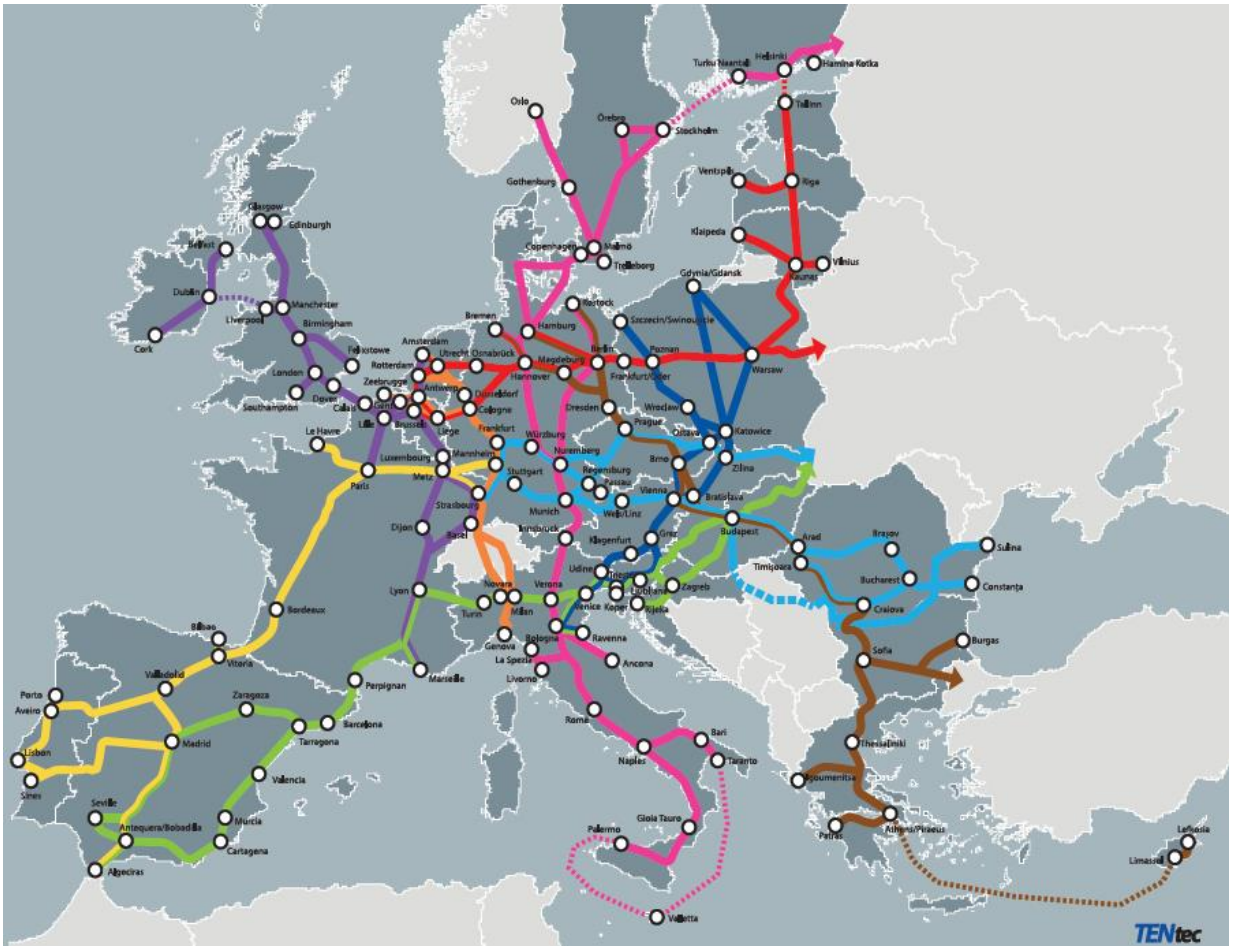

Figure 1.2 – Tran-European Transport Network: core network corridors (EC, 2013).

In the last decades, the country invested in the modernization of some of the rail lines available. The line connecting the two most populous cities, Lisbon and Oporto, was recently upgraded, allowing the increase of speed of conventional trains to around 220 km/h.

Additionally, Portugal has been preparing to install, in the next 2 decades, a few high-speed railway lines, which will allow connecting the country to the European high-speed railway network. Lines specially dedicated to freight traffic are also foreseen. The planned freight and high-speed passenger routes are illustrated in Figure 1.3.

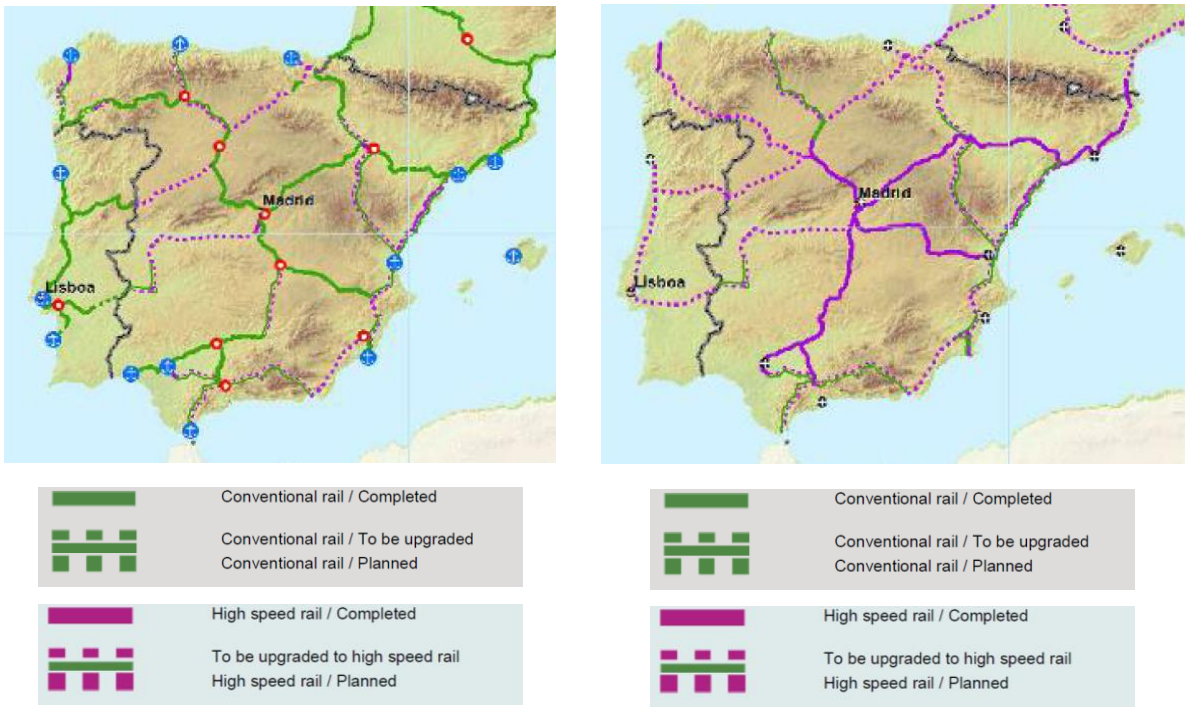

(a) (b)

Figure 1.3 – Planned railways in Portugal (EC, 2013): (a) freight and (b) passenger lines.

In addition to the high initial cost with the infrastructure construction, there is a cost that is deferred over time which refers to the inspection, maintenance, retrofitting and renewal of the track and of the Civil Engineering structures, such as bridges. In current days, more than half of the expenditure with infrastructure, in Europe, is related with maintenance and modernization of the existing infrastructure (Kühn et al., 2008). Therefore, and as the ageing process of structures continues, the economic and social relevance of an efficient and effective assessment of infrastructures structures is increasing.

In this context, fatigue arises as one of the main causes of damage during the service life of structures (Oehme, 1989). In the case of steel and composite bridges, it is often reported as the main cause of severe damage (Miki, 2010, Fisher, 1984, Al-Emrani and Kliger, 2009, Cremona et al., 2013, Clubley and Winter, 2003, Cho et al., 2001, Leander et al., 2010, Hai, 2006, Kühn et al., 2008, Wang et al., 2012). The growing speed of trains leads to dynamic amplification effects that accelerate structural degradation, by increasing the number of stress cycles and their amplitudes. Also, as traffic loads also tend to increase, the problem is even more relevant, becoming one of the main topics of investigation of several research projects, such as Details

(Chellini et al., 2009), Sustainable Bridges (Cremona et al., 2007), FADLESS (Lippi et al., 2011) and Mainline (Paulsson, 2013).

The fatigue assessment methodologies present in most of the standards are based on S-N curves and linear damage accumulation rules, derived from Palmgren-Miner rule (Miner, 1945). That is the case of the Eurocodes (CEN, 2004). But those approaches, in spite of their easy employment at the design phase, lack effective applicability when dealing with in-service structures. When fatigue damage, e.g. fatigue cracks, are found in those structures, the S-N curves do not allow computing the corresponding remaining fatigue life of the damaged component and structure. Also, they do not help defining the time lapses between inspections or the time available before maintenance and retrofitting measures are required.

On the other hand, the Infrastructure Managers and Railway Operators require that inspection, maintenance and retrofitting interventions are optimised, in order to minimise their economic impact. Line closures are expected to be as short as possible. Therefore, new experimental and numerical fatigue assessment methodologies are required in order to: i) support Infrastructure Manager decision making and planning for interventions; ii) increase safety in railway operations; iii) reduce the costs associated with infrastructure maintenance.

Current investigations focus on both the experimental characterization and numerical assessment of fatigue.

As mentioned before, most standards and procedures, e.g. (CEN, 2004, AASHTO, 2012), quantify fatigue strength on the basis of S-N curves and of linear damage accumulation concepts. This approach, based on the global stress level, is used to predict fatigue life until total failure and is widely spread as a result of its straightforward application; it presents, however, some important limitations. On the one hand, the applicable rules cover a limited number of structural details. On the other hand, the development of S-N curves for new details implies performing tests at the real scale, and these are expensive and time consuming, and consequently generally unpractical for the timings of design and construction (Fricke and Paetzold, 2010, Lotsberg and Landet, 2005, Ling and Pan, 1997). Furthermore, S-N curves are a result of tests that present an important scatter (Pedersen et al., 2010). As a safeguard against this effect the S-N curves are usually very conservative (Casavola and Pappalettere, 2009, Morel and Flacelière, 2005). Finally, fitness for purpose assessments cannot be carried out on the basis of that approach. For a given situation of damage, such as a fatigue crack identified during some non-destructive

inspection, the approach does not provide a risk assessment of that defect nor the useful remaining life (Byers et al., 1997). It does not contribute, therefore, for an improved definition of intervals between inspections (Ayala-Uraga and Moan, 2007). Other limitations of the S-N approaches were identified by several authors, concerning, for example, variable amplitude loading (Johannesson et al., 2005), or fatigue life for a very high number of load cycles (Sonsino, 2007).

Alternative approaches developed for the analysis of fatigue are based on local behaviour (Radaj et al., 2009). That is the case of the approaches based on structural stresses, structural strains, notch stresses, notch strains and Fracture Mechanics.

The application of these methodologies to the assessment of large structures poses significant challenges, which limited its use in the context of Civil Engineering structures. Usual calculations involve the application, to the structural detail of interest, of a known loading history under load or displacement control. Computation of the corresponding local stress or strain fields allows for the calculation of fatigue damage indicators. However, for some structures, the loading history is most of the times complex and the corresponding structural dynamical response is unknown in most – or even all – points of interest.

In these circumstances, even when the loading history is known, its effects in the detail under study can only be determined through dynamic analysis of the complete structure. Those analyses are generally based upon the finite element method. The algorithms for solving the numerical problem, as Newmark (Bathe, 1996) or HHT (Chung and Hulbert, 1993), require, frequently, the calculation of thousands of load steps, leading to very time consuming calculation process. High computational costs are heightened as a result of the need for highly refined finite elements meshes in the neighbourhood of the damage locations. That level of refinement cannot be extended to the remaining structure (Chan et al., 2003). This is a problem inherent to the scale difference between the detail where fatigue damage occurred or is likely to occur, of the order of mm or less, and the global structure, that may be of the order of km (Li et al., 2007).

This scale problem is also reflected in the experimental assessments. Since fatigue damage is localised at critical details of the structures, the most usual way for the infrastructure managers to assess it is by periodical or extraordinary bridge inspections (Righiniotis, 2006). When fatigue damage is detected, e.g. fatigue cracks, or expected, the actual condition of the bridge is often assessed by load tests and short term monitoring (Leander et al., 2010, Wang et al., 2012, Lippi

et al., 2011, Nagy et al., 2013, Zhou et al., 2013, Caglayan et al., 2009, Brencich and Gambarotta, 2009, Marques et al., 2009, Stamatopoulos, 2013, Srinivas et al., 2013, Fu and Zhang, 2011, Tecchio et al., 2013). In some cases the short term monitoring is also performed during the subsequent repair, strengthening and/or replacement activities (Rodrigues et al., 2012) or even later, to assess the improvements resulting from the retrofitting/enhancement measures (Andersson et al., 2013). The data obtained during the short term monitoring of fatigue prone structures is analysed and, commonly, used to extrapolate the results for longer periods of time (Zhou, 2006).

Nevertheless, it is not economically feasible to perform interventions in all underperforming bridges, at the same time. Their advanced assessment (structural health monitoring - SHM), by means of long-term monitoring systems could help on the prioritization and on the scheduling of inspections and interventions (Orcesi and Frangopol, 2011, Wong, 2012). Advances in technology, such as the development of industrial computers, the wireless communication systems (Picozzi et al., 2010) and the enhancement of all types of electronic transducers, helped increasing the number of applications of long-term monitoring systems to critical structures worldwide (Magalhães et al., 2008, Cross et al., 2013). The benefits of structural health monitoring are quantifiable (Orcesi and Frangopol, 2013) and, in some countries, the use of long-term monitoring systems is even being addressed by regulations (Moreu et al., 2012).

Most of the long-term monitoring systems are focused on detecting damage events (Cury and Crémona, 2012). As the objectives of the SHM become more ambitious, towards damage localization (Whelan and Janoyan, 2010, Dilena and Morassi, 2011, Glisic and Inaudi, 2012), damage severity assessment (Santos et al., 2013) and lifetime prediction update, the complexity of the systems and of the data analysis algorithms also increases.

The long-term monitoring of the global dynamic properties of the structures is one of the most common methods to try to detect the structural damage (Santos, 2014, Rahmatalla et al., 2014, Caglayan et al., 2011, Magalhães et al., 2012b, Ko et al., 2002). In this context, some attempts were made in the past to replace the installation of sensors in the bridge by the utilization of instrumented test vehicles (Van Bogaert, 2012).

An alternative approach is to use a long-term monitoring system that measures strain at a number of details considered of relevance in order to estimate cumulative damage (Costa and Figueiras, 2012, Guo and Chen, 2013, Ye et al., 2012, Xu et al., 2012, Chen et al., 2012, Ni et

al., 2012, Guo and Chen, 2011, Liu et al., 2010, Hakola et al., 2012) or even to detect it (Phares et al., 2013, Yao and Glisic, 2012).

Some structures, as the Tsing Ma Bridge, due to their relevance and scale, have long-term monitoring systems that combine the monitoring of their global dynamic behaviour with the local monitoring of strains (Chan et al., 2006, Li et al., 2012).

A structural health monitoring system should be able to perform damage quantification but also to relate the damage with the external actions that originated it. This is the reason why the traffic characterization is a feature of paramount importance in a permanent monitoring system (Guo et al., 2012) to be implemented either in a roadway or in a railway bridge. It allows to understand the type of traffic that has the biggest impact on the structural degradation and to forecast traffic evolution (Fu and You, 2011). The measurement of real traffic also allows avoiding the use of conservative standard load models, when assessing damage evolution and planning inspections frequency (Ottosson et al., 2012a). In the case of railway bridges, the analysis of the transversal positioning of the vehicles is highly simplified, when compared to roadway bridges, since trains are constrained to the rail track.

Several methods for railway traffic characterization are available. The Weight-In-Motion (WIM) techniques try to assess the vehicles geometry by interpreting measurements performed directly in the railway track (Meli and Pugi, 2013). Some common WIM technologies are: i) rail shear measurements using shear strain gauges welded or bonded to the neutral axis of the rail (Julián Valerio, 2005); ii) rail shear measurements, achieved by means of a circular slot drilled on the neutral line of the rail (Esveld, 2001); iii) rail bending measurements (Sekuła and Kołakowski, 2012); iv) instrumented rail pads (SensorLine, 2008). An alternative approach, the Bridge Weight-In-Motion (B-WIM), uses the structural response of the bridge to compute the vehicles geometry and axles load, after a proper calibration process (Karoumi et al., 2005, Liljencrantz et al., 2007, Seo et al., 2013).

As a complement to the SHM systems, in order to forecast the structural behaviour/degradation, due to fatigue or other causes, the development of well-calibrated numerical models of the structure is considered a very important step (Vincenzi et al., 2012, Chen et al., 2011). The calibration of a numerical model may be performed with experimental data resulting from the long-term monitoring system (Gomez and Feng, 2012, He et al., 2008) or from a short term one (Ribeiro et al., 2012, Schlune et al., 2009).

As underlined by Guo et al. (2012), the numerical model also plays an important role by allowing to extend the SHM results to the fatigue assessment of non-monitored details. Methodologies based on the influence line concept and that allow achieving those objectives are presented in (Orcesi and Frangopol, 2010) and (Zeng et al., 2012). Other alternative approach explored in the past, was to assume constant relations between the maximum stresses in different details of the bridge, and use those relations as scale factors to convert the damage measured at instrumented details into damage in the remaining points of the structure (Hakola et al., 2012). Finally, in other cases, the simulation of numerical models with real traffic was performed (He et al., 2008).

The above mentioned methodologies lack, in some cases, accuracy, and in other cases are not computationally efficient. That is the reason why, in the past, tracking fatigue damage in all critical details of long-span railway bridges was not achievable in an efficient and economical way.

The current thesis aims to provide new numerical and experimental methodologies that overcome the limitations presented above. The objectives and scope are detailed on the next Section.

1.2 OBJECTIVES AND SCOPE

As mentioned in Section 1.1, the global objective of the current thesis is to provide new numerical and experimental methodologies that allow the accurate and efficient fatigue assessment of railway bridges.

The global objective was achieved through a set of intermediate goals:

- Review the methodologies for the fatigue assessment of railway bridges available in the relevant standards;
- Review the advanced fatigue assessment methodologies available in literature;
- Develop a new numerical approach for the fatigue assessment of railway bridges, based on advanced methodologies found in literature;
- Develop a numerical model of the case study and calibrate it based on experimental measurements;

- Design and implement an innovative monitoring system allowing for the integrated fatigue monitoring of the critical details of bridges;
- Characterise the fatigue crack propagation behaviour of the material employed in the construction of the bridge that serves as case study;
- Apply the new numerical approach to the analysis of the case study bridge.

The validation of the new numerical methodology with the case study intends to demonstrate its direct applicability to the fatigue analysis of any other steel and composite bridge.

1.3 RESEARCH CONTRIBUTION

The studies performed in the current thesis originated the scientific contributions described below:

- Experimental characterization of the fatigue crack propagation behaviour of a structural steel and of thick welded connections of the same material;
- Monitoring system installed in the bridge of the new railway crossing of river Sado, Portugal, which provided an important amount of data concerning the structural behaviour and traffic characteristics;
- Routines for the automatic processing of the data generated by the monitoring system, allowing traffic characterization (train type, train speed, number of axles and load per axle) and fatigue damage estimation, for each traffic event;
- Efficient routines for the dynamic simulation of bridges loaded by railway traffic, using a combination of finite elements software (ANSYS) and MATLAB;
- Development and validation of a new methodology for the application of Linear Elastic Fracture Mechanics to the fatigue analysis of small details in large structures, under complex loading. The new methodology introduced the concept of modal stress intensity factor and takes advantage of numerical submodeling;
- Implementation of the new methodology in the fatigue crack propagation analysis of a detail of the new railway crossing of river Sado.

1.4 OUTLINE OF THE THESIS

The structure of the current thesis reflects the objective mentioned above and the intermediate steps taken to achieve it. The thesis is structured in 8 chapters.

In Chapter 1, after discussing the context of the subject of the thesis, the initial objectives and main contributions of the work are presented. The structure of the thesis is also disclosed.

Chapter 2 starts by underlining the relevance of fatigue damage in several areas of Engineering. After that, a brief historical overview encompassing the main milestones in terms of understanding of the fatigue phenomenon is performed. Finally, the subject of fatigue damage in steel and composite railway bridges is discussed. The typical causes for fatigue damage in bridges are enumerated, together with the most common locations for crack initiation and/or propagation. Some case studies of fatigue damage observed in railway bridges, found in literature, are presented.

The fatigue damage assessment methodologies present in the main international standards are debated in Chapter 3. Special emphasis is put on the Eurocodes as these are the reference structural design codes in the context of the European Union. The prescriptions found in the Eurocodes are compared with those of BS5400, AASHTO and IIW.

In Chapter 4, alternative and more advanced methodologies for fatigue analysis are described. The methodologies based on structural stresses and strains are explored first, followed by the approaches based on notch stresses and notch strains. Most of the focus is put, later, on the methodologies based on Fracture Mechanics and fatigue crack propagation laws. The theoretical background associated with Fracture Mechanics is presented. The crack propagation laws, including the retardation effect are detailed next. Finally, the latest advances in terms of the Extended Finite Elements Method (XFEM) and its application to the numerical simulation of fatigue cracks' propagation is briefly explored.

In Chapter 5, a new methodology is presented that allows for the expedite computation of stress intensity factor time histories in cracked structures under complex loading. The concept of modal stress intensity factor, required for the application of the proposed methodology, is introduced. The methodology is validated with a simple example, a simply supported beam containing a semi-elliptical crack and subject to dynamic loading.

Chapter 6 describes the bridge of the new railway crossing of river Sado, which is the case study used in current work. Both the bridge characteristics and its construction process are detailed. Subsequently, the developed global numerical model of the bridge is detailed. The validation of the numerical model by means of Ambient Vibration Test and Load Tests is also discussed. The monitoring system designed and implemented in the bridge is described next. The main results, in terms of traffic characterization and fatigue damage estimation at the monitored details, are discussed. Finally, a methodology for the fatigue damage computation at non-monitored details of the bridge is presented. The fatigue damage is computed based on the traffic characteristics captured by the monitoring system and on the modal parameters gathered from the calibrated numerical model of the bridge. The results of the application of this methodology to the case study are also discussed.

In Chapter 7, the new methodology described in Chapter 5, for the efficient computation of stress intensity factor time histories, is applied to the simulation of a fatigue crack propagation in a critical detail of the bridge of the new railway crossing of river Sado. First of all, the results of crack propagation tests performed on CT specimens made of the material used in the construction of the bridge are presented. These tests aimed at quantifying the strength of the bridge's details to fatigue crack propagation, by means of the establishment of the crack propagation laws. The local numerical model of the detail under analysis is described. Later, the results of the crack propagation simulation are discussed.

Finally, in Chapter 8, the main conclusions drawn from the work performed are presented. Scenarios for additional developments and the way forward on this subject are also discussed.

Chapter 2

FATIGUE DAMAGE OF STEEL AND COMPOSITE BRIDGES

2.1 INTRODUCTION

The human kind always aimed at designing and building infrastructures that would allow it to enhance its life conditions. Houses, bridges, roads, tunnels, ports and damns are only some examples of the human being ability and its tenacity to shape the environment to its needs.

The problem of structural integrity arose, naturally, at the time first structures were built. As early as on the XVII century BC, the sixth king of Babylon established, on the Hammurabi's Code, heavy penalties to constructers whose structures subsequently presented flaws (King, 1898). A structural failure is a situation of partial or total loss of functionality of a structure. Some examples of structural failure are: excessive deflection, brittle fracture, plastic collapse, fatigue cracks propagation, buckling, relaxation or creep, among others.

The propagation of cracks due to material's fatigue, which is therefore considered one of the most common forms of structural failure, can be defined as the process of structural degradation, caused mainly by cyclic loading and leading to the generation and/or propagation of cracks until an eventual fracture or collapse of the structural component occurs.

The current work focuses on the problem of mechanical fatigue in steel structures, since that is the more common type of fatigue in railway bridges. Nevertheless, it is important to recall that other types of fatigue may be present, such as corrosion fatigue, a high rate degrading process

which occurs in environmentally adverse conditions, such as those affecting offshore structures (ABS, 2014).

Several authors mention fatigue as the main cause of structural failures. According to Furukawa and Murakami (1999) more than 80% of machine fracturing events are due to fatigue. Oehme (1989), in a study that analysed the damage in 448 steel structures, showed that fatigue damage was very common. In the case of bridges, it was even the main cause of severe damage (Table 2.1).

Table 2.1 - Main causes of damage in Civil Engineering structures (adapted from Kühn et al. (2008)).

Damage cause (Multiple denomination possible)	**Totality**		**Buildings**		**Bridges**		**Conveyors**	
	No	%	No	%	No	%	No	%
Static strength	161	29.7	102	33.6	19	14.8	40	36.0
Stability (local or global)	87	16.0	62	20.4	11	8.6	14	12.6
Fatigue	92	16.9	8	2.6	49	38.3	35	31.5
Rigid body movement	44	8.1	25	8.2	2	1.6	17	15.3
Elastic deformation	15	2.8	14	4.6	1	0.8	0	0
Brittle fracture	15	2.8	9	3.0	5	3.9	1	0.9
Environment	101	18.6	59	19.4	41	32.0	1	0.9
Thermal loads	23	4.2	23	7.6	0	0	0	0
Others	5	0.9	2	0.7	0	0	3	2.7
Sum	543	100	304	100	128	100	111	100

In the case of aeronautic structures, and more specifically, in the case of aircraft, the existence of fatigue flaws during service phase is considered a normal situation. The focus is put on inspection and monitoring the dimension of the existing cracks, in order to guarantee that they do not reach the critical dimension that would lead to the sudden collapse of the structure, or its underperformance. Nevertheless, the complexity of the problem is significant and sporadic accidents, due to fatigue, occur (Figure 2.1).

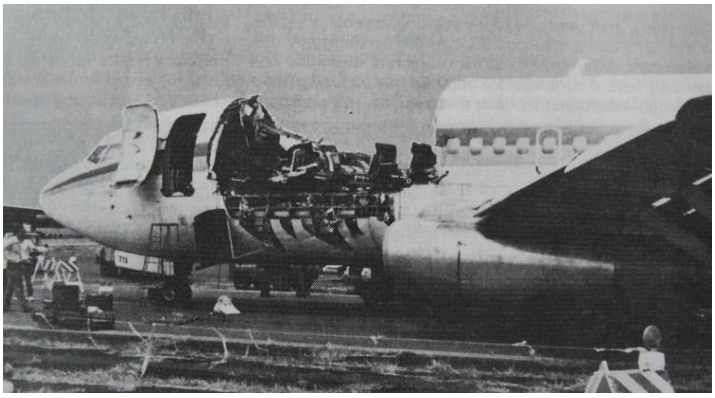

Figure 2.1 - Forced landing of a Boeing 737 due to partial ejection of the aircraft's fuselage as a consequence of the unstable propagation of fatigue cracks (NTSB, 1989).

This damage-tolerant approach implies the continuous assessment of the structural adequacy to the service conditions (fitness-for-purpose assessment).

The advantage of assuming, since the design phase, the presence of cracks at critical points of the structures is also recognised in Naval Engineering. In the case of vessels, the stable propagation of fatigue cracks is often accelerated by corrosion and the unstable propagation of those cracks may be even speeded up due to the brittle behaviour of steel at low temperatures. The brittleness of metals at low temperatures is described with more detail in (Branco et al., 1999). During World War II, this problem was aggravated by the need to build a high number of vessels in a short time period with negative consequences on the quality of the welds employed. In that period, more than 1500 brittle fractures were observed at USA vessels (Figure 2.2).

Figure 2.2 - Brittle fracture of a vessel due to unstable propagation of fatigue cracks (Hayes, 1996).

Fatigue may also affect pipelines. Series of pressure cycles inside the tubing may lead to the propagation of fatigue cracks. When those cracks reach a critical size, the inner pressure may promote their propagation throughout long distances. Figure 2.3 shows a pipeline after a crack propagated over hundreds of meters. The crack propagation was only sustained when the crack reached a connection with a thicker wall, which drastically reduced the stresses at the crack tip, acting as a crack arrester (Makino et al., 2001). This fact underlines the importance of including fatigue resistant components to delay or avoid crack propagations, at critical structures. That is the reason why modular structures may be more efficient than integral structures concerning retarding crack propagation.

Figure 2.3 – Steel pipeline after long crack propagation (Makino et al., 2001).

Railway vehicles are, also, structures potentially subjected to severe failure, due to fatigue, namely at axles and traction systems. In fact, it was a succession of train axle failures, in the XIX century, which triggered a series of fatigue tests, namely those performed by Wöhler, between 1850 and 1870, that originated the fatigue strength curves with the same name. In spite of technology and design evolutions, this type of damage still occurs (Figure 2.4).

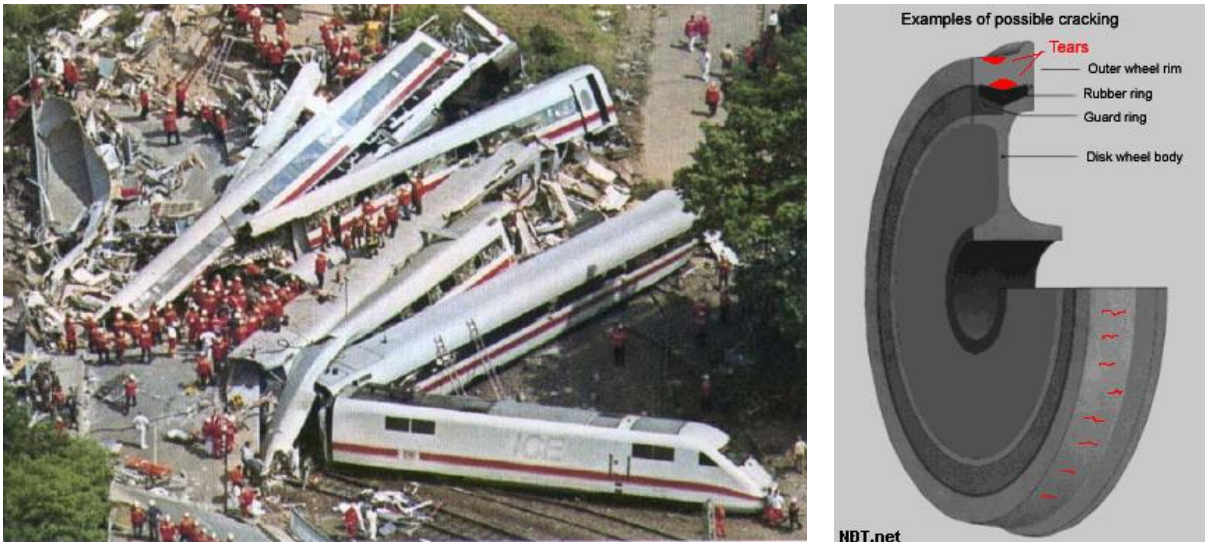

(a) (b)

Figure 2.4 - Derailment of ICE train due to fatigue damage at a wheel of one of the train's axles (O'Connor, 2007): (a) derailment and (b) location of fatigue cracks.

Even the rails are subject to fatigue cracks propagation, due to high cyclic contact forces (Figure 2.5). Several different types of fatigue cracks in rails can be found in the literature (Esveld, 2001).

(a) (b)

Figure 2.5 - Fatigue cracks on rails (Magel et al., 2004): (a) rail-wheel contact and (b) fatigue crack.

Finally, also the steel and steel-concrete composite bridges may suffer a degradation of their structural performance, due to fatigue cracks growth, when subjected to traffic, thermal and wind actions. Those cracks, if undetected during inspection periods, may reach critical dimensions, originating the collapse of the structural element and, eventually, of the whole structure. The

collapse of the Silver Bridge, in the USA, in 1967, is an example of this behaviour (Figure 2.6). Posterior studies revealed that the collapse was due to the propagation of a crack during, possibly, 40 years, at one of the eye-plate connections of one of the hangers of the deck. Since this structure did not present structural redundancy for these elements, collapse became inevitable. The particular case of fatigue in steel and composite bridges will be addressed in more detail in next sections, where more cases are presented.

(a)

(b)

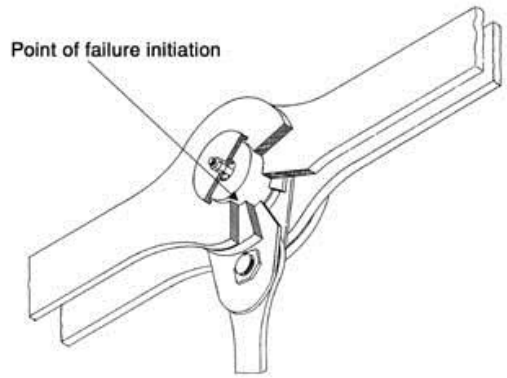

(c)

(d)

Figure 2.6 – Collapse of the Silver Bridge (Bennett and Mindlin, 1973): (a) bridge before collapse, (b) bridge after collapse, (c) point of failure and (d) fractured eye-plate.

The wide range of examples presented in this section, aims to illustrate the relevance and broad presence of fatigue as a structural failure. As a consequence, it mobilises the efforts of experts from different areas of knowledge, namely mechanics, materials science, metallurgy, dynamics, among others. From these different areas, a variety of approaches to the problem emerge, some competing, others complementing, but all contributing for increasing the understanding of this phenomenon.

2.2 THE PHENOMENON OF FATIGUE DAMAGE

The problem of fatigue started capturing more attention of worldwide experts, during the Industrial Revolution, in the XIX century. Thousands of publications about this subject are available. Comprehensive perspectives about the historical evolution of knowledge on the fatigue problem can be found in (Schijve, 2003), (Schütz, 1996) or (Suresh, 2001). In the current work, the events considered as the most relevant are mentioned.

The first known study about fatigue dates back to 1829, when the German engineer W.A.J. Albert studied the strength of iron chains, used in the mining industry, when subjected to cyclic loading. The results of that study were published in the late 1830s. In 1854, the term "fatigue" was used for the first time by Braithwaite, on a paper where he describes several failures of equipment during the service phase (Suresh, 2001).

In 1843, W.J.M. Rankine stressed the pernicious effect of stress concentrations at railway train components. Wöhler, in turn, between 1852 and 1869, performed very important tests for the fatigue strength characterization of railway train axles (Suresh, 2001). He confirmed several phenomena:

- The strength of components to cyclic loading is substantially lower than their static strength;
- The stress range is determinant to the process of degradation by fatigue;
- The mean stress value, at each cycle, is relevant but not as important as the stress range;
- The structural details with notches present a shorter fatigue life than those details that have no notches;
- There are threshold stress range values below which the problem of fatigue may be neglected.

At that same time, numerous failures of railway train axles, under service, highlighted the relevance of the investigated subject. In the course of his work, Wöhler developed equipment to characterise the maximum load applied to the axles, under service, analysed the propagation of fatigue cracks and introduced, for the first time, the concept of finite life on structural design. This concept would only be considered again 75 years later. Wöhler revealed, yet, sensitivity for

the proper treatment of the dispersion of experimental results. His work led to the characterization of strength to fatigue in terms of S-N curves (also mentioned as Wöhler curves). However, the representation of S-N curves in double logarithmic scale occurred only in 1910, by Basquin, who described them on a very simple form:

$$N_i \cdot \Delta\sigma_i^m = C \tag{2.1}$$

where N_i is the fatigue life expressed as the number of loading cycles with a stress range of $\Delta\sigma_i$. Parameters m and C are dependent on each detail and material.

H. Gerber, in 1874, and Goodman, in 1899, developed methods for the computation of fatigue life taking into account the mean value of the applied stress cycles (Gerber, 1874, Goodman, 1899). Those methods led to the Gerber and Goodman curves (ESDEP, 1996), respectively.

In 1886, Bauschinger identified the variation of the elastic limit of metals by application of successive loading cycles (Bauschinger, 1886). This phenomenon is the starting point of most of the methods employed in the study of fatigue for low number of loading cycles, the low-cycle fatigue (Buciumeanu et al., 2011, Dowling, 2007).

Ewing and Rosenhain, in 1900, and Ewing and Humphrey, in 1903, demonstrated the development of microscopic slip bands at the surface of metallic materials subjected to cyclic loading (Ewing and Rosenhain, 1900, Ewing and Humphrey, 1903). Those slip bands ended up forming superficial elevations and depressions, named extrusions and intrusions, respectively. This was the first metallurgic description of fatigue phenomenon.

The concept of linear damage accumulation was first proposed by Palmgren, in 1924, and later by Miner, in 1945 (Palmgren, 1924, Miner, 1945). The main advantage of this concept is its simplicity, reflected on the well-known Palmgren-Miner rule:

$$D = \sum_i \frac{n_i}{N_i} \tag{2.2}$$

In that equation, D is the total fatigue damage accumulated over a certain period, n_i is the number of load cycles with stress range $\Delta\sigma_i$ during that period and N_i is the fatigue life of the detail for cycles having that same stress range. Nevertheless, several later studies highlighted many limitations to the application of this rule, which lacks of a sound physical basis and that may lead to non-conservative results (Sonsino, 2007).

In 1954, Coffin and Manson proposed, in different works, a relation between the range of plastic strain, $\Delta\varepsilon_p$, and the fatigue life, N_f (equation (2.3)). That relation is since then designated the Coffin-Manson equation and represents the most significant evolution on the analysis of low-cycle fatigue problems since the above mentioned discovery of the Bauschinger effect.

$$\frac{\Delta\varepsilon_p}{2} = \varepsilon_f'(2 \cdot N_f)^c \tag{2.3}$$

Parameter c is the fatigue ductility exponent, which is a characteristic of the material. ε_f' is the fatigue ductility coefficient.

Meanwhile, the stress analysis performed by Inglis (1913) and the energy concepts of Griffith (1921) were the first steps of Fracture Mechanics. Irwin (1957) showed that the magnitude of the stress field singularity around the crack tip can be described by the scalar parameter known as stress intensity factor, K. That scalar parameter depends on the geometry of the crack and of the detail and from the applied load, as denoted by equation (2.4).

$$K = Y \cdot \sigma \cdot \sqrt{\pi \cdot a} \tag{2.4}$$

On the previous equation, a represents the crack dimension, σ is the far actuating stress and Y is a parameter dependent on the detail geometry and crack dimension.

In 1961, Paris, Gomez and Anderson gave a decisive contribution on this subject (Paris et al., 1961). They suggested that, on the elastic domain and for constant amplitude loading, the advance of a fatigue crack, for each stress cycle (crack propagation rate) could be related to the range of the stress intensity factor, ΔK, in the same cycle. That relation is referred to as the Paris law (equation (2.5)):

$$\frac{da}{dN} = C \cdot \Delta K^m \tag{2.5}$$

The increase of the crack dimension at each load cycle, da/dN, is a function of the stress intensity factor range on that cycle, ΔK. Parameters C and m are material dependent.

This step had significant consequences, namely the reduction of the effort with fatigue crack propagation tests, since one single strength curve (or set of curves) was associated to each material, independently of the geometry of the detail under analysis.

Afterwards, Elber (1971) contributed to the enhancement of the computation of the crack propagation rate in cases of variable amplitude loading. He showed, with his work, that the fatigue cracks may be kept closed when subject to traction stress cycles after a cycle of higher

traction stress. He demonstrated also that in order to account for this crack closure effect, the effective values of ΔK, lower than the nominal values, should be considered (Figure 2.7).

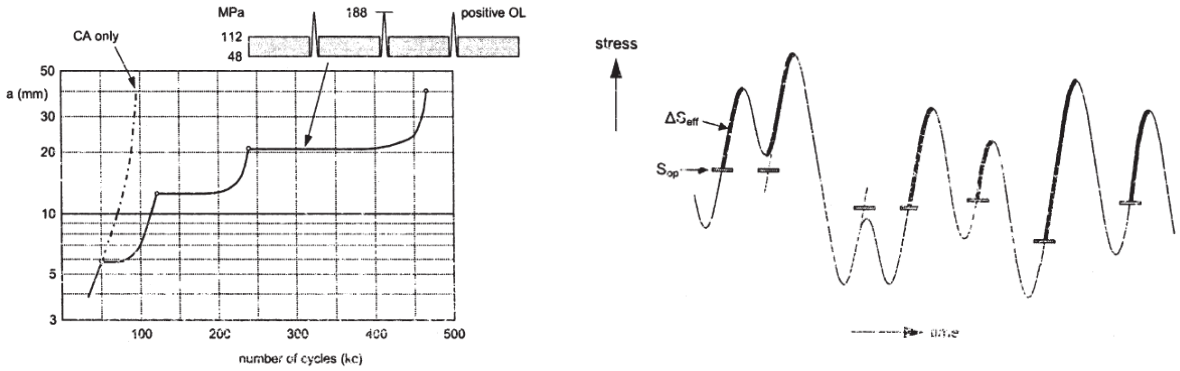

(a) (b)

Figure 2.7 - Effect of crack propagation retardation under variable loading conditions (Schijve, 2003): (a) crack propagation retardation and (b) effective stresses around the crack.

In the beginning of the 1980s, several researchers showed that the plasticity at the crack tip is only one of the several mechanisms of crack closure. The oxidation of crack faces, the phase modifications induced by stress and the inflections on crack propagation path are other factors to consider.

The relevance of the loading sequence on the fatigue damage had already been recognised in the beginning of the XX century. The 1st equipment destined to the characterization of loading appeared in the aeronautic industry, on the 1930s. Nevertheless, at that time, no test equipment was available that would be able to apply arbitrary load cycles over time. Consequently, several fatigue tests were performed using programmed loading blocks, with amplitude and mean value of the cycles varying from block to block (programme fatigue tests). In this field, the work performed by Gassner and published in 1939 is particularly relevant (Figure 2.8).

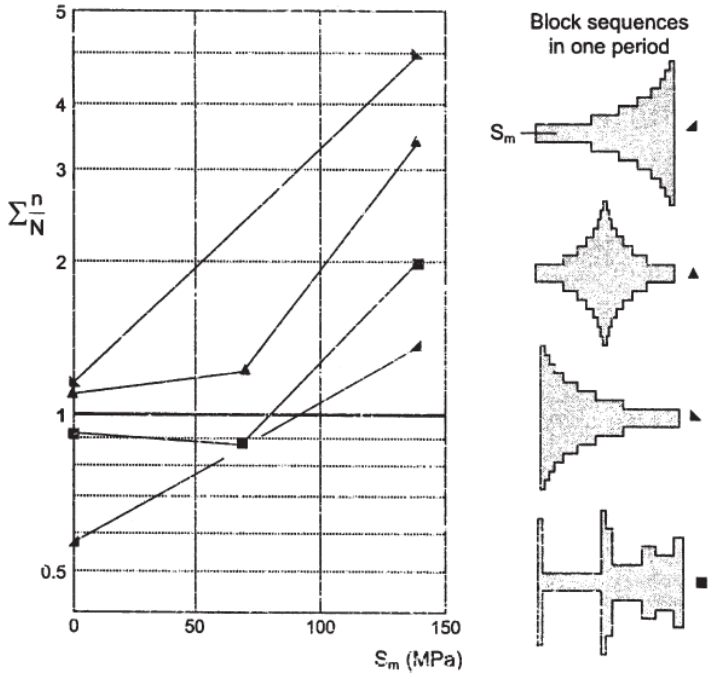

Figure 2.8 - Experimental results of variable amplitude fatigue tests (Schijve, 2003).

Still related to the problem of fatigue damage due to variable amplitude loading, it was only in 1968 that a method able to quantify the small load cycles present inside larger load cycles was developed. That method, designated as rainflow method was presented by Matsuishi and Endo (1968).

In the middle of XX century, the advances on electronic microscopy allowed increasing the comprehension of the phenomena of cyclic deformation and cracks initiation. In 1956, Thompson showed that the slip bands where the deformation was concentrated reappeared on the same locations even after their removal from surface (permanent slip bands). In 1951, Zapffe and Worden documented the observation of wavy marks on the fatigue fracture surfaces, with this marks being designated fatigue striation (Zapffe and Worden, 1951). The spacing between adjacent striations was correlated, for the first time, with the rate of fatigue crack propagation, by Forsyth and Ryder (1960). Since then, the analysis of the fracture surface (fractography) has been playing an important role on the analysis of fatigue induced structural failures and on the development of theories concerning fatigue crack propagation.

Many other important steps were made, such as the more recent evolutions in the fatigue analysis of composite materials (Zubillaga et al., 2014, Haojie et al., 2014) and the evolution on

the numerical methods of analysis, such as X-FEM (Rannou et al., 2010, Giner et al., 2009). Nevertheless, addressing all of them would make the present work excessively extensive.

As mentioned before, the fatigue problem consists on the initiation, stable propagation and, ultimately, unstable propagation of cracks, in structural details when subjected to cyclic loading (Figure 2.9). This is, therefore, a problem whose dimensional scale spans several orders of magnitude (Figure 2.10): it starts, usually, at the material crystals level (order of nanometres) and it may extend to the dimension of the structural elements (order of meters).

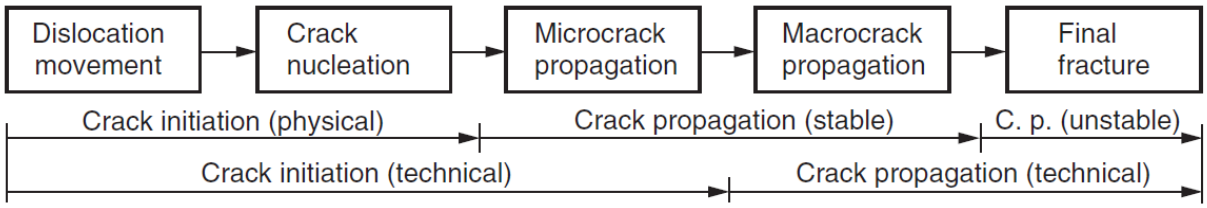

Figure 2.9 - Phases of fatigue damage (Radaj et al., 2006).

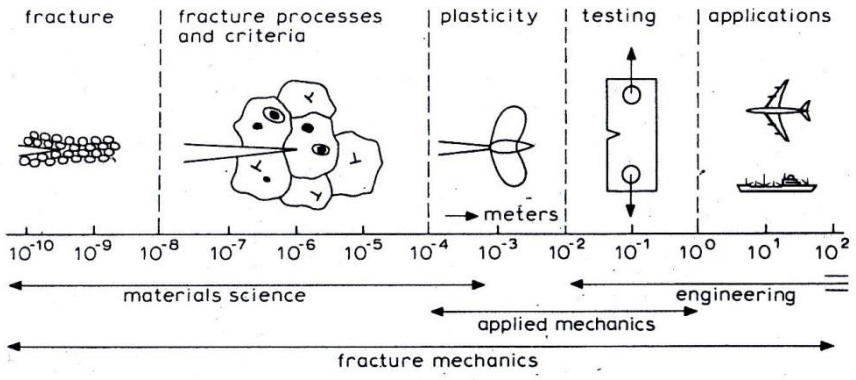

Figure 2.10 – Schematic representation of the orders of magnitude of the fatigue problem (Broek, 1987).

The process of degradation, by fatigue, usually starts at the crystals that compose the material matrix, by atomic dislocations, when shear stress cycles are present (Figure 2.11).

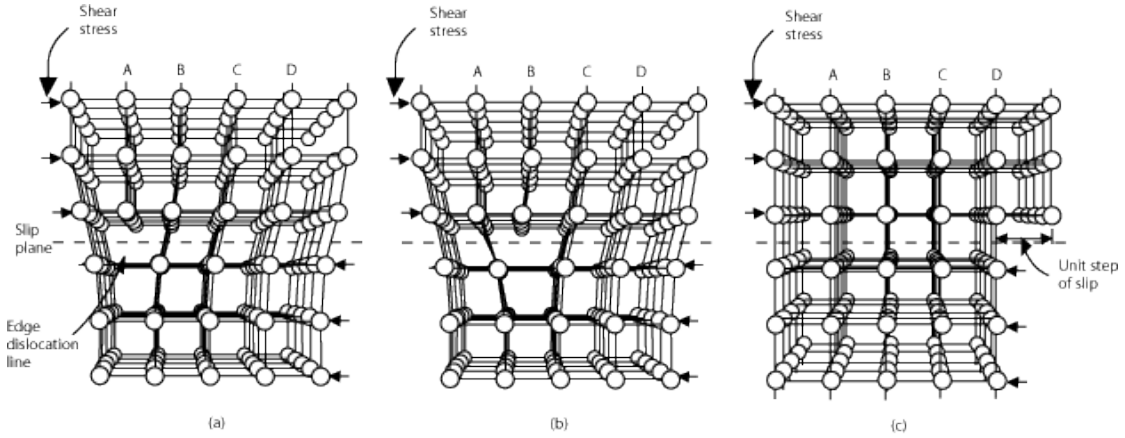

Figure 2.11 - Illustration of the atomic dislocations phenomenon (NDTRC, 2014).

During the fatigue cracks initiation, stress ranges, considered as elastic at macroscopic scale, induce the cyclic movement of microscopic misalignments without any detectable change on the global behaviour of the structural component. At the critical point, slip bands are generated and some of them originate superficial intrusions and extrusions. One of those intrusions and extrusions starts gaining ascendancy over the others and subsequent deformations concentrate on it. That dominant extrusion/intrusion acquires the dimension of a micro-crack, with the dimension of some material grains and with a direction nearly parallel to the direction of maximum shear stress. It can be considered that that micro-crack becomes a crack when it starts propagating on a plane perpendicular to the normal stress (Figure 2.12).

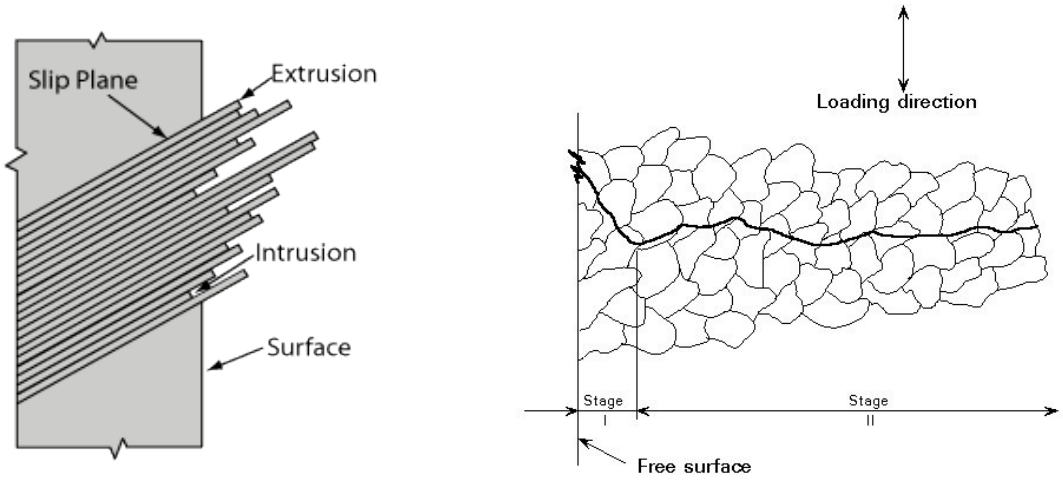

(a) (b)

Figure 2.12 - Cracks initiation and micro-cracks propagation: (a) generation of extrusions and intrusions (NDTRC, 2014) and (b) micro-crack and crack propagation from extrusions and intrusions (ESDEP, 1996).

After the initiation phase, the crack propagation is no longer controlled by the stress range. The determinant factor is, then, the range of the stress intensity factor, *K*. That propagation occurs slowly, until the maximum stress intensity factor, K_{max}, reaches the material toughness, K_C, or until another rupture mechanism manifests. The striation formed by the successive loading cycles is a characteristic image of this phase of the fatigue life (Figure 2.13).

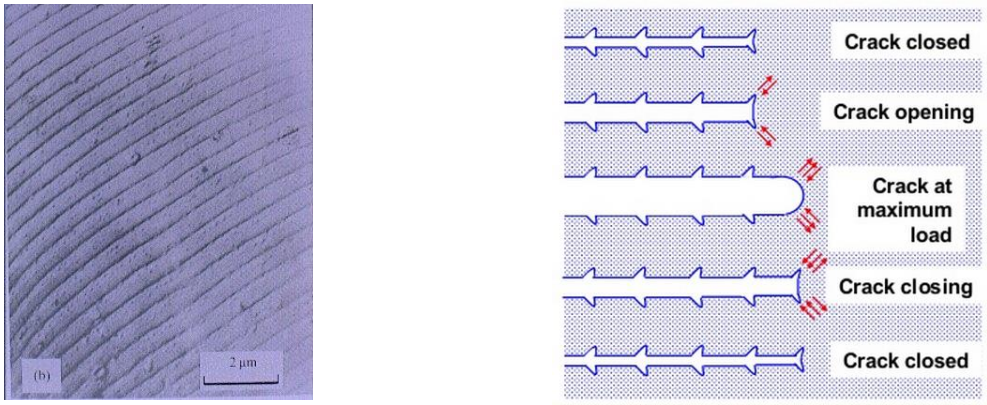

(a) (b)

Figure 2.13 - Fatigue striation: (a) example of a fracture surface with fatigue striation (ESDEP, 1996) and (b) process of striation generation (NDTRC, 2014).

The observation of fracture surfaces (fractography), namely, the analysis of the spacing, pattern and direction of the striation present on the fatigue cracks surface (Figure 2.14) are a precious aid for the interpretation of structural failure events. Among other aspects, it helps to interpret the type of loading that induced that failure and its frequency. In spite of striations not being visible with the naked eye, concentric corrugation is generally visible macroscopically, departing from the crack initial point. It should be noted, however, that the aspect of the fatigue striations in Civil Engineering structural steel is not as well defined as for other metallic alloys, namely aluminium alloys commonly employed in aerospace engineering.

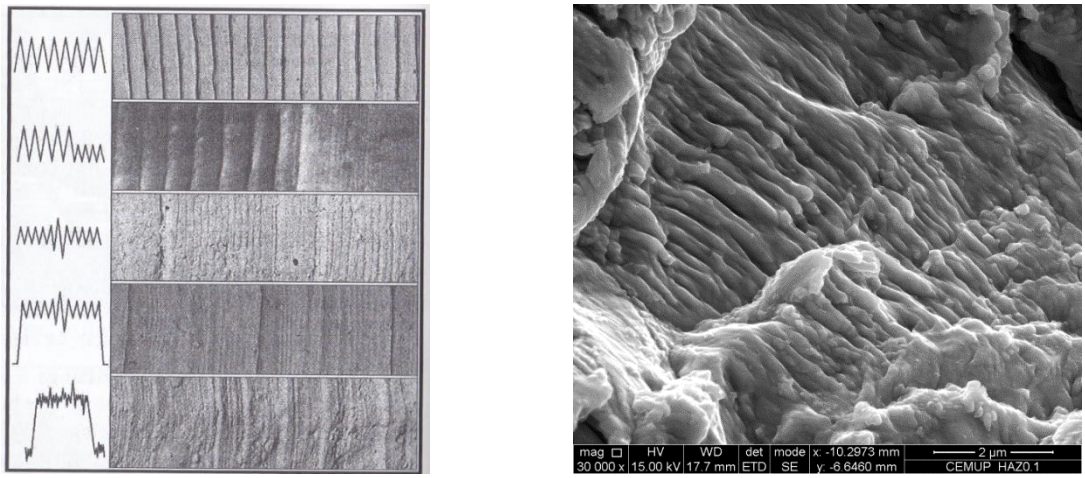

(a) (b)

Figure 2.14 - Fatigue cracks surface: (a) relation between cyclic loading and crack surface striation appearance (de Castro and Meggiolaro, 2009a) and (b) striation on the fracture surface of a structural steel (Richter-Trummer et al., 2011).

When the crack reaches a certain critical dimension, the fracture of the structural element begins, in a brittle or in a ductile way. If the fracture is ductile, it happens due to cavitation and coalescence of internal micropores, from particles on suspension at the material matrix (Figure 2.15(a)). Fractographically, small pores are observed at the fracture surface (Figure 2.15(b)). One favourable feature of ductile fracture is that the high plastic deformations associated are a visible warning about the poor condition of the structural component. On the other hand, the fracture mechanism observed on the brittle fractures is cleavage. The fracture surface presents plane steps and facets. The energy absorbed during this process is much lower than that absorbed on a ductile rupture, and that is the reason why the brittle fractures may progress in an unstable and sudden way.

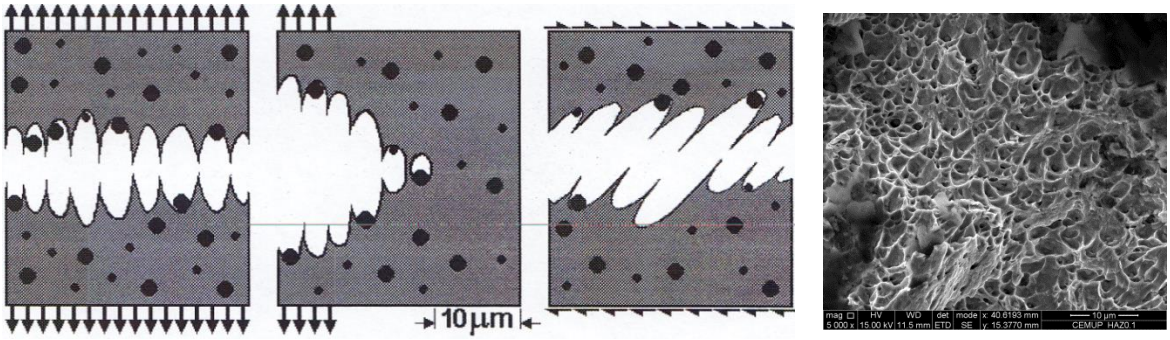

(a) (b)

Figure 2.15 - Ductile fracture: (a) cavitation phenomenon (de Castro and Meggiolaro, 2009a) and (b) ductile fracture surface (Richter-Trummer et al., 2011).

2.3 CAUSES FOR FATIGUE DAMAGE OF STEEL AND COMPOSITE BRIDGES

The problem of fatigue occurs on steel and steel-concrete composite bridges due to a variety of factors. According to Miki (2007), the most relevant are: i) the existence of defects on welds; ii) the adoption of details with poor fatigue behaviour; iii) the occurrence of unattended stresses and deformations at some of the connections (secondary distortions and tensions); iv) excessive vibrations. Furthermore, when in the presence of aggressive environments, the worsening due to corrosion must be considered.

Each one of these factors may justify, alone, the occurrence of fatigue damage. Nevertheless, often, this damage results from the simultaneous contribution of more than one parameter.

The understanding of the root causes of a fatigue crack is fundamental when evaluating the timing of action and the definition of an eventual maintenance/retrofitting operation.

2.3.1 Presence of defects on the welds

The defects present on the welds result from the welding process and vary in shape and dimension. They may be located in the base material, in the weld metal (WM) or in the heat affected zone (HAZ). The following may be included among the most common types of defects: partial penetrations, inclusions, voids (worm hole) and cracks (Figure 2.16).

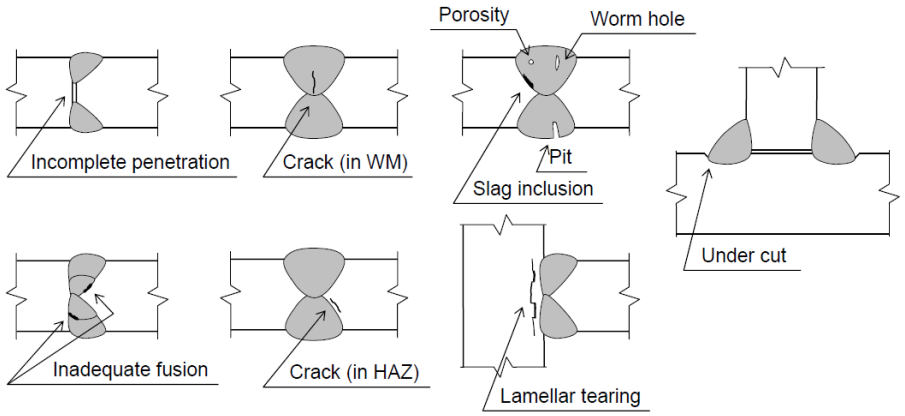

Figure 2.16 - Different types of defects found in welds (Miki, 2010).

Nevertheless, it must be underlined that, even in the absence of initial defects, the stress concentrations induced by the geometry of the weld may be enough to initiate a fatigue crack (Figure 2.17).

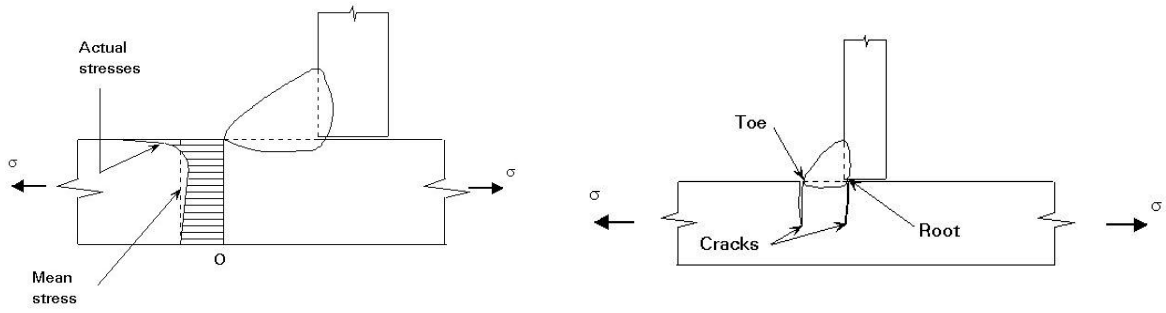

(a) (b)

Figure 2.17 - Crack initiation in the welds due to stress concentrations (ESDEP, 1996): (a) stress concentrations on the weld and (b) potential crack locations.

2.3.2 Adoption of details with poor fatigue behaviour

The adoption of details with poor fatigue behaviour may be due to an inadequate evaluation by the structural designer/engineer. That can happen when performing the original design of the structure but also when designing retrofitting measures for existing structures (Cho et al., 2001). Structural components with high stress concentrations, no structural redundancy, limited loads re-distribution capacity or inaccessible for inspections are more prone to show poor fatigue performance. Excessive level of constraint at extremities of beam type elements or the use of materials with inappropriate mechanical properties (such as excessive hardness and brittleness) can also be considered as causes for inadequate fatigue behaviour.

Furthermore, in some cases, the stresses considered as allowable by the standards end up being inappropriate. In fact, the construction of standard S-N curves for welded connections was in many cases, based on small scale specimens. Even if, in the recent years the standards were upgraded, the structures conceived in the light of the previously existing regulations may be, in a limited number of situations, undersized to fatigue (Pedersen et al., 2010).

2.3.3 Secondary deformations and stresses

Significant discrepancies between the stresses and strains forecasted at design phase, and those observed in reality, are frequently noted. That is due, often, to simplifications adopted at design phase. Those simplifications occur mainly at joints and support conditions.

In the case of joints, in reality they have a certain level of flexibility. Nevertheless, when modelling, generally extreme conditions are assumed: total continuity or, alternatively, a hinge.

Moreover, the use of simplified models, such as beam finite elements, does not allow to take into consideration the distortional and secondary effects that arise at connections and that only shell and brick element models can reproduce (Figure 2.18). Finally, real structures present eccentricities, as a result of the construction process, that originate secondary bending moments and a significant increase in stresses.

Regarding the support conditions, in the design phase, unconstrained horizontal displacements (longitudinal and transversal) and free rotations are often assumed. However, after the construction of the structures those movements may become progressively constrained, due to debris accumulation and corrosion. That phenomenon originates additional stress cycles that may cause fatigue problems.

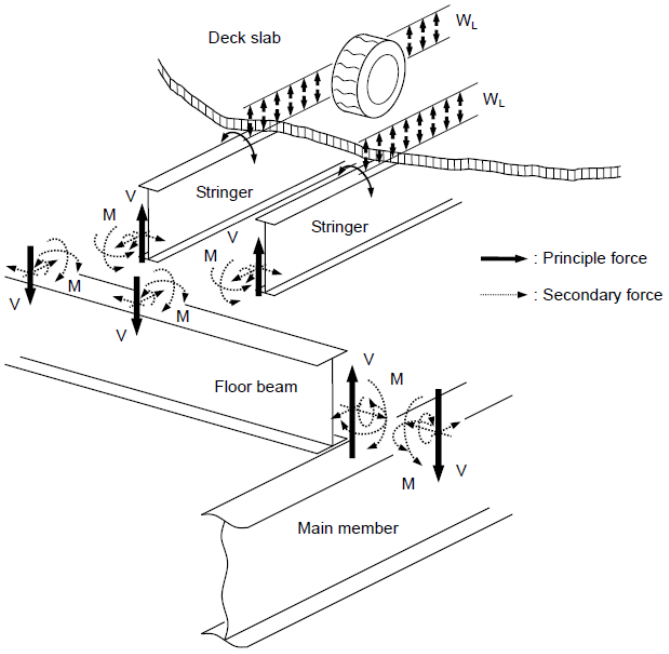

Figure 2.18 - Example of main and secondary connection forces (Miki, 2010).

2.3.4 Excessive vibrations

The explicit analysis of the dynamic behaviour of Civil Engineering structures can be considered as a recent practice. Moreover, those analyses focus, usually, on the main structural elements and/or, in the case of bridges, on the elements directly loaded by traffic.

As a consequence, excessive unforeseen vibrations are a frequent phenomenon. Those vibrations originate, on the one hand, the increase on the amplitudes of stresses/deformations and on the other hand an increase in the number of stress/deformation cycles, thus contributing to a higher tendency of those structures to the fatigue problem (Sakamoto et al., 1990).

2.4 EXAMPLES OF FATIGUE DAMAGE ON STEEL AND COMPOSITE BRIDGES

There are numerous examples of fatigue damage in steel and composite bridges reported in bibliography. Special reference should be made here to the publications, on this subject, of Chitoshi Miki (2010), John W. Fisher (1984) and Al-Emrani and Kliger (2009).

The experience and knowledge about past manifestations of fatigue are a valuable instrument when evaluating the potential critical points of new and/or existing structures. Those analogues are useful not only on the design phase but also when preparing for inspection activities.

Some of the cases of fatigue damage reported in the bibliography are described below, grouped according to the location of the fatigue cracks found:

- Eyebars and hangers;
- Flange cover plates;
- Diaphragms and cross-bracing connections and connections between floor-beams and the main load-carrying members;
- Web penetration and orthotropic decks;
- Structural elements with changes in cross section;
- Weld defects;
- Lamellar tearing;
- Others.

Haghani et al. (2012) present a categorization of fatigue failures of steel bridges, by type, as illustrated in Figure 2.19.

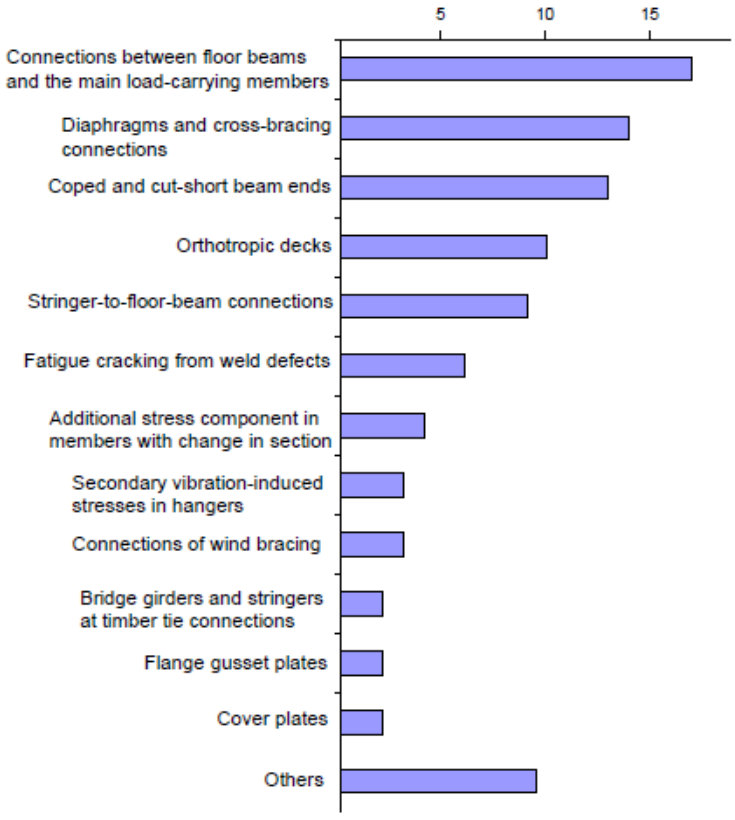

Figure 2.19 - Categorization of fatigue failures of steel bridges (Haghani et al., 2012).

That categorization is in good agreement with the results presented by Demers and Fisher (1989) and Walker et al. (1992), summarised in Table 2.2 and Lindberg and Schultz (1997), summarised in Table 2.3.

Table 2.2 – ATLSS survey of cracking in bridges (Walker et al., 1992).

Classification of Cracking Problem	No. of Cases
Coped Members	22
Diaphragm Connection Plates (web gaps cited)	15
Connecting End Angles on Webs	7
Web Gap -- Web to Gusset Details	13
Flange–Gusset Plate Connection	10
Cover Plate Splices	5
Welded Cover Plate Termination	5

Table 2.3 – Minnesota (USA) Department of Transportation survey of cracking in bridges (Lindberg and Schultz, 1997).

	Detail Symbol**										
Responding Authorities	α	β	γ	δ	ε	ζ	η	θ	κ	λ	μ
Arkansas	7	5	3	4	6	0	1	2	0	0	0
California	5	2	3	4	0	0	0	0	1	0	0
Delaware	2	3	4	0	0	1	0	0	0	0	0
Georgia	3	2	0	0	1	0	0	0	0	0	0
Illinois	5	6	3	2	4	0	1	0	0	0	0
Indiana**	6	5	4	3	1	2	0	0	0	0	0
Minnesota	9	6	8	5	7	4	3	2	0	1	0
Mississippi	4	3	0	2	1	0	0	0	0	0	0
Missouri	8	4	2	5	7	6	3	0	0	0	1
Montana	5	1	9	8	7	4	0	3	6	0	2
New Jersey	2	1	0	0	0	3	0	0	0	0	0
Tennessee	4	1	2	5	0	0	0	3	0	0	0
Texas	4	2	0	0	1	0	3	0	0	0	0
Washington	4	7	1	6	2	0	0	0	5	3	0
Wyoming	5	4	3	0	2	0	0	0	0	0	1
Army Corps-New England	0	0	1	0	0	0	0	0	0	0	0
TOTALS	73	52	43	44	39	20	11	10	12	4	4

α = transverse stiffener web gap
β = insufficient cope radius
γ = partial length cover plate
δ = shelf plate welded to girder web
ε = stringer to floor-beam truss bracket
ζ = transverse groove weld (welded horizontal stiffener & haunch insert)
η = web penetration
θ = cantilever floor-beam bracket
κ = continuous longitudinal weld: box girder corner
λ = tied arch floor-beam
μ = cantilever: lamellar tear

In the following sections, some examples of bridges presenting typical fatigue crack patterns are presented and discussed.

2.4.1 Eyebars and hangers

The propagation of fatigue cracks in hangers and eyebars can be particularly critical, if one considers that those cracks are frequently located in places with difficult access and that, most of the times, the hangers are elements for which the structure has no structural backup or redundancy. There are various causes for fatigue cracks in these elements, as demonstrated by several events reported in the past.

2.4.1.1 Silver Bridge

The Silver Bridge was concluded in 1928, in USA. The deck, with a total length of 534.3 m was supported by chains of hangers associated to lattice girders, as illustrated in Figure 2.20.

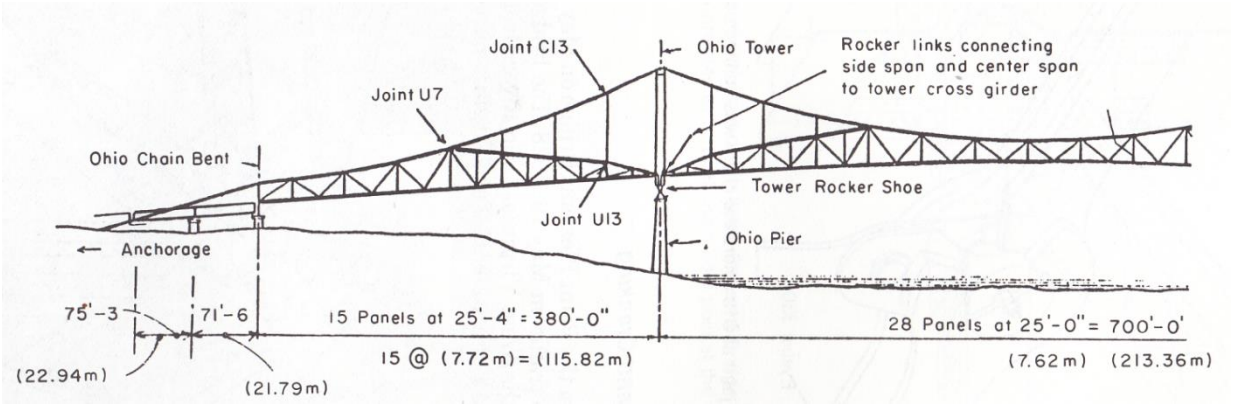

Figure 2.20 - Schematic elevation view of the Silver Bridge (Fisher, 1984).

The bridge collapsed in December 1967, almost 40 years after its inauguration. Subsequent investigations clearly showed that the nominal stresses installed on the hangers of the bridge at the time of the accident did not exceed the stresses allowable by design. The principal cause of the collapse was the unstable propagation of 2 cracks located in the hole of the eye-plate of one of the hangers of C13N connection, identified in Figure 2.20.

The cracks initiated and developed due to corrosion induced fatigue, since the material used on the fabrication of the hangers proved to be highly susceptible to the aggressiveness of the environment and the cracks surface showed high content of corrosion products. In addition, the stress concentration in the eye-plate contributed to the increase of the actuating stresses. At the same time, the cracks developed in a section of the hanger where the hardness was higher and consequently the toughness was lower. Finally, the low temperatures recorded at the time of the accident (-1 °C) led to even lower toughness values, originating the brittle fracture of the element and of the structure.

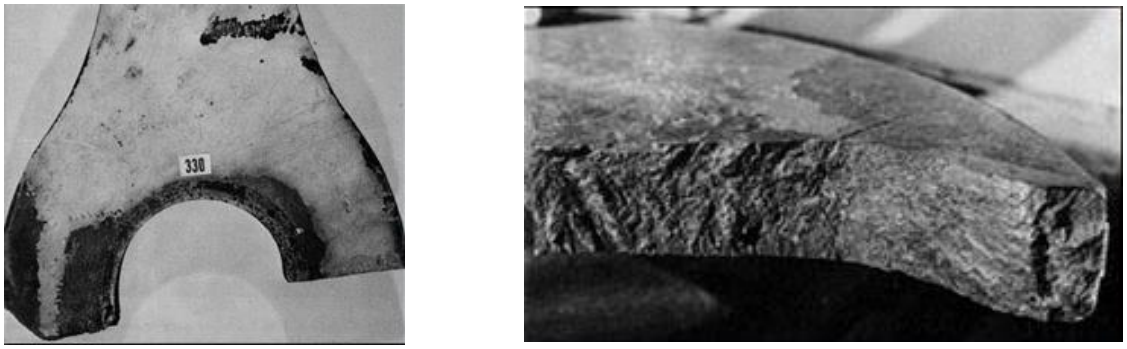

(a) (b)

Figure 2.21 - Eye-plate of the *Silver Bridge* after collapse (Fisher, 1984): (a) eye-plate and (b) fracture surface.

2.4.1.2 Sungsoo Grand Bridge

The Sungsoo Grand Bridge is a multi-span Gerber-type structure, located in Seoul, South Korea, where it crosses the Han River. In the 21st October of 1994 one of its spans (Figure 2.22) collapsed (Cho et al., 2001).

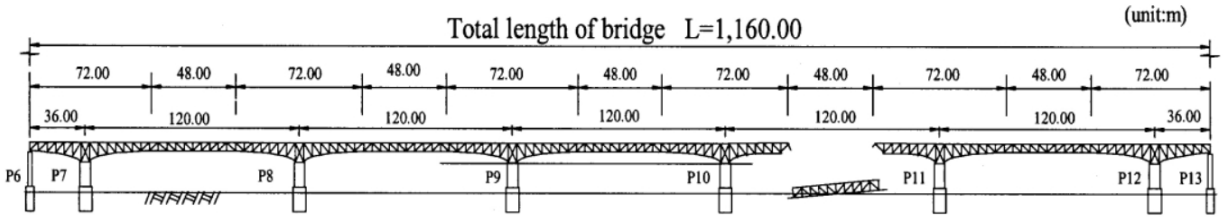

Figure 2.22 – Elevation view of the collapsed Sungsoo Grand Bridge (Cho et al., 2001).

Subsequent investigation of the accident has demonstrated that the cause for the collapse was the fatigue crack propagation and fracture of one of the vertical hangers that connected the suspended truss to the anchor trusses.

The fatigue cracks were initiated due to poor welding at the extremities of the H-section hangers (Figure 2.23).

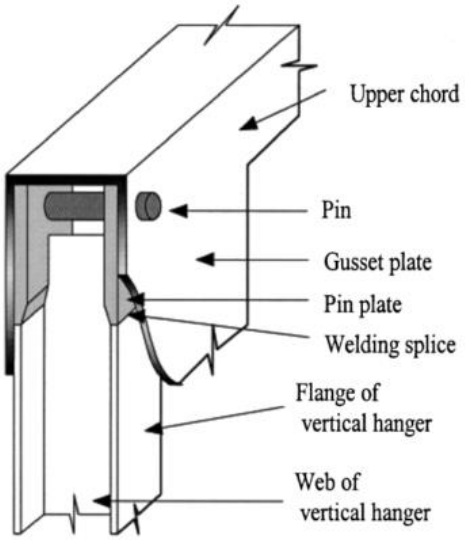

Figure 2.23 – Typical connection of vertical hanger (Cho et al., 2001).

Crack propagation was accelerated by inappropriate structural reinforcement measures that were put in place to mitigate excessive deflection of end floor beams. Those measures originated much larger loads and stress ranges at the welded joints than those for which the structure had originally been designed for.

Finally, poor maintenance of the bridge and excessive truck traffic were additional reasons found for crack propagation and final fracture.

2.4.1.3 Illinois Route 157 Bridge

Another case of cracks propagation at eye-plates and hangers was the Illinois Route 157 Bridge, in USA (Figure 2.24(a)). This skewed bridge, with 7 spans totalizing 144.7 m presents 13 longitudinal beams, parallel and 1.67 m apart each other's. The 2nd and 6th span present a 30.5 m length, from which a 18.3 m segment is suspended. The suspended segments have double support in one of their extremities and a simple support on the other one. That simple support is materialised by hangers, as illustrated at Figure 2.24(b).

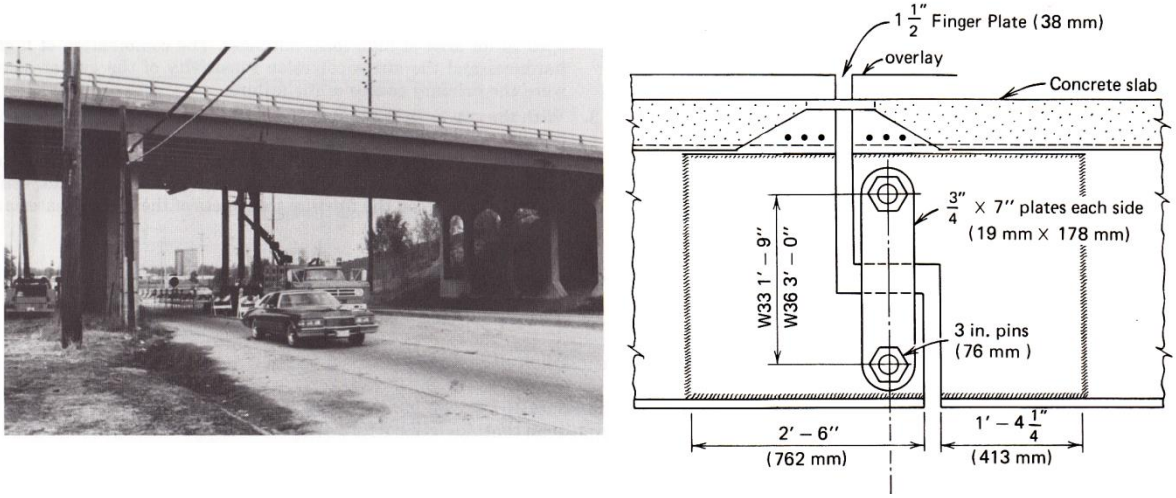

(a) (b)

Figure 2.24 - Illinois Route 157 Bridge (Fisher, 1984): (a) perspective of one suspended segment and (b) scheme of a hanger.

The bridge was built in 1945. In 1978, several of the above mentioned hangers were found to be fractured. The analysis of this case revealed that the cracked hangers, as well as the remaining ones, presented the lower hinge blocked by debris and corrosion products. Consequently, these elements were not only under axial forces, but also under bending on their plan, due to the thermal expansion and traffic. In light of the high actuating stress levels, fatigue cracks initiated and propagated until the final fracture of the elements.

2.4.1.4 Bridge over river Skellefte

The bridge over the river Skellefte, in Sweden, is a 61 m span bowstring bridge, built in 1943. The arches are localised on each side of the deck, suspending the main girders. The main girders are connected by cross girders. The hangers are composed by steel cables with 79 mm diameter. These elements are usually designed to axial stress, with the extremities considered as hinges. However, that does not correspond to reality, as can be observed in Figure 2.25. In the beginning of the 1980s, fatigue damage was found in several hangers. Some of them had their connection to the arches totally broken. The fatigue cracks were justified by the high number of stress cycles induced by excessive vibration and by secondary bending.

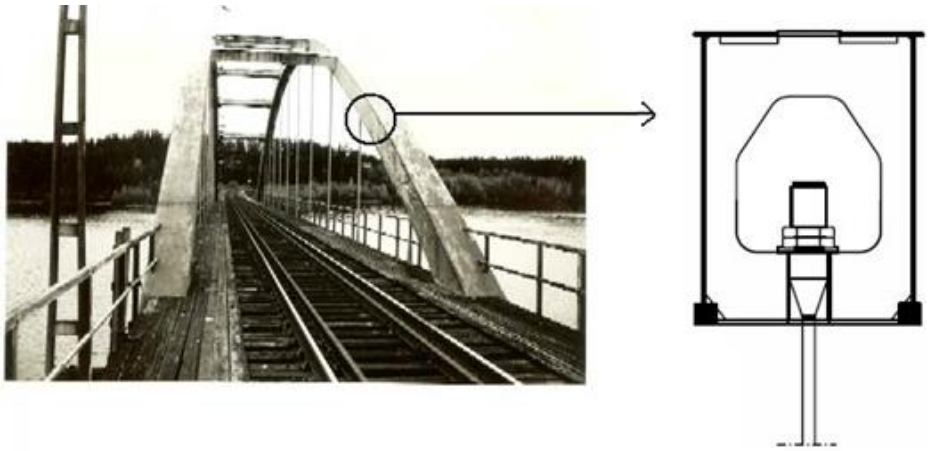

Figure 2.25 - Bridge over the river Skellefte and hanger-to-arch connection (Al-Emrani and Kliger, 2009).

2.4.2 Flange gussets and cover-plates

The flanges of steel girders, like I-section beams, box girders, or others, are elements that suffer significant stress cycles. Consequently, any geometric discontinuity that induces stress concentrations in those flanges may be considered as a privileged location for the initiation of fatigue damage. Some examples of those discontinuities are the extremities of the cover-plates welded to the flanges and the gussets welded laterally to them.

2.4.2.1 King's Bridge

The collapse of the King's Bridge, in Melbourne, Australia, is a case of serious damage resulting from the propagation of fatigue cracks from the weld of a flange's cover-plate. The structure is illustrated in Figure 2.26.

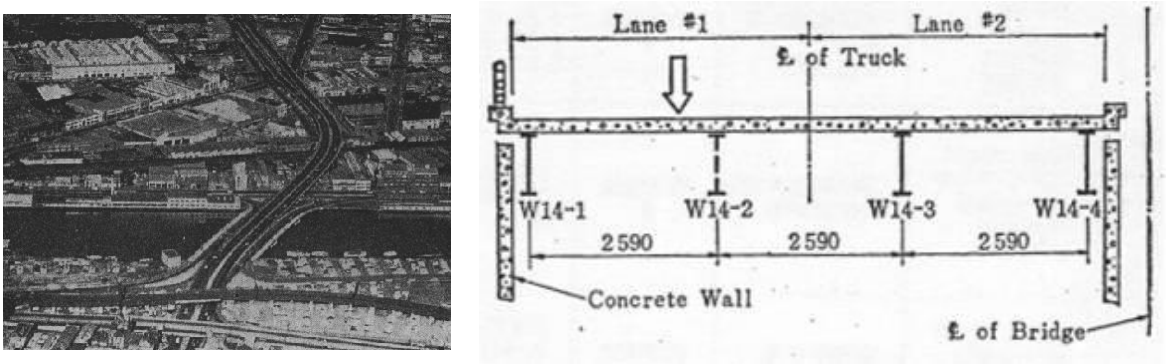

(a) (b)

Figure 2.26 - King's Bridge, Melbourne, Australia (Miki, 2010): (a) overview and (b) typical cross-section.

The bridge was concluded on April 1961. On July 1962, in a very cold day in Melbourne, one of the spans of the bridge collapsed. The analysis of the accident revealed the brittle propagation of fatigue cracks from the fillet weld of a flange's cover-plate (Figure 2.27).

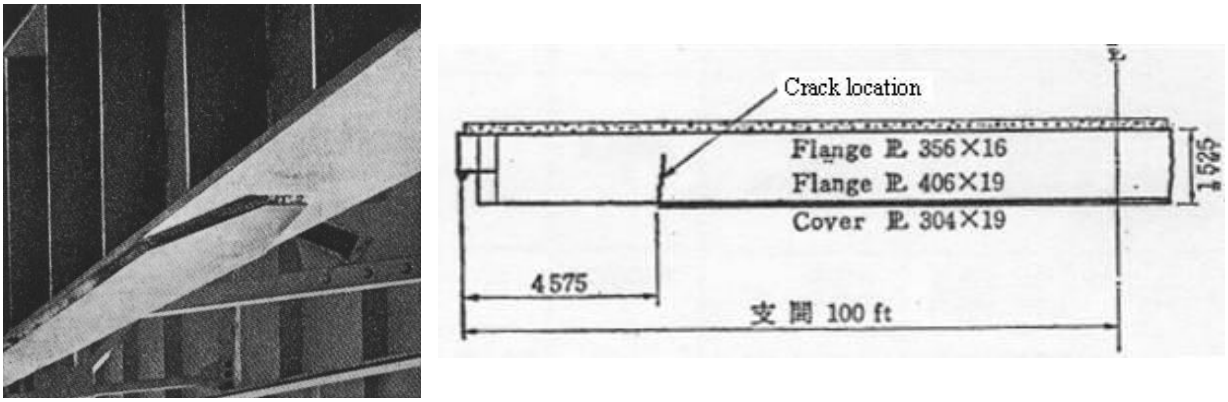

(a) (b)

Figure 2.27 - Cover-plate at King's Bridge (Miki, 2010): (a) cover-plate and (b) schematic of the crack propagation.

2.4.3 Diaphragms, cross-bracing connections and connections between floor beams and the main load-carrying members

The transverse connections to the webs of longitudinal girders are, frequently, points prone to fatigue damage, due to the introduction of out of plane bending moments and secondary stresses and deformations. This phenomenon is particularly relevant considering that diaphragms, cross-bracing connections, floor beams and cross-girders are very common in steel and composite bridges. Usually, in those connections, there are vertical loads applied to the webs and to the welds, thus perpendicular to the directions of the main stress cycles.

2.4.3.1 Lafayette Street Bridge

The bridge of the Lafayette Street, is located in the USA and crosses the Mississipi river. This bridge presents 2 parallel structures, each one of them having 3 spans, the central with 110 m and the extremes with 82 m (Figure 2.28). Each structure is composed by two main I-section girders, stringers and cross-girders that sustain a thin concrete slab.

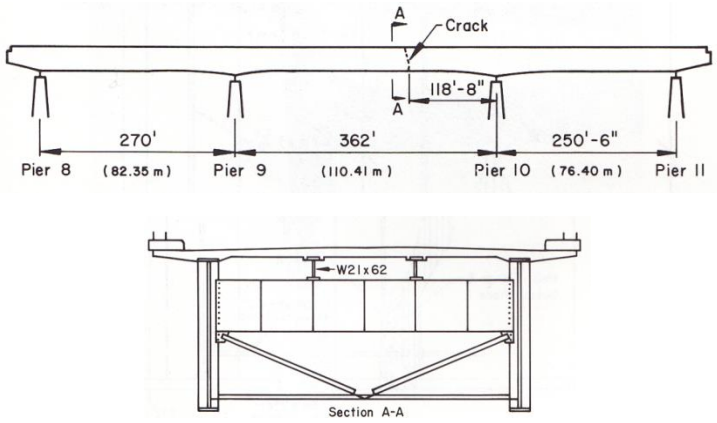

Figure 2.28 - Bridge of Lafayette street (Fisher, 1984).

The bridge was opened to traffic in 1968. In 1975, a fatigue crack was found in one of the main girders of the central span. That crack had totally fractured the lower flange and had propagated through the web until it reached 200 mm below the upper flange, which represents almost the total fracture of the girder's section (Figure 2.29).

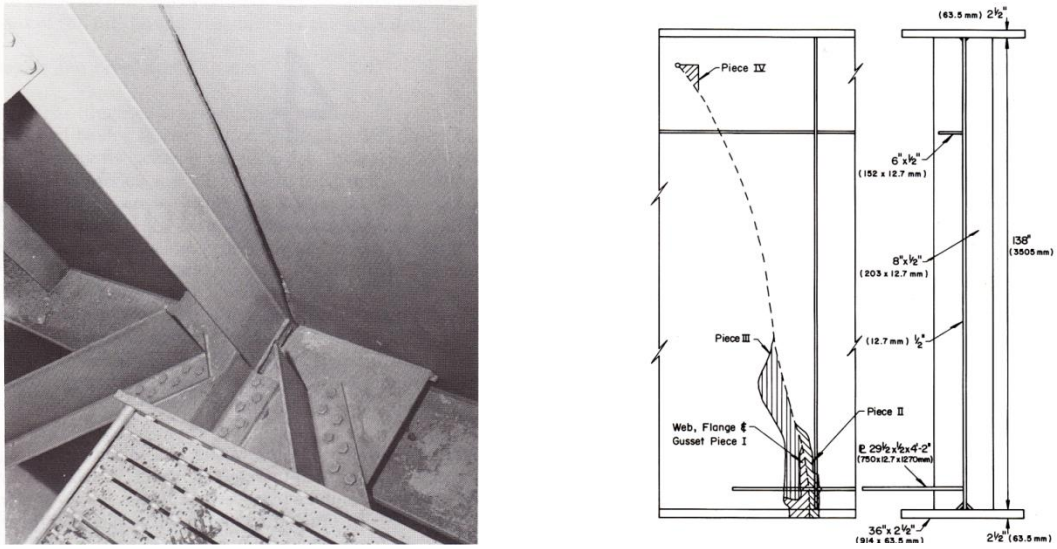

(a) (b)

Figure 2.29 - Fatigue crack at the Lafayette Bridge (Fisher, 1984): (a) fatigue crack and (b) schematics of the crack propagation.

Further investigations showed that the crack initiated in one of the gussets used in the connection, at a weld where partial penetration occurred (Figure 2.30).

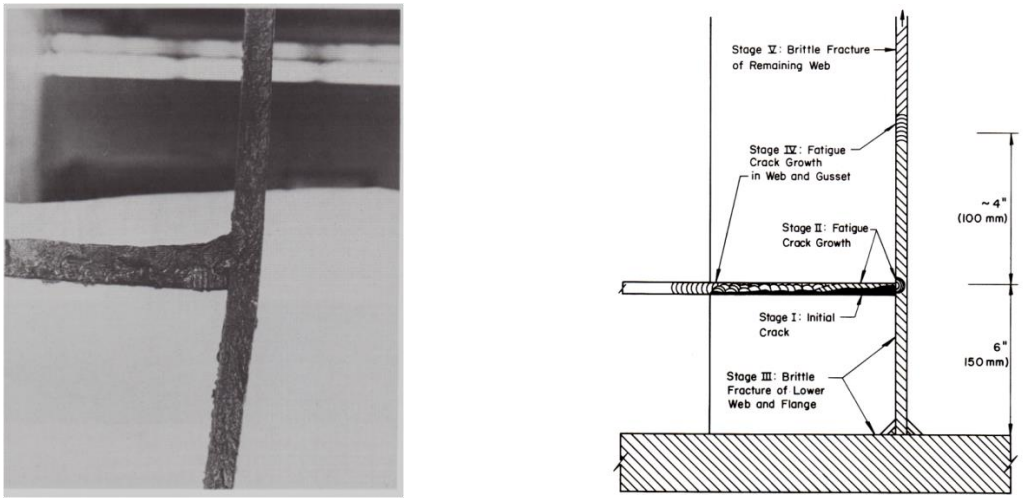

(a) (b)

Figure 2.30 - Fatigue crack initiation zone (Fisher, 1984): (a) fractured section and (b) stages of the crack propagation.

2.4.3.2 Panaro Bridge

The Panaro Bridge is a steel bowstring railway bridge (Figure 2.31), located in the Bologna-Verona railway line, Italy (Lippi et al., 2011).

Figure 2.31 – Panaro Bridge (Lippi et al., 2011).

This 75.6 m span bridge has developed, during its service life, fatigue cracks in some structural elements such as the track's cross beams. Those cracks originated at the extremities of the beams, where the bolted connection to the main girders created high distortion induced stresses. In order to mitigate this problem, the cross beams were cut to stop the crack propagation (Figure 2.32)

and the external bolts of the connections to the main girder were removed so that the distortion bending moments could be reduced.

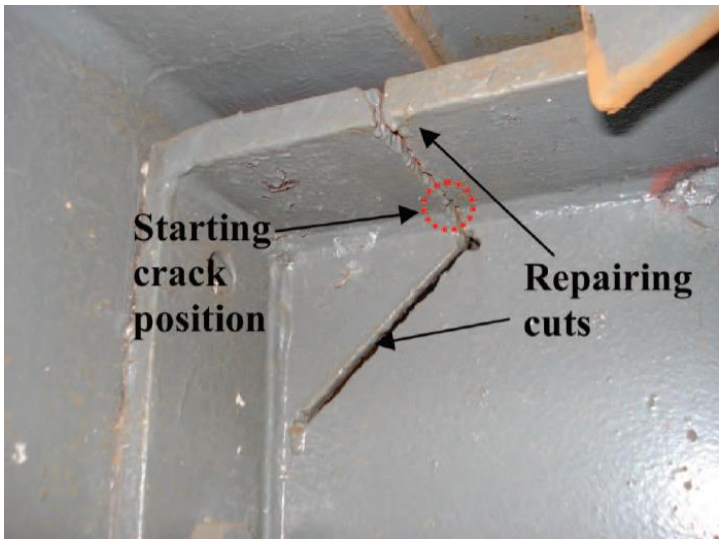

Figure 2.32 – Distortion induced fatigue crack at track's cross beam (Lippi et al., 2011).

This bridge also experienced fatigue cracks at the longitudinal welds between the top flange and web of the main girders, as a consequence of tight sleepers-longitudinal girder connection by catch bolts (Figure 2.33). In this case, the cracks were induced by the resulting high vibration levels.

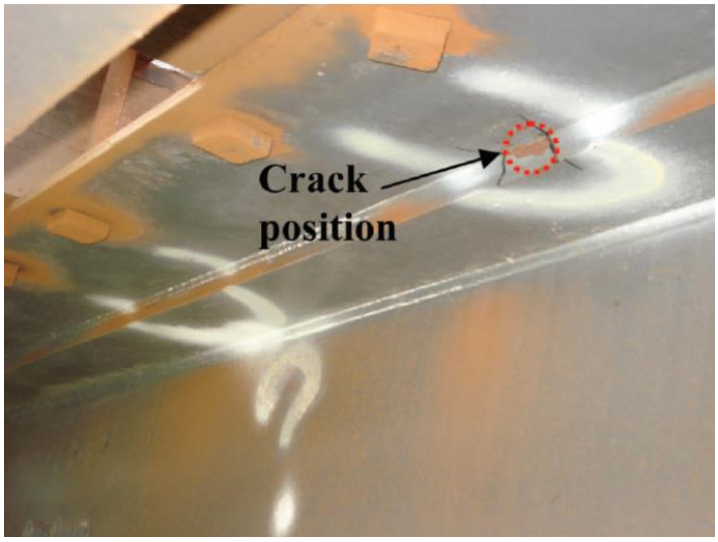

Figure 2.33 – Vibration induced fatigue crack at sleepers-longitudinal girder connection (Lippi et al., 2011).

2.4.3.3 Bridge over river Belle Fourche

As mentioned before, the transverse connection of diaphragms to the webs may also promote the initiation of fatigue cracks. That was the case observed at the bridge over river Belle Fourche. That structure, located in the USA and open to traffic in 1958, presents 3 continuous spans with a total length of 104.2 m and 4 simply supported spans, 18.3 m each. The composite section is composed by 7 I-section beams supporting a concrete slab (Figure 2.34). The several beams are braced by diaphragms built with angle bars.

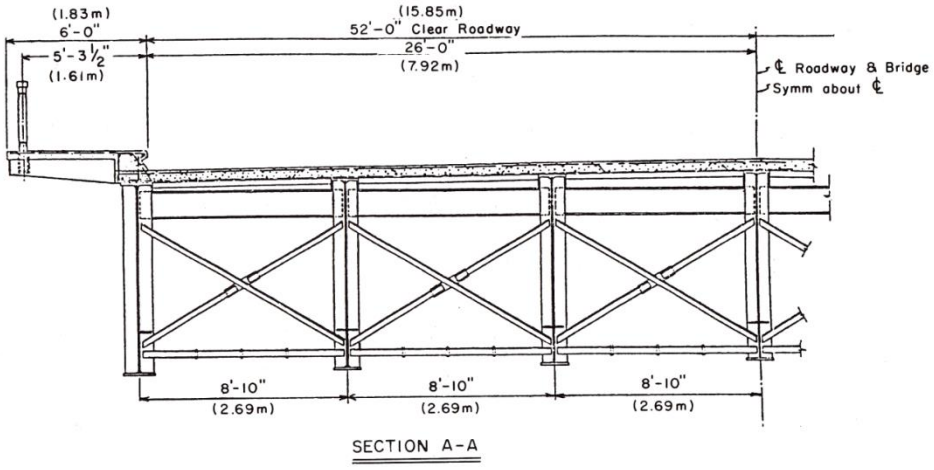

Figure 2.34 - Fatigue crack initiation zone (Fisher, 1984): (a) fractured section and (b) stages of the crack propagation.

In 1976, during the routine inspection to the deck of the bridge, numerous fatigue cracks were found in the webs of the longitudinal beams. Most of the cracks were localised between the vertical web stiffeners holding the diaphragms and the upper flanges (Figure 2.35) and developed due to out-of-plane bending (distortion) of the web.

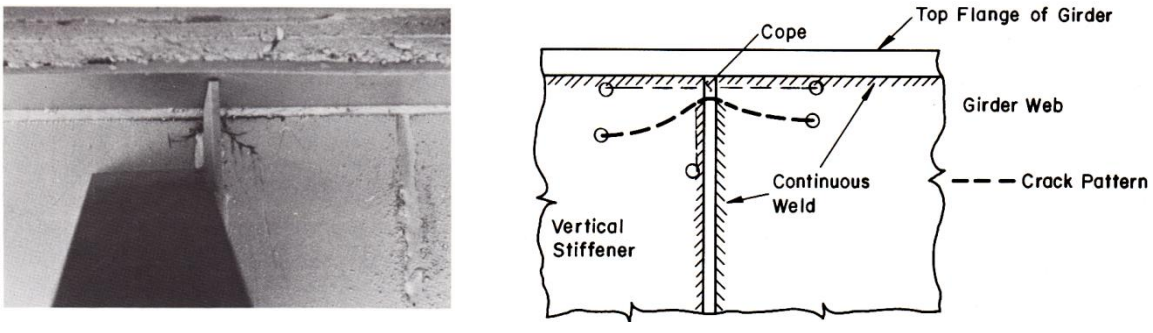

(a) (b)

Figure 2.35 - Fatigue cracks in the bridge crossing the river Belle Fourche (Fisher, 1984): (a) fractured detail and (b) schematics of crack propagation.

2.4.4 Web penetration and orthotropic decks

In some bridges, the longitudinal structural elements cross directly the transverse elements originating discontinuities at the later. That is the case of steel bridges supported and fixed directly in steel bents or the case of floor beams passing through cross beams. In those situations, two reasons contribute to the occurrence of fatigue cracks. In the one hand, the geometric discontinuity originates high stress concentrations; on the other hand, the welding process conditions are, many times, difficult, leading to initial defects at the welds. Some examples are presented next.

2.4.4.1 Dan Ryan railway viaduct

The Dan Ryan railway viaduct (Figure 2.36(a)), open to traffic in 1969, is a steel structure, with circular development connecting the centre of Chicago, USA, with the south and west areas of the city (Sulloway et al., 1979). The deck is formed by 4 continuous beams (Figure 2.36(b)), which support a concrete slab and, on the top of it, 2 ballasted tracks. The beams are supported by steel bents, with rectangular section. The lower flange and part of the web of the longitudinal beams cross the bents and are connected to them by but welds.

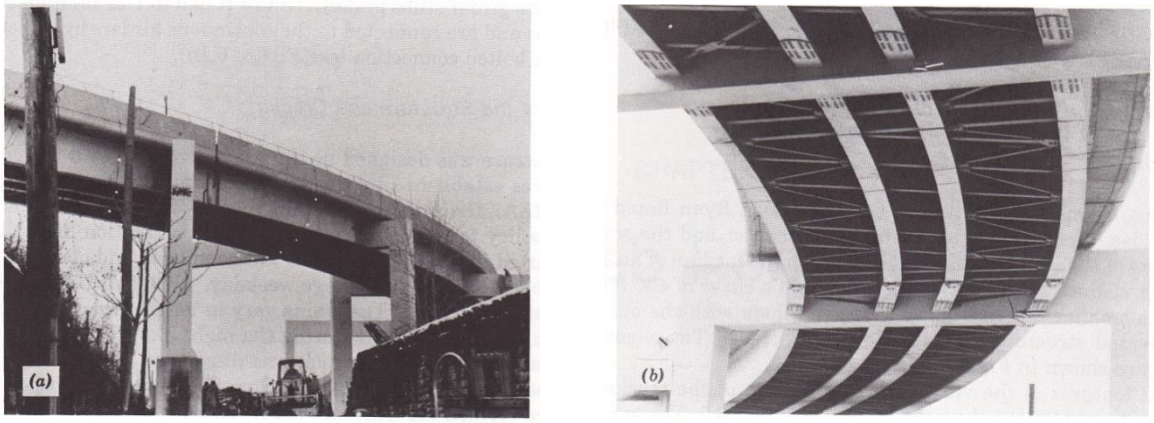

(a) (b)

Figure 2.36 - Dan Ryan railway viaduct (Fisher, 1984): (a) overview and (b) structure of the deck.

During an inspection, in 1968, several fatigue cracks were found in connections between the beams and the bents (Figure 2.37). All cracks started on the side of the bottom flange of the beams and caused complete separation between the flange and the lateral walls of the bent. The path of the cracks highlights the tension, shear and bending actuating loading.

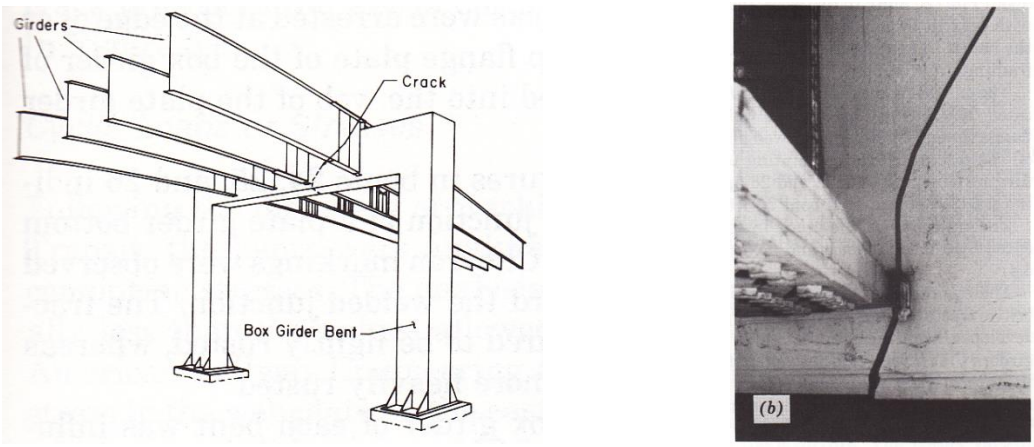

(a) (b)

Figure 2.37 - Fatigue cracks at the Dan Ryan railway viaduct (Fisher, 1984): (a) crack's typical location and (b) detail of the crack.

The analysis of the causes of the observed cracks revealed the presence of welds with low quality in the connection between the lower flange of the beams and the webs of the bents. The presence of inclusions and of partial penetration zones contributed to the start of fatigue cracks propagation. Other determinant factor was the high level of traffic of this railway line, with more than 450 daily train passages in average, between the moment of inspection and the opening to traffic. Finally, Charpy tests revealed the reduced toughness of the material, especially for temperatures below 0ºC. Temperatures lower than that value were common in the region, which may have promoted the propagation of brittle cracks.

2.4.4.2 Maihama Bridge

The Maihama bridge is a bridge with orthotropic deck, located near Tokyo, Japan. It has 3 spans, with 77 m each. The deck (Figure 2.28), 14.25 m wide, sustains 3 lanes of traffic, where more than 80 000 vehicles circulate per day.

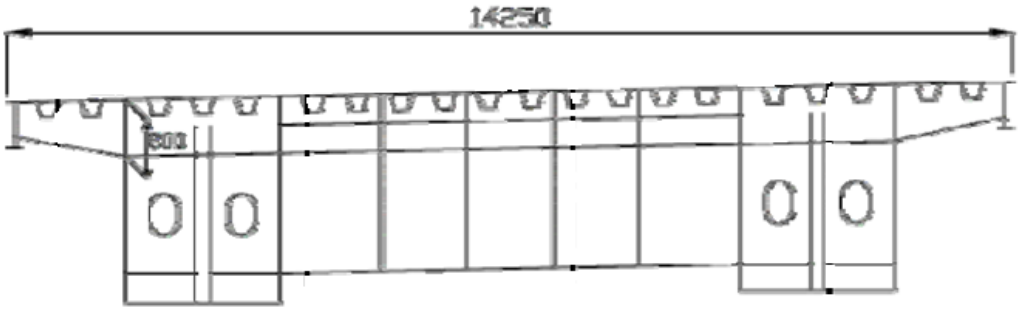

Figure 2.38 - Cross section of the Maihama bridge (Miki, 2010)

The orthotropic decks have the advantage of being light when compared to decks having a concrete slab. But, as the steel components of orthotropic decks support directly the traffic loads and are very flexible, the stress ranges observed on the structural elements are generally high.

That is also the case of the Maihama bridge, where the development of several fatigue cracks, with the patterns presented in Figure 2.39, was observed.

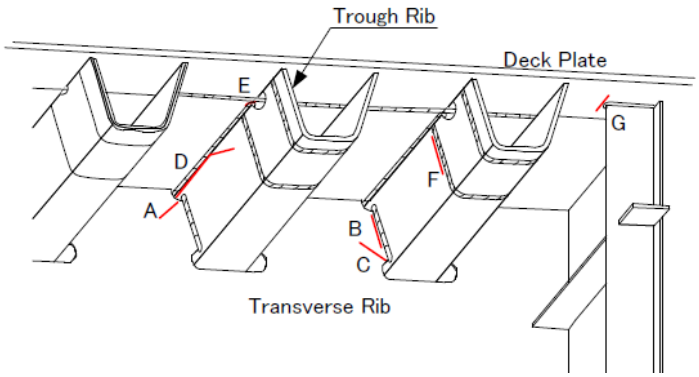

Figure 2.39 - Typical locations of fatigue cracks observed in the Maihama bridge (Miki, 2010)

The cracks of type A, B and C initiated in the fillet welds that connect the longitudinal rib to the cross girder in a process in some way similar to the previous example of the Dan Ryan viaduct (section 2.4.4.1). They are determined by the high stress concentrations originated by the geometry of the detail and by the welds.

The cracks of type D appear in the longitudinal welds and propagate, in the worst cases, through the deck plate. In these cases, the main reason for the crack's initiation is the geometry of the weld, which is typically a fillet weld, and the high deformations that affect it. The cracks of type E and G appear in the corresponding fillet welds and are due, mainly, to the stress concentrations induced by them. Finally, the F-type cracks appear in butt welds and are due to low quality welding, most of the times performed with the aid of a backing plate.

2.4.5 Weld defects

Poor welds are a frequent cause of fatigue cracks initiation and propagation. This applies to but welds, when perpendicular to the main direction of loading but also to longitudinal welds.

Fatigue cracks initiated at the butt welds of a girder's flange may propagate into the web. In other cases, the crack initiation happens at the butt welds of longitudinal stiffeners and propagates until reaching the web of the beam.

Also, several structures showed transverse fatigue cracks in the longitudinal welds, during the service phase. Typically, those cracks initiate by hydrogen cracking, during the welding process, with the fatigue crack propagation continuing from that point onwards. The box girders are structures where the development of this type of cracks is frequent, if the welds are not performed with adequate quality.

2.4.5.1 Bridge over Quinnipiac River

The bridge over river Quinnipiac, USA, is a composite structure, with 4 spans. The first span is simply supported, while the remaining 3 spans form a cantilever-type structure. The suspended segment has a length of 50.3 m. The section presents 9 longitudinal I-section girders, linked by a cross-bracing system. A thin concrete slab is supported by those longitudinal girders (Figure 2.40).

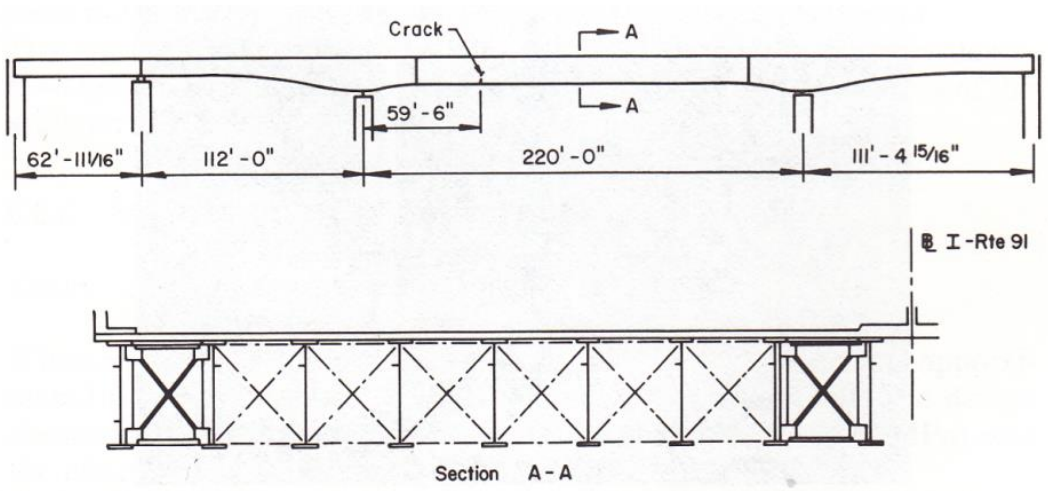

Figure 2.40 - Bridge over river Quinnipiac (Fisher, 1984)

The bridge was open to traffic in 1964. In 1973 a crack with big dimensions was found in one of the webs of one of the girders. Fractographic analysis of the fracture surface allowed concluding that the crack initiated in an inclusion present at the butt weld of a longitudinal stiffener before propagating to the web and penetrating the lower flange of the deck (Figure 2.41).

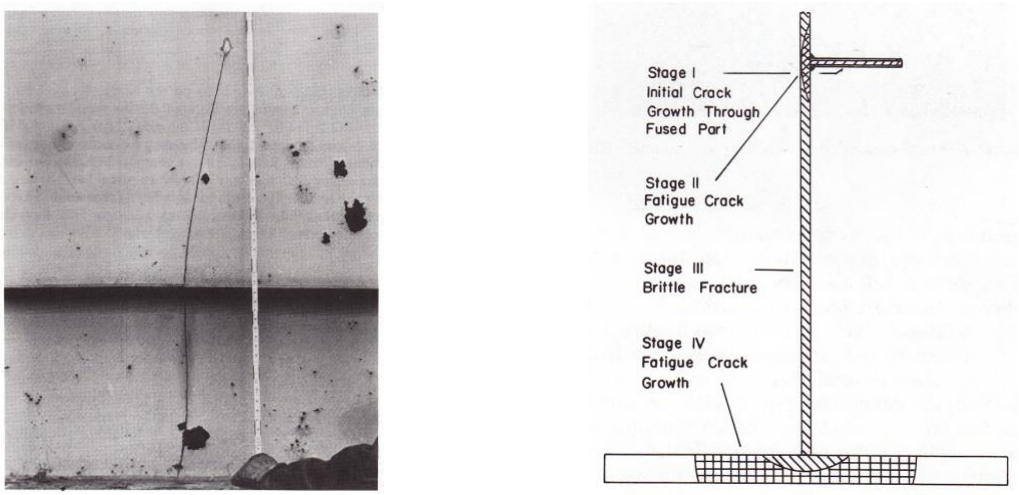

(a) (b)

Figure 2.41 - Fatigue crack at the bridge over river Quinnipiac (Fisher, 1984): (a) visible crack and (b) fatigue crack propagation stages.

2.4.5.2 River Mardle Viaduct

The River Mardle Viaduct (Figure 2.42), in UK, is a curved roadway bridge composed of four continuous spans (Clubley and Winter, 2003). The bridge is composed by two longitudinal steel box girders that support steel cross and cantilever beams 3 m apart. Over these elements, a reinforced concrete slab bears the roadway pavement.

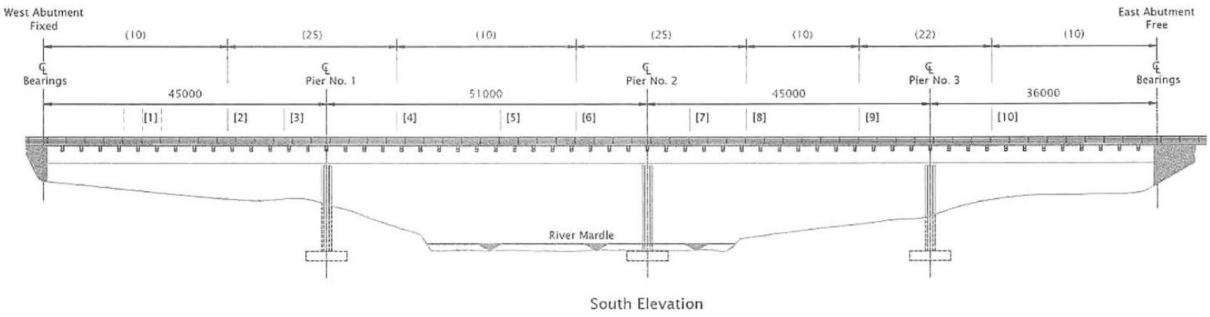

Figure 2.42 – Elevation view of River Mardle Viaduct (Clubley and Winter, 2003).

The bridge was completed in 1977 and in 2001-2002 a detailed inspection performed on the two steel box girders detected many imperfections in the butt weld splices joining the box girders (Figure 2.43).

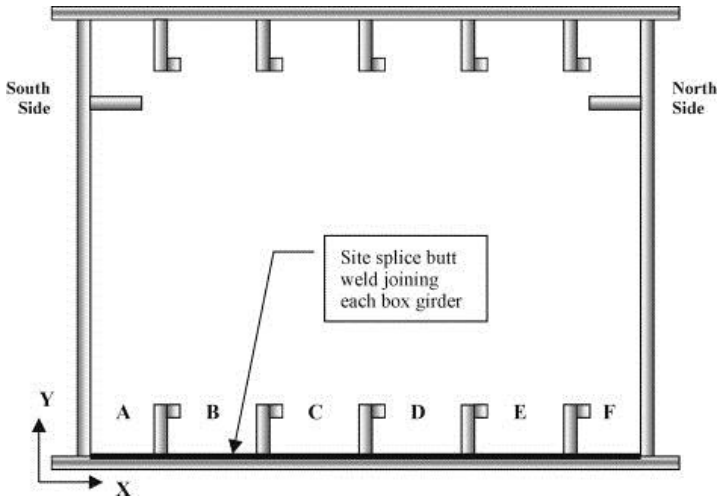

Figure 2.43 – Cross section of one of the box girders (Clubley and Winter, 2003).

Due to the severity of the defects found, advanced Phased Array ultrasonic tests were performed, allowing to assess their size and location. Most common issues found were lack of fusion, slag and planar cracks, both in the weld and in the heat affected zone. In some cases, the maximum dimensions of the flaws exceeded 200 mm in length and 10 mm in height. The main reason for the observed cracks was poor weld quality.

As a response to the findings of the study performed in the bridge, the critical welds were subject to repair, monitoring or strengthening. The mitigation action applied to each weld depended on the respective size of imperfections found and level of tension stresses observed.

2.4.5.3 Gulf Outlet Bridge

The bridge of Gulf Outlet, in the USA, is a lattice structure, with 3 spans of 83.21 m + 213.96 m + 83.21 m length. The intermediate span is suspended by an arch (Figure 2.44). The two trusses are 22.9 m apart each other.

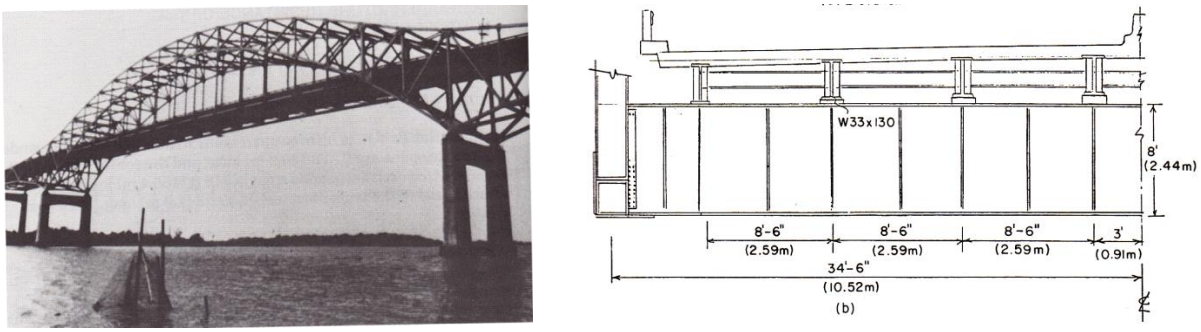

(a) (b)

Figure 2.44 - Gulf Outlet bridge (Fisher, 1984): (a) overview and (b) cross section.

The bridge was opened to traffic in 1965. In 1978, a detailed inspection was performed, which included ultra-sonic and radiographic tests to the welds. During that inspection, fatigue cracks were found at the corner welds of the deck's box girders (Figure 2.45).

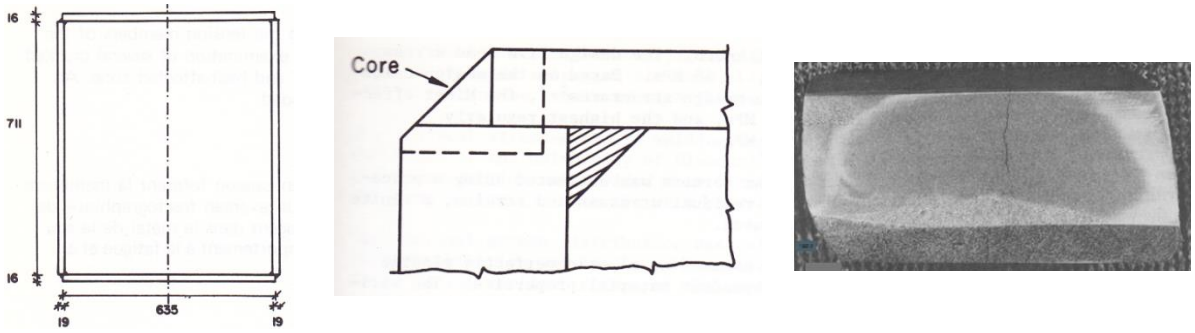

(a) (b) (c)

Figure 2.45 - Location of fatigue cracks of Gulf Outlet bridge (Fisher, 1984): (a) cross section of one of the deck's box girder, (b) core extracted and (c) visible location of the crack.

Most of the cracks did not progress behind the weld and were only visible after grinding. It was observed that all the cracks were located in zones were the welds, initially performed by the submerged arc welding, had been manually reinforced, a posteriori. In all those locations, inclusions or voids, responsible for crack initiation, were found.

2.4.6 Lamellar tearing

Generally, the structural elements with welded plates are conceived and assembled in such a way that the loads and the residual stresses develop in a direction parallel to the direction of the rolling of the plate. When that is not possible, the adoption of a steel grade with adequate metallurgic properties and homogeneous through-thickness structure may help minimizing the problem.

2.4.6.1 Rigid box girder frames of Ft. Duquesne Bridge access viaducts

The access viaducts preceding the bridge Ft. Duquesne, in Pittsburgh, USA, were concluded in 1968. Those viaducts are composed by several continuous segments, with 2 or 3 spans each. The composite decks of the several viaducts have different widths and are formed by 1 or 2 steel box girders with an overlaying concrete slab. The viaducts are supported by rigid steel box girder frames, with a rectangular section (Figure 2.46).

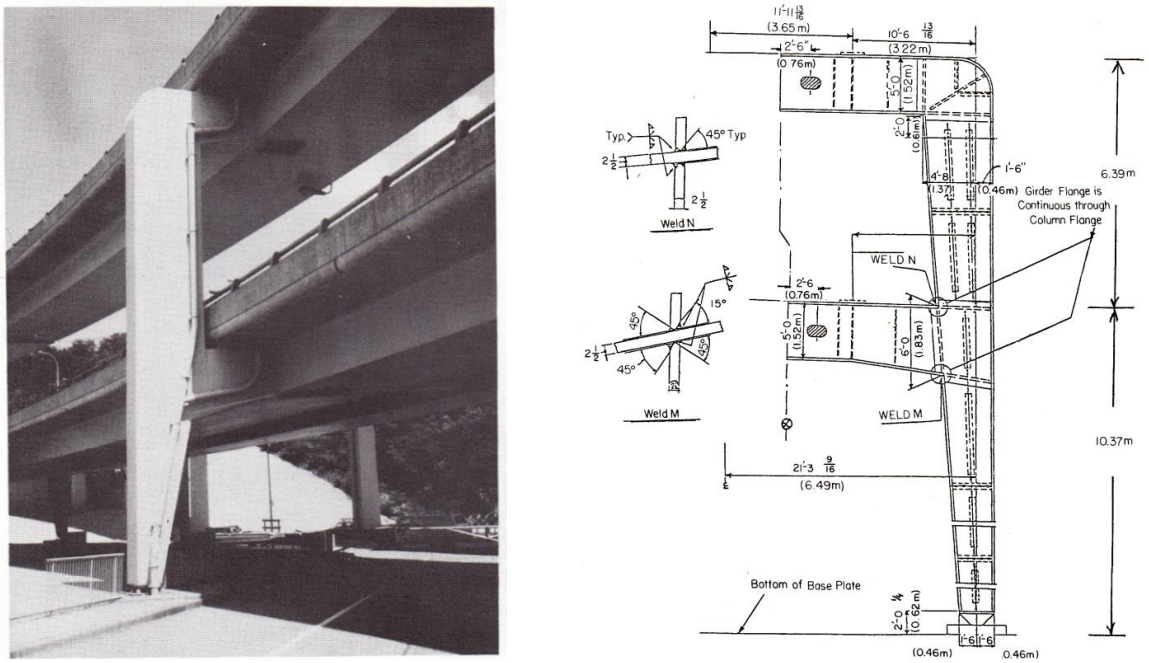

(a) (b)

Figure 2.46 - Rigid box girder frames of the Ft. Duquesne Bridge's access viaducts (Lindberg and Schultz, 1997): (a) overview and (b) design.

In 1978, fatigue cracks were found in the upper flange of the transverse beams of several box girder frames. After analysing the causes for fatigue cracks initiation and propagation, it was concluded that these were generically from 2 types: some of them originated at the weld between the flange of the pile and the flange of the transverse beam; the others originated at the upper flange of the transverse beam, due to the lamellar tearing of its material (Figure 2.47), probably during the structure's construction phase.

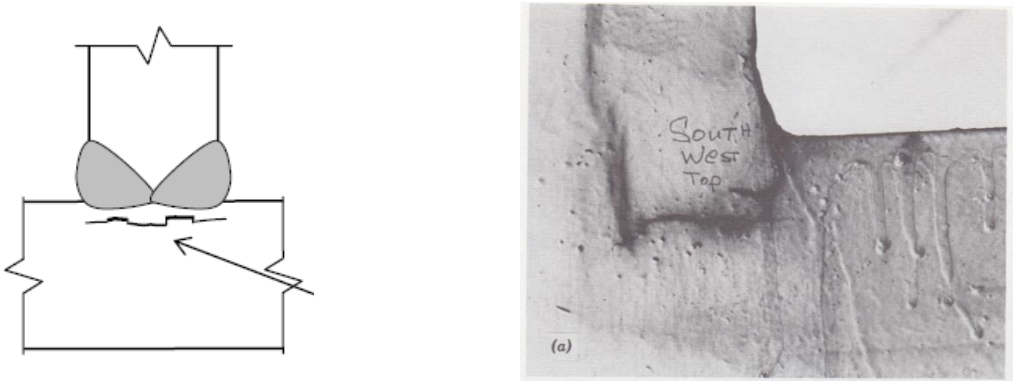

(a) (b)

Figure 2.47 - Fatigue crack due to lamellar tearing (Fisher, 1984): (a) schematics of crack development and (b) observed crack.

2.4.7 Other cases

The details presented above highlight the variety of situations where fatigue cracks may arise. Nevertheless, other types of details could be mentioned. For example, it is common to find fatigue cracks in holes that were performed in the structure, for construction process, and latter filled with filler material (Figure 2.48). That is due to inadequate fusion, slag inclusions or other defects.

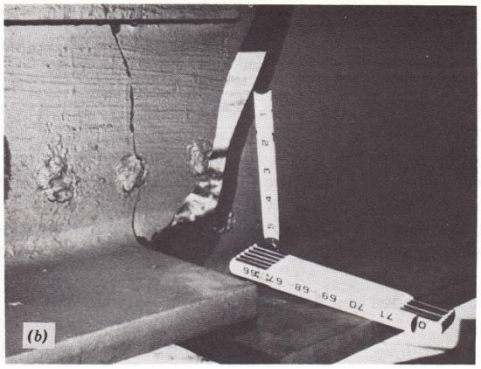

Figure 2.48 - Fatigue cracks initiated in holes filled with filler material.

The zones where a sudden change in the cross-section happens are also prone to fatigue damage, as can be illustrated in Figure 2.49.

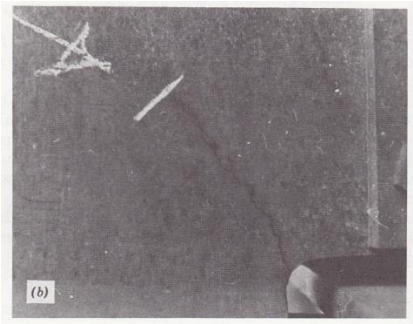

(a) (b)

Figure 2.49 - Fatigue cracks in components with change in section: (a) due to tension and (b) due to shear stresses.

Other types of details of steel and composite bridges, prone to fatigue damage, may be found in Miki (2010), Fisher (1984) and Al-Emrani and Kliger (2009).

2.5 CONCLUDING REMARKS

In this Chapter, an introduction to the fatigue problem of structures is performed. In the first place, examples of fatigue cracks propagation in several areas of engineering are presented, such as aerospace, naval engineering, oil and gas, railways and civil engineering. In the case of bridges, the impact of fatigue as one of the main causes of severe structural damage and collapse is underlined.

Fatigue is also described as a multi-scale problem which, due to its nature, mobilised different areas of knowledge, namely, physics, metallurgy and engineering. An historical perspective of the main steps on the understanding of fatigue is presented, starting on the first tests performed in the XIX century, in the mining industry.

After that, the study focused on the fatigue damage in steel and composite bridges. The main causes for fatigue damage were identified: i) the presence of defects on the welds of welded components; ii) adoption of details with poor fatigue behaviour; iii) secondary deformations and stresses due to sections distortion; iv) excessive vibrations of structural components. Corrosion may also accelerate fatigue cracks propagation but was not covered in detail in this work. Finally, a collection of cases of bridges where fatigue crack propagation was observed is presented. Those examples were grouped by type of detail where the fatigue cracks were found (Table 2.4).

Table 2.4 – Collection of fatigue damage cases in bridges.

Causes / **Locations**	**Defects on the weld**	**Details with poor fatigue behavior**	**Secondary deformation and stresses**	**Excessive vibrations**	**Corrosion**
Eyebars and hangers	- Sungsoo	- Silver Bridge - Sungsoo	- Illinois Route 157 - Skellefte	- Skellefte	- Silver Bridge - Illinois Route 157
Flange gussets and cover-plates	- King's Bridge	- King's Bridge			
Diaphragms, cross-bracing connections and floor beams to main load-carrying member connections	- Lafayette Street	- Panaro	- Lafayette Street - Panaro - Belle Fourche	- Panaro	
Web penetration and orthotropic decks	- Dan Ryan - Maihama	- Dan Ryan - Maihama	- Maihama		
Weld defects	- Quinnipiac River - River Mardle - Gulf Outlet				
Lamellar tearing	- Ft. Duquesne	- Ft. Duquesne			

In the next Chapter, the main fatigue assessment methodologies proposed by standards are discussed.

Chapter 3

STANDARDS FOR THE FATIGUE ASSESSMENT OF RAILWAY BRIDGES

3.1 INTRODUCTION

Chapter 2 underlined the relevance of assessing fatigue damage in steel and composite bridges. As this problem is widely recognised in Civil Engineering, most of the structural design Standards present methodologies for the assessment of fatigue strength of structures. Those methodologies are discussed in this Chapter.

In the European Union context, the reference Standards are the Eurocodes. For that reason, special emphasis is placed on those codes here. The linear damage accumulation method is the most complete methodology foreseen in the Eurocodes. Under some conditions, the simplified method of equivalent constant amplitude stress range can be used, instead. Both methods are described in the next section.

Other international Standards such as the British Standard 5400 (BSI, 1980) and the codes of the American Association of State Highway and Transportation Officials (AASHTO, 2012) and of the International Institute of Welding (IIW, 2008) are also addressed in this Chapter; nevertheless, the focus is put on the main differences on the methodology, when compared with the Eurocodes.

3.2 FATIGUE ASSESSMENT ACCORDING TO THE EUROCODES

3.2.1 Introduction

The Eurocodes result from an effort of compiling and combining the knowledge on structural design that exists in different parts of Europe. They try to unify the best practices currently available. That is also the objective of the Eurocodes in the case of structural fatigue damage assessment. These standards define 2 different methods for fatigue analysis:

- Method of the equivalent constant amplitude stress range;
- Method of the linear damage accumulation.

The analysis of the problem of fatigue of railway bridges should focus on the structural steel components, the concrete-steel shear connectors, the reinforcement and pre-stress steel and the concrete. In order to address the fatigue analysis of these structural components, the most relevant Eurocodes are:

- Eurocode 0: EN 1990 – Basis of structural design.
    - Annex A2 – Bridges.
- Eurocode 1: EN 1991 – Actions in structures.
    - Part 2 – Traffic loads in bridges.
- Eurocode 2: EN 1992 – Design of concrete structures.
    - Part 2 – Concrete bridges. Design rules.
    - Part 2, Annex NN – Damage equivalent stresses for fatigue assessment.
- Eurocode 3: EN 1993 – Design of steel structures.
    - Part 1.9 - Fatigue.
    - Part 2 – Steel Bridges.
- Eurocode 4: EN 1994 – Design of concrete-steel composite structures.
    - Part 2 – Composite bridges.

The rules defined in the Eurocodes, in order to perform the fatigue analysis of the structural steel components of railway bridges, are presented in the following sections.

3.2.2 Standard fatigue loads and load cases

The fatigue assessment should be performed, whenever possible, using one of the standard traffic scenarios, in agreement with the type of traffic forecasted for the railway bridge under study: standard traffic mix, heavy traffic mix and light traffic mix. These traffic scenarios correspond to different combinations of 12 standard fatigue trains, presented in Eurocode 1 (CEN, 2003). In Figure 3.1 one of the 12 fatigue trains is presented.

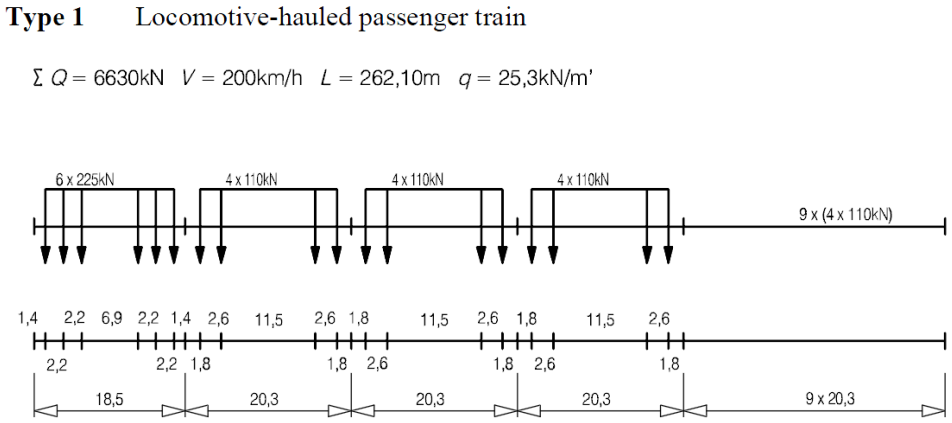

Figure 3.1 - Example of a fatigue train: Train Type 1 – Locomotive-hauled passenger train (CEN, 2003).

On Table 3.1 a brief summary of the characteristics of the 12 trains is presented.

Table 3.1 - Standard fatigue trains (adapted from CEN (2003)).

Train	Total Weight [kN]	Speed [km/h]	L [m]	q [kN/m]	Max. axle load [kN]	Description
1	6630	200	262.1	25.3	225	Locomotive-hauled passenger train
2	5300	160	281.1	18.9	225	Locomotive-hauled passenger train
3	9400	250	385.52	24.4	200	High speed passenger train
4	5100	250	237.6	21.5	170	High speed passenger train
5	21600	80	270.3	80	225	Locomotive-hauled freight train
6	14310	100	333.1	43	225	Locomotive-hauled freight train
7	10350	120	196.5	52.7	225	Locomotive-hauled freight train
8	10350	100	212.5	48.7	225	Locomotive-hauled freight train
9	2960	120	134.8	22	130	Suburban multiple unit train
10	3600	120	129.6	27.8	150	Underground
11	11350	120	198.5	57.2	250	Locomotive-hauled freight train
12	11350	100	212.5	53.4	250	Locomotive-hauled freight train

Each traffic scenario corresponds to approximately 25 million t/year, according to the combinations shown in the following tables:

Table 3.2 - Standard traffic mix (adapted from CEN (2003)).

Train	Total Weight [kN]	Total mass [t]	Number of trains/day	Traffic volume [10^6 t/year]	Description
1	6630	663	12	2.90	Locomotive-hauled passenger train
2	5300	530	12	2.32	Locomotive-hauled passenger train
3	9400	940	5	1.72	High speed passenger train
4	5100	510	5	0.93	High speed passenger train
5	21600	2160	7	5.52	Locomotive-hauled freight train
6	14310	1431	12	6.27	Locomotive-hauled freight train
7	10350	1035	8	3.02	Locomotive-hauled freight train
8	10350	1035	6	2.27	Locomotive-hauled freight train
Total			**67**	**24.95**	

Table 3.3 - Heavy traffic mix (adapted from CEN (2003)).

Train	Total Weight [kN]	Total mass [t]	Number of trains/day	Traffic volume [10^6 t/year]	Description
5	21600	2160	6	4.73	Locomotive-hauled freight train
6	14310	1431	13	6.79	Locomotive-hauled freight train
11	11350	1135	16	6.63	Locomotive-hauled freight train
12	11350	1135	16	6.63	Locomotive-hauled freight train
Total			**51**	**24.78**	

Table 3.4 - Light traffic mix (adapted from CEN (2003)).

Train	Total Weight [kN]	Total mass [t]	Number of trains/day	Traffic volume [10^6 t/year]	Description
1	6630	663	10	2.42	Locomotive-hauled passenger train
2	5300	530	5	0.97	Locomotive-hauled passenger train
5	21600	2160	2	1.58	Locomotive-hauled freight train
9	2960	296	190	20.53	Suburban multiple unit train
Total			**207**	**25.49**	

According to Eurocode 1 (CEN, 2003) and Eurocode 3 (CEN, 2006), when the standard traffic mixes adequately reproduce the real traffic and no dynamic analysis is required, the fatigue analysis may be performed using the equivalent constant amplitude stress range method. The loading to consider, in that case, is the load model LM71 (Figure 3.2), including the dynamic factor, Φ, but excluding the load classification factor, α (CEN, 2003).

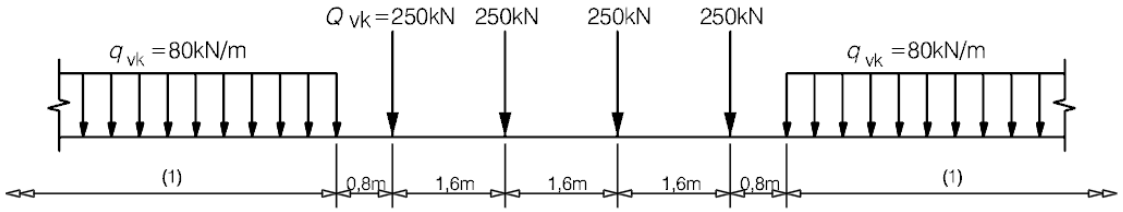

Key
(1) No limitation

Figure 3.2 - Load model LM71 (CEN, 2003).

When the standard traffic scenarios do not represent the real traffic (e.g. when a restricted variety of train types circulate on the bridge and/or dominate the induced fatigue damage) an alternative traffic scenario should be specified, e.g. a traffic mix composed of real trains.

The loads to be considered in fatigue analysis are the vertical and centrifugal forces. Nosing and longitudinal forces may be neglected.

When dynamic analyses are required, there are additional requirements for fatigue assessment. The requirements for a dynamic analysis are defined in Eurocode 1, and represented schematically in the flow chart of Figure 3.3.

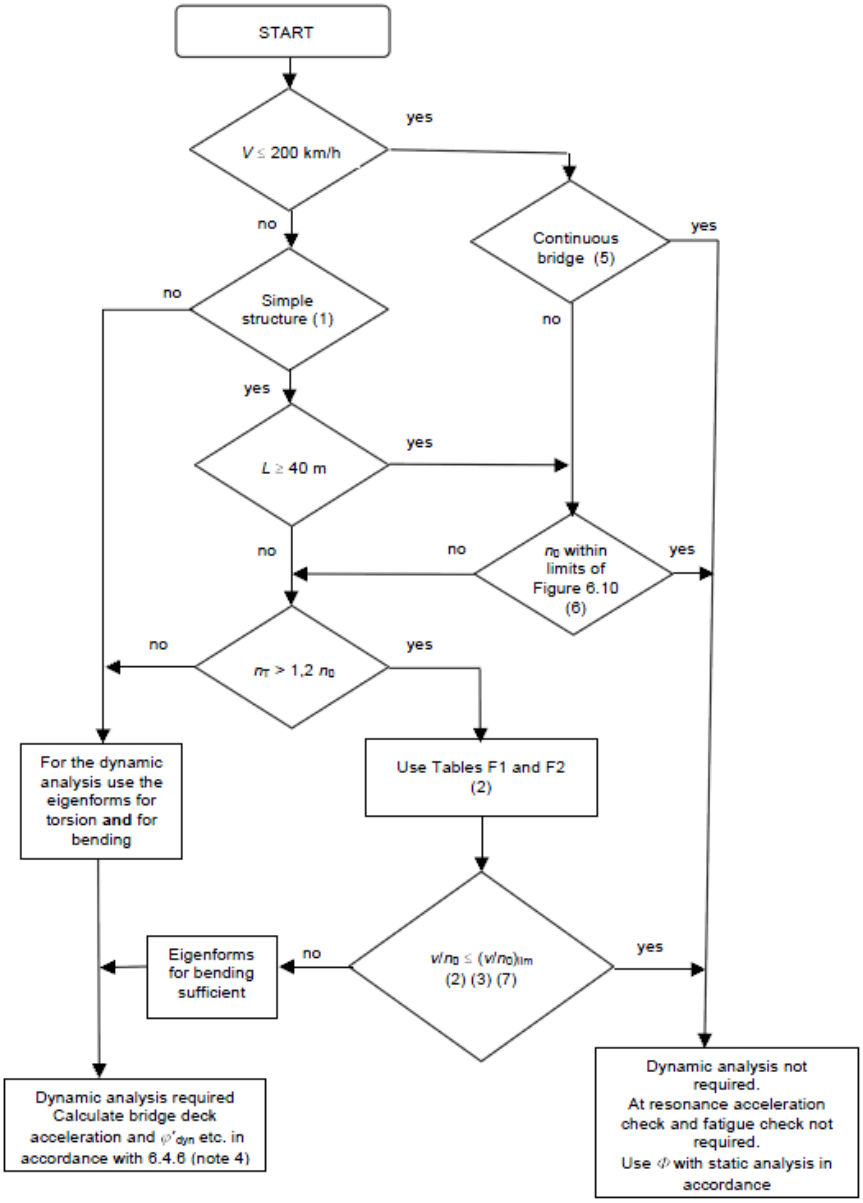

Figure 3.3 - Flow chart for determining whether a dynamic analysis is required (CEN, 2003).

When, according to the flow chart above, no dynamic analysis is required, the dynamic amplification, for each train, can be defined using Equation (3.1), as defined in EN 1991-2, Annex D (CEN, 2003):

$$1+\frac{1}{2}\cdot(\varphi'+\varphi''/2) \tag{3.1}$$

The parameters φ' and φ'' in the previous expression are also defined on the EN 1991-2, Annex D.

When the dynamic analysis is required, two loading scenarios need to be considered:

- the dynamic response for the trains circulating at high speeds and in resonance;
- the loading with ϕ x LM71 (and, if necessary, with ϕ x LM SW/0 for continuous structures).

The worst case scenario, from the two above, should then be used in design.

The fatigue assessment should allow accounting the stress cycles resulting from:

- Additional vibrations resulting from the impact of axle loads running at high speed;
- Resonance effects;
- Free vibrations observed after the passage of the trains.

For the fatigue assessment, the range of speeds to be considered should go up to the Maximum Nominal Speed. That Maximum Nominal Speed should take into account future increments of the operation speed, due to modifications to the infrastructure and rolling stock.

The increment on the computed dynamic response (stresses, displacements, accelerations, among others) due to track defects or rolling stock imperfections should be estimated by multiplying the computed effects by:

$$(1+\varphi''/2) \tag{3.2}$$

for a track with good maintenance, or:

$$(1+\varphi'') \tag{3.3}$$

for a track with normal maintenance, with φ'' defined in EN 1991-2, Annex C and never considered lower than zero.

In the case of structures that bear multiple tracks, the fatigue load should be applied to a maximum of 2 tracks, simultaneously, on the most unfavourable positions.

3.2.3 Fatigue strength

The fatigue strength of structural steel components is given by series of S-N curves, $\log(\Delta\sigma_R)$ vs. $\log(N)$ and $\log(\Delta\tau_R)$ vs. $\log(N)$, presented in Eurocode 3 (CEN, 2004) and expressed in terms of characteristic values. Thus, both the strength to direct, σ, and shear, τ, stresses can be considered.

Three different stress range levels characterise those strength curves:

- $\Delta\sigma_D$ – Constant amplitude fatigue limit: direct stresses range below which no damage occurs, assuming constant amplitude loading. When variable amplitude loading occurs, no damage will be observed if all the stress cycles have a range lower than this value;
- $\Delta\sigma_L$ or $\Delta\tau_L$ – Cut-off limit: value of direct or shear stress range below which cycles do not contribute to the damage accumulation;
- $\Delta\sigma_C$ or $\Delta\tau_C$ – Detail category: reference strength to fatigue, corresponding to 2 million constant amplitude load cycles ($N = 2\times10^6$). This value identifies each S-N curve present on Eurocode 3.

The S-N curves present in EN 1993-1-9 are meant to be applicable for analysis using nominal stresses.

3.2.3.1 S-N curves for normal stresses

The S-N curves for direct stress ranges, $\Delta\sigma_i$, may present two different configurations:

- If the actuating direct stress is composed by constant amplitude cycles, the curve is characterised by a single linear trend, with a 1/3 slope and initiating at $N = 5$ million cycles. For lower stress ranges no fatigue damage occur. That curve configuration is applicable also when variable amplitude intervals are present but do not exceed $\Delta\sigma_D$. In that case, no damage occurs;
- If the direct stresses are composed by variable amplitude cycles and at least one of those cycles has a stress range higher than $\Delta\sigma_D$, then the S-N curve has 2 linear trends, with slopes of 1/3 and 1/5, respectively.

EN 1993-1-9 defines 14 S-N curves for direct stresses, corresponding to 14 different fatigue strength levels. Each curve is designated and identified, as mentioned before, by its reference value, $\Delta\sigma_C$.

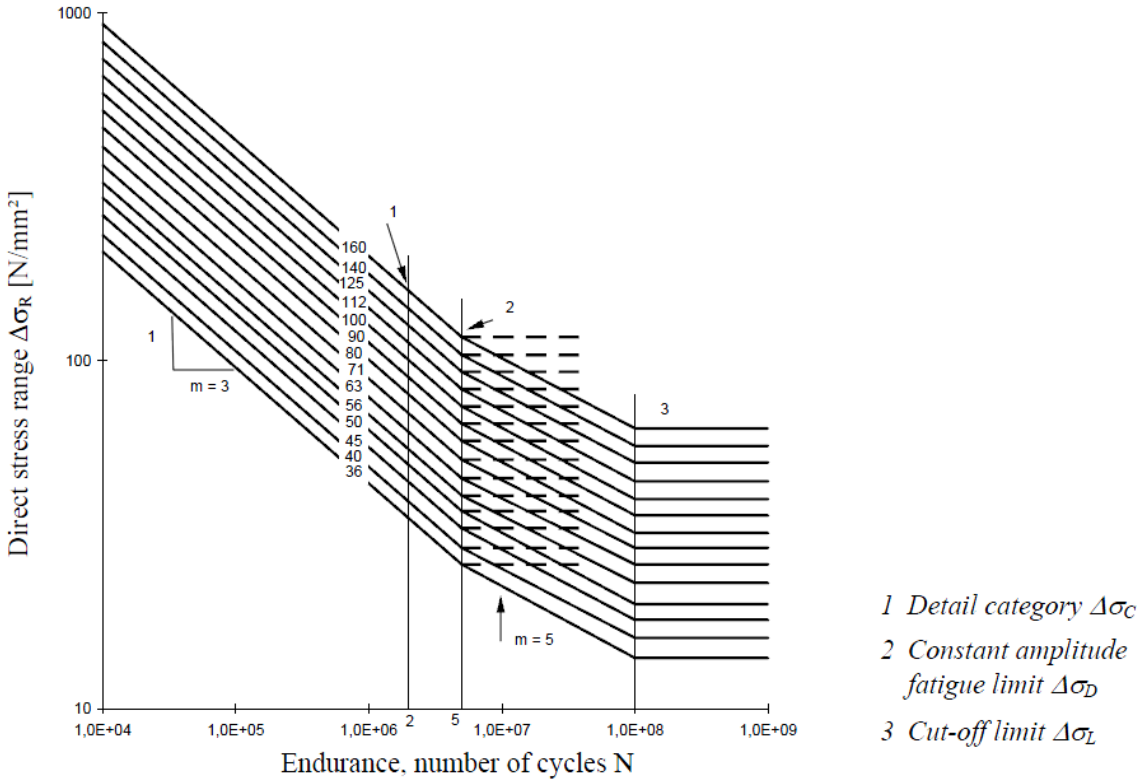

Figure 3.4 - S-N curves for direct stress ranges (CEN, 2004).

The design value of the S-N curves are obtained by dividing $\Delta\sigma_c$ by the partial factor for fatigue strength, γ_{Mf}. Then, when only constant amplitude cycles are present or when the maximum stress range is lower than $\Delta\sigma_D/\gamma_{Mf}$, the generic expression for the S-N curve is:

$$N_i = \begin{cases} +\infty & \Leftarrow \Delta\sigma_i \leq \Delta\sigma_D/\gamma_{Mf} \\ 5\times10^6 \cdot \left(\frac{\Delta\sigma_D/\gamma_{Mf}}{\Delta\sigma_i}\right)^3 & \Leftarrow \Delta\sigma_D/\gamma_{Mf} \leq \Delta\sigma_i \end{cases} \tag{3.4}$$

When variable amplitude cycles occur and at least one of them has a stress range higher than $\Delta\sigma_D/\gamma_{Mf}$, the generic expression for the S-N curve becomes:

$$N_i = \begin{cases} +\infty & \Leftarrow \Delta\sigma_i \leq \Delta\sigma_L/\gamma_{Mf} \\ 5\times10^6 \cdot \left(\frac{\Delta\sigma_D/\gamma_{Mf}}{\Delta\sigma_i}\right)^5 & \Leftarrow \Delta\sigma_L/\gamma_{Mf} \leq \Delta\sigma_i \leq \Delta\sigma_D/\gamma_{Mf} \\ 5\times10^6 \cdot \left(\frac{\Delta\sigma_D/\gamma_{Mf}}{\Delta\sigma_i}\right)^3 & \Leftarrow \Delta\sigma_D/\gamma_{Mf} \leq \Delta\sigma_i \end{cases} \tag{3.5}$$

Some structural details do not fit in any of the 14 S-N curves presented above. In those cases, in order for the analysis to be conservative, the details are classified one category below the one

they could be associated to. Those details are identified with the $\Delta\sigma_C^*$ designation. Nevertheless, an alternative assessment can be performed, assuming a higher detail category but imposing, at the same time, that the value of $\Delta\sigma_D$ is the fatigue strength for 10 million cycles, as illustrated in Figure 3.5.

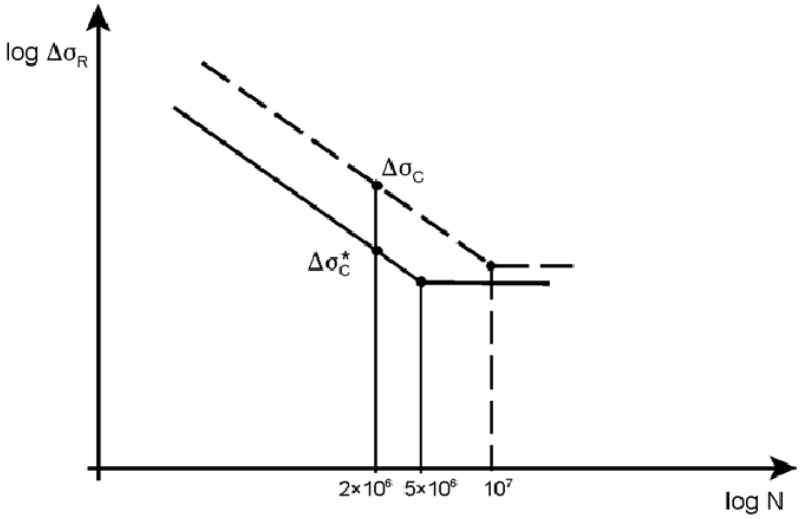

Figure 3.5 - Alternative strength curve for details with special classification, $\Delta\sigma_C^*$ (CEN, 2004).

The fatigue strength of some types of structural details are especially dependent on dimensional parameters such as, e.g., the thickness of their components. In those cases, the Eurocode foresees a reduction on fatigue strength, by means of a coefficient, k_s:

$$\Delta\sigma_{C,\,red} = k_s \cdot \Delta\sigma_C \tag{3.6}$$

3.2.3.2 S-N curves for shear stresses

The S-N curves for shear stress ranges, $\Delta\tau_i$, are characterised by a linear segment with a slope of 1/5 and a cut-off of $\Delta\tau_L$ defined at 100 million cycles. The shear stress S-N curves are designated by their fatigue strength at 2 million cycles ($\Delta\tau_C$), in the same way as direct stress S-N curves. In the EN1993-1-9 only 2 shear stress S-N curves are presented, for 2 distinct detail categories (Figure 3.6).

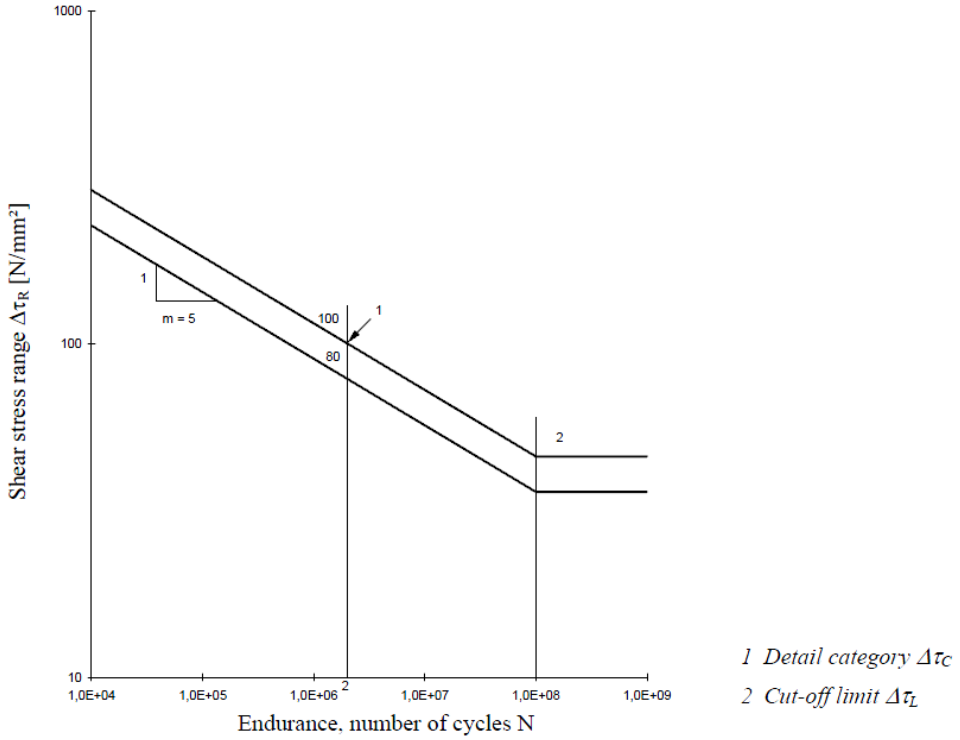

Figure 3.6 - S-N curves for shear stress ranges (CEN, 2004).

Also in this case, the design values are obtained from the characteristic values, dividing them by γ_{Mf}. The generic expression for fatigue life, N_i, for stress cycles with ranges of $\Delta\tau_i$, is, then:

$$N_i = \begin{cases} +\infty & \Leftarrow \Delta\tau_i \leq {\Delta\tau_L}/{\gamma_{Mf}} \\ 2\times10^6 \cdot \left(\dfrac{\Delta\tau_C/\gamma_{Mf}}{\Delta\tau_i}\right)^5 & \Leftarrow \Delta\tau_i \geq {\Delta\tau_L}/{\gamma_{Mf}} \end{cases} \tag{3.7}$$

3.2.3.3 Partial safety factor for fatigue

The value of the partial safety factor for fatigue strength, γ_{Mf}, depends on 2 different factors:

- Accessibility of the detail during inspection and maintenance procedures;
- Consequences of the collapse of the structural detail for the global stability of the structure.

The EN 1993-1-9 standard proposes 2 different approaches to the problem of fatigue:

- Damage tolerant – This approach requires the structure to be redundant, with loads redistribution and global stability being guaranteed in case of failure of the structural

element. It also requires the existence of regular maintenance and of good accessibility to the details for inspection and repair;

- Safe life – This approach is adequate for structures and/or elements without structural redundancy and/or with reduced accessibility to inspection and repair. The structure should have a safety level for the Service Limit State to Fatigue equal to those of Ultimate Limit State verifications.

Distinguishing these different concepts, Eurocode presents 4 possible values for γ_{Mf}:

Table 3.5 - Partial safety factor for fatigue strength, γ_{Mf} (CEN, 2004).

Assessment method	Consequence of failure	
	Low consequence	High consequence
Damage tolerant	1,00	1,15
Safe life	1,15	1,35

3.2.3.4 Detail categories

The detail categories presented in Eurocode 3, part 1-9, fit in the following groups:

- Plain members and mechanically fastened joints (Table 8.1 of EN 1993-1-9);
- Welded built-up sections (Table 8.2 of EN 1993-1-9);
- Transverse butt welds (Table 8.3 of EN 1993-1-9);
- Weld attachments and stiffeners (Table 8.4 of EN 1993-1-9);
- Load carrying welded joints (Table 8.5 of EN 1993-1-9);
- Hollow sections (Table 8.6 of EN 1993-1-9);
- Lattice girder node joints (Table 8.7 of EN 1993-1-9);
- Closed stringers at orthotropic decks (Table 8.8 of EN 1993-1-9);
- Open stringers at orthotropic decks (Table 8.9 of EN 1993-1-9);
- Top flange to web junction of runway beams (Table 8.10 of EN 1993-1-9).

On Table B.1 of Annex B of the EN 1993-1-9 standard, other detail categories are defined, for use with geometric stresses:

- Toes of butt welds;

- Toes of fillet welded attachments;
- Toes of fillet welds in cruciform joints.

As an example, Tables 8.4 and B.1 of EN 1993-1-9 are presented below.

Detail category	Constructional detail	Description	Requirements
80	$L \leq 50$mm	Longitudinal attachments: 1) The detail category varies according to the length of the attachment L.	The thickness of the attachment must be less than its height. If not see Table 8.5, details 5 or 6.
71	$50 < L \leq 80$mm		
63	$80 < L \leq 100$mm		
56	$L > 100$mm		
71	$L > 100$mm $\alpha < 45°$	2) Longitudinal attachments to plate or tube.	
80	$r > 150$mm	3) Longitudinal fillet welded gusset with radius transition to plate or tube; end of fillet weld reinforced (full penetration); length of reinforced weld > r.	Details 3) and 4): Smooth transition radius r formed by initially machining or gas cutting the gusset plate before welding, then subsequently grinding the weld area parallel to the direction of the arrow so that the transverse weld toe is fully removed.
90	$\frac{r}{L} \geq \frac{1}{3}$ or $r > 150$mm	4) Gusset plate, welded to the edge of a plate or beam flange.	
71	$\frac{1}{6} \leq \frac{r}{L} \leq \frac{1}{3}$		
50	$\frac{r}{L} < \frac{1}{6}$		
40		5) As welded, no radius transition.	
80	$t \leq 50$mm	Transverse attachments: 6) Welded to plate. 7) Vertical stiffeners welded to a beam or plate girder. 8) Diaphragm of box girders welded to the flange or the web. May not be possible for small hollow sections. The values are also valid for ring stiffeners.	Details 6) and 7): Ends of welds to be carefully ground to remove any undercut that may be present. 7) $\Delta\sigma$ to be calculated using principal stresses if the stiffener terminates in the web, see left side.
71	$50 < t \leq 80$mm		
80		9) The effect of welded shear studs on base material.	

Figure 3.7 - Details described in “Table 8.4: Weld attachments and stiffeners” of (CEN, 2004).

Detail category	Constructional detail	Description	Requirements
112	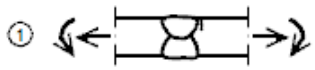	1) Full penetration butt joint.	1) - All welds ground flush to plate surface parallel to direction of the arrow. - Weld run-on and run-off pieces to be used and subsequently removed, plate edges to be ground flush in direction of stress. - Welded from both sides, checked by NDT. - For misalignment see NOTE 1.
100	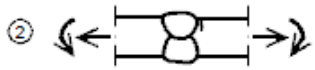	2) Full penetration butt joint.	2) - Weld not ground flush - Weld run-on and run-off pieces to be used and subsequently removed, plate edges to be ground flush in direction of stress. - Welded from both sides. - For misalignment see NOTE 1.
100	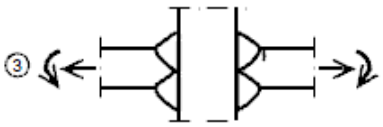	3) Cruciform joint with full penetration K-butt welds.	3) - Weld toe angle ≤60°. - For misalignment see NOTE 1.
100	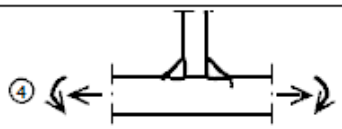	4) Non load-carrying fillet welds.	4) - Weld toe angle ≤60°. - See also NOTE 2.
100	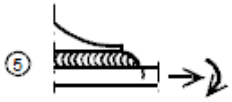	5) Bracket ends, ends of longitudinal stiffeners.	5) - Weld toe angle ≤60°. - See also NOTE 2.
100	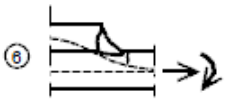	6) Cover plate ends and similar joints.	6) - Weld toe angle ≤60°. - See also NOTE 2.
90	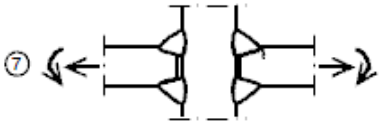	7) Cruciform joints with load-carrying fillet welds.	7) - Weld toe angle ≤60°. - For misalignment see NOTE 1. - See also NOTE 2.

Figure 3.8 - Details described in "Table B.1: Detail categories for use with geometric (hot spot) stress method" of (CEN, 2004).

3.2.4 Determination of actuating stresses

Eurocode 3 contemplates three different definitions of actuating stresses:

- Nominal stress – "The stress in the parent material or in a weld adjacent to a potential crack location, calculated in accordance with elastic theory and excluding stress concentration effects" (Figure 3.9);

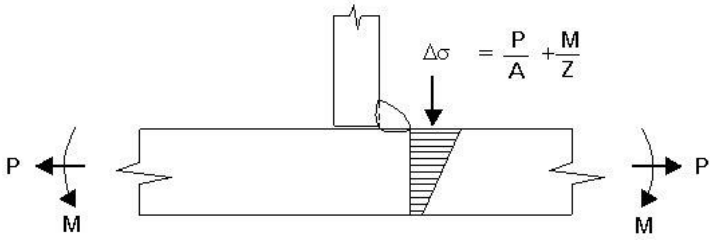

Figure 3.9 - Nominal stress example (ESDEP, 1996).

- Modified nominal stress – "A nominal stress multiplied by an appropriate stress concentration factor, k_f, to allow for a geometric discontinuity that has not been taken into account in the classification of a particular construction detail" (Figure 3.10);

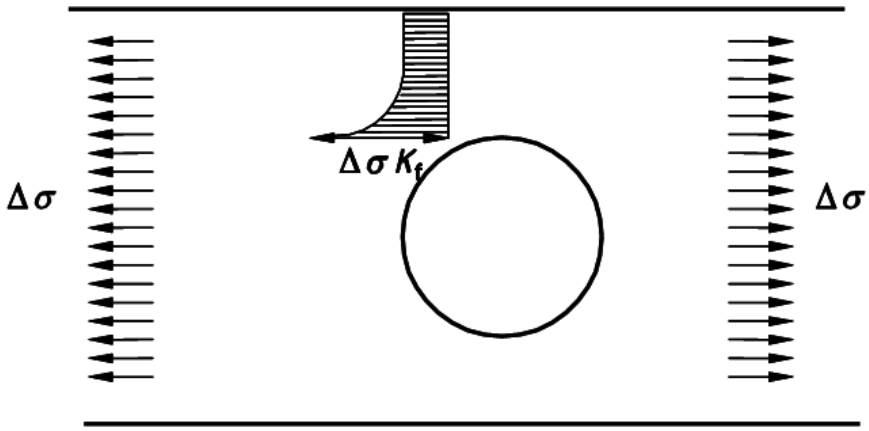

Figure 3.10 - Modified nominal stress example.

- Geometric stress – "The maximum principal stress in the parent material adjacent to the weld toe, taking into account stress concentration effects due to the overall geometry of a particular constructional detail" (Figure 3.11).

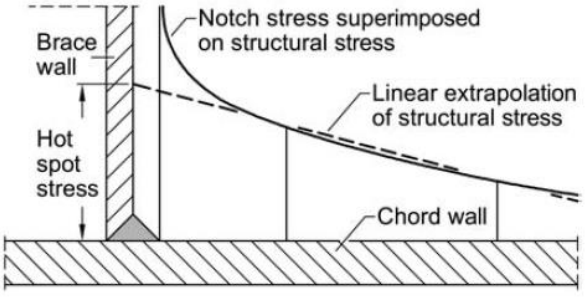

Figure 3.11 – Geometric (hot spot) stress (Radaj et al., 2006).

The finite element models developed with the intent to reproduce the nominal stresses actuating on the structures, should allow to account with all the effects namely distortion and

secondary effects, and should be based on the linear elastic analysis of the elements and their connections.

In the case of hollow section lattice girders, models are typically very simple, assuming hinged connections. The secondary moments can be considered, in a simplified way, by introducing a factor, k_1, that should be multiplied by the stresses obtained with the simplified model. Values of k_1 are available in EN 1993-1-9:

Table 3.6 - Example of k_1 factors, for circular hollow sections, in order to account for secondary moments (CEN, 2004).

Type of joint		Chords	Verticals	Diagonals
Gap joints	K type	1.5	1.0	1.3
	N type / KT type	1.5	1.8	1.4
Overlap joints	K type	1.5	1.0	1.2
	N type / KT type	1.5	1.65	1.25

Any geometric particularity of a detail, capable of inducing stress concentrations in the mentioned detail additional to those already forecasted in the Eurocode, should be accounted for by the introduction of a concentration factor, k_f. The resulting stress is the designated modified nominal stress.

For the fatigue strength assessment at base material, the relevant stresses are the direct stress, σ, and the shear stress, τ. At the welds, the relevant stresses are the direct stresses perpendicular to the welds, $\sigma_{wf} = \sqrt{\sigma_{\perp f}^2 + \tau_{\perp f}^2}$ and the shear stresses parallel to the same axis, $\tau_{wf} = \tau_{\parallel f}$, defined according to Figure 3.12.

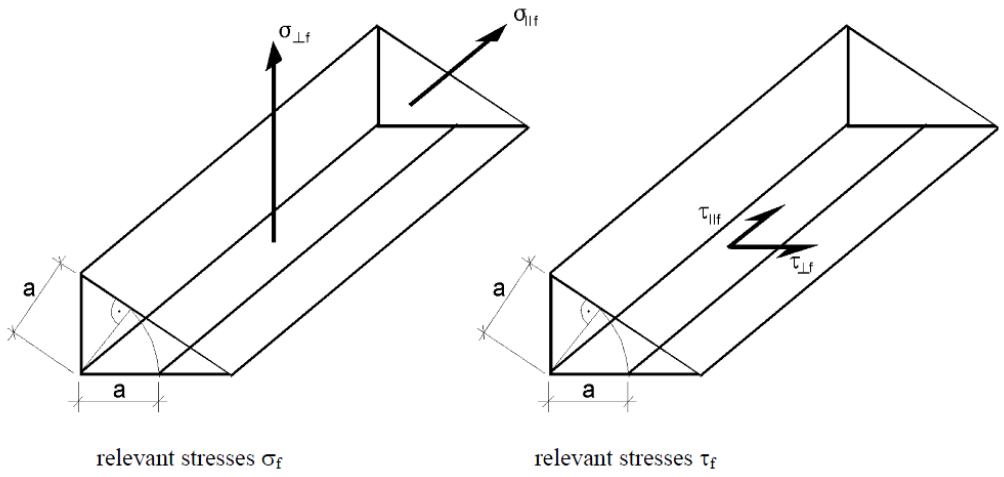

Figure 3.12 - Relevant stresses at fillet welds (CEN, 2004).

In the case of non-welded details or stress-relieved welded details and whenever compressive stresses occur at the load cycles, effective values of stress ranges can be computed. The effective stress range results from summing the maximum tension stress with 60% of the maximum compressive stress. The consideration of the effective value of the stress ranges is only possible if the permanent loading is also taken into account in the analysis.

In the case of Class 4 sections (potential local instability for stresses lower than the yield stress) the actuating stresses should be computed in accordance with EN 1993-1-5.

3.2.5 Assessment methods

3.2.5.1 Equivalent constant amplitude stress range method

3.2.5.1.1 Applicability conditions

This assessment methodology uses some significant simplifications, namely the consideration of standard traffic scenarios and the computation of the equivalent constant amplitude stress range using damage equivalent factors that result from parametric studies.

For this methodology to be applicable, the bridge should fit the requisites that allow avoiding the dynamic analysis. Furthermore, the real traffic must be adequately reproduced by the standard traffic mix scenarios presented by EN 1991-2: normal traffic mix, heavy traffic mix and light traffic mix.

3.2.5.1.2 Fatigue verification

Fatigue assessment, according to the equivalent constant amplitude stress range (CEN, 2006), consists in the verification of the following conditions:

$$\gamma_{Ff} \cdot \Delta\sigma_{E2} \leq \Delta\sigma_c / \gamma_{Mf} \tag{3.8}$$

and

$$\gamma_{Ff} \cdot \Delta\tau_{E2} \leq \Delta\tau_c / \gamma_{Mf} \tag{3.9}$$

where:

- $\gamma_{Ff} = 1$ is the partial factor for equivalent constant amplitude stress range (affects fatigue loading) (CEN, 2006);

- $\Delta\sigma_{E2} = \lambda \cdot \Phi \cdot \Delta\sigma_{71}$ and $\Delta\tau_{E2} = \lambda \cdot \Phi \cdot \Delta\tau_{71}$ are the equivalent constant amplitude stress ranges for $N = 2 \times 10^6$ cycles of direct and shear stresses, respectively;
- λ is the damage equivalent factor, defined in (CEN, 2006) and described in the following section;
- $\Delta\sigma_{71}$ and $\Delta\tau_{71}$ are the maximum stress ranges, obtained by positioning the load model LM71 in the most unfavourable positions for the direct and shear stresses, respectively.

When there is a simultaneous action of direct and shear stresses, $\Delta\sigma_{E2}$ and $\Delta\tau_{E2}$, the following condition should be observed:

$$\left(\frac{\gamma_{Ff} \cdot \Delta\sigma_{E2}}{\Delta\sigma_c / \gamma_{Mf}}\right)^3 + \left(\frac{\gamma_{Ff} \cdot \Delta\tau_{E2}}{\Delta\tau_c / \gamma_{Mf}}\right)^5 \leq 1 \tag{3.10}$$

unless special reference to a different assessment method is made in the detail classification tables.

3.2.5.1.3 Damage equivalence factor - λ

The damage equivalence factor, λ, for railway bridges with a span up to 100m, should be determined according to the following expression (CEN, 2006):

$$\lambda = \lambda_1 \cdot \lambda_2 \cdot \lambda_3 \cdot \lambda_4 \leq 1.4 \tag{3.11}$$

where:

- λ_1 is the factor that accounts for the type of traffic and that depends on the length of the influence line of the detail under analysis;
- λ_2 is the factor that accounts for different volumes of traffic (traffic intensities);
- λ_3 is the factor that accounts for the design life of the structure;
- λ_4 is the factor accounting for simultaneous traffic, in bridges that have more than 1 track.

When determining λ_1, the critical distance of the influence line should be determined according to the section 9.5.3 of EN1993-2. The corresponding values of λ_1, in accordance with the type of traffic, are represented in Table 3.7.

Table 3.7 - λ_1 for different traffic scenarios (CEN, 2006).

L	EC Mix
0,5	1,60
1,0	1,60
1,5	1,60
2,0	1,46
2,5	1,38
3,0	1,35
3,5	1,17
4,0	1,07
4,5	1,02
5,0	1,03
6,0	1,03
7,0	0,97
8,0	0,92
9,0	0,88
10,0	0,85
12,5	0,82
15,0	0,76
17,5	0,70
20,0	0,67
25,0	0,66
30,0	0,65
35,0	0,64
40,0	0,64
45,0	0,64
50,0	0,63
60,0	0,63
70,0	0,62
80,0	0,61
90,0	0,61
100	0,60

	Express multiple units and underground		Rail traffic with 25 t axles
L	Type 9	Type 10	25 t Mix
0,5	0,97	1,00	1,65
1,0	0,97	1,00	1,65
1,5	0,97	1,00	1,65
2,0	0,97	0,99	1,64
2,5	0,95	0,97	1,55
3,0	0,85	0,94	1,51
3,5	0,76	0,85	1,31
4,0	0,65	0,71	1,16
4,5	0,59	0,65	1,08
5,0	0,55	0,62	1,07
6,0	0,58	0,63	1,04
7,0	0,58	0,60	1,02
8,0	0,56	0,60	0,99
9,0	0,56	0,55	0,96
10,0	0,56	0,51	0,93
12,5	0,55	0,47	0,90
15,0	0,50	0,44	0,92
17,5	0,46	0,44	0,73
20,0	0,44	0,43	0,68
25,0	0,40	0,41	0,65
30,0	0,37	0,42	0,64
35,0	0,36	0,44	0,65
40,0	0,35	0,46	0,65
45,0	0,35	0,47	0,65
50,0	0,36	0,48	0,66
60,0	0,39	0,48	0,66
70,0	0,40	0,49	0,66
80,0	0,39	0,49	0,66
90,0	0,39	0,48	0,66
100,0	0,40	0,48	0,66

The values of λ_2, as a function of the annual volume of traffic, are presented in Table 3.8, while the values of λ_3, as a function of the design life of the bridge, are presented in Table 3.9. As can be observed the reference traffic volume is 25 million t/year and the reference design life is 100 years.

Table 3.8 - λ_2 for different traffic volumes (CEN, 2006).

Traffic per year [10^6 t/track]	5	10	15	20	25	30	35	40	50
λ_2	0,72	0,83	0,90	0,96	1,00	1,04	1,07	1,10	1,15

Table 3.9 - λ_3 for different design lives (CEN, 2006).

Design life [years]	50	60	70	80	90	100	120
λ_3	0,87	0,90	0,93	0,96	0,98	1,00	1,04

The values of λ_4 are given by the following expression:

$$\lambda_4 = \sqrt[5]{n+[1-n]\cdot\left[a^5+(1-a)^5\right]} \tag{3.12}$$

where:

- $a = \Delta\sigma_1 / \Delta\sigma_{1+2}$ is the ratio between the stress in the detail when only one track is loaded and the stress in the same detail when both tracks are loaded;

- n is the percentage of simultaneous traffic over the bridge. If n is not specified and/or no other information is available, a value of n = 12% should be adopted.

Table 3.10 presents the values of λ_4 for n = 12% and for different values of $\Delta\sigma_1/\Delta\sigma_{1+2}$.

Table 3.10 - λ_4 for n = 12% and for different values of $\Delta\sigma_1/\Delta\sigma_{1+2}$ (CEN, 2006).

$\Delta\sigma_1/\Delta\sigma_{1+2}$	1,00	0,90	0,80	0,70	0,60	0,50
λ_4	1,00	0,91	0,84	0,77	0,72	0,71
$\Delta\sigma_1$ is the stress range at the section to be checked due to load model 71 on one track;						
$\Delta\sigma_{1+2}$ is the stress range at the same section due to load model 71 according to EN 1991-2 on any two tracks.						

3.2.5.2 Linear damage accumulation method

3.2.5.2.1 Applicability conditions

This is the most comprehensive method for the fatigue analysis present in the Eurocodes. It can be used in most of the cases, but its applicability may be conditioned by the type of details existing in the structure to be analysed, since the range of details covered by the Eurocodes is limited.

Nevertheless, it is also the more complex and time consuming method of analysis, since it requires the dynamic or quasi-static analysis of the structure and obtaining the corresponding structural response at the critical detail, for the real traffic or standard traffic mixes.

3.2.5.2.2 Fatigue verification

The fatigue assessment using the damage accumulation method, consists in the verification of the well-known Palmgren-Miner rule (CEN, 2004):

$$D = \sum \frac{n_i}{N_i} \leq 1 \tag{3.13}$$

where:

- n_i is the number of stress cycles of stress range equal to $\Delta\sigma_i$, resulting from loading. n_i should be computed considering all the design life of the structure and the traffic type and traffic intensity evolutions forecasted;
- N_i is the fatigue strength for stress cycles with a constant range of $\Delta\sigma_i$.

The steps required for the fatigue analysis using linear damage accumulation, are presented in the Annex A of (CEN, 2004). Those steps are:

- Definition of the loading events, after characterization of the traffic scenarios;
- Determination of the stress histories, at the details;
- Stress cycles counting using an appropriate methodology, such as the rainflow method;
- Determination of the histogram of stress ranges (n_i);
- Identification of the S-N curve that better represents the fatigue strength of the detail and computation of the constant amplitude fatigue strength for each stress range (N_i).
- Damage computation using the Palmgren-Miner rule.

In the same document a chart illustrates the global process (Figure 3.13).

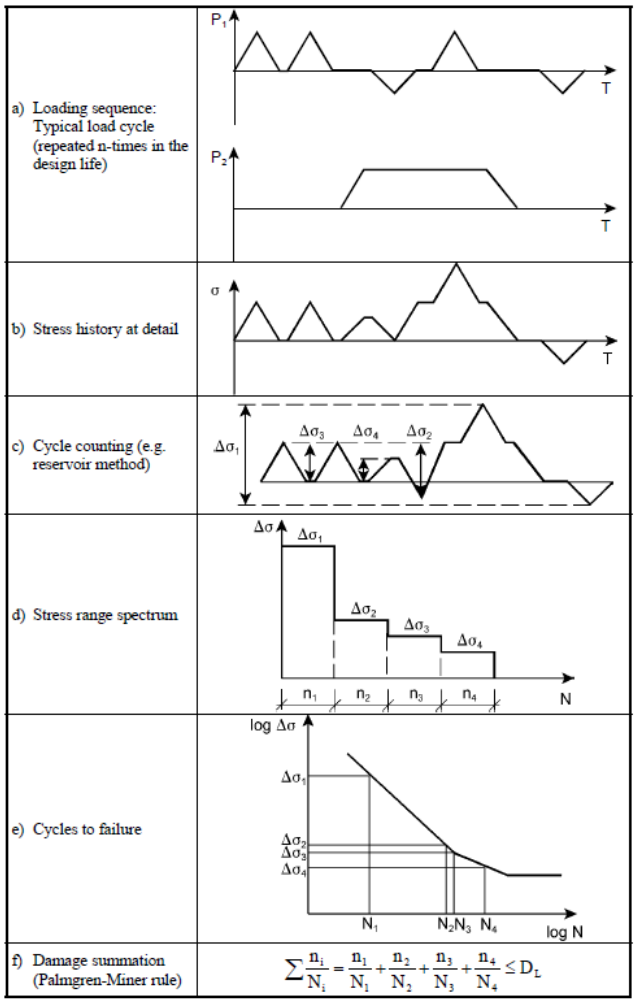

Figure 3.13 - Workflow of the linear damage accumulation method (CEN, 2004).

3.3 FATIGUE ASSESSMENT ACCORDING TO OTHER INTERNATIONAL STANDARDS

3.3.1 BS5400 - Steel, concrete and composite bridges. Part 10. Code of practice for fatigue

3.3.1.1 Introduction

The British Standard *BS5400 – Steel, concrete and composite bridges* was recently superseded in UK by the Eurocodes. Nevertheless, its *Part 10 – Code of practice for fatigue* (BSI, 1980) is worth analysing since it considered additional aspects of the fatigue behaviour of bridges when compared with the Eurocodes, namely:

- Additional structural details are categorised;
- Probability of failure can be modelled explicitly;
- Workmanship and inspection are considered directly in details categorization.

These differences are analysed next.

3.3.1.2 Standard fatigue loads and load cases

BS5400 defines two types of standard railway bridge live load:

- RU loading – allows for all combinations of vehicles currently running or projected to run on railways in Europe and is to be adopted for the design of bridges carrying main line railways of 1.4m gauge and above;
- RL loading – it is a reduced loading for use only on passenger rapid transit railway systems on lines where main line locomotives and rolling stock do not operate.

For the RU loading, three different standard traffic mixes are defined: heavy, medium and light, which is similar to the approach used in the Eurocodes. For the RL loading, one standard traffic mix is defined. These traffic mixes correspond to different combinations of 15 standard fatigue trains (which compares with the 12 standard fatigue trains presented in the Eurocodes). Figure 3.14 and Figure 3.15 show two examples of the standard fatigue trains used by BS5400.

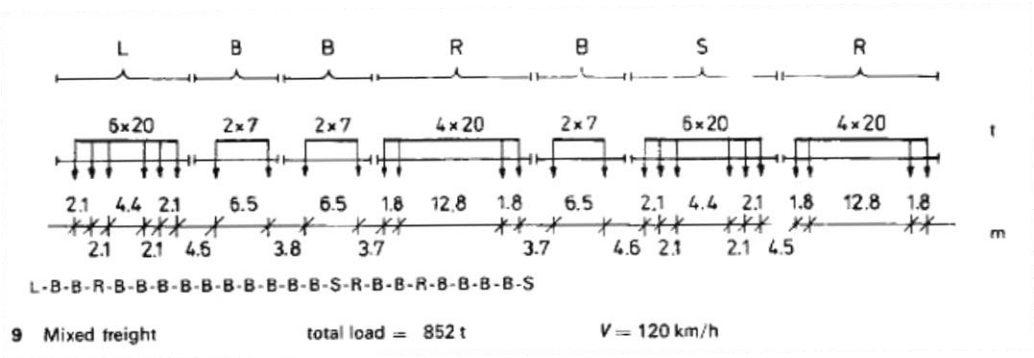

Figure 3.14 – Example of train (Train 9) considered in RU type of loading (BSI, 1980).

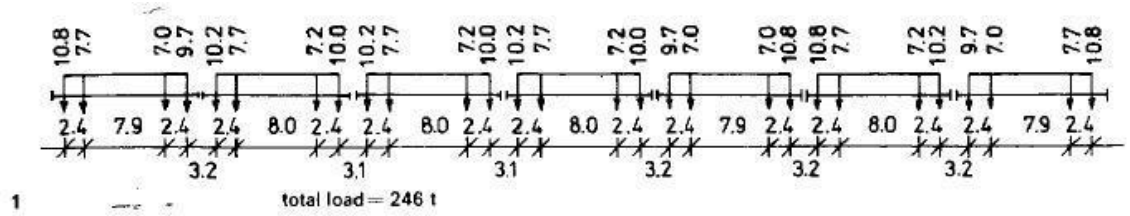

Figure 3.15 - Example of train (Train 1) considered in RL type of loading (BSI, 1980).

Another difference between these standards is that the traffic mixes in the BS5400 have a total annual tonnage of 27 million t, which is higher than the 25 million t considered in the Eurocodes. Tables 3.11 to 3.14 summarise the contribution of each train to the total annual tonnages of each traffic mix.

Table 3.11 - RU loading: heavy traffic mix (adapted from BSI (1980)).

Train	**Total train weight [t]**	**Number of trains per annum**	**Total annual tonnage [10^6 t]**	**Description**
7	1120	4821	5.4	Heavy freight
8	1120	7232	8.1	Heavy freight
9	852	15845	13.5	Mixed freight
Total			27.0	

Table 3.12 - RU loading: medium traffic mix (adapted from BSI (1980)).

Train	Total train weight [t]	Number of trains per annum	Total annual tonnage [10^6 t]	Description
5	600	22500	13.5	Diesel hauled passenger train
7	1120	2411	2.7	Heavy freight
8	1120	6027	6.75	Heavy freight
1	1794	2257	4.05	Steel train
Total			**27.0**	

Table 3.13 - RU loading: light traffic mix (adapted from BSI (1980)).

Train	Total train weight [t]	Number of trains per annum	Total annual tonnage [10^6 t]	Description
1	1794	752	1.35	Steel train
2	372	14516	5.40	Electric multiple unit
3	344	23546	8.10	Southern Region suburban
4	172	47093	8.10	Southern Region suburban
5	600	4500	2.70	Diesel hauled passenger train
6	572	2360	1.35	Electric hauled passenger train
Total			**27.0**	

Table 3.14 - RL loading: traffic mix (adapted from BSI (1980)).

Train	Total train weight [t]	Number of trains per annum	Total annual tonnage [10^6 t]	Description
1	246	11545	2.84	RL Train 1
2	253	54032	13.67	RL Train 2
3	280	9786	2.74	RL Train 3
4	203	6453	1.31	RL Train 4
5	209	26986	5.64	RL Train 5
6	231	3463	0.80	RL Train 6
Total			**27.0**	

Besides the vertical and centrifugal forces considered by Eurocodes, the BS5400 also considers the impact and lurching forces. In welded members the dead load stress does not need to be considered. In non-welded members the dead load stress may be considered if the effective stress range is to be computed (when compression stresses occur).

3.3.1.3 Fatigue strength

3.3.1.3.1 S-N curves

BS5400 defines the strength of details to fatigue in the form of S-N curves, similarly to Eurocode 3. These S-N curves relate normal or tangential stress range, denoted σ_R, to the corresponding number of cycles to failure, N. They are defined generically by Figure 3.16.

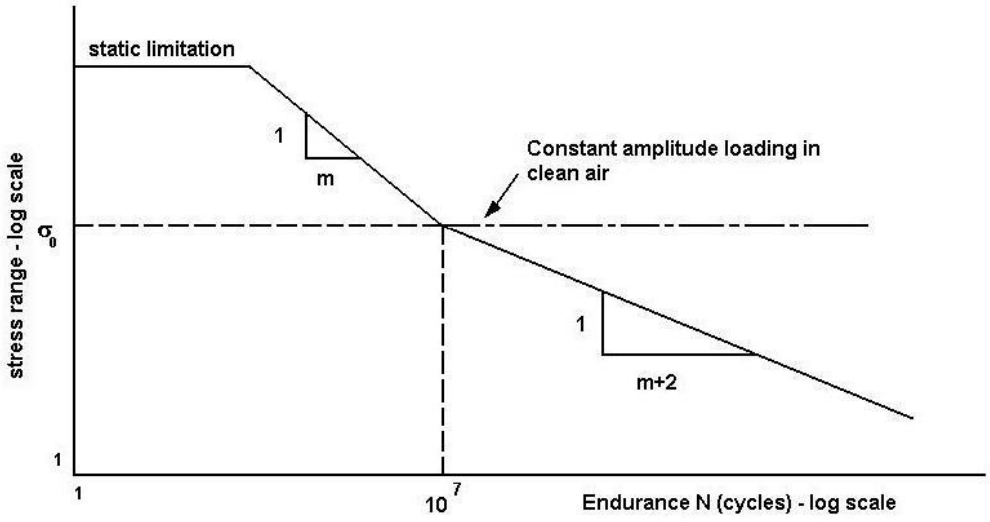

Figure 3.16 - Typical σ_R – N relationship (BSI, 1980).

As can be observed only one stress range characterises the S-N curve, which is:

- σ_0 – Constant amplitude non-propagating stress range. This concept is identical to the one in Eurocode 3 ($\Delta\sigma_D$). It reflects the understanding that under fluctuating stress of constant amplitude, there is a certain stress range below which an indefinitely large number of cycles can be sustained. Nevertheless, the constant amplitude non-propagating range, σ_0, is defined for $N = 10^7$ which differs from the $N = 5\text{x}10^7$ adopted in the Eurocode.

The S-N curves can have two configurations:

- When the applied fluctuating stress has constant amplitude, the S-N curves are characterised by a single curve with slopes varying according to the detail category. It is defined as 1/3 for detail classes W, G, F2, F, E and D, 1/3.5 for detail class C, 1/4 for detail class B and 1/8 for detail class S. All of those curves are defined by the stress

range σ_0 above for $N = 10^7$. This configuration is also applicable to fluctuating stress with varying amplitude as long as the maximum stress range is always less than σ_0.

- If the fluctuating stress has varying amplitude, so that some of the stress ranges are greater and some less than σ_0, the S-N curve is characterised by two slopes equal to $1/m$ and $1/(m+2)$ respectively (Figure 3.16).

The fact that the BS5400 S-N curves are characterised by only one stress range is a difference when comparing with the Eurocodes, where the S-N curves are characterised by three distinct stress ranges, $\Delta\sigma_D$, $\Delta\sigma_C$ and $\Delta\sigma_L$. It is worth mentioning the fact that in BS5400 the several S-N curves have 4 different slopes, instead of the unique slope defined in Eurocode 3.

Finally, in BS5400 there are only nine S-N curves defined (Figure 3.14), against the 14 S-N curves for direct stresses defined in Eurocodes. However, in BS5400 there is the possibility of explicitly considering different levels of probability of failure for each detail type. The design σ_R-N relationships should be obtained from Equation 3.14:

$$N \cdot \sigma_R^m = K_2 \tag{3.14}$$

where N is the predicted number of cycles to failure of a stress range σ_R, m is the inverse slope of the mean-line $\log(\sigma_R)$-$\log(N)$ curve and K_2 has the values given in Table 3.15. Damage computation, can then be performed according to Equation (3.15).

$$\frac{n}{N} = \begin{cases} \frac{n\sigma_r^m}{K_2} = \frac{n}{10^7}\left(\frac{\sigma_r}{\sigma_0}\right)^m & \text{when } \sigma_r \geq \sigma_0 \\ \frac{n\sigma_r^{m+2}}{K_2\sigma_0^2} = \frac{n}{10^7}\left(\frac{\sigma_r}{\sigma_0}\right)^{m+2} & \text{when } \sigma_r < \sigma_0 \end{cases} \tag{3.15}$$

The standard design curve described by Equation (3.15) corresponds to a probability of failure of 2.3% within the design life. To account for different probability of failure, Equation (3.15) may be written in the following way:

$$N \cdot \sigma_R^m = K_0 \cdot \Delta^d \tag{3.16}$$

where K_0 is the constant term relating to the mean line of the experimental tests results, Δ is the reciprocal of the anti-log of the standard deviation of $\log(N)$ and d is the number of standard deviations below the mean-line. The values of K_0 and Δ are also defined in Table 3.15. The standard design σ_R-N curve corresponds to a probability of failure of 2.3% within the design life. For other values of probability of failure the value d should be as described in Table 3.16.

Table 3.15 – σ_r-N relationships constants (adapted from BSI (1980)).

Class	**m**	σ_0 **[N/mm²]**	K_2	K_0	Δ
W	3	25	$0{,}16\text{x}10^{12}$	$0{,}37\text{x}10^{12}$	0,654
G	3	29	$0{,}25\text{x}10^{12}$	$0{,}57\text{x}10^{12}$	0,662
F2	3	35	$0{,}43\text{x}10^{12}$	$1{,}23\text{x}10^{12}$	0,592
F	3	40	$0{,}63\text{x}10^{12}$	$1{,}73\text{x}10^{12}$	0,605
E	3	47	$1{,}04\text{x}10^{12}$	$3{,}29\text{x}10^{12}$	0,561
D	3	53	$1{,}52\text{x}10^{12}$	$3{,}99\text{x}10^{12}$	0,662
C	3.5	78	$4{,}23\text{x}10^{13}$	$1{,}08\text{x}10^{14}$	0,625
B	4	100	$1{,}01\text{x}10^{15}$	$2{,}34\text{x}10^{15}$	0,657
S	8	82	$2{,}08\text{x}10^{22}$	$2{,}13\text{x}10^{25}$	0,313

Table 3.16 - Probability factors (adapted from BSI (1980)).

Probability of failure [%]	***d***
50,0	0,0
31,0	0,5
16,0	1,0
2,3	2,0
0,14	3,0

Figure 3.17 summarises the mean-line S-N curves available in BS5400 while Figure 3.18 gives an example of the impact of assuming different probabilities of failure for a certain S-N curve.

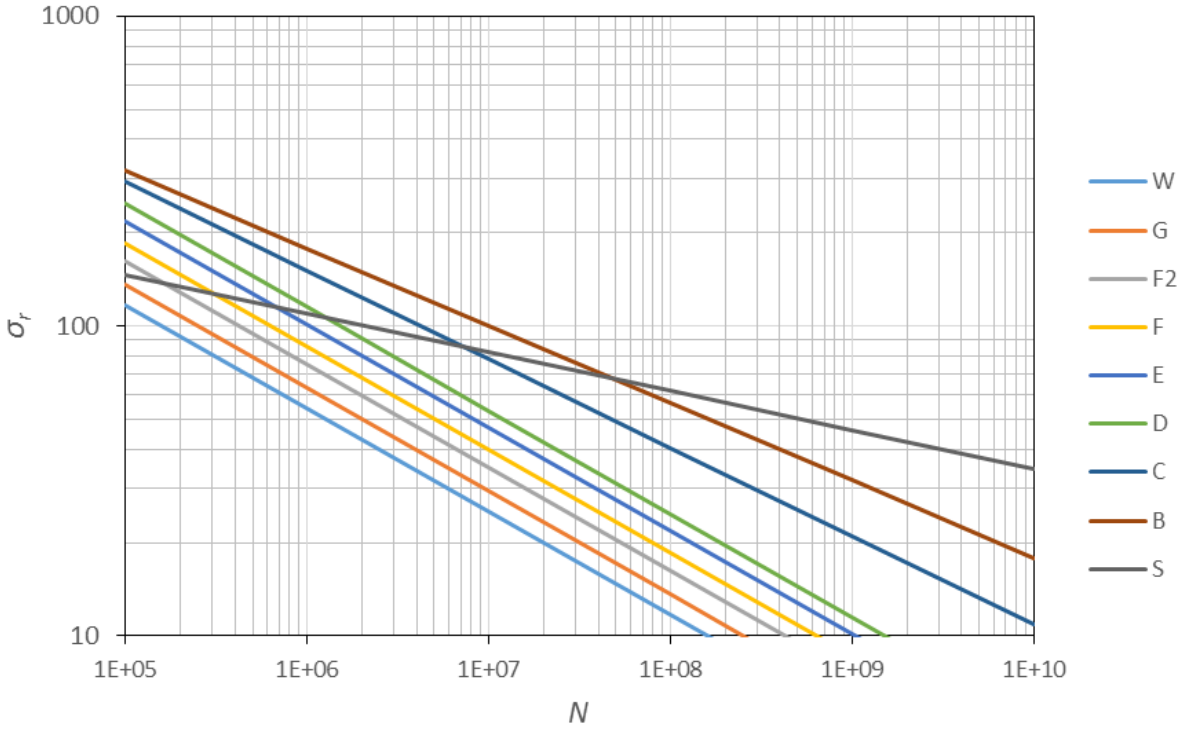

Figure 3.17 - Summary of mean-line σ_R – N curves (adapted from BSI (1980)).

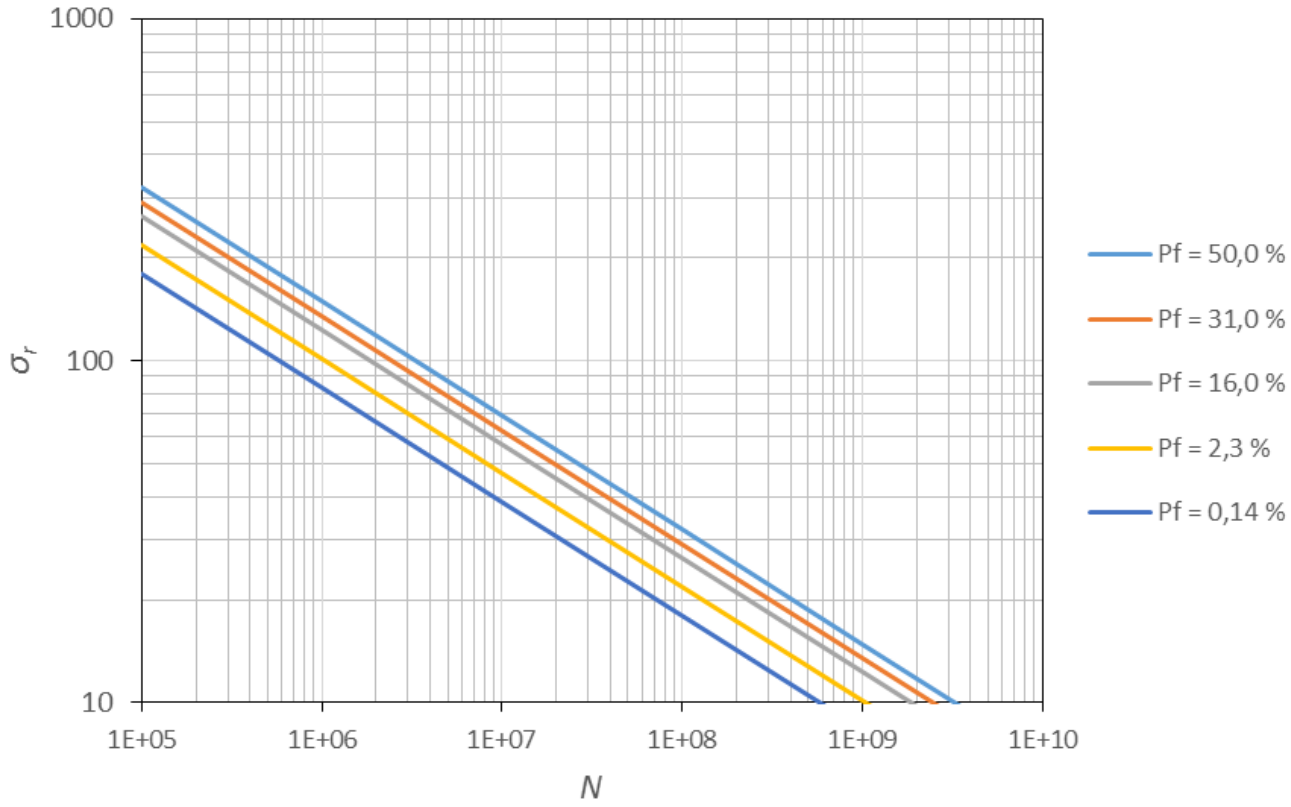

Figure 3.18 - $\sigma_R - N$ curves of detail class E for different probabilities of failure (adapted from BSI (1980)).

3.3.1.3.2 Detail categories

The details are classified according to Table 17 of BS5400. This table is divided into three parts which correspond to the three basic types into which details may be classified:

a) Non-welded details;

b) Welded details on surface of member;

c) Welded details at end connections of members.

As an example, an extract of non-welded details classification is presented in Figure 3.19. The fatigue strength classification of each part of a detail depends upon the following:

- direction of the fluctuating stress relative to the detail;
- location of possible crack initiation;
- geometrical arrangement and proportions of the detail;
- methods of manufacture and inspection.

BS5400 classifies some details not covered in the Eurocodes. One example is the classification of riveted connections.

Details not fully covered in BS5400 should be treated as class G, or class W for load carrying weld metal, unless a superior resistance to fatigue is proved by special tests. Such tests should be sufficiently extensive to allow the design of σ_r-N curve to be determined.

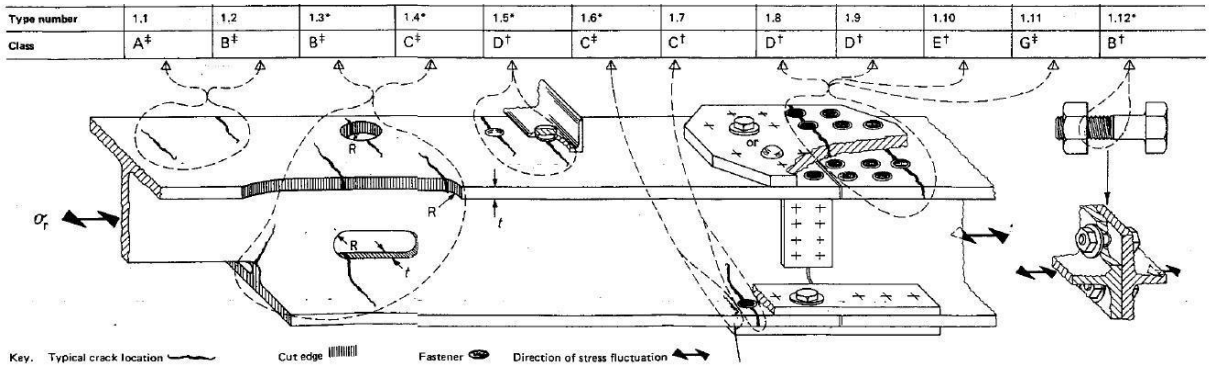

Figure 3.19 - Example of classification of non-welded details (BSI, 1980).

3.3.1.4 Determination of actuating stresses

The type of stresses foreseen in BS5400 are similar to the ones considered in the Eurocode 3, namely nominal stresses and modified nominal stresses, calculated using elastic theory.

The stress range in a plate or element to be used for fatigue assessment is the greatest algebraic difference between principal stresses occurring on principal planes not more than 45º apart in any one cycle.

For non-welded details, where the stress range is entirely in the compression zone, the effects of fatigue loading may be ignored. For non-welded details subject to stress reversals, the stress range should be determined as previously stated. The effective stress range to be used in the fatigue assessment should be obtained by adding 60% of the range from zero stress to maximum compressive stress to that part of the range from zero stress to maximum tensile stress.

The reference stress for fatigue assessment should be the principal stress in the parent metal adjacent to the potential crack location, as shown in Figure 3.20. Principal stresses adjacent to the potential crack location should be used. Stress concentration is to be included according to Table 17 of BS5400 or special analysis and factors given in Appendix H of the same standard (Figure 3.21).

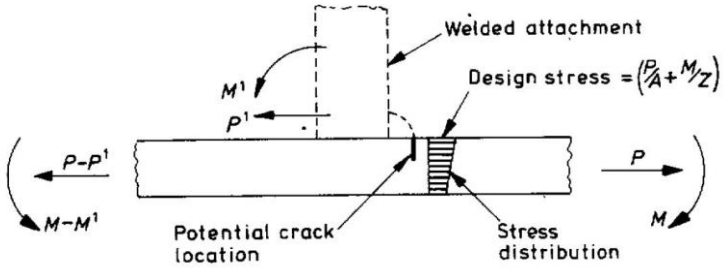

Figure 3.20 - Reference stress in parent metal (BSI, 1980).

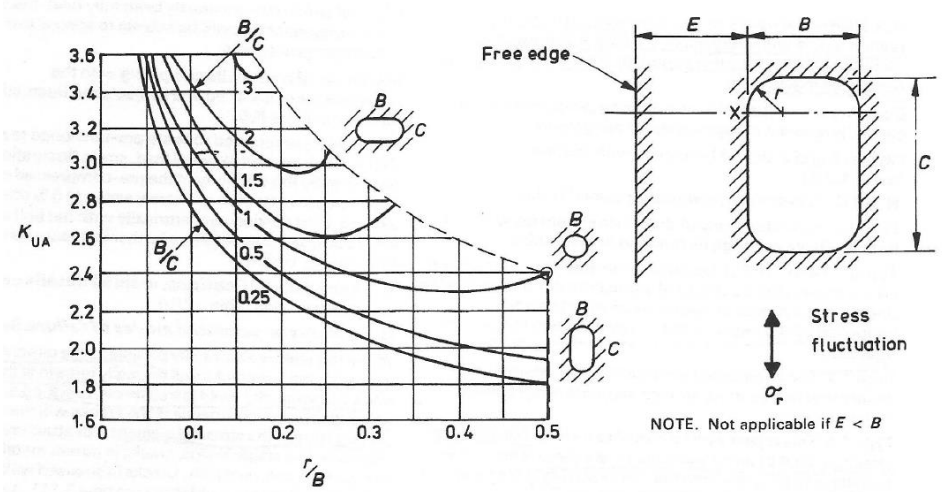

Figure 3.21 – Example of stress concentration factors provided in Appendix H of BS5400 (BSI, 1980).

3.3.1.5 Assessment methods

According to BS5400 - Part 10 the structural components of bridges that are subjected to dynamic loading (varying stresses) should have the fatigue behaviour assessed through one of the two methods described in the same standard:

- Assessment without damage calculation (simplified method) – this method is similar to the equivalent constant amplitude stress ranges method presented by the Eurocodes. It is applicable to parts of bridges with classified details and which are subjected to standard loadings. It determines the limiting value of the maximum range of stress for the specified design life;
- Assessment with damage calculation – this method is identical to the linear damage accumulation method also presented in the Eurocodes. Therefore, it is a more precise alternative to the previous method. It involves a calculation of Miner's rule and it can be used for any detail for which the S-N curve is known and for any load spectra.

The Standard assumes a design life of 120 years.

3.3.1.5.1 Simplified method of fatigue assessment without damage calculation

This method should only be used when the following conditions are satisfied:

- the detail category is in accordance with Table 17 of BS5400;
- the loading of the bridge is well represented by the standard railway bride loading of BS5400.

According to the above mentioned standard, the following procedure should be used:

a) Apply the standard loading;

b) Determine the maximum and minimum values of stress $\sigma_{p\,max}$ and $\sigma_{p\,min}$, occurring at the detail being assessed;

c) Determine the maximum range of stress $\sigma_{R\,max} = \sigma_{p\,max} - \sigma_{p\,min}$;

d) Obtain the appropriate limiting stress σ_T from Equations (3.17) or (3.18):

$$\sigma_T = k_1 \cdot k_2 \cdot k_3 \cdot k_4 \cdot k_5 \cdot \sigma_0 \text{ for RU loading} \tag{3.17}$$

$$\sigma_T = k_1 \cdot k_2 \cdot k_4 \cdot k_5 \cdot k_6 \cdot \sigma_0 \text{ for RL loading} \tag{3.18}$$

where:

- k_1 takes into account the design life of the structure. k_1 = 1 if the design life is 120 years, otherwise k_1 should be the lesser of Equations (3.19) and (3.20):

$$\left(\frac{120}{\textit{design life}\ [\text{years}]}\right)^{1/m} \tag{3.19}$$

$$\left(\frac{120}{\textit{design life}\ [\text{years}]}\right)^{1/(m+2)} \tag{3.20}$$

- k_2 takes into account the number of stress cycles per loading event. k_2 = 1 if the loading event produces only one cycle of stress. Otherwise, the number of cycles should be counted using a cycles counting procedure, such as the reservoir method and the value of k_2 should be obtained from:

$$k_2 = \left(1 + \left(\frac{\sigma_{R2}}{\sigma_{R1}}\right)^m + \left(\frac{\sigma_{R3}}{\sigma_{R1}}\right)^m + \ldots\right)^{-\frac{1}{m}} \tag{3.21}$$

where σ_{R1}, σ_{R2}, σ_{R3}, and so forth are the stress ranges in descending order of magnitude of each individual cycle produced by the approach, passage and departure of a unit uniformly distributed load.

- k_3 takes into consideration the length of the influence line of each structural component under analysis, for RU loading;
- k_4 takes into consideration the annual traffic tonnage per track, over the bridge;
- k_5 takes into consideration the effects of simultaneous loading of more than one track, when the bridge holds more than one track;
- k_6 takes into consideration the length of the influence line of each structural component under analysis, for RL loading.

As it can be observed, the different k_i factors are the equivalent, in BS5400, to the damage equivalence factors used in Eurocode 3.

According to this method, each detail is considered to have a fatigue life in excess of the specified design life when:

$$\sigma_{R\,max} \leq \sigma_T \tag{3.22}$$

When comparing this assessment method, in BS5400, with the equivalent constant amplitude stress range method presented in Eurocode 3, it can be seen that there is no equivalent load to the LM71. Instead, the standard loading mentioned in section 3.3.1.3 is used.

3.3.1.5.2 Method with damage calculation

This method is similar to the linear damage accumulation method proposed in Eurocode 3. It involves computing fatigue damage through the application of Palmgren-Miner´s rule and may be used for any detail for which the $\sigma_R - N$ relationship is defined.

Where the loading does not comply with the standard loading, the appropriate train should be traversed across the structure and the resulting stress histories should be analysed using a cycles counting method, such as rainflow method, to derive the respective stress ranges spectra.

In assessing an existing structure the design spectrum may be compiled from strain readings or traffic records. Where a non-standard loading is used or stress ranges are obtained from strain gauges readings, the design spectrum should be divided into at least 10 equal intervals of stress.

The total damage computed for the traffic scenario considered and for the design life adopted should not exceed 1 for the fatigue life of the detail to be acceptable (see Equation (3.13)).

3.3.2 AASHTO - LRFD Bridge Design Specifications

3.3.2.1 Introduction

The AASHTO (American Association of State Highway and Transportation Officials) standard is the reference standard in the United States for highway bridge design. Because of its focus on highway rather than railway traffic, it is not an adequate point of comparison with Eurocodes in terms of loading. Nevertheless, it presents its own details classification proposal and fatigue S-N curves which are worth comparing with Eurocode 3. Moreover, its specifications concerning fatigue complement the Eurocodes in some aspects, namely, the explicit distinction between load induced fatigue and distortion induced fatigue and the inclusion of considerations concerning fracture and toughness of the materials. These differences are detailed in the next sections.

3.3.2.2 Standard fatigue loads and load cases

AASHTO LRFD Bridge Design Specifications does not include provisions for bridges used solely for railways. Namely, the railway load models and traffic mixes that should be used for the fatigue assessment of railway bridges are not specified.

Nevertheless, it is mentioned that in cases where the bridges carry both highway and railway the owner shall specify the transit load characteristics and the expected interaction between rail transit and highway traffic. These may include loads, load distribution, load frequency, dynamic allowance and dimensional requirements. However, the bridge should not have less strength than if designed as a highway bridge of the same width.

According to AASHTO, the fatigue load combination to be used should include the dynamic live load and the centrifugal forces, if applicable. Different load factors shall be applied depending on the design philosophy. If infinite fatigue life is aimed, the Fatigue I load combination and corresponding load factor should be adopted. If finite fatigue life is allowed, the Fatigue II load combination is to be considered (Table 3.17).

Table 3.17 – Load combinations and load factors (AASHTO, 2012).

Load Combination Limit State	*DC DD DW EH EV ES EL PS CR SH*	*LL IM CE BR PL LS*	*WA*	*WS*	*WL*	*FR*	*TU*	*TG*	*SE*	Use One of These at a Time				
										EQ	*BL*	*IC*	*CT*	*CV*
Strength I (unless noted)	γ_p	1.75	1.00	—	—	1.00	0.50/1.20	γ_{TG}	γ_{SE}	—	—	—	—	—
Strength II	γ_p	1.35	1.00	—	—	1.00	0.50/1.20	γ_{TG}	γ_{SE}	—	—	—	—	—
Strength III	γ_p	—	1.00	1.40	—	1.00	0.50/1.20	γ_{TG}	γ_{SE}	—	—	—	—	—
Strength IV	γ_p	—	1.00	—	—	1.00	0.50/1.20	—	—	—	—	—	—	—
Strength V	γ_p	1.35	1.00	0.40	1.0	1.00	0.50/1.20	γ_{TG}	γ_{SE}	—	—	—	—	—
Extreme Event I	γ_p	γEQ	1.00	—	—	1.00	—	—	—	1.00	—	—	—	—
Extreme Event II	γ_p	0.50	1.00	—	—	1.00	—	—	—	—	1.00	1.00	1.00	1.00
Service I	1.00	1.00	1.00	0.30	1.0	1.00	1.00/1.20	γ_{TG}	γ_{SE}	—	—	—	—	—
Service II	1.00	1.30	1.00	—	—	1.00	1.00/1.20	—	—	—	—	—	—	—
Service III	1.00	0.80	1.00	—	—	1.00	1.00/1.20	γ_{TG}	γ_{SE}	—	—	—	—	—
Service IV	1.00	—	1.00	0.70	—	1.00	1.00/1.20	—	1.0	—	—	—	—	—
Fatigue I— *LL, IM & CE* only	—	1.50	—	—	—	—	—	—	—	—	—	—	—	—
Fatigue II— *LL, IM & CE* only	—	0.75	—	—	—	—	—	—	—	—	—	—	—	—

3.3.2.3 Fatigue strength

3.3.2.3.1 S-N curves

According to AASHTO, the nominal fatigue resistance may be calculated through Equation (3.23):

$$(\Delta F)_n = \left(\frac{A}{N}\right)^{\frac{1}{3}} \geq \frac{1}{2}(\Delta F)_{TH} \tag{3.23}$$

where:

- A is a constant defined in Table 3.18;
- $(\Delta F)_n$ is the fatigue resistance (in MPa);
- N is the number of stress cycles to failure, for cycles with a range of $(\Delta F)_n$;
- $(\Delta F)_{TH}$ is the fatigue resistance threshold for constant amplitude stress ranges (MPa), taken from Table 3.19.

If the loading on a structural detail is always inferior to $(\Delta F)_{TH}$ it implies that there is no damage in the detail.

Table 3.18 - Detail Category Constant, *A* (adapted from AASHTO (2012)).

Detail Category	$\boldsymbol{Ax10^{11}}$ **[MPa^3]**
A	82.00
B	39.30
B'	20.00
C	14.40
C'	14.40
D	7.21
E	3.61
E'	1.28

Table 3.19 - Constant Amplitude Fatigue Thresholds (adapted from AASHTO (2012)).

Detail Category	$\boldsymbol{(\Delta F)_{TH}}$ **[Mpa]**
A	165.0
B	110.0
B'	82.7
C	69.0
C'	82.7
D	48.3
E	31.0
E'	17.9

As it can be observed, the eight different values of *A* and $(\Delta F)_{TH}$ define, according to Equation 3.23, eight different standard S-N curves (Figure 3.22).

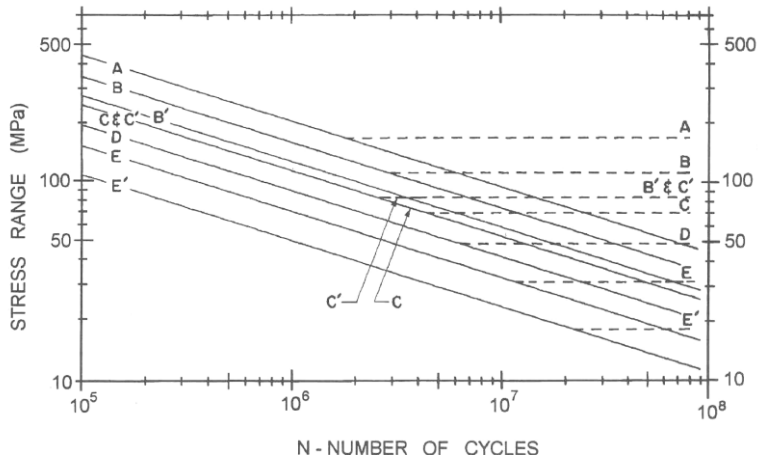

Figure 3.22 – S-N curves specified in AASHTO standard (AASHTO, 2012).

These curves are applicable to both redundant and non-redundant structural elements. The differentiation between redundant and non-redundant members is achieved through the

imposition of a higher toughness requirements to the materials used in non-redundant structural elements.

3.3.2.3.2 Detail categories

The structural details have been grouped into eight categories by fatigue resistance. An example of the structural details classification is shown in Figure 3.23.

Description	Category	Constant A (ksi^3)	Threshold $(\Delta F)_{TH}$ ksi	Potential Crack Initiation Point	Illustrative Examples
Section 1—Plain Material away from Any Welding					
1.1 Base metal, except noncoated weathering steel, with rolled or cleaned surfaces. Flame-cut edges with surface roughness value of 1,000 μ-in. or less, but without re-entrant corners.	A	250×10^8	24	Away from all welds or structural connections	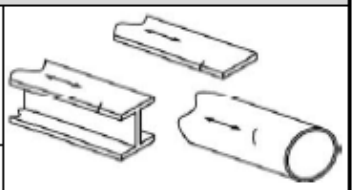
1.2 Noncoated weathering steel base metal with rolled or cleaned surfaces designed and detailed in accordance with FHWA (1989). Flame-cut edges with surface roughness value of 1,000 μ-in. or less, but without re-entrant corners.	B	120×10^8	16	Away from all welds or structural connections	
1.3 Member with re-entrant corners at copes, cuts, block-outs or other geometrical discontinuities made to the requirements of AASHTO/AWS D1.5, except weld access holes.	C	44×10^8	10	At any external edge	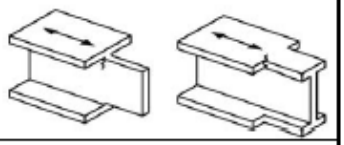
1.4 Rolled cross sections with weld access holes made to the requirements of AASHTO/AWS D1.5, Article 3.2.4.	C	44×10^8	10	In the base metal at the re-entrant corner of the weld access hole	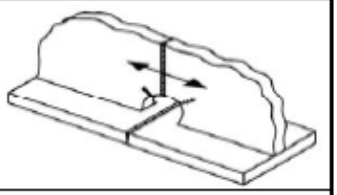
1.5 Open holes in members (Brown et al., 2007).	D	22×10^8	7	In the net section originating at the side of the hole	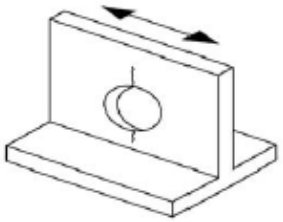

Figure 3.23 - Example of detail categories for Load-Induced Fatigue (adapted from AASHTO (2012)).

3.3.2.4 Assessment methods and other considerations

3.3.2.4.1 Load-induced fatigue

For load-induced fatigue assessment, structural details must satisfy Equation (3.24).

$$\gamma(\Delta f) \leq (\Delta F)_n \tag{3.24}$$

where γ is the load factor specified in this standard for fatigue load combination; (Δf) is the force effect, live load stress range (MPa); $(\Delta F)_n$ is the nominal fatigue resistance (MPa). For this purpose, the force effect considered shall be the live load stress range. Alternatively, the assessment can be performed by the application of the Palmgren-Miner rule.

3.3.2.4.2 Distortion-induced fatigue

AASHTO provides some design specifications in order for distortion-induced fatigue to be minimised. Some of those specifications are listed below:

- Load paths which are sufficient to transmit all intended and unintended forces shall be provided by connecting all transverse members to appropriate components which comprise the cross-section of the longitudinal member;
- The load paths shall be provided by attaching the various components through either welding or bolting;
- Connection plates shall be welded or bolted to both the compression and tension flanges of the cross-section;
- In the absence of better information, the welded or bolted connection should be designed to resist a 90000 N lateral load for straight, non-skewed bridges.

For lateral connection plates the AASHTO standard specifies minimum distances which are intended to reduce out-of-plane distortion in the web between the lateral connection plate and the flange. These requirements reduce potential distortion-induced stresses in the gap between the web or stiffener and the lateral members on the lateral plate, which could result from vibration in the latter.

3.3.2.4.3 Fracture strength considerations

According to AASHTO, all primary longitudinal superstructure components and connections sustaining tensile stress as well as transverse floorbeams shall require mandatory Charpy V-notch testing. The appropriate temperature zone shall be determined from the applicable minimum service temperature, as specified in Table 3.20. Fracture toughness requirements shall be in accordance with Table 3.21 for the appropriate temperature zone. Moreover, the Engineer shall have the responsibility for determining which structural elements are fracture-critical members

(FCM), for which more demanding fracture toughness requirements are to be imposed (Table 3.21). A fracture-critical member is a non-redundant member whose failure is expected to result in the collapse of the bridge or in the bridge's inability to perform its function.

Table 3.20 - Temperature Zone Designations for Charpy V-notch Requirements (AASHTO, 2012).

Minimum Service Temperature	Temperature Zone
-18 º C and above	1
-19 º C to -34 º C	2
-35º C to -51 º C	3

Table 3.21 - Fracture Toughness Requirements (AASHTO, 2012).

Grade (Y.P./Y.S.)	Thickness (in.)	Fracture-Critical				Nonfracture-Critical		
		Min. Test Value Energy (ft-lbs.)	Zone 1 (ft-lbs. @ °F)	Zone 2 (ft-lbs. @ °F)	Zone 3 (ft-lbs. @ °F)	Zone 1 (ft-lbs. @ °F)	Zone 2 (ft-lbs. @ °F)	Zone 3 (ft-lbs. @ °F)
36	$t \leq 4$	20	25 @ 70	25 @ 40	25 @ 10	15 @ 70	15 @ 40	15 @ 10
50/50S/50W	$t \leq 2$	20	25 @ 70	25 @ 40	25 @ 10	15 @ 70	15 @ 40	15 @ 10
	$2 < t \leq 4$	24	30 @ 70	30 @ 40	30 @ 10	20 @ 70	20 @ 40	20 @ 10
HPS 50W	$t \leq 4$	24	30 @ 10	30 @ 10	30 @ 10	20 @ 10	20 @ 10	20 @ 10
HPS 70W	$t \leq 4$	28	35 @ −10	35 @ −10	35 @ −10	25 @ −10	25 @ −10	25 @ −10
HPS 100W	$t \leq 2-1/2$	28	35 @ –30	35 @ –30	35 @ −30	25 @ –30	25 @ –30	25 @ −30
	$2\text{-}1/2 < t \leq 4$	36	not permitted	not permitted	not permitted	35 @ –30	35 @ –30	35 @ −30

3.3.3 International Institute of Welding – Recommendation for Fatigue Design of Welded Joints and Components

3.3.3.1 Introduction

The International Institute of Welding (IIW) has its own standard fatigue classification system, intended for welded details (IIW, 2008). Its focus is on the welded details strength to fatigue irrespective of the type of loading. Therefore, no standard railway fatigue loading (or other) is proposed in the same standard.

Concerning the methodologies for the fatigue assessment, a wider range of approaches is proposed by IIW when comparing with Eurocodes, namely:

- Nominal stresses approach (also included in Eurocode 3);
- Hot spot stresses approach (also included in Eurocode 3);
- Effective notch stresses approach (not included in Eurocode 3);
- Stress intensity factors approach (not included in Eurocode 3).

In the current section, only the approaches using nominal stresses and hot spot stresses are analysed. The approaches using effective notch stresses and stress intensity factors will be discussed in Chapter 4, as they are considered advanced fatigue assessment methodologies.

3.3.3.2 Fatigue strength

3.3.3.2.1 S-N curves

The S-N curves proposed by IIW are divided into 15 curves for normal stresses and 2 curves for shear stresses.

In the case of normal stresses, the slope is usually $m = 3$, unless stated otherwise. The constant amplitude knee is set at $N = 10^7$ cycles and the curves are identified by its fatigue strength, in MPa for $N = 2$ million cycles. For constant amplitude stress ranges or variable amplitude stress ranges where all the cycle ranges are lower than the constant amplitude fatigue limit, the S-N curves configuration is the one presented in Figure 3.24. For applications with variable amplitude loading, with part of the cycle ranges exceeding the constant amplitude fatigue limit, IIW proposes the continuation of the S-N curve beyond the knee point with a slope of $m = 5$ (Figure 3.25).

Concerning shear stress S-N curves, they have a slope of $m = 5$ and the knee point is assumed to be at $N = 10^8$ cycles (Figure 3.26).

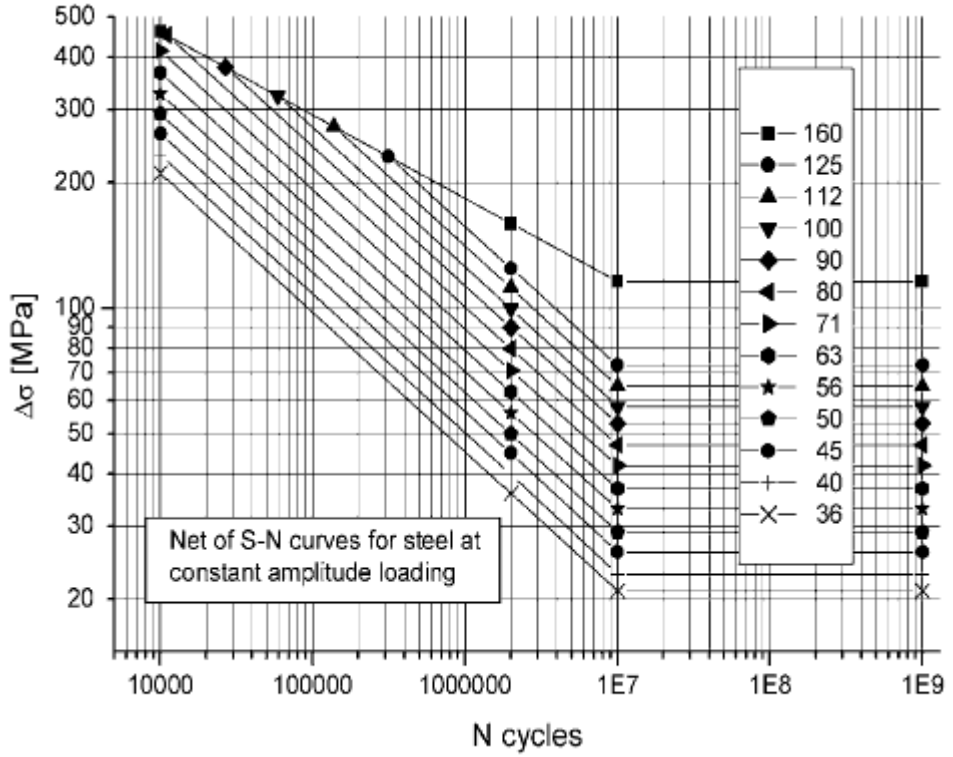

Figure 3.24 – S-N curves for normal stresses and standard applications (IIW, 2008).

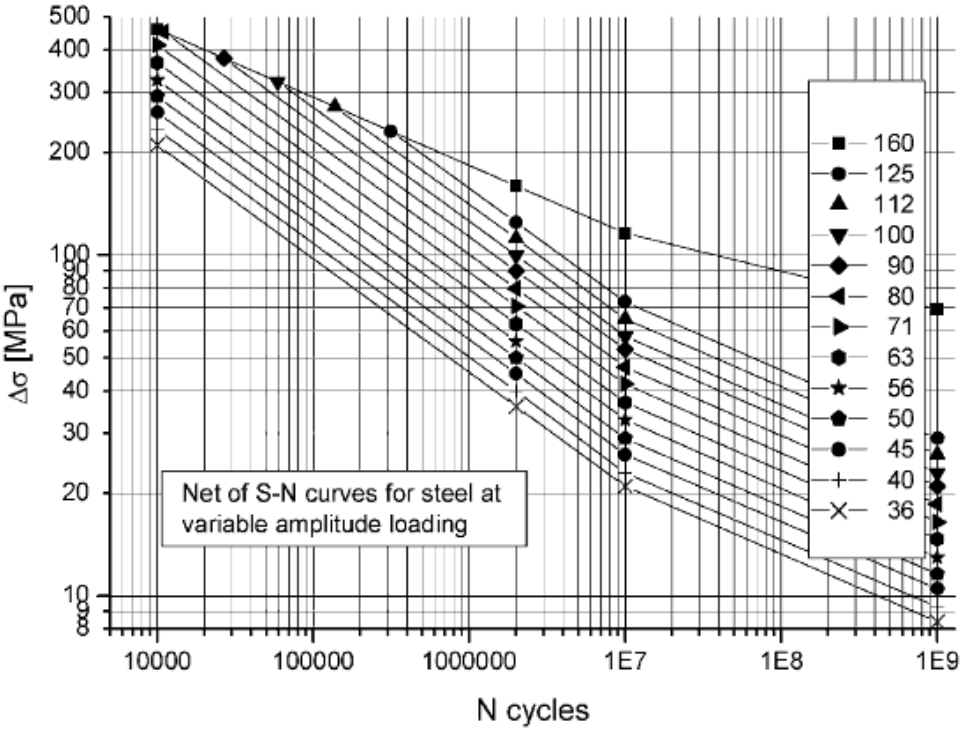

Figure 3.25 – S-N curves for normal stresses and very high cycles applications (IIW, 2008).

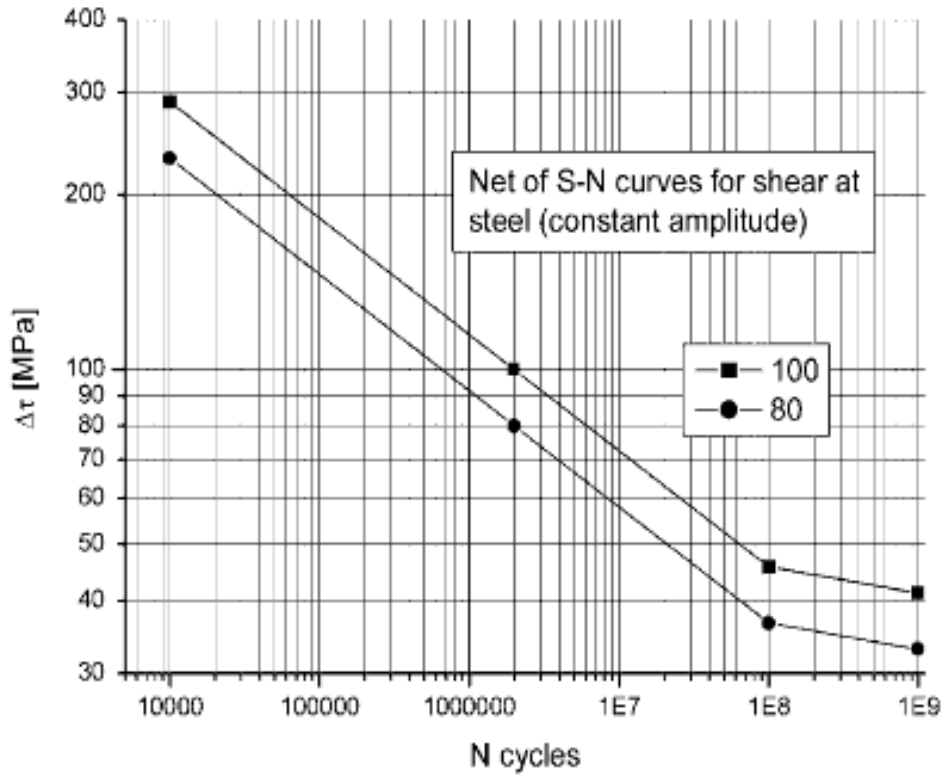

Figure 3.26 – S-N curves for shear stresses (IIW, 2008).

3.3.3.2.2 Detail categories

IIW classifies an extensive list of details, many of them not present in Eurocode 3. An example of the details classified in IIW is shown in Figure 3.27 which refers to nominal stresses. Figure 3.28 presents an example of details classified according to the hot spot stresses.

No.	Structural Detail	Description (St.= steel; Al.= aluminium)	FAT St.	FAT Al.	Requirements and Remarks
200	**Butt welds, transverse loaded**				
211		Transverse loaded butt weld (X-groove or V-groove) ground flush to plate, 100% NDT	112	45	All welds ground flush to surface, grinding parallel to direction of stress. Weld run-on and run-off pieces to be used and subsequently removed. Plate edges ground flush in direction of stress. Welded from both sides. Misalignment < 5% of plate thickness. Proved free from significant defects by appropriate NDT
212		Transverse butt weld made in shop in flat position, NDT weld reinforcement < 0.1 · thickness	90	36	Weld run-on and run-off pieces to be used and subsequently removed. Plate edges ground flush in direction of stress. Welded from both sides. Misalignment <5% of plate thickness.
213		Transverse butt weld not satisfying conditions of 212, NDT Al.: Butt weld with toe angle ≤50° Butt welds with toe angle >50°	80	 32 25	Weld run-on and run-off pieces to be used and subsequently removed. Plate edges ground flush in direction of stress. Welded from both sides. Misalignment <10% of plate thickness.

Figure 3.27 – Example of fatigue resistance classification against nominal stresses (IIW, 2008).

No.	Structural detail	Description	Requirements	FAT Steel	FAT Alu.
1	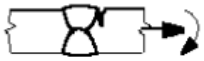	Butt joint	As welded, NDT	100	40
2	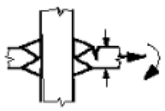	Cruciform or T-joint with full penetration K-butt welds	K-butt welds, no lamellar tearing	100	40
3	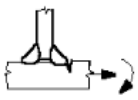	Non load-carrying fillet welds	Transverse non-load carrying attachment, not thicker than main plate, as welded	100	40
4	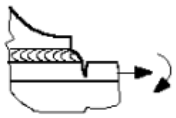	Bracket ends, ends of longitudinal stiffeners	Fillet welds welded around or not, as welded	100	40
5		Cover plate ends and similar joints	As welded	100	40

Figure 3.28 – Example of fatigue resistance classification against hot spot stresses (IIW, 2008).

3.3.3.3 Assessment methods

IIW establishes some criteria that, if met, may exempt from a fatigue assessment. Those criteria are as follows:

- The highest nominal design stress range satisfies Equation (3.25)

$$\Delta\sigma_{S,d} \leq 36\ [\text{MPa}]/\gamma_M \tag{3.25}$$

  where γ_M should be taken from the applicable design code;

- The damage computed according to Palmgren-Miner rule is $D \leq 0.5$ when evaluated using fatigue class FAT 36;

- The highest nominal design stress range is lower than the constant amplitude fatigue limit, $\Delta\sigma_{R,L}/\gamma_M$, of the detail.

If these criteria are not met, the fatigue assessment must be performed. In that case, IIW proposes the linear damage accumulation method, similar to the Eurocode 3. It also provides the

expression needed to convert the stress ranges spectra into an equivalent constant amplitude stress range (Equation (3.26)):

$$\Delta\sigma_{eq,S,d} = \sqrt[m_1]{\frac{1}{D}\cdot\frac{\sum\left(n_i\cdot\Delta\sigma_{i,S,d}{}^{m_1}\right)+\Delta\sigma_{L,d}{}^{(m_1-m_2)}\cdot\sum\left(n_j\cdot\Delta\sigma_{j,S,d}{}^{m_2}\right)}{\sum n_i+\sum n_j}} \tag{3.26}$$

where:

- D is the specified Palmgren-Miner summation (damage);
- $\sigma_{eq,S,d}$ is the design value of the equivalent constant amplitude stress range;
- m_1 is the slope above the knee point of the S-N curve;
- m_2 is the slope below the knee point of the S-N curve;
- $\sigma_{i,S,d}$ is the design value of stress ranges above the knee point;
- $\sigma_{j,S,d}$ is the design value of stress ranges below the knee point;
- $\sigma_{L,d}$ is the design value of stress ranges at the knee point of the S-N curve;
- n_i is the number of cycles at applied stress range $\Delta\sigma_i$;
- n_j is the number of cycles at applied stress range $\Delta\sigma_j$.

Finally, the IIW also proposes a nonlinear damage accumulation method which combines the current S-N curve concepts with Fracture Mechanics.

3.4 CONCLUDING REMARKS

In this Chapter, different structural design standards were analysed in terms of their fatigue assessment procedures and recommendations. Since in Europe the Eurocodes are the reference standards, special emphasis was placed on them. Other codes considered were the BS5400, the AASHTO Bridge Design Specifications and the IIW Fatigue Design Recommendations.

It was observed that each code has its proposal in terms of S-N curves and of details classification. In addition, they all include the possibility of assessing the fatigue damage through the application of the Palmgren-Miner rule of damage computation. Eurocodes, BS5400 and IIW also allow for the computation of equivalent constant amplitude stress ranges, which is considered a simplified fatigue assessment.

Nevertheless, when compared with Eurocodes, the other standards complement the information there available:

- BS5400:
    - Includes classification of additional variety of structural details, namely riveted joints;
    - Allows to model the probability of failure explicitly;
    - Considers workmanship and inspection conditions directly in the detail categorization;
    - Provides algorithms for computation of stress concentration factors in some typical details.
- AASHTO:
    - Includes classification of additional variety of structural details;
    - Distinguishes load induced fatigue from distortion induced fatigue, providing recommendations in order to the latter to be avoided;
    - Establishes the concept of fracture-critical members, for which more demanding fracture toughness requirements should apply;
    - Includes the mandatory assessment of material toughness, in order to characterise the strength to fracture.
- IIW:
    - Includes classification of additional variety of structural details;
    - Considers extra assessment methods, namely the non-linear damage accumulation approach, the effective notch stresses approach and the stress intensity factors approach;
    - Allows the assessment of structural details which already have fatigue cracks at the time of the fatigue assessment (e.g. cracks found as a result of bridge's inspection) through the stress intensity factors (Fracture Mechanics) approach;
    - Provides simple rules to assess for the necessity of a comprehensive fatigue analysis.

It can be observed that, with the exception of the IIW, the standards analysed in this Chapter use simple methodologies, based on S-N curves and on the Palmgren-Miner rule. Those methodologies present some drawbacks, such as the limited variety of structural details covered by the standards and the cumbersome task of obtaining new S-N curves for new structural details. In order to overcome these limitations, more advanced fatigue damage assessment techniques were developed and can be found in literature. Some of those methodologies are explored in Chapter 4.

Chapter 4

ADVANCED METHODOLOGIES FOR THE FATIGUE ASSESSMENT OF STRUCTURES

4.1 INTRODUCTION

The fatigue analysis in Civil Engineering is usually based on S-N curves and in the concept of linear damage accumulation, as per the Palmgren-Miner rule. As seen in Chapter 3, the Eurocodes, as most of the standards, use this methodology, presenting categories of details and the corresponding fatigue strength curves. That approach has, as main advantage, the ease of implementation and application. It can be considered as a global approach as it deals with nominal values of the actuating stresses.

Nevertheless, the S-N curves present some limitations:

- The S-N curves used nowadays cover a limited variety of structural details;
- The tests that allow building new S-N curves are performed on real scale details, making those tests expensive and time consuming and therefore usually incompatible with the pace of design and construction;
- The results of the tests performed for the determination of S-N curves present a high dispersion. This is the reason why the adopted curves are, most of the times, excessively conservative;

- The computation of damage, from S-N curves only gives information about the final status of the detail and does not give any indication about damage evolution over time;
- When a fatigue crack is found, as a consequence of inspection/maintenance activities, this methodology does not give information about the level of structural risk that it represents;
- The evolution of available commercial FEM software and the steep increase of computational processing capability led to an increasing use of advanced and detailed stress analysis, in which the concept of nominal stress loses preponderance when compared with local stresses.

In order to overcome these constraints, several more advanced approaches arose, which tried to take into account the local characteristics of geometry, loading and materials. These approaches are based on:

- Structural stresses or structural strains;
- Notch stresses;
- Notch strains;
- Fracture Mechanics and crack propagation laws.

The above mentioned methodologies, which are indicated to assess the strength to fatigue in different stages of the fatigue damage and/or at different structural scales (Figure 4.1), are briefly described in the next sections.

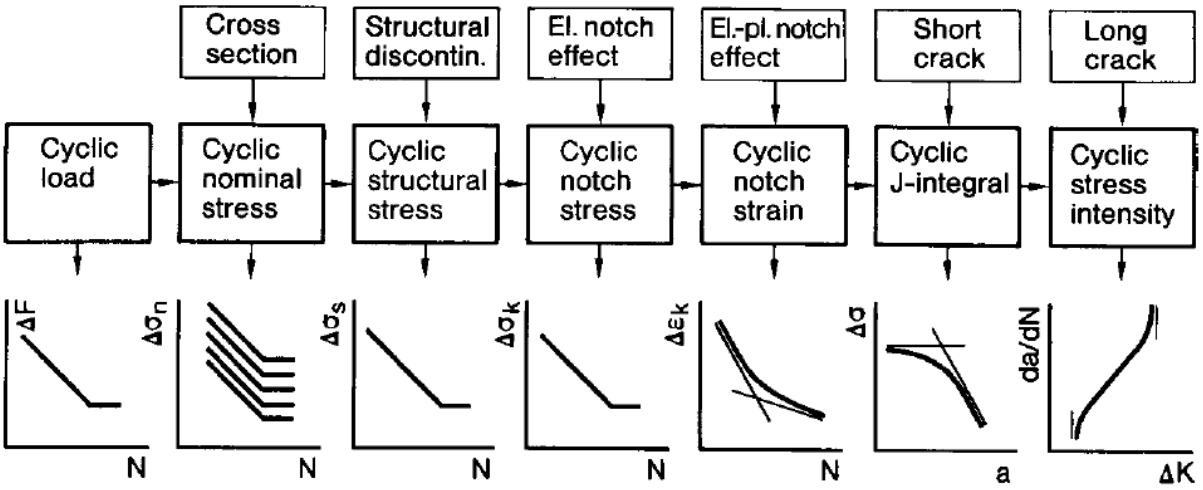

Figure 4.1 - Range of applicability of different methodologies of fatigue analysis (Radaj et al., 2006).

From these, only the Fracture Mechanics approach will be dealt with in more detail, as it is the basis of the advanced technique developed in this work in order to address the fatigue problem.

4.2 FATIGUE ASSESSMENT BASED ON STRUCTURAL STRAINS AND STRUCTURAL STRESSES

4.2.1 Introduction

The structural stresses and strains are the maximum principal stresses/strains observed at the base material surrounding the weld, having into account the stress concentration due to global geometry of the detail but excluding the stress concentrations originated by the geometry of the weld.

These structural stresses/strains may be obtained experimentally, measuring with strain gauges or computed with empiric expressions or finite element models.

The structural stress/strain is sometimes referred to as "geometric" stress/strain. Because the point where geometric stresses are characterised is a probable point of crack initiation, the designation of "hot spot" is also used. This is an association with the energy released during the process of cyclic plastic deformation that anticipates the crack initiation.

4.2.2 General approach

Haibach (Radaj et al., 2006) showed that the measurement of strains with a strain gauge of reduced dimensions, at a small distance from the weld, allows characterizing the fatigue strength of welded joints, independently of the type of joint, the shape of the weld and the type of loading. Its methodology was applied to the analysis of motor vehicles, pressure vessels and cranes among other types of structures along the line of early work by Peterson (1963) and Manson (1965). Those developments were the basis of the rules present at AWS (American Welding Society) (AWS, 2010) and API (American Petroleum Institute) (API, 2014).

Later, Atzori and Meneghetti (2001) performed a parametric analysis of stresses at a cruciform joint, with the help of finite elements method. Besides confirming Haibach's theory, that analysis also allowed understanding that (i) the structural stress is greater the lower the radius of the weld and (ii) the distance of the strain gauge should be conditioned to a function of the thickness of the plate under analysis.

Typically, in the most common formulation, the structural stresses/strains are obtained from linear or quadratic extrapolation of superficial stresses/strains at points near the weld to the weld toe (Figure 4.2).

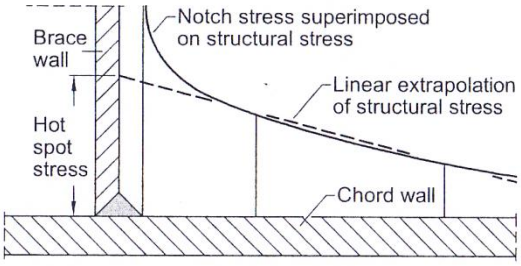

Figure 4.2 - Structural stress (Radaj et al., 2006).

There are several different proposals for the distances at which the stress/strain measurements should be performed. Figure 4.3 shows a variety of proposals, for the case of hollow section connections.

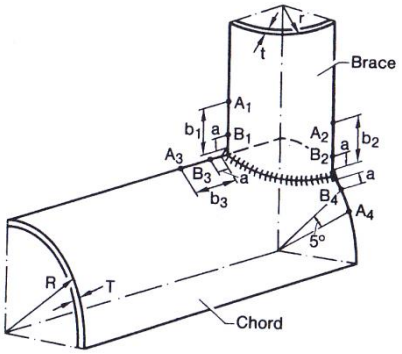

(a)

Reference	a	b_1, b_2	b_3
Dijkstra, de Back	$0.2\sqrt{rt}$	$0.65\sqrt{rt}$	$0.5\sqrt{RT}$
Gurney, van Delft	$0.4\,t$	$0.65\sqrt{rt}$	$0.4\sqrt[4]{rtRT}$
AWS, API	$0.1\sqrt{rt}$	–	–
DEn, ECSC, CIDECT	$0.4\,t$	$1.0\,t$	$1.0\,T$

(b)

Figure 4.3 - Structural stress measurement in hollow section connections (Radaj et al., 2006): (a) conditioning geometric parameters and (b) proposed distances.

Figure 4.4 presents, also, some reference distances for the strain measurements in welded connections of plain elements.

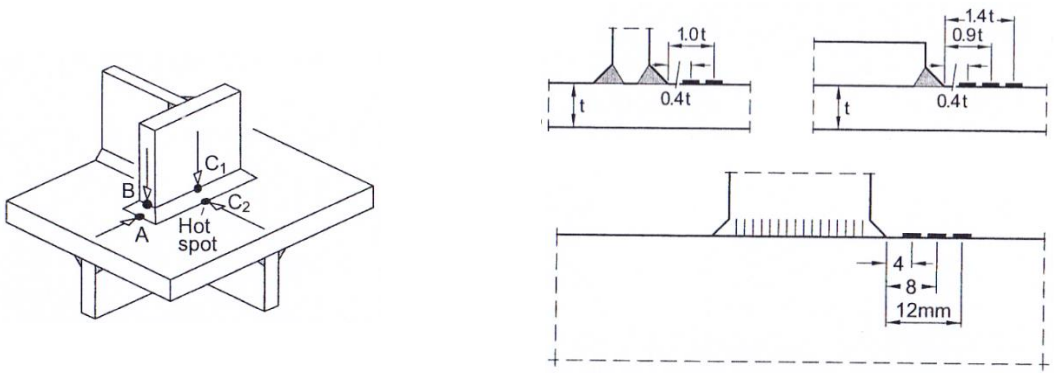

(a) (b)

Figure 4.4 - Structural stress/strain measurements in welded connections of plain elements (Radaj et al., 2006): (a) conditioning geometric parameters and (b) reference distances.

Concerning the use of finite element models, indications about adequate modelling techniques can be found in several references, allowing to increase the reliability of the results obtained. The finite element models employed in these applications may use shell or volume elements. In the latter case, the plates can be modelled with one or several layers of elements across the thickness (Figure 4.5).

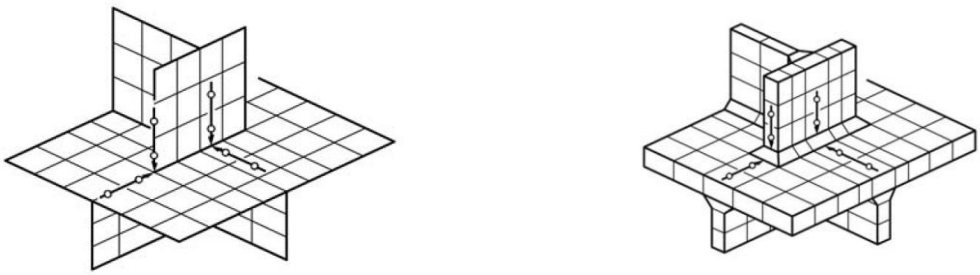

(a) (b)

Figure 4.5 - Example of finite element models of welded connections between plain components and points for the stress/strain assessment (Radaj et al., 2006): (a) model using shell elements and (b) model using volume elements.

The results obtained in several analysis and parametric studies performed, allowed defining laws that relate the structural stresses and the nominal stresses, as a function of a set of geometric variables and loading, such as those illustrated in Figure 4.6 (Radaj et al., 2006).

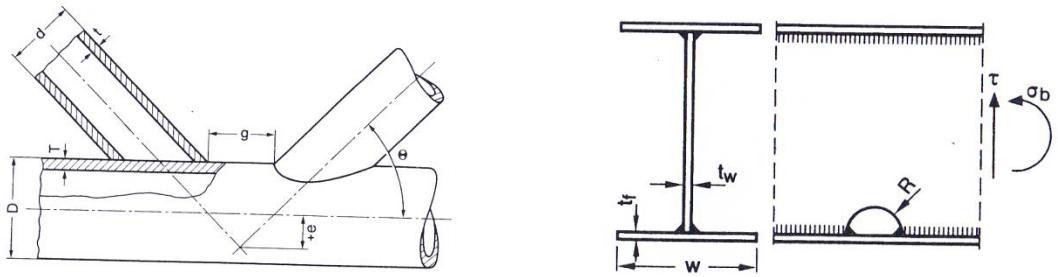

(a) (b)

Figure 4.6 - Geometric and loading variables influencing the definition of stress concentration factors (Radaj et al., 2006): (a) hollow section connections and (b) cope hole at I-section girder.

The structural stress strength curves can be found in a variety of standards. Figure 4.7 presents, as an example, the strength curves available in different standards, for a particular type of tubular joints.

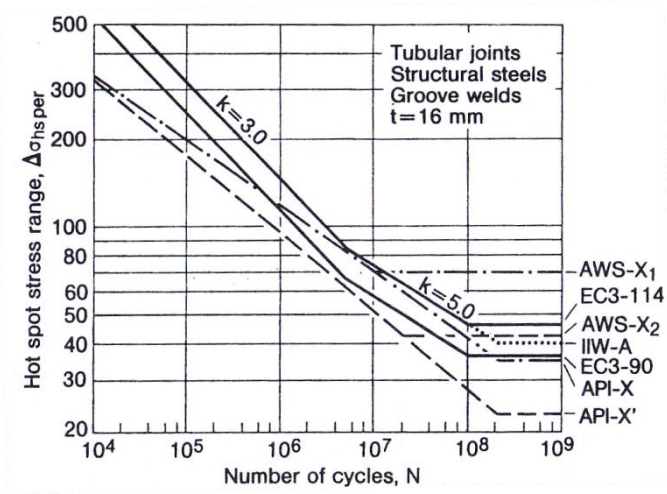

Figure 4.7 - Structural stress strength curves for tubular joints (Radaj et al., 2006).

4.2.3 Dong's Approach

The general approach presented above, for determining the structural stress, uses the extrapolation of surface stresses or strains to the weld toe. Nevertheless, there are other approaches that use the extrapolation of the stresses through the thickness of the element.

Radaj (1990) showed that the linearization of stresses through the thickness allows obtaining consistent results for the structural stress in the critical point. Nevertheless, the values obtained with this approach are, often, slightly higher than those obtained by linear extrapolation at the surface.

Later, Dong modified the through thickness linearization procedure in such a way that the fatigue tests of different specimens would adequately adjust to one single fatigue strength curve (Dong, 2001). In this case, different linearization schemes should be adopted, for different types of welded joints, as illustrated in Figure 4.8:

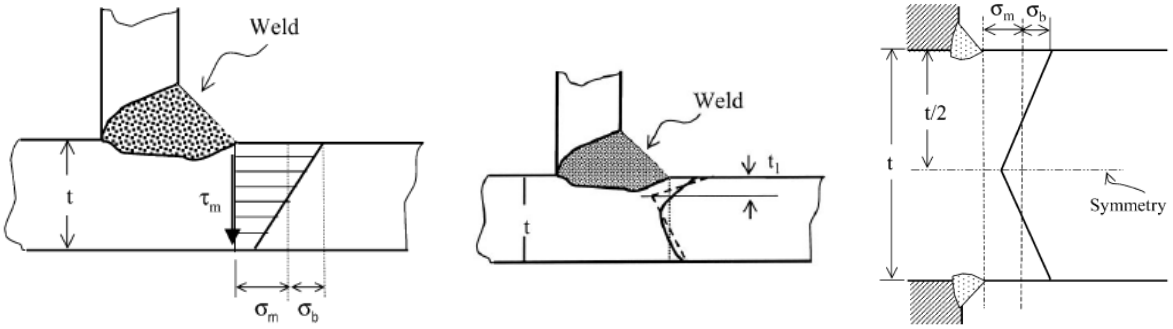

(a) (b) (c)

Figure 4.8 - Through thickness linearization of stresses, according to Dong: (a) elements with normal thickness (Dong, 2001), (b) element with high thickness or welded connection to the lateral surface of a plate (Dong, 2005) and (c) symmetric welded connection (Dong, 2001).

As it can be understood, the definition of t_1 (Figure 4.8) is of paramount importance in this methodology. Nevertheless, no evidence was found of one single value being valid for the results of all the tests. That value should then be adjusted for each test under analysis.

According to this approach, the value of the structural stress in the critical point is obtained by equilibrium conditions with the shear stresses and direct stresses at a close distance to the weld toe (Figure 4.9).

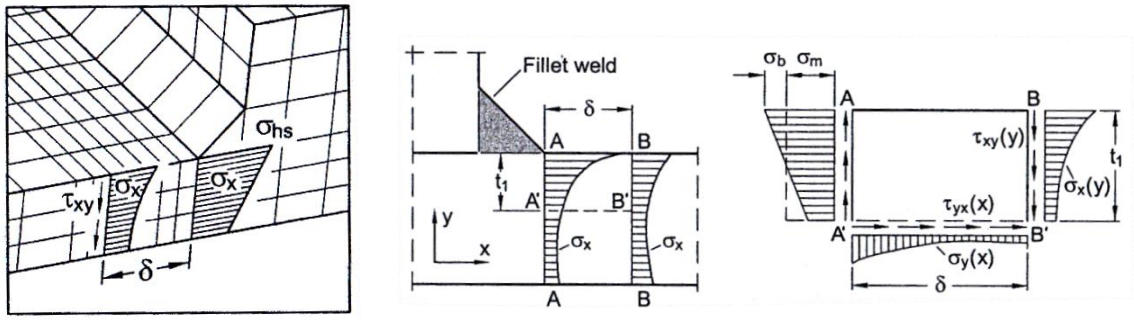

(a) (b)

Figure 4.9 - Linearization of stresses according to Dong (Radaj et al., 2006): (a) linearization through the entire thickness and (b) linearization through a fraction of the thickness.

The fatigue strength, in the approach proposed by Dong, is assessed using the structural stress parameter ΔS_s as a function of the number of cycles and defining one single fatigue strength curve (Figure 4.10). That parameter depends on the structural stress range, $\Delta\sigma_s$, on the plate's thickness, t, on the reference thickness, t_0, on the parameter m of Paris' law (see Section 4.5.5) and on the crack growth integral, $I(\delta_b)$ (Dong, 2005).

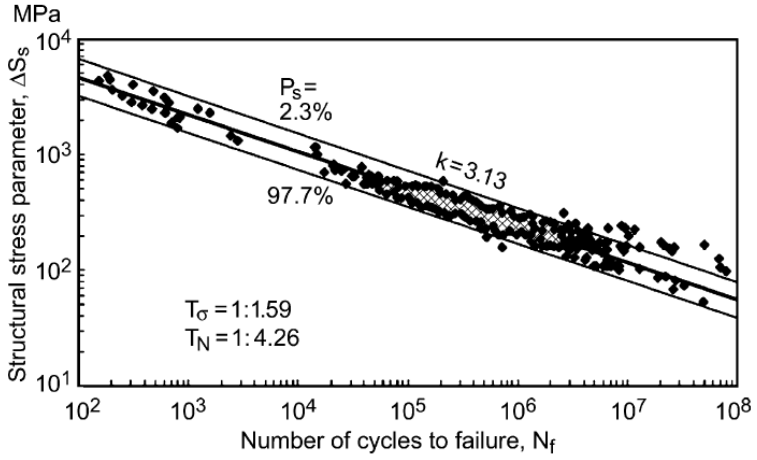

Figure 4.10 - Fatigue strength curve according to Dong (Radaj et al., 2009).

4.2.4 Xiao-Yamada Approach

This method is adequate for the analysis of fatigue damage initiated at the weld toe. In such situation, Xiao and Yamada (Xiao and Yamada, 2004) demonstrated that the fatigue life related with crack propagation may be expressed as a function of the stress measured 1 mm below the surface, at the expected path of a potential fatigue crack. That stress at 1 mm depth allows correlating the fatigue strength of the detail with the fatigue strength of a reference specimen with 10 mm thickness (Figure 4.11).

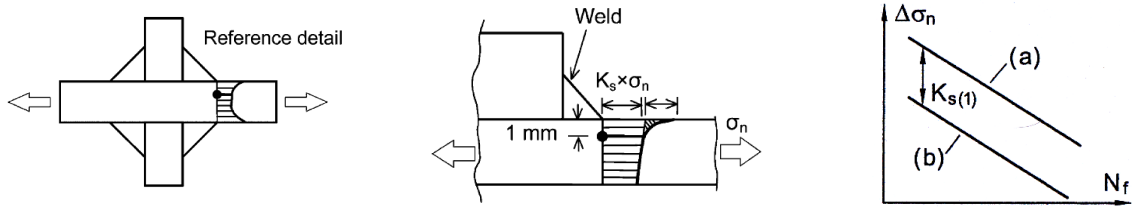

(a) (b) (c)

Figure 4.11 - Xiao-Yamada approach (Xiao and Yamada, 2004): (a) reference detail, with t = 10 mm, (b) plate with dimensions different from reference and (c) corresponding S-N curve.

4.3 FATIGUE ASSESSMENT BASED ON NOTCH STRESSES

4.3.1 Introduction

The fatigue strength of a structural component depends very much on the severity of its notches. High stress concentration factors are present around those notches, making those regions prone to the initiation of fatigue cracks.

The stress concentration factor, K_t, is determined by the geometry of the detail and by the type of loading. Concerning the geometry, the relevant parameters are the ratios between the different dimensions and not the absolute value of those dimensions. Nevertheless, the factor conditioning the effective fatigue strength is not the stress concentration factor but, instead, the fatigue notch factor, K_f, illustrated in Figure 4.12.

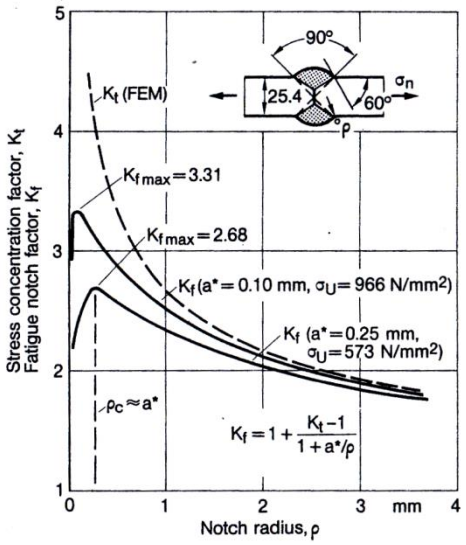

Figure 4.12 - Stress concentration factor (K_t) vs. Fatigue notch factor (K_f) (Radaj et al., 2006).

This coefficient takes into consideration the notch microstructural support hypothesis. That hypothesis states that the maximum stress, computed according to elastic theory, is not decisive for the crack initiation or propagation. The relevant parameter is the average stress measured in a small volume with a size dependent on the material (grain structure, micro-plasticity and crack initiation). The microstructural support occurs in sharp notches but also in smooth notches, as long as they are small in size. The fatigue notch factor, on the top of the variables that affect the stress concentration factor, K_t, depends also on the notch radius and on the material-dependent length of microstructural support (Radaj et al., 2006).

Different approaches for the computation of notch microstructural support can be found in the literature, namely the stress gradient approach (Adib-Ramezani and Jeong, 2007), the average stress approach (Topper et al., 1967, Neuber, 1961), the critical distances approach (Metkar et al., 2011, Righiniotis et al., 2008, Susmel, 2008, Peterson, 1959) and the highly stressed volume (Sonsino, 1995, Adib and Pluvinage, 2003, Zehsaz et al., 2010, Kuguel, 1961).

Comparative analyses were performed, showing small differences between the different approaches (Bellett et al., 2005, Crupi et al., 2005, Taylor et al., 2002, Taylor and Wang, 2000, Susmel, 2014, Mahdavi Shahri and Sandström, 2012, Spaggiari et al., 2011). It should be stressed that some relations were established between the material-dependent parameters characterizing the microstructural support and the material-dependent parameters intervening on Fracture Mechanics (El Haddad et al., 1979a, El Haddad et al., 1979b, Taylor, 1999, Yin et al., 2015), namely the threshold stress intensity factor, K_{th}.

The notch stress approaches should be used when the approaches based on nominal stresses or structural stresses are not possible or inadequate. It is particularly useful when performing parametric studies, on details geometry, at design stage. The simplest assessment procedure, from those based on notch stress, consists in guaranteeing infinite life to fatigue. Thus, the crack's initiation or its propagation must be avoided. For assessment of finite life fatigue strength, this methodology must be combined with the notch strain and Fracture Mechanics approaches.

The first step of the fatigue analyses is the identification of the most probable location for crack initiation. A stress analysis at the notch is required in order to determine the elastic stress concentration factor, which on the other hand will help determining the fatigue crack initiation life. The stress field on the crack propagation path is needed for the determination of the crack propagation life (Lawrence et al., 1981).

4.3.2 Critical distances approach

The determination of the notch-induced stress concentration factor, K_t, can be achieved by means of stress analyses on a finite element model. The fatigue notch factor, K_f, is obtained from K_t, using the critical distances method proposed by Peterson (1959). The value of K_f is reduced when comparing with K_t, mainly on sharp notches, due to the microstructural support effect. That reduction is dependent on the relation a^*/ρ, where a^* is a material-dependent constant and ρ is the notch radius. The worst case scenario occurs when $a^* \approx \rho$.

The first step on this approach is the determination of the notch stress concentration factor, K_t. Once K_t is defined, it becomes possible to relate the nominal or structural stress values, σ_n, with the maximum elastic stresses at the notch, σ_k:

$$K_t = \frac{\sigma_k}{\sigma_n} \tag{4.1}$$

The maximum notch stress can be obtained by the finite elements method. The stress concentration factor may also be determined by the finite elements method or, alternatively, using algorithms or expressions available in the literature (Peterson, 1974).

The following step concerns to the determination of K_f, which, in this approach is given by:

$$K_f = 1 + \frac{K_t - 1}{1 + a^*/\rho} \tag{4.2}$$

Once the fatigue notch factor is computed, it is finally possible to determine the effective notch stress, $\overline{\sigma_k}$:

$$\overline{\sigma_k} = K_f \cdot \sigma_n \tag{4.3}$$

4.3.3 Notch fictitious radius approach

The notch fictitious radius approach, developed by Radaj (Radaj, 1997), includes the verification of the microstructural support effect at the root and toe of welds, according to the microstructural support hypothesis of Neuber. The sharp notches are fictitiously rounded, in order to achieve, in the notch, the maximum effective fatigue stress. The fictitious radius is given by:

$$\rho_f = \rho + s\rho^* \tag{4.4}$$

where ρ is the real notch radius, ρ^* is a material constant and s is Neuber's multiaxial coefficient.

The method is defined for each notch radius. Nevertheless, it is commonly used assuming the worst scenario, which corresponds to a notch radius equal to zero. For steels, this becomes $\rho_f \approx 1$ mm.

The employment of this methodology requires, at first place, the computation of the structural stresses at the root and/or toe of the weld, without considering the notch effect. Subsequently, the internal forces or stresses are transferred to a plane model of the welded joint, as applied external loads. The plane model of the joint should have the notches with the fictitious radius, in order to allow determining the notch fatigue coefficients.

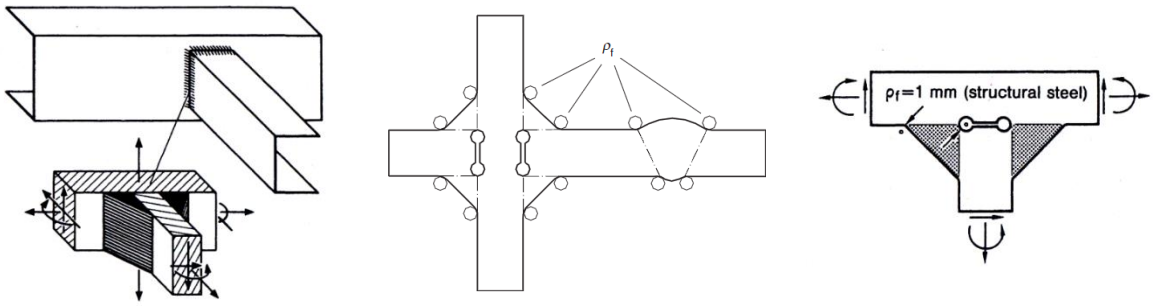

(a) (b) (c)

Figure 4.13 - Notch fictitious radius method: (a) computation of structural stresses (Radaj et al., 2006), (b) plane model with fictitious notch rounding (Fricke, 2012) and (c) transference of the internal forces to the plane model (Radaj et al., 2006).

The stresses obtained with this methodology should be compared with the nominal stresses strength curves.

Köttgen et al. (1987), proposed an update to this methodology. This update included, among other improvements, setting the notch radius as 1 mm for the case of steel elements.

The determination of K_t and of the maximum notch stress is performed in the same manner as in the previous approach, although considering the fictitious radius. The fatigue notch factor, on the other hand, is obtained using the following expression:

$$K_f = 1 + \frac{K_t\text{-}1}{\sqrt{1+\frac{s\rho^*}{\rho_f}}} \tag{4.5}$$

In some cases, the consideration of a fictitious radius may lead to an exaggerated increase of stresses, due to the net section reduction effect. In those cases, the notch fatigue factor must be corrected (Radaj et al., 2006).

4.3.4 Highly stressed volume approach

This approach, proposed by Sonsino (1995), assumes that crack initiation ($a_i \approx 0.5\text{-}1.0$ mm) in the high number of cycles domain, may be described based on the critical amplitude of local stress, which depends on the high stress concentration volume. Bigger volumes are linked to lower critical stresses. Therefore, the quantitative assessment depends on the definition of that volume. Sonsino uses a depth, below the notch root, where the maximum stress falls to 90% and a notch surface area containing also that 10% decrease.

This approach may be extended to cases of multiaxial fatigue by considering an equivalent stress, such as e.g. von Mises stress.

The determination of K_t and of the maximum notch stress is performed in the same way as the critical distances approach. The notch fatigue factor, on the other hand, is obtained using the following expression:

$$K_f = \frac{\sigma_{aE}}{\sigma_{kaE}} \cdot K_t \tag{4.6}$$

where σ_{aE} is the material strength limit and σ_{kaE} is the notch strength limit, function of the high stress concentration volume:

$$\sigma_{kaE} = f(V_{0.9}) \tag{4.7}$$

4.4 FATIGUE ASSESSMENT BASED ON NOTCH STRAINS

4.4.1 Introduction

The notch strain approach allows assessing the fatigue life up to the fatigue crack initiation. It uses a history of elasto-plastic strains at the root of the notch and compares it with the strain S-N curve of the material, obtained by testing several un-notched specimens.

The main hypothesis supporting this approach is that the mechanical behaviour of the material at the notch's root, concerning to elasto-plastic deformation, localised damage and cracks initiation, is comparable to the behaviour of a small scale un-notched specimen under axial loading (Figure 4.14).

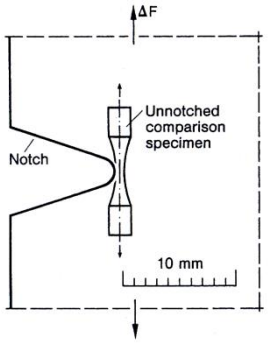

Figure 4.14 - Basic hypothesis of the notch strain approach (Radaj et al., 2006).

4.4.2 General approach

4.4.2.1 Strength assessment

The strain S-N curves characterise the material fatigue strength using the notch strains and are determined by adjusting it to the experimental tests on reduced scale specimens, according to ASTM E606 standard (ASTM, 2012).

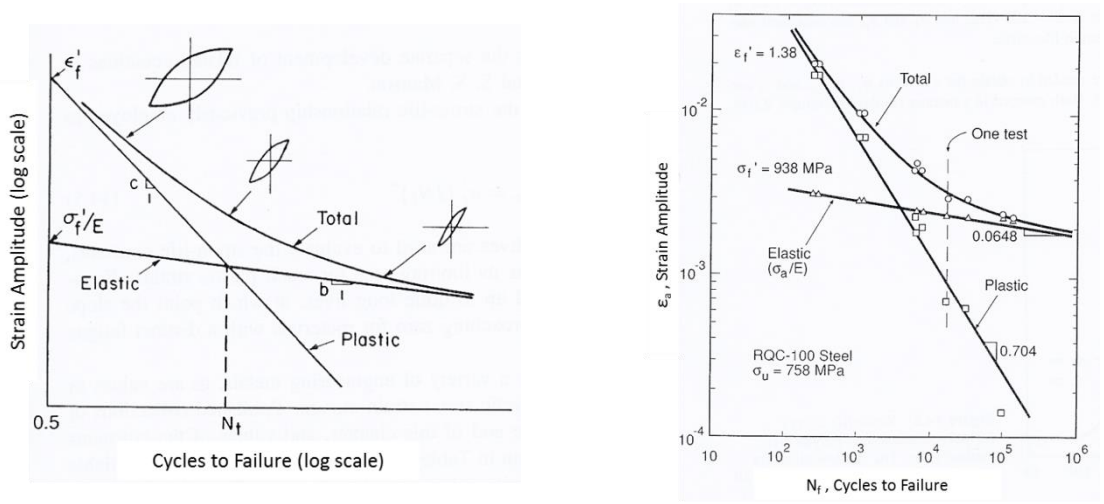

(a) (b)

Figure 4.15 - Strain S-N curves (Dowling, 2007): (a) generic curve and (b) strain S-N curve for a structural steel.

These curves are properly adjusted by the Coffin-Manson relationship:

$$\frac{\Delta\epsilon}{2} = \underbrace{\frac{\sigma_f'}{E}\cdot\left(2\cdot N_f\right)^b}_{\frac{\Delta\epsilon_e}{2}} + \underbrace{\epsilon_f'\cdot\left(2\cdot N_f\right)^c}_{\frac{\Delta\epsilon_p}{2}} \tag{4.8}$$

where σ_f', b, ϵ_f' and c are material dependent parameters.

The fatigue strength curves obtained according to ASTM E606 are appropriate for cases where R = -1, which means totally reversible loading cycles.

Several proposals are available in the literature, in order to adjust the above mentioned curves to loading cases with an average stress higher than zero. The most common is, maybe, the Morrow equation, which results in a change in fatigue strength according to the law presented below:

$$N^{*} = N_f\left(1 - \frac{\sigma_m}{\sigma_f'}\right)^{\frac{1}{b}} \tag{4.9}$$

where σ_m is the average stress (Dowling, 2007).

4.4.2.2 Loading characterization

In most cases, the notch strains are unknown. Nevertheless, they can be determined from the notch stress history, σ, according to the cyclic stress-strain curve, given by the Ramberg-Osgood equation (Dowling, 2007):

$$\epsilon = f(\sigma) = \frac{\sigma}{E} + \left(\frac{\sigma}{K'}\right)^{\frac{1}{n'}} \tag{4.10}$$

combined with the Neuber's rule:

$$\frac{(K_f \cdot \sigma_n)^2}{E} = \sigma \cdot \epsilon \tag{4.11}$$

The notch strain history can therefore be computed from the nominal stresses, σ_n:

$$\epsilon = f(\sigma) = g(\sigma_n) \tag{4.12}$$

After determining the strain time history, rainflow method is employed as the cycles-counting algorithm. For each cycle, both the strain range and the average strain must be stored. After counting the cycles, the strain S-N curve can be used to compute the cumulative damage and the remaining fatigue life.

4.4.3 Further improvements to the general approach

Some of the main improvements to the general approach consist in adaptations to include the residual stresses effect and multiaxial stress states. Concerning to multiaxial stress states, biaxial problems can be adequately solved by using equivalent stresses such as e.g. von Mises stress (Dowling, 2007).

4.5 FATIGUE ASSESSMENT BASED ON FRACTURE MECHANICS AND CRACK PROPAGATION LAWS

4.5.1 Introduction

The study of Fracture Mechanics has evolved significantly over time and it can be considered as a highly mature discipline. In addition, the employment of Fracture Mechanics when studying fatigue cracks propagation is widely validated by successful applications in different engineering fields.

Fatigue crack propagation laws, based on Fracture Mechanics concepts, allow to assess the different phases of fatigue crack propagation up to the eventual final collapse of the structural components. In this section, a general description of this approach is performed and its basic concepts and foundations are presented.

4.5.2 Griffith and the Energy Release Rate, G

The study of Fracture Mechanics started with Griffith works, in the 1920s. In order to better understand its work, it is important to present the concepts of work and of strain energy of an elastic body.

When a body is loaded, the movement of the applied loads performs work, *F*, over that body. That work is stored as strain energy. It is possible to express the energy stored per unit volume as a function of the different components of the actuating stress. The elastic strain energy stored per unit volume, *U*, is a potential energy (it can be later released in the form of work), and it can be expressed in the following way (Parker, 1981):

$$U = \frac{1}{2E}\cdot\left[\sigma_x{}^2+\sigma_y{}^2+\sigma_z{}^2-2\cdot\nu\cdot\left(\sigma_x\cdot\sigma_y+\sigma_y\cdot\sigma_z+\sigma_z\cdot\sigma_x\right)\right]+2\cdot(1+\nu)\cdot\left(\tau_{xy}{}^2+\tau_{yz}{}^2+\tau_{zx}{}^2\right) \qquad (4.13)$$

If only uniaxial stress, σ, is present, the previous expression becomes:

$$U = \frac{\sigma^2}{2E} \qquad (4.14)$$

The deduction of this expression is illustrated in Figure 4.16:

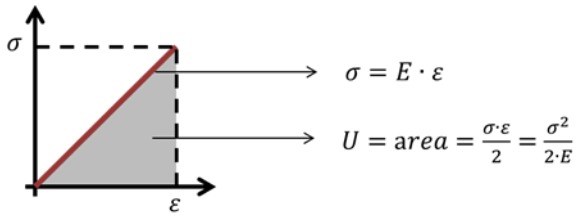

Figure 4.16 - Strain energy per unit volume, for uniaxial stress.

The analysis of stress fields around elliptic notches showed that they may create very high stress concentrations. It can also be observed that those high stress concentrations do not originate, necessarily, the collapse of the structural element.

In order to solve this ambiguity, Griffith, in the 1920s, focused its analysis on a brittle material containing a single crack of length 2*a* and assessed the energy exchanges in the system, during an incremental extension of the crack (Griffith, 1921). He observed two necessary conditions for a crack extension to occur:

e) The stresses in the crack tip must reach a certain critical value, σ_c;

f) The crack propagation only occurs if it originates a decrease on the total energy of the system.

It should be noted that the total energy of the system results from the balance between the potential energy, *U*, the work performed by the external load *P*, *F*, and the surface energy, *W*. This notation is in agreement with the one presented in (Broek, 1987). For a crack to increase its dimension from *a* to $a+\delta a$, it is necessary that the increase provides an amount of energy (release of strain energy and work performed by the external loads) at least equal to the energy needed to overcome the superficial links through that distance δa (when a crack propagates, the free surface of the body increases, increasing the total surface energy of the body).

Let us consider a plate of brittle material, without any crack, and that it is uniformly loaded and blocked at its boundaries, in order to keep that stress state (Figure 4.17(a)). In that case, the strain energy (potential) per unit volume at any location of the plate is $\sigma^2/(2\cdot E)$.

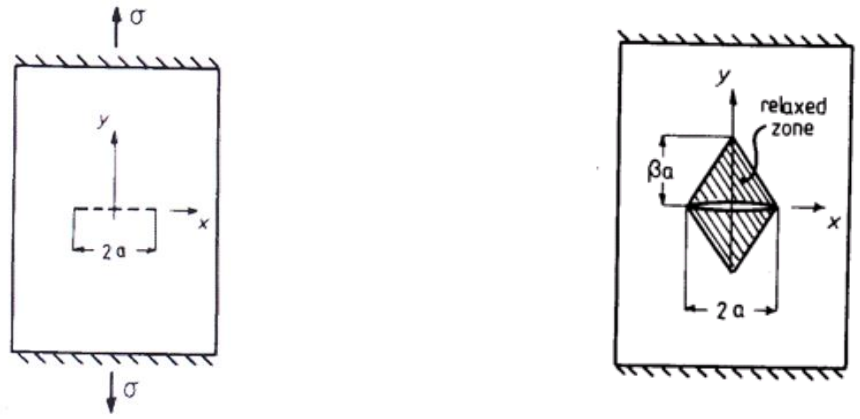

(a) (b)

Figure 4.17 - Strain energy per unit volume at a plate under uniaxial stress (Parker, 1981): (a) uncracked plate under uniaxial stress and (b) cracked plate.

If a crack, with length $2a$ is introduced, it will generate the material relaxation above and below the crack, and therefore some strain energy, U, is released – the potential elastic energy decreases. Assuming, according to Figure 4.17(b), that the height of the relaxed zone is $(\beta \cdot a)$, and for a thickness t of the plate, the volume of the relaxed zone becomes:

$$V_{relaxed} = 2 \cdot \left(\frac{(2 \cdot a) \cdot (\beta \cdot a)}{2} \cdot t \right) = 2\beta a^2 t \tag{4.15}$$

which means that the volume of relaxed material associated with each crack tip is:

$$V_{relaxed\ per\ crack\ tip} = \beta a^2 t \tag{4.16}$$

The energy released per crack tip and per unit thickness is, therefore:

$$U_{J/m} = \left[\frac{\sigma^2}{(2 \cdot E)} \right] \cdot \left[\frac{\beta a^2 t}{t} \right] = \frac{\sigma^2}{(2 \cdot E)} \cdot \beta a^2 \tag{4.17}$$

This expression is in close agreement with Griffith's rigorous solution for plane stress state:

$$U_{J/m} = \frac{\sigma^2}{(2 \cdot E)} \cdot \pi a^2 \tag{4.18}$$

Consequently, the energy release rate as a function of the crack dimension becomes:

$$\frac{\partial U_{J/m}}{\partial a} = \frac{\sigma^2}{E} \cdot \pi a \tag{4.19}$$

On the other side, for plane strain state, the expression of the energy release is:

$$U_{J/m} = \frac{\sigma^2}{(2 \cdot E)} \cdot \pi a^2 \cdot (1 - \nu^2) \tag{4.20}$$

and the energy release rate, as a function of the dimension a of the crack is given by:

$$\frac{\partial U_{J/m}}{\partial a} = \frac{\sigma^2}{E} \cdot \pi a \cdot (1-\nu^2) \tag{4.21}$$

As it can be observed from Figure 4.16, the strain energy released, U, increases steeply as the crack dimension increases. As U represents an energy release, it is assigned with a negative value.

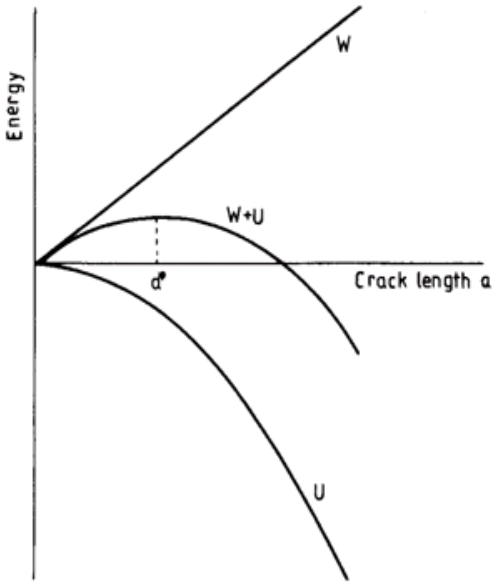

Figure 4.18 – Change in energy as a function of cracks length (Parker, 1981).

Before any U energy may be released as a result of the relaxing process associated with crack growth, some energy must be provided, in order to originate that crack increment. W is the energy required to break the atomic bounds and it is therefore assigned with a positive signal. In a simplified way, it can be considered that the energy required for each crack increment is constant, meaning, W varies linearly with a. This is equivalent to say that the energy required to break a certain atomic energy it's equal to the energy necessary to break the next one and so on. The theoretical strength of a material under traction is much higher than the actual strength observed in practice. That is due to the impurities and defects always present in real materials (Branco et al., 1999). Nevertheless, it is important to analyse Figure 4.19, in order to understand the reason why a certain amount of energy W needs to be provided to the system:

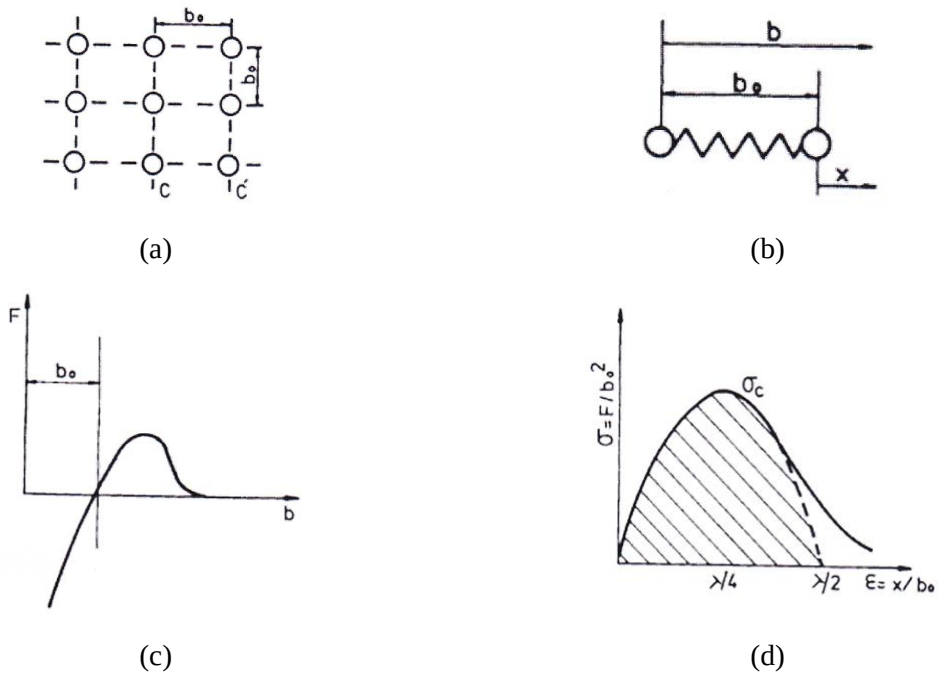

Figure 4.19 – Theoretical resistance of a material under traction (Branco et al., 1999): (a) schematics of a cubic lattice, (b) relative coordinates of 2 consecutive atoms, (c) displacement vs. atomic force and (d) atomic σ-ε curve.

It becomes apparent, from observation of Figure 4.19, that for $a \leq a^*$ it is necessary to provide energy to the system (e.g. work performed by external forces) in order to increase the crack length, because the elastic energy released on its own is not enough. Nevertheless, for $a > a^*$ the energy released due to the crack extension is higher than the energy required for the next extension and, therefore, the crack propagates in a unstable and sudden way (Parker, 1981).

The crack instability clearly depends on the stationary point of the energy curve: after that point, the energy released during a crack increment exceeds the energy required to create new free crack surfaces.

The value of $G = \partial U/\partial a$ defines the energy release rate for an incremental increase in the crack's length. Therefore, according to Equations (4.19) and (4.21), it becomes:

$$G = \begin{cases} \frac{\sigma^2}{E} \cdot \pi a \,, & \text{Plane Stress} \\ \frac{\sigma^2}{E} \cdot \pi a \cdot (1\text{-}\nu^2), & \text{Plane Strain} \end{cases} \qquad [\text{J/m/m}] \qquad (4.22)$$

On the other hand, $R = \partial W/\partial a$ defines the absorbed energy rate during the crack increment.

The limit condition for an unstable crack increment can then be expressed as:

$$\frac{\partial U}{\partial a} = \frac{\partial W}{\partial a} \Leftrightarrow G = R \tag{4.23}$$

If we consider, for the sake of simplicity, that R is constant, a critical and constant value of G can be defined for which the unstable crack propagation occurs. That value, G_c, is a property of the material, because it depends on the energy required to break the atomic bounds inside that same material.

For determining G_c, a specimen containing a crack of dimension $2a$ is tested and the collapse tension, σ_c, is recorded, allowing its computation:

$$G_c = \begin{cases} \frac{\sigma_c^2}{E} \cdot \pi a \,, & \text{Plane Stress} \\ \frac{\sigma_c^2}{E} \cdot \pi a \cdot (1-\nu^2), & \text{Plane Strain} \end{cases} \qquad [\text{J/m/m}] \tag{4.24}$$

These expressions can be rearranged in order to get the following expression:

$$\begin{cases} \sqrt{G_c E} = \sigma_c \sqrt{\pi a}, & \text{Plane Stress} \\ \sqrt{G_{Ic} E} = \sigma_c \sqrt{\pi a}\ (1-\nu^2)^{1/2}, & \text{Plane Strain} \end{cases} \tag{4.25}$$

It should be noted that the left hand side of the previous expressions contain material dependent properties only while the right hand side contain geometrical and loading parameters. It should also be underlined that the energy release rate for a plane strain is denoted G_{Ic} and is considered a measure of the material toughness.

4.5.3 Westergaard and the Stress Intensity Factor, *K*

Let us now consider the problem of characterization of the displacements field around a crack in a plate of infinite dimensions, made of an isotropic material with linear-elastic behaviour, when loaded by a remote stress perpendicular to the crack faces (Figure 4.20). The length of the crack is $2a$.

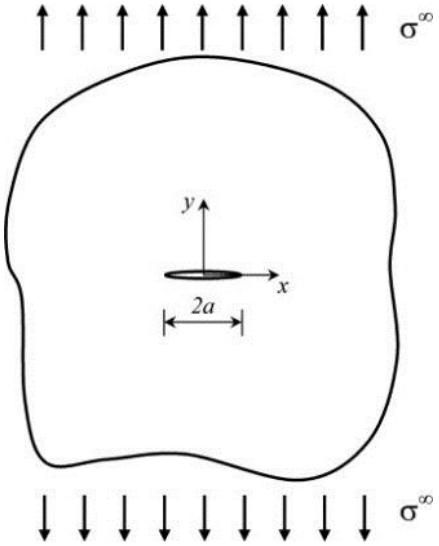

Figure 4.20 – Infinite plate with a crack perpendicular to the direction of loading.

From Elasticity Theory it is known that generically, the elasticity problems may be solved if the function ϕ (also designated as Airy function or stress function) which solves the bi-harmonic equation (4.26) is known, for the boundary conditions of that problem (Parker, 1981, de Castro, 2008):

$$\nabla^4 \phi = 0 \tag{4.26}$$

The resolution of Equation (4.26) allows defining the stress field of the problem, because:

$$\sigma_x = \frac{\partial^2 \phi}{\partial y^2} \tag{4.27}$$

$$\sigma_y = \frac{\partial^2 \phi}{\partial x^2} \tag{4.28}$$

$$\tau_{xy} = -\frac{\partial^2 \phi}{\partial x \partial y} \tag{4.29}$$

For the problem under analysis, of a crack in an infinite plate, Westergaard deduced the corresponding Airy function (4.30) that satisfies the condition (4.26):

$$\phi = R\bar{\bar{Z}} + y \cdot I\bar{Z} \tag{4.30}$$

where R and I are the real and imaginary components of a complex variables function, respectively. $\bar{\bar{Z}}$ and $\bar{Z}$ are functions that are in agreement with the following notation:

$$z = x + iy \tag{4.31}$$

$$Z' = \frac{\partial Z}{\partial z} \Leftarrow Z = f(z) = \frac{\partial \bar{Z}}{\partial z} \Leftarrow \bar{Z} = \frac{\partial \bar{\bar{Z}}}{\partial z} \tag{4.32}$$

The definition of the $Z = f(z)$ equation is a fundamental step for the resolution of this problem. That equation will be described with more detail later. Before that, the values of σ_x, σ_y and τ_{xy} stresses, derived by the substitution of Equation (4.30) in equations (4.27), (4.28) and (4.29) are presented:

$$\sigma_x = RZ - y \cdot IZ' \tag{4.33}$$

$$\sigma_y = RZ + y \cdot IZ' \tag{4.34}$$

$$\tau_{xy} = -y \cdot RZ' \tag{4.35}$$

Those expressions, only get a physical meaning after detailing the function $Z = f(z)$, also after Westergaard:

$$Z = \frac{\sigma \cdot z}{\sqrt{z^2 - a^2}} \tag{4.36}$$

As an example, the values of σ_y, for $y = 0$ are presented:

$$\sigma_y = RZ + y \cdot IZ' = RZ + 0 = \begin{cases} 0, & \text{for } |x| < a \\ +\infty, & \text{for } |x| \rightarrow a \\ \sigma, & \text{for } |x| \gg a \end{cases} \tag{4.37}$$

These results are in agreement with the expected behaviour.

Moving now to the problem of computing the displacements field around a crack. For simplicity, let us assume the plane stress state ($\sigma_z = \tau_{xz} = \tau_{yz} = 0$). In that case, we get:

$$\varepsilon_x = \frac{\partial u}{\partial x} = \frac{1}{E}\left(\sigma_x - \nu \cdot \sigma_y\right) \tag{4.38}$$

$$\varepsilon_y = \frac{\partial v}{\partial y} = \frac{1}{E}\left(\sigma_y - \nu \cdot \sigma_x\right) \tag{4.39}$$

$$\varepsilon_{xy} = \frac{\partial v}{\partial y} = \frac{1+\nu}{E}\tau_{xy} = 0 \tag{4.40}$$

For the problem under analysis, where the remote stress is perpendicular to the crack, the shear stresses are null, so $\varepsilon_{xy} = 0$. Therefore, the displacements in the y direction become:

$$\varepsilon_y = \frac{\partial v}{\partial y} \Leftrightarrow$$

$$\Leftrightarrow \partial v = \varepsilon_y \cdot \partial y \Leftrightarrow$$

$$\Leftrightarrow v = \int \varepsilon_y \cdot \partial y \Leftrightarrow$$

$$\Leftrightarrow v = \int \frac{1}{E}\left(\sigma_y\text{-}v\cdot\sigma_x\right)\cdot\partial y \tag{4.41}$$

Developing expression (4.41) by substitution of σ_x and σ_y by expressions (4.33) and (4.34), it becomes:

$$v = \frac{1}{E}\int[(RZ+y\cdot IZ')\text{-}v\cdot(RZ\text{-}y\cdot IZ')]\cdot\partial y \Leftrightarrow$$

$$\Leftrightarrow v = \frac{1}{E}(1\text{-}v)\int RZ\cdot\partial y + \frac{1}{E}(1+v)\int y\cdot IZ'\cdot\partial y \Leftrightarrow$$

$$\Leftrightarrow v = \frac{1}{E}(1\text{-}v)I\bar{Z} + \frac{1}{E}(1+v)(\text{-}y\cdot RZ\text{-}I\bar{Z}) \Leftrightarrow$$

$$\Leftrightarrow v = \frac{1}{E}[2\cdot I\bar{Z}\text{-}(1+v)\cdot y\cdot RZ] \tag{4.42}$$

For $y = 0$ it can be written as:

$$v = \frac{1}{E}(2\cdot I\bar{Z}) = \frac{2\sigma}{E}\sqrt{a^2\text{-}x^2} \tag{4.43}$$

As can be observed, the crack shape is an ellipse:

$$v^2 = \frac{4\sigma^2}{E^2}\left(\sqrt{a^2\text{-}x^2}\right)^2 \Leftrightarrow$$

$$\Leftrightarrow v^2 = \frac{4\sigma^2}{E^2}(a^2\text{-}x^2) \Leftrightarrow$$

$$\Leftrightarrow \frac{v^2}{\frac{4\sigma^2}{E^2}} + x^2 = a^2 \Leftrightarrow$$

$$\Leftrightarrow \frac{v^2}{\frac{4\sigma^2 a^2}{E^2}} + \frac{x^2}{a^2} = 1 \Leftrightarrow$$

$$\Leftrightarrow \frac{v^2}{C_1} + \frac{x^2}{C_2} = 1 \tag{4.44}$$

In all previous considerations, the coordinates system was located in the centre of the crack. For convenience, a change of variable can be performed corresponding to a translation of the coordinates system to the crack tip (Figure 4.21):

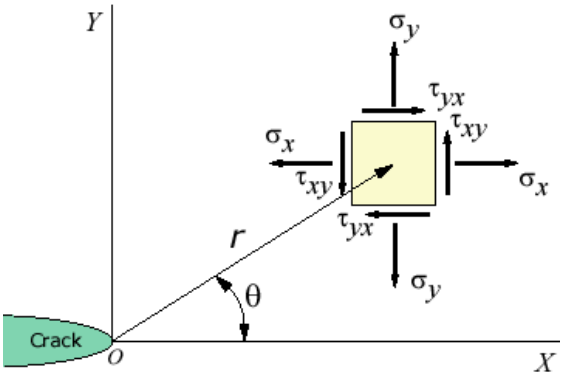

Figure 4.21 – Change of the coordinates system to the crack tip.

In that situation it becomes:

$$Z = \frac{\sigma \cdot z}{\sqrt{z^2 - a^2}} = \frac{\sigma \cdot (\zeta + a)}{\sqrt{(\zeta + a)^2 - a^2}} = \frac{\sigma \cdot (\zeta + a)}{\sqrt{\zeta} \cdot \sqrt{\zeta + 2a}} \tag{4.45}$$

When ζ is very small:

$$Z \approx \frac{\sigma \cdot a}{\sqrt{\zeta} \cdot \sqrt{2a}} = \frac{\sigma \cdot \sqrt{a}}{\sqrt{2 \cdot \zeta}} = \frac{\sigma \cdot \sqrt{\pi \cdot a}}{\sqrt{2 \cdot \pi \cdot \zeta}} = \frac{K}{\sqrt{2 \cdot \pi \cdot \zeta}} = \frac{K}{\sqrt{2 \cdot \pi}} \cdot \zeta^{-\frac{1}{2}} =$$

$$= \frac{K}{\sqrt{2 \cdot \pi}} \cdot r^{-\frac{1}{2}} \cdot \left(\cos \frac{1}{2}\theta - i \sin \frac{1}{2}\theta \right) =$$

$$= \frac{K}{\sqrt{2 \cdot \pi \cdot r}} \cdot \left(\cos \frac{1}{2}\theta - i \sin \frac{1}{2}\theta \right) \tag{4.46}$$

where $K = \sigma \cdot \sqrt{\pi \cdot a}$ is the stress intensity factor, a key parameter in the analysis of fatigue cracks propagation, based on Fracture Mechanics.

On the other hand:

$$Z' \approx -\frac{1}{2} \frac{K}{\sqrt{2 \cdot \pi}} \cdot \zeta^{-\frac{3}{2}} = -\frac{1}{2} \frac{K}{\sqrt{2 \cdot \pi}} \cdot r^{-\frac{3}{2}} \cdot \left(\cos \frac{3}{2}\theta - i \sin \frac{3}{2}\theta \right) \tag{4.47}$$

Applying (4.46) and (4.47) to (4.33) and (4.34), the following expressions for the stresses are obtained:

$$\sigma_x = \frac{K}{\sqrt{2 \cdot \pi \cdot r}} \cdot \cos \frac{\theta}{2} \cdot \left(1 - \sin \frac{\theta}{2} \cdot \sin \frac{3}{2}\theta \right) \tag{4.48}$$

$$\sigma_y = \frac{K}{\sqrt{2 \cdot \pi \cdot r}} \cdot \cos \frac{\theta}{2} \cdot \left(1 + \sin \frac{\theta}{2} \cdot \sin \frac{3}{2}\theta \right) \tag{4.49}$$

The expression of displacements in the *y* direction, as a function of *r* and θ can therefore be obtained by substitution of the stress values in Equation (4.41) by expressions (4.48) and (4.49):

$$v = \frac{1}{E}\frac{K}{\sqrt{2\cdot\pi\cdot r}}\int\left\{\left[\cos\frac{\theta}{2}\cdot\left(1+\sin\frac{\theta}{2}\cdot\sin\frac{3}{2}\theta\right)\right]-v\cdot\left[\cos\frac{\theta}{2}\cdot\left(1-\sin\frac{\theta}{2}\cdot\sin\frac{3}{2}\theta\right)\right]\right\}\cdot\partial y =$$

$$= \frac{K}{G}\sqrt{\frac{r}{2\cdot\pi}}\cdot\sin\frac{\theta}{2}\cdot\left(\frac{2}{1+v}-\cos^2\frac{\theta}{2}\right) \tag{4.50}$$

In the previous expression, $G = E/[2\cdot(1+v)]$, is the shear modulus of the material.

By observing equations (4.48) and (4.50) it can be understood that the stress intensity factor, K, plays a fundamental role in the characterization of the stress and displacement fields surrounding cracks. In the case of cracks located in complex details and/or under complex loading, K can be described in the following way:

$$K = C\sqrt{\pi a}\cdot\sigma \tag{4.51}$$

where C is a parameter which depends on the geometry of both the crack and the detail.

The relationships reviewed up to this point, refer to cracks perpendicular to the loading direction, situation that corresponds to mode I of cracks propagation. For that reason, in this context, the stress intensity factor and the energy release rate may be designated as K_I and G_I. Nevertheless, it must be stressed that there are 3 different modes of crack propagation (Figure 4.22), I, II and III, which define K_I, K_{II}, K_{III}, G_I, G_{II} and G_{III}.

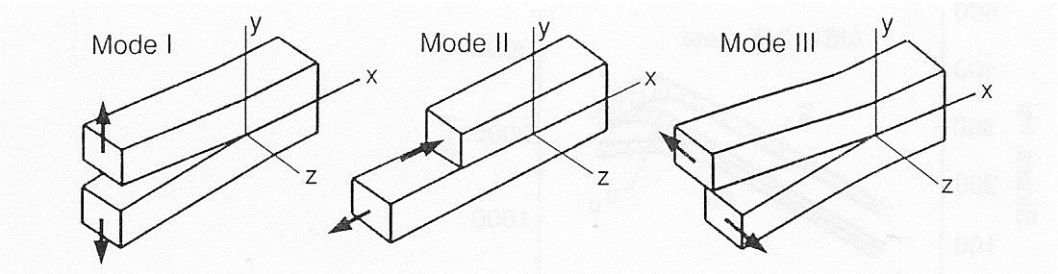

Figure 4.22 – Modes I, II and III of crack propagation.

For each material, there is a critical value of K for which unstable crack propagation of cracks occur. That critical value is designated as K_c. In the case of mode I of cracks propagation, that value is named material toughness, K_{Ic}.

4.5.4 Relationship between the energy release rate and the stress intensity factor

The energy release rate, G, and the stress intensity factor, K, are two different measures of the stress state surrounding the crack. Equation (4.52) expresses the relation between both entities:

$$\begin{cases} G = \dfrac{K^2}{E}, & \text{Plane Stress} \\ G = (1\text{-}\nu^2)\dfrac{K^2}{E}, & \text{Plain Strain} \end{cases} \tag{4.52}$$

Due to its important role in clarifying the fundaments of Fracture Mechanics, the deduction of such relationship is presented next.

Let us consider a plate of infinite dimensions, with fixed boundaries and with a crack of dimension 2*a* (Figure 4.23).

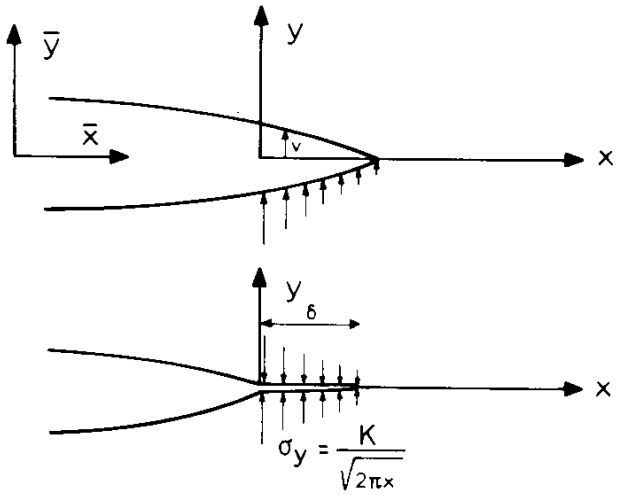

Figure 4.23 – Closure of the crack tip (Broek, 1987).

The stresses close enough to the crack tip perform work when an infinitesimal increment of the crack occurs. That work will be released, in some form of energy, when the connections between the new portions of crack surfaces break. It can therefore be written:

$$G_{\mathrm{I},average} = \frac{2}{\delta}\int_0^{\delta} \frac{\sigma_y \cdot v}{2} dr \tag{4.53}$$

and, consequently:

$$G_{\mathrm{I}} = \lim_{\delta \to 0} \frac{2}{\delta}\int_0^{\delta} \frac{\sigma_y \cdot v}{2} dr \tag{4.54}$$

If the origin of the coordinate system is located at the centre of the crack ($\overline{O}\overline{X}\overline{Y}$), it is acknowledged that:

$$v = \frac{2\cdot\sigma}{E}\cdot\sqrt{a^2\text{-}x^2} = \frac{2\cdot K_I}{E}\cdot\sqrt{\frac{a\text{-}\frac{x^2}{a}}{\pi}} \tag{4.55}$$

Considering $x = r+a\text{-}\delta$ and ignoring the second other terms, it becomes:

$$v = \frac{2\cdot K_I}{E\cdot\sqrt{\pi}}\cdot\sqrt{2\delta\text{-}2r+\frac{2r\delta}{a}\text{-}\frac{r^2}{a}} \cong \frac{2\cdot K_I}{E\cdot\sqrt{\pi}}\cdot\sqrt{2\cdot(\delta\text{-}r)} \tag{4.56}$$

Moreover, it can be considered that:

$$\sigma_y = \frac{K_I}{\sqrt{2\pi r}} \tag{4.57}$$

Replacing (4.56) and (4.57) in (4.54), the following expression is obtained:

$$G_I = \lim_{\delta\to 0}\frac{2\cdot K_I{}^2}{\pi\cdot E\cdot\delta}\int_0^{\delta}\sqrt{\frac{1\text{-}\frac{r}{\delta}}{\frac{r}{\delta}}}\,dr \tag{4.58}$$

That equation can be solved by performing a variable substitution: $r/\delta = \sin^2\varphi$. The associated transformations are translated into equations (4.59) to (4.62)

$$\frac{r}{\delta} = \sin^2\varphi \Leftrightarrow r = \sin^2\varphi\cdot\delta \tag{4.59}$$

$$\frac{dr}{d\varphi} = 2\cdot\sin\varphi\cdot\cos\varphi\cdot\delta \tag{4.60}$$

$$r = \delta \Leftrightarrow \sin^2\varphi = 1 \Leftrightarrow \varphi = \frac{\pi}{2}\ \text{rad} \tag{4.61}$$

$$r = 0 \Leftrightarrow \sin^2\varphi\cdot\delta = 0 \Leftrightarrow \varphi = 0\ \text{rad} \tag{4.62}$$

Applying those transformations:

$$\int_0^{\delta}\sqrt{\frac{1\text{-}\frac{r}{\delta}}{\frac{r}{\delta}}}\,d\,r = \int_0^{\frac{\pi}{2}}\sqrt{\frac{1\text{-}\sin^2\varphi}{\sin^2\varphi}}\cdot(2\cdot\sin\varphi\cdot\cos\varphi\cdot\delta)\cdot d\varphi =$$

$$= 2\cdot\delta\cdot\int_0^{\frac{\pi}{2}}\cos^2\varphi\cdot d\varphi = 2\cdot\delta\cdot\left[\frac{\sin\varphi\cdot\cos\varphi}{2}+\frac{\varphi}{2}\right]_0^{\frac{\pi}{2}} =$$

$$= 2\cdot\delta\cdot\left[0+\frac{\pi}{4}\text{-}0\text{-}0\right] = \frac{\pi\cdot\delta}{2} \tag{4.63}$$

It then becomes:

$$G_I = \lim_{\delta \to 0} \frac{2K_I^2}{\pi E \delta} \cdot \frac{\pi \delta}{2} = \frac{K_I^2}{E} \tag{4.64}$$

as it was intended. Similarly to Mode I, relationships between G and K can be found for Modes II and III. The relationships established for the 3 modes, in plane strain state, are the following (Broek, 1987):

$$\begin{cases} G_I = (1-\nu^2)\frac{K_I^2}{E} \\ G_{II} = (1-\nu^2)\frac{K_{II}^2}{E} \\ G_{III} = (1+\nu)\frac{K_{III}^2}{E} \end{cases} \tag{4.65}$$

The total energy release rate associated with combined mode cracking is (Broek, 1987):

$$G = G_I + G_{II} + G_{III} = \frac{(1-\nu^2)}{E}\left(K_I^2 + K_{II}^2 + \frac{K_{III}^2}{1-\nu}\right) \tag{4.66}$$

4.5.5 Fatigue cracks growth as a function of *K*

Under cyclic loading conditions, cracks can originate and propagate in materials for K levels below the material toughness, K_{Ic} (Saxena, 1998). This crack growth is designated as sub-critical growth and it is of paramount importance in determining the remaining life of components containing cracks smaller than the critical size.

Considering a cracked body, under a cyclic loading where the load P varies between a minimum and maximum values, P_{min} and P_{max}, respectively, the increase in crack dimension per loading cycle can be described, in general terms, in the following way:

$$\frac{da}{dN} = f(\Delta P, R, a) \tag{4.67}$$

where:

$$\Delta P = P_{max} - P_{min} \tag{4.68}$$

$$R = \frac{P_{min}}{P_{max}} \tag{4.69}$$

In the 1960s, Paul Paris and his colleagues suggested that the influence of the loading cycle and of the crack dimension on the crack propagation rate could be combined in a single parameter, $\Delta K = K_{max} - K_{min}$, in which K_{max} e K_{min} are the stress intensity factors associated with

the maximum and minimum loading, respectively (Paris et al., 1961). More specifically, the 3 crack propagation modes (I, II and III) relate with ΔK_I, ΔK_{II} and ΔK_{III}, respectively.

For a situation where both constant amplitude and constant R are observed, it can be written that:

$$\frac{da}{dN} = f(\Delta K) \tag{4.70}$$

Based on Paris' proposal, several experimental tests were performed and demonstrated that the relationship between $\frac{da}{dN}$ and ΔK is unique for a constant value of R and for a wide range of crack propagation rates. The analysis through the entire range of ΔK shows 3 distinct zones (Figure 4.24):

- Region I is the region close to the crack propagation threshold ΔK_{th}, where none (or very little) crack propagation occurs. In that region, it can be written:

$$\lim_{\Delta K \to \Delta K_{th}} \frac{da}{dN} = 0 \tag{4.71}$$

  The value of ΔK_{th} is a characteristic of each material. In practical terms, that limit is considered as the one corresponding to a crack propagation rate of 10^{-10}m/cycle (Saxena, 1998);

- Region II can be represented by a straight line, in logarithmic scaled corresponds to the range of application of Paris law;

- Region III is the region where the slope of the curve starts increasing, reflecting the change in behaviour towards an unstable crack propagation, observed when the maximum stress intensity factor observed in the cycle reaches the critical value, K_c.

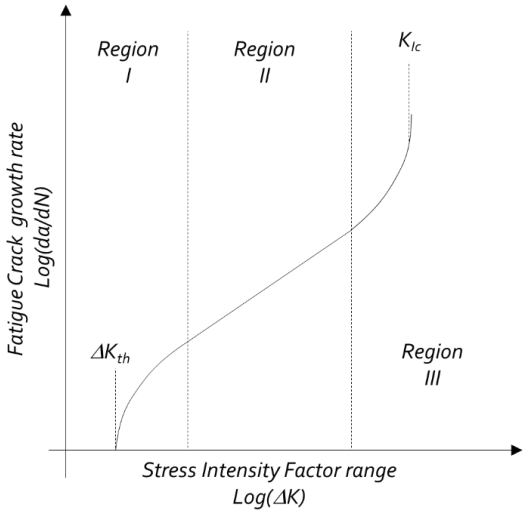

Figure 4.24 – Generic relationship between crack propagation rate and stress intensity factor range (adapted from Roylance (2001)).

Several expressions were developed in order to represent some or even all the above mentioned regions of the crack propagation rate curve. The Paris law (Equation (4.72)) can be used to describe the stable crack propagation. In that law, a is the semi-dimension of the crack, N is the number of loading cycles, C and m are material-dependent constants and ΔK is the variation of K at each loading cycle:

$$\frac{da}{dN} = C \cdot \Delta K^m \tag{4.72}$$

Other more complex laws, such as the Forman law (Equation (4.73)) were latter developed (Ewalds and Wanhill, 1985).

$$\frac{da}{dN} = \frac{C \cdot \Delta K^m}{(1-R) \cdot K_c - \Delta K} \tag{4.73}$$

Those laws usually allow to account for extra variables such as the ratio between maximum and minimum K, $R = \frac{K_{min}}{K_{max}}$, the threshold stress intensity factor, ΔK_{th}, and the critical stress intensity factor for which collapse occurs, K_c. A very wide variety of crack propagation laws can be found in Appendix 5 of (de Castro and Meggiolaro, 2009b).

From the observation of Equations (4.72) and (4.73) it becomes apparent that for determining the increment of a fatigue crack due to a complex loading, it is necessary to know:

- Some parameters characteristic of the material (C, m, K_c, K_{th}…);
- The loading and the corresponding evolution of K through time at the crack front, $K(t)$.

The workflow is summarised in Figure 4.25. In that same Figure, the field of application of the methodology proposed in Chapter 5 is also highlighted.

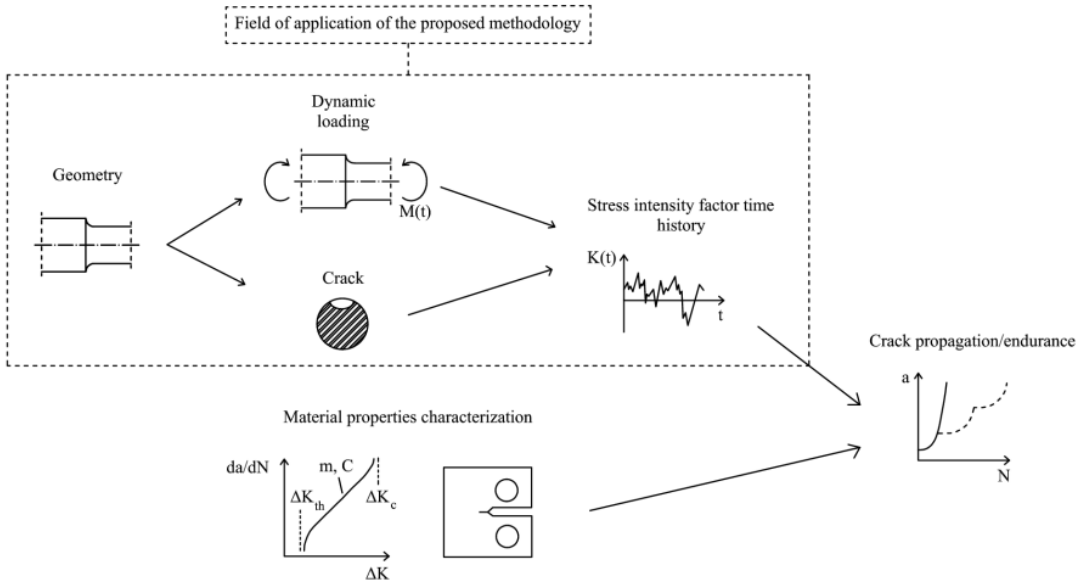

Figure 4.25 – Information required for a fatigue crack propagation analysis (Albuquerque et al., 2012a).

The determination of parameters characteristic of materials is performed through experimental tests, e.g. (ASTM, 2000). Alternatively, in some cases, namely when similar materials have already been tested before, the same parameters can be found in the literature (Dowling, 2007).

On the other hand, obtaining *K* time history due to a certain loading requires characterizing the stresses actuating on the detail. Once those stresses are known, *K* can be computed using a variety of methods: analytical, weighting functions, boundary elements method and finite elements method (Parker, 1981, Fett and Munz, 1997, Aliabadi and Rooke, 1991).

Regarding the finite elements method, different techniques can be used: displacements extrapolation (Guinea et al., 2000), forces method (de Morais, 2007), J-integral (Rice, 1968), Virtual Crack Closure Technique (VCCT) (Krueger, 2002), among others.

The application of the different methods for computing *K* to parametric studies of typical details allowed, also, the construction of reference curves and expressions, which are accessible in compilations built for that purpose. This is an additional way of obtaining *K* for those typical details and loads (Murakami, 1987, Tada et al., 2000, Rooke and Cartwright, 1976).

The determination of *K* through analytical ways is only possible for a limited number of simple, academic cases.

For structures with complex geometry and also under complex loading, it is necessary to use numerical methods applied to 3D finite element models.

Usually, those numerical models are computationally demanding, making its application in dynamic analysis difficult or even impossible. Three main facts contribute for those high computational requirements of the numerical models used in Fracture Mechanics:

a) Volumetric finite element models are usually needed;

b) Obtaining accurate results require a fine finite elements grid around the crack front (Menandro et al.);

c) Every time there is an increment in the crack, the finite elements grid needs to be re-meshed (Lin and Smith, 1999).

Chapter 5 describes a new methodology developed in order to overcome the limitations stated above, while keeping the advantages of the approaches that use Fracture Mechanics and crack propagation laws.

4.5.6 Crack propagation retardation laws in LEFM

As mentioned previously, in Section 2.2, the crack propagation rates are highly dependent on the sequence of variable amplitude load cycles. Since Elber, in the 1970s, identified the plasticity induced crack closure, it is widely accepted that retardation in crack propagation occurs after sudden and sporadic increases in load cycle amplitude (Schijve, 2003). A comprehensive review on the results of variable amplitude loading experiments, focusing on the consequences in terms of fatigue cracks propagation retardation can be found in (Skorupa, 1999, Skorupa, 1998).

Nevertheless, other causes of crack propagation retardation can be found (McEvily and Ritchie, 1998), namely:

- Crack closure due to corrosion and roughness of the crack faces;
- Crack path bifurcation;
- Residual stresses.

The relative impact of each mechanism will depend on the size of the crack and of the detail, on the stress state at the crack tip, on the range and maximum value of the loading, on the

environment and on the material microstructure. These different mechanisms may add or cancel each other, depending on the situations.

In spite of the different retardation mechanisms stated above, the plasticity induced crack closure is the mechanism usually employed when forecasting the fatigue life of details under complex loads. For that reason, attention is paid in next paragraphs to some ways of modelling it. Moreover, it is important to stress that when estimating fatigue crack propagation, if the interaction effects between successive cycles are neglected and no retardation of crack growth is considered, this will lead to a conservative estimate (Broek, 1987).

Early models were developed by Wheeler (1972) and Willenborg et al. (1971) to take into account plasticity induced crack closure. Wheeler model introduced the retardation parameter, Φ, which allowed to compute the retarded crack propagation rate as a function of the original crack propagation rate:

$$\left(\frac{da}{dN}\right)_{retardation} = \Phi \left(\frac{da}{dN}\right)_{no\ retardation} \tag{4.74}$$

The retardation model is defined according to Equation (4.75):

$$\Phi = \left(\frac{r_{pi}}{a_o + r_{po} - a_i}\right)^m \tag{4.75}$$

where:

- r_{po} is the the size of the crack tip plastic zone caused by the overload;
- r_{pi} is the size of the crack tip plastic zone caused by the subsequent i^{th} stress cycle;
- a_o is the size of the crack, before the overload;
- a_i is the size of the crack after propagating further;
- m is a parameter to be determined empirically.

The parameters intervening in this model are illustrated in Figure 4.26.

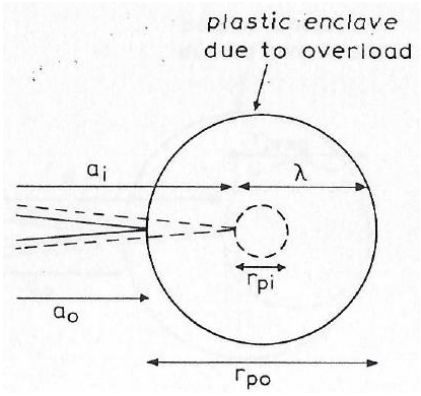

Figure 4.26 – Parameters intervening in the Wheeler model (Broek, 1987).

Other models, more sophisticated, were developed later (Forman et al., 2000). Most of them assume that the parameter controlling the fatigue crack propagation it is the effective stress intensity factor range (Equation (4.76)):

$$\Delta K_{eff} = K_{max} - K_o \tag{4.76}$$

where K_o is the stress intensity factor required to open the crack, therefore overcoming the crack closure.

One of such models is the one proposed by Forman-Newman and included in the software NASGRO (Forman et al., 2000):

$$\frac{da}{dN} = A \cdot \Delta K_{eff}^{\ m} \frac{(1-\Delta K_{th}/\Delta K)^p}{(1-\Delta K_{max}/K_C)^q} \tag{4.77}$$

where A, m, p and q are empirical coefficients and where K_o is computed according to the K_o/K_{max} established in (Newman, 1984).

4.5.7 Recent advances of the Extended Finite Element Method (XFEM)

More recently, the development of the Extended Finite Element Method (XFEM) and its application in the context of Fracture Mechanics (Giner et al., 2009, Moës and Belytschko, 2002) has been giving promising results. The XFEM is a numerical method that enables the local enrichment of approximation spaces, through the partition of unit concept. It is useful for the approximation of solutions with pronounced non-polynomial characteristics in restricted areas of the computational domain. That is the case of the discontinuities and singularities represented by the crack and crack-tip, respectively, when included in numerical models of details.

The main advantage of XFEM, when compared to traditional approaches, is that it allows simulating crack propagation without the need for re-meshing around the crack faces and crack tip. It also introduces the crack tip singularity directly in the formulation of the elements containing the crack tip, therefore exempting from the use of special quarter-point elements (Barsoum, 1977). These two characteristics allow developing numerical models of the cracked details with less nodes and elements (Shi et al., 2010).

As mentioned before, the XFEM derives from the Partition of Unit Method (Babuška and Melenk, 1997), which may be expressed in the following format:

$$u^h = \sum_{i \in I} N_i(x)\, u_i + \sum_{j=1}^{m} \sum_{i \in I} N_i(x)\, \psi^j(x) a_i^j \tag{4.78}$$

where:

- u^h is the approximated function;
- $N_i(x)$ is the standard FEM function of node i;
- u_i is the unknown of the standard FEM part at node i;
- I is the set of all nodes in the domain;
- $\psi^j(x)$ is the global enrichment function for the enrichment j;
- a_i^j is the unknown of enrichment j at node i.

The important difference of the XFEM method is that the local enrichment functions are defined to only a subset of nodes, I_j^*, of the entire domain: $I_j^* \subset I$. The XFEM approximation of the function $u(x)$ is of the following form:

$$u^h = \sum_{i \in I} N_i(x)\, u_i + \sum_{i \in I_1^*} M_i^1(x) a_i^1 + \ldots + \sum_{i \in I_m^*} M_i^m(x) a_i^m \tag{4.79}$$

where:

$$M_i^m(x) = N_i^*(x) \cdot \psi^j(x) \tag{4.80}$$

with $N_i^*(x)$ being the partition of unity functions and $\psi^j(x)$ the global enrichment functions. An important point to consider is that for a certain enrichment j, the functions $N_i^*(x)$ compose a partition of unity inside the sub-domain Ω_j^*:

$$\sum_{i \in I_j^*} N_i^*(x) = 1 \tag{4.81}$$

A crack is a strong discontinuity in the displacements field. In order to characterise that discontinuity, the Heaviside function (Equation (4.82)) is used along in the crack path:

$$H(x)=\begin{cases}0 \text{ if } \phi(x)\leq 0\\ 1 \text{ if } \phi(x)>0\end{cases} \tag{4.82}$$

At the crack tip, the singularity of stresses is achieved through Equations (4.83) to (4.86):

$$\psi^1(x)=\sqrt{r}\sin\frac{\theta}{2} \tag{4.83}$$

$$\psi^2(x)=\sqrt{r}\sin\frac{\theta}{2}\sin\theta \tag{4.84}$$

$$\psi^3(x)=\sqrt{r}\cos\frac{\theta}{2} \tag{4.85}$$

$$\psi^4(x)=\sqrt{r}\cos\frac{\theta}{2}\sin\theta \tag{4.86}$$

Now let us consider that I_1^* is the set of the nodes of the elements completely cut by the crack and that I_2^* is the set of the nodes of the elements containing the crack tip (Figure 4.27).

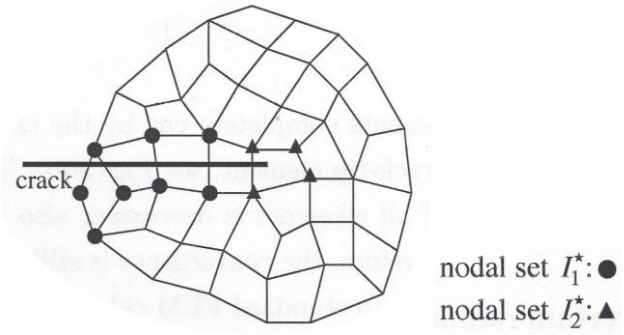

Figure 4.27 – Enriched nodal sets for cracks (adapted from Fries and Belytschko (2010)).

In that case, the XFEM approximation would take the form given by Equation (4.87):

$$u^h = \sum_{i\in I} N_i(x)\, u_i + \sum_{i\in I_1^*} N_i^1(x) H(x) a_i^1 + \sum_{j=1}^{4}\sum_{i\in I} N_i^*(x)\, \psi^j(x) b_i^j \tag{4.87}$$

This said, it should be stressed that when comparing XFEM with standard FEM, for the same mesh, the amount of computational work is increased due to the additional enrichment functions, which involve more complex terms, such as trigonometric functions. However, in that situation, the accuracy of XFEM is higher. When comparing XFEM with standard FEM for the same level of accuracy, usually the XFEM requires much less computational resources.

4.6 CONCLUDING REMARKS

In spite of its wide implementation in Civil Engineering context and in design standards, fatigue assessment procedures based on nominal stresses present important limitations, which are well acknowledged. Several other methodologies were developed throughout the last decades in an attempt to:

- overcome some of those limitations;
- complement the approaches based on nominal stresses by addressing specific problems, e.g. low cycle fatigue, location of cracks initiation, cracks propagation paths, among others.

In the current Chapter, some of those methodologies were presented.

The assessment methods based on structural stresses and strains showed to be useful when determining the fatigue life of welded details, when the crack is expected to initiate or propagate from the weld toe. This allows analysing a wide variety of welded details.

The notch stresses approach, on the other hand, allowed to expand the fatigue assessment to all type of sharp notches, whether they are due to the weld profile or not.

The notch strain assessment methodology has the advantage of covering both the low-cycle and high-cycle fatigue damage. In addition, the fatigue strength curves for the notch strain approach depend on the material of the detail and not on the type of detail. This reduces the experimental burden, when new fatigue strength curves need to be defined. It is also important to stress that the fatigue strength curves are obtained from experiments on small scale specimens and not in full-scale structural details, as it is common for nominal stress approaches.

Finally, concerning the assessments based on Fracture Mechanics and crack propagation laws, it was shown in this Chapter that they have a sound theoretical background which was already demonstrated through many applications in different areas of Engineering. Similarly to the notch strain approach, the fatigue strength curves, in the form of crack propagation laws, are material dependent and can be determined through testing of small scale specimens. Moreover, it is the only method that has the advantage of allowing the assessment of the remaining fatigue life of structural components that are found to have fatigue cracks in some moment of the structures life. This is a very important benefit from this approach if we consider that the main objectives of inspection of bridges is to detect structural damage and that if some damage is found, which

happens often, the risk, structural integrity and remaining fatigue life of the structure must be assessed.

In spite of all the strengths of the fatigue assessments based on Fracture Mechanics, the computational requirements of that approach are still an important limitation. This is even more evident for situations where complex loading is present and when the fatigue cracks are confined to a small region of a bigger structure. Even if the XFEM is showing very good results in improving the accuracy and ease of implementation of fatigue crack propagation simulations in numerical models of structures, the challenges remain.

In order to tackle these constraints, a new methodology for the determination of stress intensity factor time histories, when dealing with complex loading and flexible structures, was developed and validated. That new methodology is presented in Chapter 5.

Chapter 5

CRACK ANALYSIS OF DYNAMICALLY LOADED STRUCTURES USING MODAL SUPERPOSITION OF STRESS INTENSITY FACTORS

5.1 INTRODUCTION

Chapter 2 aimed to show the relevance of fatigue in the context of structural integrity, namely in the case of railway bridges.

In Chapter 3, it was stressed that the methodologies based on S-N curves and nominal stresses are the most common in design codes but that several important limitations can be pointed out to those approaches. On the one hand, the applicable rules cover a limited number of structural details; on the other hand, the development of S-N curves for new details implies performing tests at the real scale, which are expensive and time consuming, and consequently generally unpractical for the timings of design and construction (Fricke and Paetzold, 2010, Lotsberg and Landet, 2005, Ling and Pan, 1997). Furthermore, S-N curves are a result of tests that present an important scatter (Pedersen et al., 2010). As a safeguard against this effect the S-N curves are usually very conservative (Casavola and Pappalettere, 2009, Morel and Flacelière, 2005). Finally, fitness for purpose assessments cannot be carried out on the basis of that approach. For a given situation of damage, such as a fatigue crack identified during some non-destructive

inspection, such approach does not provide a risk assessment of that defect nor the useful remaining life (Byers et al., 1997). Therefore, it does not contribute for an improved definition of intervals between inspections (Ayala-Uraga and Moan, 2007). Other limitations of the S-N approaches were identified by several authors, concerning, for example, variable amplitude loading (Johannesson et al., 2005), or fatigue life for a very high number of load cycles (Sonsino, 2007).

Therefore, in Chapter 4, more advanced methodologies for the fatigue assessment, which consider the local behaviour of details and materials, were discussed. It becomes apparent that the methodologies based on Fracture Mechanics concepts and on fatigue crack propagation laws are among the most mature ones, with wide acceptance and application in multiple areas of Engineering. A main advantage identified was the fact that crack propagation laws are the only method available for determining the remaining fatigue life of details that present fatigue cracks or other planar defects. This is of paramount importance for the follow up of inspection activities performed on railway bridges. Also, its application in cases of fitness for purpose assessment proves to be almost irreplaceable (Zerbst, 2007).

However, it was also mentioned in Chapter 4 that the Fracture Mechanics approach has its own drawbacks, which are mainly related with the computational burden involved. This may explain its lower receptivity for the fatigue assessment of Civil Engineering structures. In fatigue analyses based upon Fracture Mechanics concepts, the usual calculations involve the application to the structural detail of interest containing one or more cracks, of a known loading history, under load or displacement control. The computation of the corresponding stress intensity factor values allows for the calculation of crack growth behaviour (Radaj et al., 2006). However, in Civil Engineering structures, loading is most of the times complex and the corresponding structural dynamical response is unknown in most – or even all – points of interest. In these circumstances, even when loading is known, its effects in the detail under study can only be determined through dynamic analysis of the complete structure. Those analyses are generally based upon the Finite Element Method (FEM). The algorithms for solving the numerical problem, as Newmark (Bathe, 1996) or HHT (Chung and Hulbert, 1993), frequently require the calculation of thousands of load steps, leading to very time consuming calculation processes. The high computational costs are heightened as a result of the need for highly refined finite elements meshes in the neighbourhood of the damage locations (Menandro et al.). That level of refinement cannot be extended to the remaining structure (Chan et al., 2003). This is a problem inherent to

the scale difference between the detail where fatigue damage occurred or is likely to occur, of the order of mm or less, and the global structure, that may be of the order of km (Li et al., 2007). The need for grid remeshing after each fatigue crack increment is an additional point of concern (Lin and Smith, 1999).

Finally, Chapter 4 also presented the recent advances on Extended Finite Element Method (XFEM) (Giner et al., 2009, Moës and Belytschko, 2002) which may help increasing the accuracy and/or reduce the computational cost associated with fatigue crack propagation simulations. It allows avoiding mesh refinement and remeshing to adapt the grid to the crack increments. However, even in that case, challenges remain. On one hand, XFEM is not readily available in most of the commercial FEM software packages. On the other hand, the dynamic simulations performed on a coarse model of a structure containing enriched elements will take more time than the same simulation on a similar model that does not have enriched elements.

Therefore, a novel methodology was developed (Albuquerque et al., 2012a) aiming to increase the computational efficiency of fatigue studies performed in dynamically loaded civil engineering structures using Fracture Mechanics concepts. That methodology is presented in the current Chapter.

The modal superposition method (Clough and Penzien, 1975) is applied in the context of Fracture Mechanics, leading to a concept of modal stress intensity factor (modal-*K*), resulting in a drastic reduction of computational time whilst preserving the precision of the analyses. The adoption of sub-modelling techniques, widely used in detail analyses of large scale structures, constitutes an additional, optional, contribution to the proposed methodology. The methodology is validated with a simple case, a moving load traveling over a simply supported beam containing a semi-elliptical crack.

5.2 MODAL SUPERPOSITION OF STRESS INTENSITY FACTORS APPLIED TO THE FATIGUE ANALYSIS

5.2.1 Dynamic analysis using modal superposition

When moving loads pass over a certain structure, they originate its dynamic response/vibration. If the loads are known, the dynamic response can be simulated numerically using a finite element model of the structure. The positions of the moving loads, at a certain time step, may be computed based on their initial position and on their velocity. Once each load

position is defined, it is converted into equivalent vertical nodal forces, applied to the nodes of the structure. The position of the moving loads and the corresponding nodal forces need to be updated at each time step. Two common numerical methods employed to perform the dynamic analysis are the direct integration and the modal superposition methods (Clough and Penzien, 1975).

For finite element models with a high number (N) of degrees-of-freedom, the direct integration method becomes highly time and resources consuming, as it implies solving Equation (5.1) directly, without additional assumptions:

$$\mathbf{M}\cdot\ddot{\mathbf{u}}(t)+\mathbf{D}\cdot\dot{\mathbf{u}}(t)+\mathbf{K}\cdot\mathbf{u}(t) = \mathbf{F}(t) \tag{5.1}$$

In Equation (5.1) **M**, **D** and **K** are the mass, damping and stiffness matrices, respectively, and have a $N\times N$ dimension, each. $\mathbf{F}(t)$ is the $N\times 1$ vector of the nodal forces acting in the structure for a certain time-step and $\mathbf{u}(t)$ is the $N\times 1$ vector of displacements associated with each degree-of-freedom at the same time step.

On the other hand, the modal superposition method is computationally more efficient since the global dynamic response of the structure can be accurately reproduced superimposing the individual modal responses of a limited number (J) of modes of vibration. This approach can be applied to the case of flexible structures with elastic behaviour, such as composite railway bridges.

Using modal superposition, the full $N\times N$ system of simultaneous equations is converted into N uncoupled single-variable equations (Equation (5.2)) that can be solved independently:

$$\ddot{Y}_j(t) + 2\omega_j\cdot\xi_j\cdot\dot{Y}_j(t) + \omega_j^2\cdot Y_j(t) = f_j(t) \tag{5.2}$$

where Y_j is the modal coordinate, ω_j is the natural frequency, ξ_j is the modal damping ratio and f_j represents the modal forces, for the j^{th} mode of vibration. The efficiency of the modal superposition technique arises not only from the uncoupling of the system of equations but also from the fact that the total number of modes of vibration needed to accurately reproduce the dynamic response of the flexible structure, J, is usually much lower than the total number of degrees of freedom ($J << N$).

5.2.2 Fatigue crack propagation laws

In Chapter 4, the stress intensity factor, K, was mentioned as a key parameter of Linear Elastic Fracture Mechanics theory, characterizing the stress field in the vicinity of a crack tip (Irwin, 1957). Since the historical publication of Paris et al. (1961), huge experimental evidence supports the correlation of fatigue crack growth rate, da/dN, with the range of the stress intensity factor, ΔK. More specifically, the three basic modes of rupture or crack propagation – I, II and III – are related with ΔK_{I}, ΔK_{II} and ΔK_{III}, respectively (Schijve, 2009).

Figure 4.24 presented the configuration of the typical da/dN *versus* ΔK_{I} relationship. In the following sections, all considerations will concern mode I and therefore the index I will be omitted from K_{I} and K will be written. However, the proposed methodology can be extended to modes II and III, as will be seen in Chapter 7.

Figure 4.24 also showed three different regions: the first, beginning at the threshold for crack growth ΔK_{th}, is phase I, the second corresponds to the applicability of Paris law, phase II, whereas in the third (phase III) the crack accelerates as a result of proximity to final rupture conditions. In Equation (5.3), the Paris law, a is a characteristic of the crack geometry, N is the number of loading cycles, C and m are constants depending upon the material of interest, and ΔK is the stress intensity factor range in each loading cycle.

$$\frac{da}{dN}=C\cdot\Delta K^{m} \tag{5.3}$$

As already discussed in Chapter 4, other laws, addressing additional features of the problem, were subsequently proposed (Ewalds and Wanhill, 1985, Forman et al., 1967). These subsequent laws take into account additional parameters, such as the ratio between minimum and maximum K, $R = K_{min}/K_{max}$, the threshold for crack propagation, ΔK_{th} below which no fatigue crack growth takes place, and K_C corresponding to final unstable rupture.

The observation of such laws indicates that, for determining the variation of crack length given a loading history, some material parameters should be known (C, m, K_c, K_{th},…), further to the loading and corresponding evolution of K over time, $K(t)$, see Figure 4.25.

The common ways of obtaining the relevant properties of materials and $K(t)$ were already discussed in Chapter 4. The methodology now proposed seeks to provide an answer to the need of expediting the calculation of $K(t)$ using the finite element method.

5.2.3 Modal stress intensity factors

The next paragraphs present the considerations leading to the concept of modal-*K*. Generically, *K* can be represented as (Equation (5.4)):

$$K(t) = C\sqrt{\pi a}\cdot\sigma \tag{5.4}$$

where C is a function of the geometry of the structure and of the crack dimensions, σ is the nominal stress acting on the detail and a is the crack dimension.

Now let us consider a structure containing a crack with the dimension a_n. The static loading acting on the structure (e.g. structure's self-weight or internal residual stresses due to manufacturing) induce a certain stress state on it, σ_{sta}, originating a stress intensity factor, K_{sta}, through the crack front, according to:

$$K_{sta}(t) = C_n\sqrt{\pi a_n}\cdot\sigma_{sta} \tag{5.5}$$

If the same structure is subjected to a dynamic loading, the latter will produce a stress field variable in time, $\sigma_{dyn}(t)$. Admitting that, during each loading event, the crack remains with approximately constant dimensions, then, it can be written:

$$K_{dyn}(t) = C_n\sqrt{\pi a_n}\cdot\sigma_{dyn}(t) \tag{5.6}$$

Considering the simultaneous action of the static and dynamic loadings, the total stress intensity factor acting on the structure, through time, becomes:

$$K^*_{total}(t) = K_{sta}+K_{dyn}(t) \tag{5.7}$$

where K^*_{total} is the total stress intensity factor before a "sign" correction presented in later paragraphs. The process of crack opening and crack closure is a non-linear phenomenon, namely due to the contact between the crack faces. Nevertheless, for small cracks, the referred non-linear phenomenon does not induce a global non-linear behaviour. Thus, in such cases, the determination of the temporal evolution of the stress intensity factor, $K_{dyn}(t)$, through the crack front, can be achieved using the modal superposition method.

The application of the modal superposition method allows writing:

$$\sigma_{dyn}(t) = \sum_j \sigma_j\cdot Y_j(t) \tag{5.8}$$

where the *j* subscript refers to the number of each mode of vibration, σ_j is the nominal stress in the j^{th} mode shape and $Y_j(t)$ is the modal coordinate of the j^{th} mode of vibration (Clough and Penzien, 1975). Replacing the Equation (5.8) in the Equation (5.6) it becomes:

$$K_{dyn}(t) = C_n\sqrt{\pi a_n}\cdot \sum_j \sigma_j \cdot Y_j(t) = \sum_j C_n\sqrt{\pi a_n}\cdot\sigma_j \cdot Y_j(t) = \sum_j K_j \cdot Y_j(t) \quad (5.9)$$

In the previous equation, the modal stress intensity factor, K_j, is the stress intensity factor obtained with the configuration of the j^{th} mode shape.

Replacing the Equation (5.9) in the Equation (5.7) it finally becomes:

$$K^*_{total}(t) = K_{sta} + \sum_j K_j \cdot Y_j(t) \quad (5.10)$$

In conclusion, to obtain the temporal evolution of *K* only the calculation of K_{sta} and of the different K_j is required. Thus, the calculation of *K* for each time step of the analysis is avoided.

An important reflection to consider, relates to the "sign" of K_{sta} and of the several K_j. As it is generally accepted, disregarding the crack closure effects due to local plasticity in the surroundings of the crack front, the stress intensity factor associated with rupture mode I, K_I, only takes positive values when the crack is open, assuming a null value when it is closed and/or under compression.

Nevertheless, a numerical analysis with a linear elastic finite element model, built without contact elements at the crack faces, will not detect the overlap between the two crack faces, when the crack surroundings are subjected to compression. Consequently, two opposite loading situations, e.g. a tension nominal stress of σ and a compression nominal stress of $-\sigma$ will lead to the same positive value of the energy release rate, *G*. As *K* is generally obtained from *G*, as a function of its square root, the same positive value of *K* will be obtained in the two opposite situations.

Not taking the above mentioned effect into account would mislead the obtained results. To enable the modal superposition of stress intensity factors, it is fundamental to determine the sign of K_{sta} and of each K_j.

Two different and alternative criteria can be used (Figure 5.1) to distinguish between both situations:

a) The relative displacement between the crack faces, measured in two points located near the crack front, δ, will be positive if the crack is open and will be negative if the crack is closed (overlapping);

b) The stress component perpendicular to the crack plane, in a node belonging to the crack front, σ_{ct}, is positive if the crack is open and is negative if it is closed (overlapping).

The application of any of these criterion allow for the definition of the sign of K_{sta} and of each K_j.

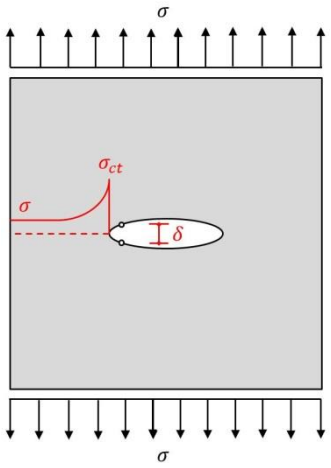

Figure 5.1 - Criteria for the definition of the K_{sta} and K_j signs.

Once K_{sta} and each K_j are defined, the final expression of the total value of K through time is defined as follows (Equation (5.11)):

$$K_{total}(t)=\begin{cases} K_{sta}+\sum_j K_j \cdot Y_j(t) & \Leftarrow K_{sta}+\sum_j K_j \cdot Y_j(t) \geq 0 \\ 0 & \Leftarrow K_{sta}+\sum_j K_j \cdot Y_j(t) < 0 \end{cases} \tag{5.11}$$

5.2.4 Submodelling

The global dynamic behaviour of bridges and other large civil engineering structures is generally well reproduced by numerical models built with relatively coarse meshes of shell or beam elements.

Modelling fatigue cracks, however, require much more refined meshes on the relevant details. Up to relatively large crack dimensions, details are often modelled with brick elements. At later stages of crack propagation, when the cracks under study are already through cracks, it is frequently enough to model the details with shell elements, even if a good refinement level of the meshes is still required.

The inclusion of refined models of the details directly into the global models of the structure may lead to significant computational costs. Nevertheless, successful applications of this kind can be found in literature (Li et al., 2007). The direct inclusion of the refined models of the details is necessary when they strongly interact with the global structure.

An alternative approach that consumes fewer resources consists on the analysis of the global model and the subsequent imposition of the obtained displacement field to the refined models of the details (Kiss and Dunai, 2000, Kiss and Dunai, 2002).

In this context, techniques such as the shell-to-shell and the shell-to-solid submodelling can be particularly useful, as they do not require the global model to have "pilot" nodes and the boundary nodes of the local model do not need to be spatially coincident with the nodes of the global one. Instead, the displacement field applied to the boundary nodes of the local model is obtained by extrapolation, based on the shape functions of the relevant elements in the global model (ANSYS, 2009a).

When defining the submodel, namely the position of its boundaries, two criteria should be considered. First of all, the selected boundaries should be far enough from the stress concentration points under analysis, avoiding the introduction of disturbance on the referred stress field. On the other hand, the submodel should be small enough so that the inertia load field acting on it may be considered negligible when compared with the elastic force field imposed by the displacements applied to the boundary nodes. It should be reminded that the shapes of the modes of vibration correspond to situations where the inertia loads are in perfect equilibrium with the elastic forces. The former condition can be obeyed by means of a sensitivity analysis of each case study, e.g. according to (Cormier et al., 1999). The second condition is generally respected when modelling a detail of reduced dimensions, when compared with the dimensions of the global structure. An additional check can be made by comparing of the elastic strain energy of the global model in the surroundings of the detail with the elastic strain energy of the submodel.

5.2.5 Computational algorithm

Considering the above arguments, it can be concluded that, when a fatigue crack is present in a structure, the calculation of the stress intensity factor through time, at the crack front, when it is subjected to a dynamic loading, can be summarised on the following steps:

a) Calculation of the displacement field of the structure due to the static loading, Φ_{sta}, and extraction of K_{sta} and the corresponding sign;

b) Modal analysis of the structure and obtaining, for each j^{th} mode of vibration, the value of K_j and the corresponding sign. Modal frequencies, ω_j, modal masses, m_j, and mode shapes, Φ_j, are also computed. Modal damping ratios, ξ_j, are generally defined based on standards or on experimental results;

c) Characterization of the dynamic loading, $F(t)$, and calculation of the modal forces, $F_j(t)$;

d) Obtaining the time histories of the modal coordinates, $Y_j(t)$;

e) Obtaining $K_{total}(t)$ by application of the Equation (5.11).

These steps may include, or not, the application of submodelling techniques (Figure 5.2). The presented method has three main advantages:

a) For a structure which dynamic behaviour is well characterised by N vibration modes, the stress intensity factor has to be computed only N+1 times. The time history of the modal coordinate of each mode of vibration may be determined subsequently, in an efficient way, solving each one of the single degree-of-freedom problems;

b) The contribution of each mode of vibration to the value of $K_{total}(t)$, at each time step, can be obtained directly, allowing to understand which modes of vibration contribute more decisively to the crack propagation;

c) The consideration of different dynamic loads only implies the recalculation of the modal coordinates $Y_j(t)$.

In contrast, a traditional analysis would imply the analysis of the whole structure through time and the calculation of K for each time step (typically thousands of times).

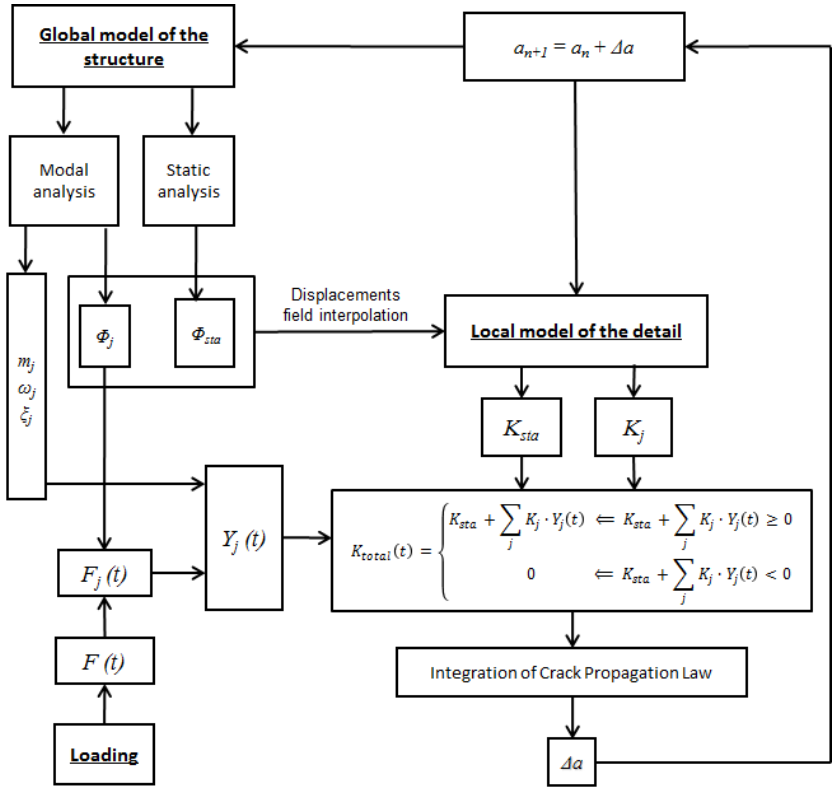

(a)

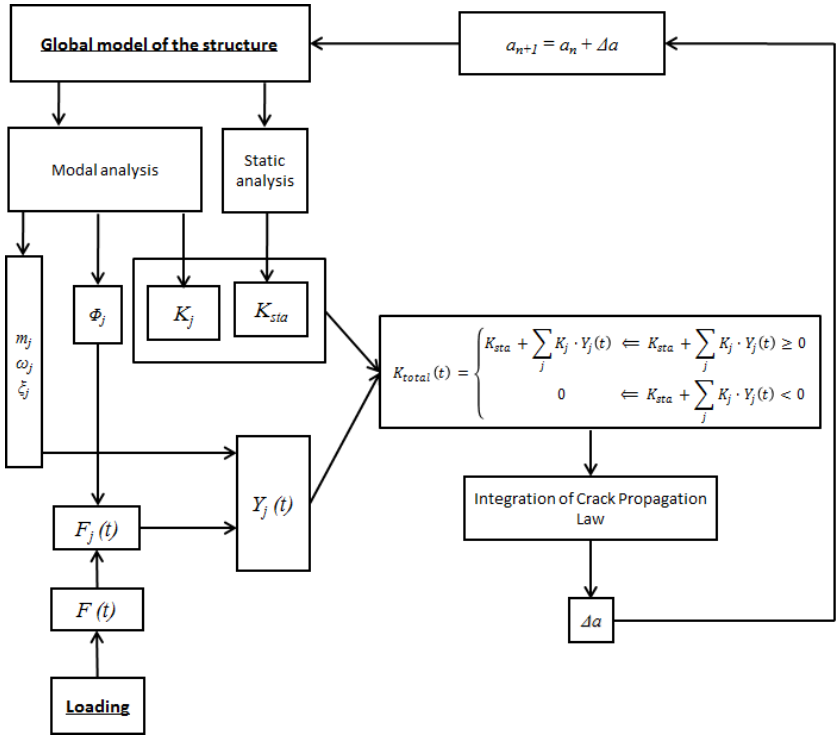

(b)

Figure 5.2 - Flow chart for the application of the proposed methodology: (a) with submodelling and (b) without submodelling.

5.3 APPLICATION

5.3.1 Introduction

In order to validate and illustrate the proposed method, the behaviour of a simply supported beam containing a semi-elliptical crack, when subjected to the simultaneous action of a static loading and a dynamic loading, is analysed.

Thus, an initial description of the structure and of the developed numerical models is made. Next, the values of the static and modal stress intensity factors, all through the crack front, obtained with the different numerical models are presented. Finally, the dynamic analysis of the structure is performed and the time history of the stress intensity factor, $K(t)$, is obtained, both by the proposed and by the conventional methods. The results are compared in terms of computational efficiency and the accuracy is evaluated by comparison with the results obtained with widely accepted expressions present at references.

5.3.2 Description of the structure

The structural element under analysis is a simply supported beam, with a 10 m span and a rectangular section with 0.4 m of width and 0.15 m of height.

A semi-elliptical crack is present at the bottom face of the beam, 2.9 m far from the initial extremity of it, i.e. in a point located between 1/4 span and 1/3 span. This intended to guarantee that all the considered vibration modes have non-null displacements and stresses at the section where the crack is present and contribute, consequently, to its dynamic response.

The crack presents a length of 0.10 m on the surface, and a total depth of 0.05 m (Figure 5.3).

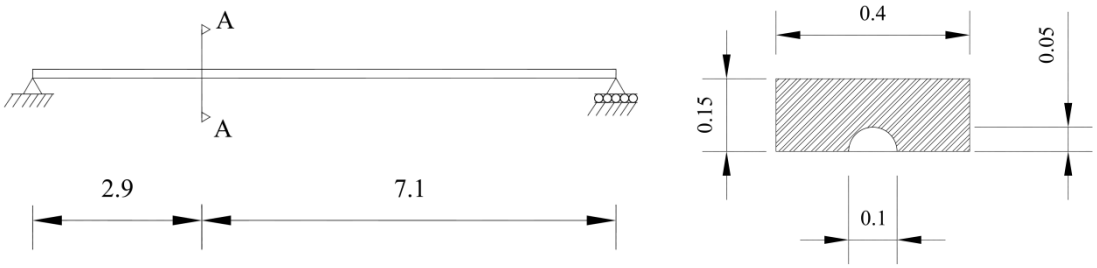

(a) (b)

Figure 5.3 - Geometric properties of the application: (a) beam dimension and crack location [m] and (b) crack dimensions (section A-A) [m].

A linear-elastic, isotropic and homogeneous material was considered, with mechanical properties similar to those of current structural steels: a Young Modulus of 210 GPa, a Poisson ratio equal to 0.3 and a density of 7850 kg/m^3.

Two different numerical models of the structure were built:

- BRM – Model built exclusively with brick elements and with the crack modelled explicitly (Figure 5.4);
- SSM – Coarse model of the structure built with shell elements. Refined submodel of the crack region, built with brick elements and with explicit crack modelling (Figure 5.5).

Both models were developed and analysed with software ANSYS®.

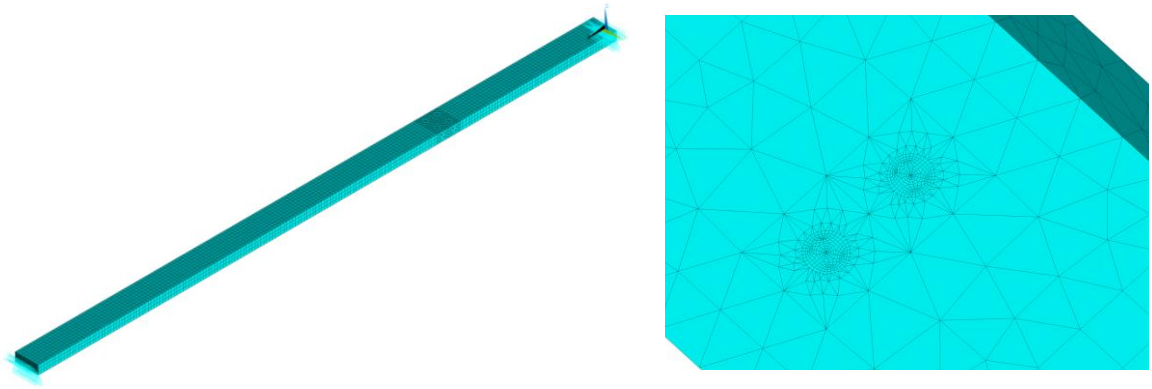

(a) (b)

Figure 5.4 - Finite element model BRM: (a) overview and (b) zoom to the mesh near the crack.

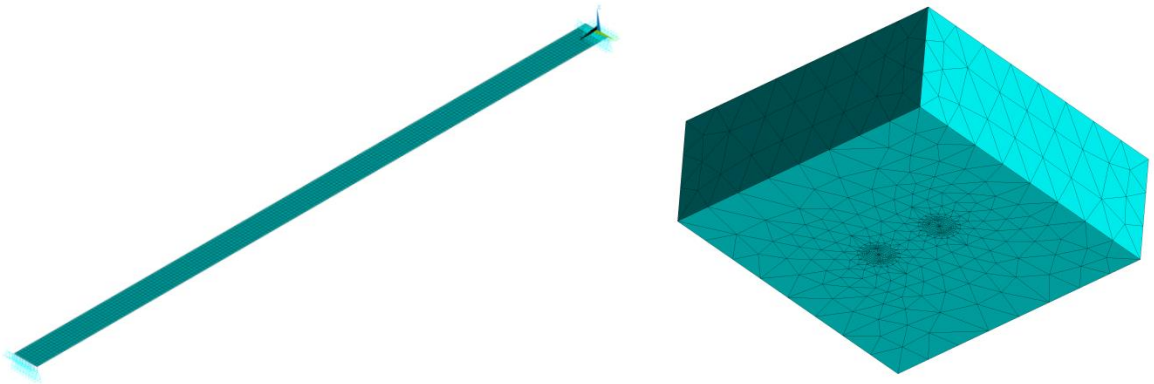

(a) (b)

Figure 5.5 - Finite element models SSM: (a) overview of the global coarse shell model and (b) local refined brick model.

The results obtained with the referred models will be presented next.

5.3.3 Modal and static stress intensity factors

Both the numerical models were subjected to a modal analysis and the modes of vibration present at the 0 Hz to 100 Hz range were extracted. The corresponding frequencies are presented in Table 5.1. Only the vertical bending vibration modes were considered, as only these are mobilised by the dynamic load, a moving vertical load applied at the beam's top surface. It should be noted that the differences between the natural frequencies of both numerical models are residual.

Table 5.1 - Natural frequencies of vertical bending vibration modes: BRM vs. SSM.

Number of the mode	Freq. [Hz]		$\varepsilon = \frac{f_{SSM} - f_{BRM}}{f_{BRM}}$ [%]	Description
	BRM	SSM		
1	3.51	3.52	0.1%	1st vertical bending
2	14.01	14.02	0.1%	2nd vertical bending
3	31.39	31.41	0.1%	3rd vertical bending
4	55.31	55.41	0.2%	4th vertical bending
5	84.63	85.12	0.6%	5th vertical bending

For the deformed configuration of each vibration mode, the corresponding modal stress intensity factor (K_j) was obtained, in several points of the crack front (Figure 5.6). The angle Φ is used as a reference, to specify the position in the crack front (see Figure 5.7).

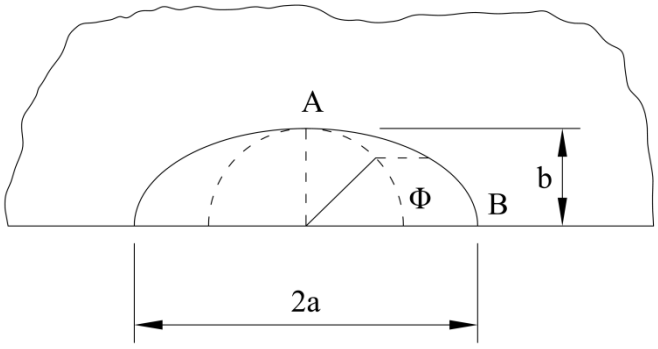

Figure 5.6 - Crack front: major points A and B and location based on angle Φ (adapted from Murakami (1987)).

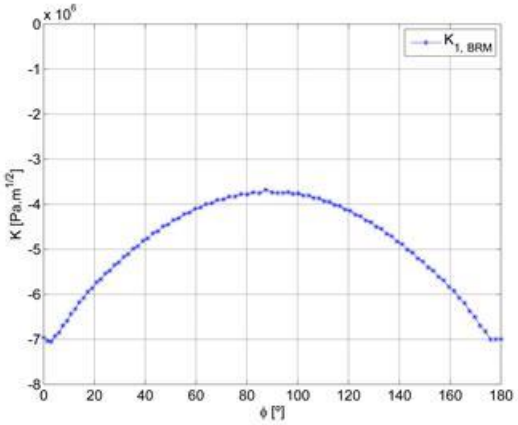

(a) Mode 1 – Modal stress intensity factor

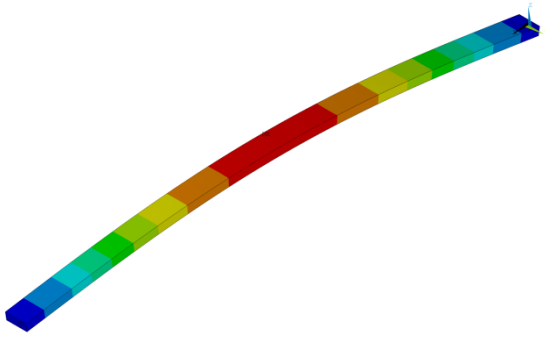

(b) Mode 1 – Mode shape

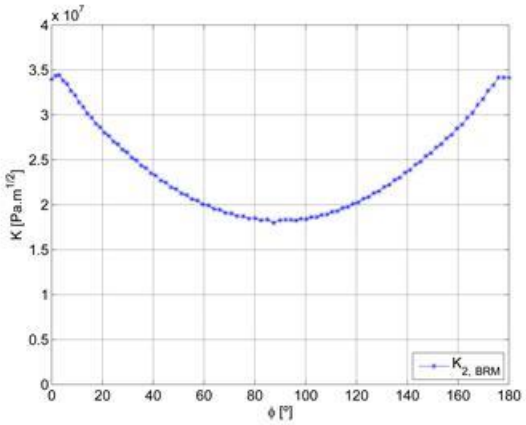

(c) Mode 2 – Modal stress intensity factor

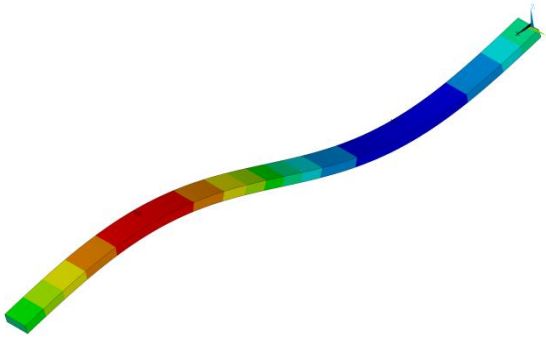

(d) Mode 2 – Mode shape

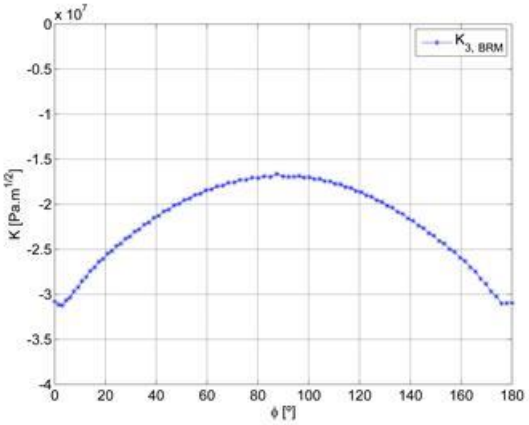

(e) Mode 3 – Modal stress intensity factor

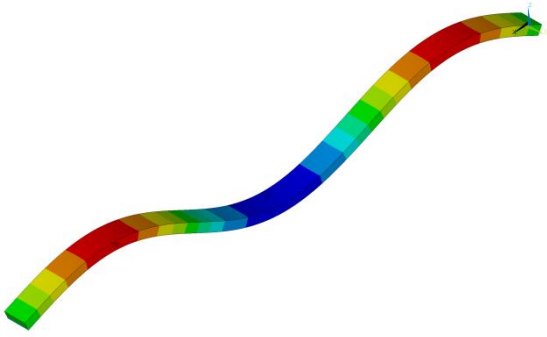

(f) Mode 3 – Mode shape

Figure 5.7 - Modal stress intensity factors through the crack front and corresponding mode shapes (cont.).

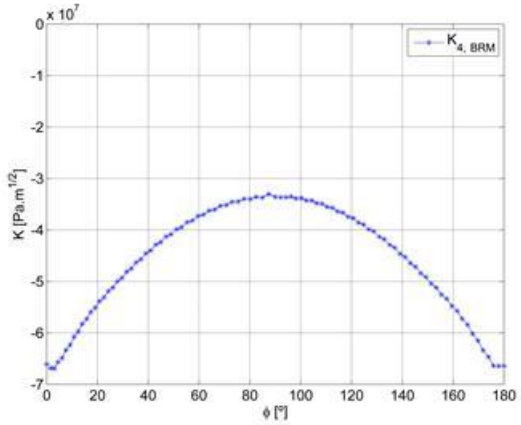

(g) Mode 4 – Modal stress intensity factor

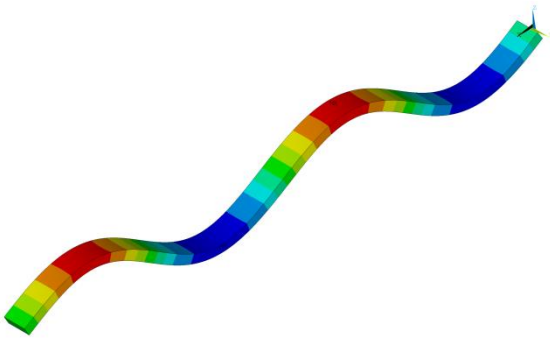

(h) Mode 4 – Mode shape

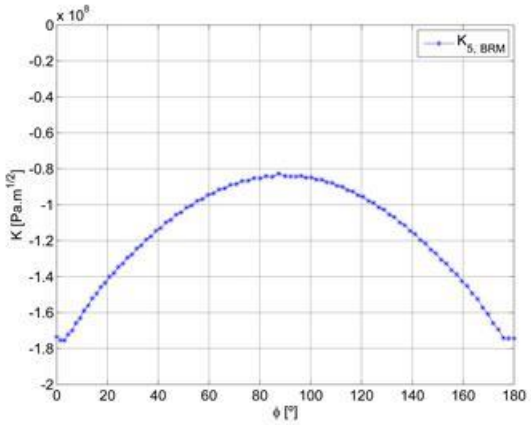

(i) Mode 5 – Modal stress intensity factor

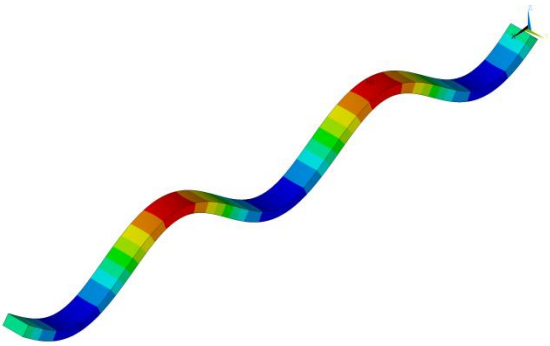

(j) Mode 5 – Mode shape

Figure 5.7 - Modal stress intensity factors through the crack front and corresponding mode shapes.

It should be noted that the modes of vibration 1, 3, 4 and 5, present deformations that induce compressive stresses at the bottom face of the beam, in the section of the crack, and the consequent closure of it. That leads to negative modal stress intensity factors, K_1, K_3, K_4 and K_5, throughout the entire crack front.

The numerical models were then analysed concerning static loading. In this case the only static loading considered was the structure's self-weight, which originates the crack opening. The corresponding value of K_{sta} is presented in Figure 5.8.

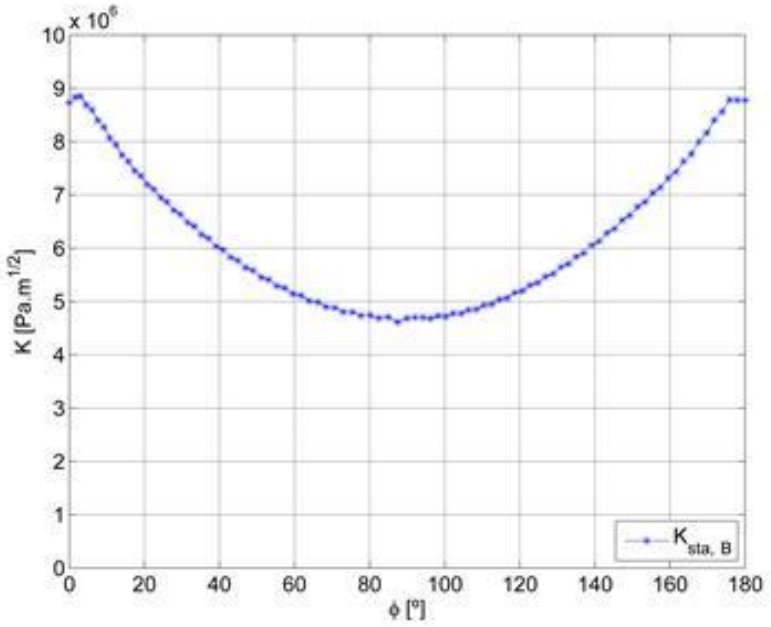

Figure 5.8 - Static stress intensity factor through the crack front.

The VCCT method (*virtual crack closure technique*) (Krueger, 2002) was programmed in APDL language and implemented in ANSYS, allowing for the calculation of the presented values of *K*.

5.3.4 Global response

5.3.4.1 Loading scenario

The dynamic loading considered was a load of 100 kN, vertical and descendent, moving at 250 m/s over the beam. Considering the speed of the load, it can be considered as a highly impulsive action.

The contribution of the 5 vertical vibration modes present in the frequency range under analysis (0 Hz to 100 Hz) was considered. A constant modal damping ratio of $\xi = 0.25\%$ was adopted for all the referred modes of vibration.

When solving the numerical problem, an increment time step of $\Delta t = 0.0001$ s and a period of free vibration after loading of approximately 5 seconds was considered, corresponding to a total of 50 000 time steps.

5.3.4.2 Time history of K obtained with model BRM

The time history of K, was obtained in the model BRM, based on the concept of modal stress intensity factors and in the new proposed methodology, described in section 5.2. The process was, thus, composed by the following steps:

- Static analysis of the model and obtaining K_{sta} (ANSYS);
- Modal analysis of the model and obtaining K_j (ANSYS);
- Determination, in MATLAB, of the time histories of the modal coordinates, $Y_j(t)$, using the Newmark method, applied to each mode of vibration; the following input information is previously provided to the MATLAB routine:
    - Modal properties extracted from the BRM model: modal frequencies, ω_j, modal masses, m_j and modal displacements on the loads path nodes, $\overline{\Phi_j}$;
    - Modal damping ratios, ξ_j;
    - Information about the loading: load magnitude, speed and path nodes;
- Calculation of the time history $K_{total}(t)$ and of the several modal contributions, $K_j \cdot Y_j(t)$.

The contribution of the static component and of the different modes of vibration to the total response, expressed as $K(t)$, at point B, is represented in Figure 5.9.

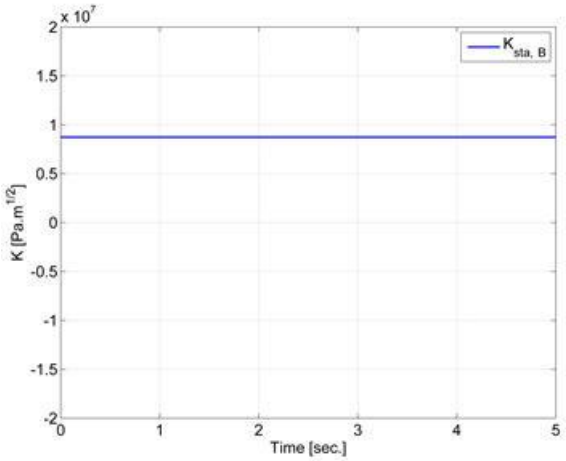

(a) Static

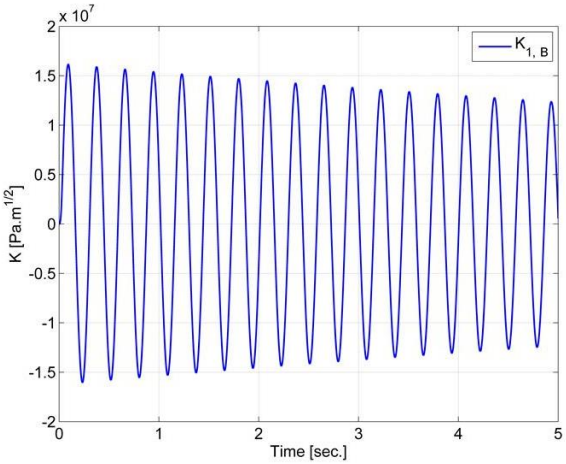

(b) Mode 1

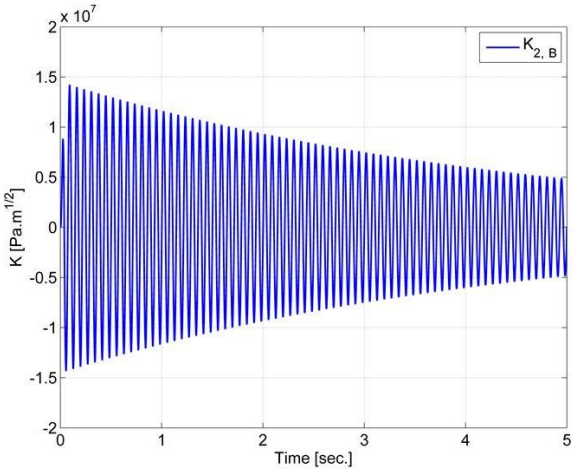

(c) Mode 2

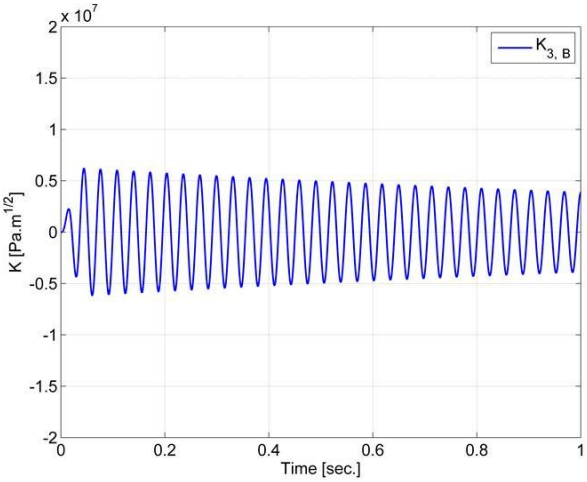

(d) Mode 3

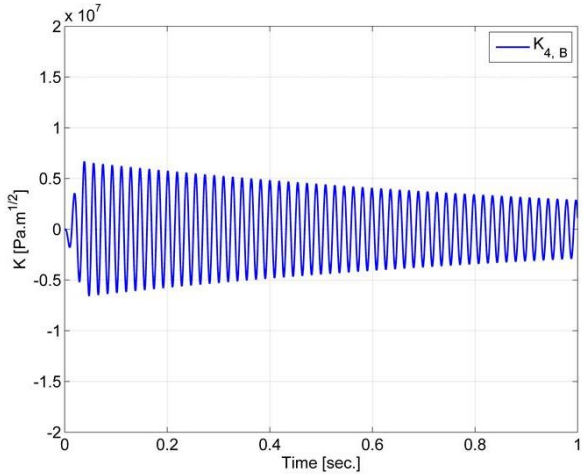

(e) Mode 4

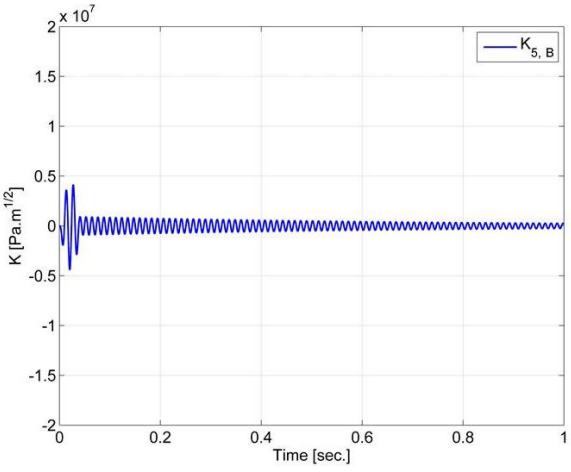

(f) Mode 5

Figure 5.9 - Contribute of the static loading and of the different modes of vibration to $K_{total}(t)$ at point B.

As it can be observed, the 5 modes of vibration contribute to the dynamic response, with the 1st mode having a major contribution, while the 5th mode has the smallest contribution. The corresponding total responses, at points A and B, are presented in Figure 5.10. After application of expression (5.11) the total value of $K(t)$ is limited to positive values.

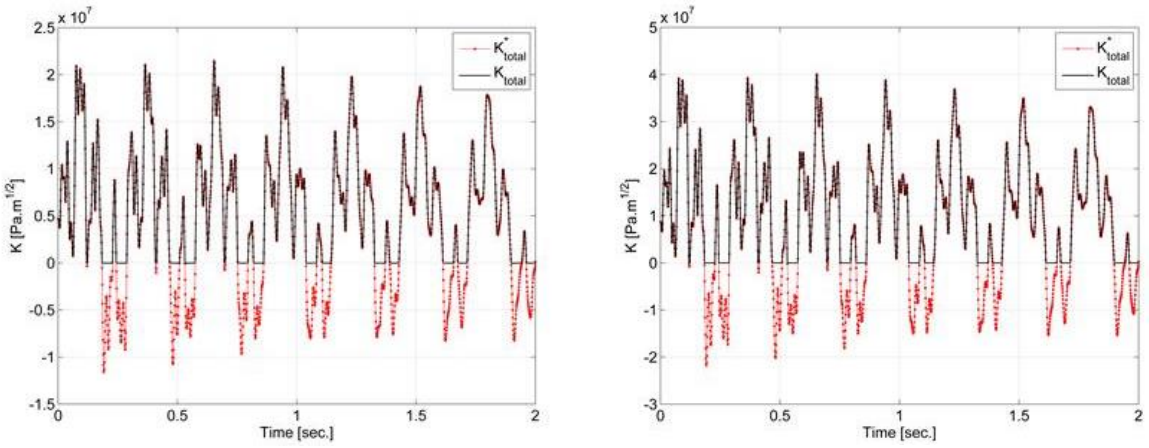

(a) (b)

Figure 5.10 - Total response: $K_{total}(t)$ and $K^{*}_{total}(t)$: (a) at point A and (b) at point B.

In order to underline the computational efficiency of the proposed method, the calculation of the stress intensity factors was performed by the conventional way, which is solving the dynamic problem and computing the stress intensity factor for each time step. The results are identical, as can be observed on Figure 5.11. Nevertheless, when the computing time of both methodologies is compared, it becomes evident that the proposed methodology is more efficient. This advantage is even higher if different loading scenarios have to be considered, because the proposed methodology only requires the recalculation of the modal coordinates' time histories.

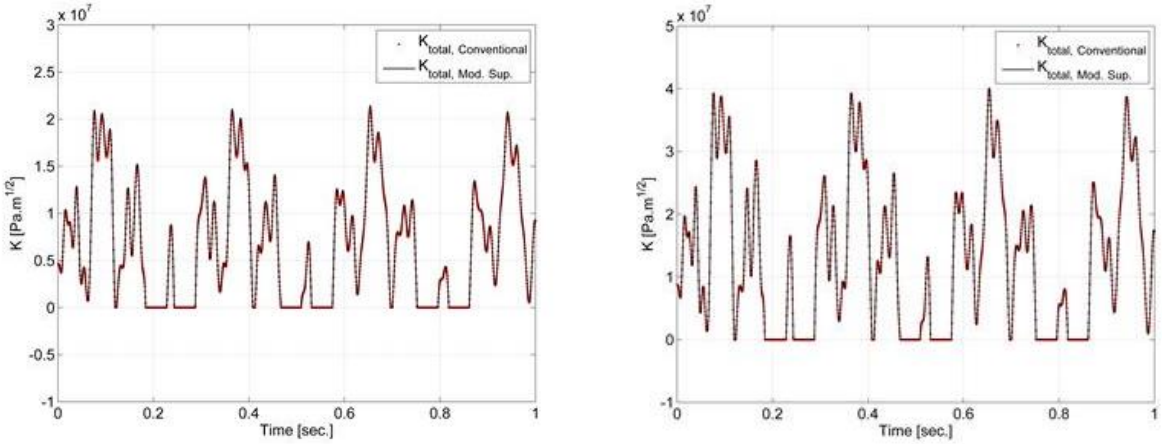

(a) (b)

Figure 5.11 - Results comparison between novel and conventional methodologies: (a) at point A and (b) at point B.

Finally, it was intended to demonstrate the applicability of the finite element model built and of the VCCT method to obtain *K*. Thus, *K*(*t*) was computed using the well-known expressions of Newman Jr. and Raju (1981). As an input, the stress time history, $\sigma(t)$, at the bottom fibre of the section containing the crack was used. Care was taken in using the stresses obtained far from the crack, avoiding the inherent stress concentrations, as the use of nominal stresses is an applicability condition of the expressions of Newman and Raju. The results, almost identical (Figure 5.12) confirm the suitability of the models and of the methods used.

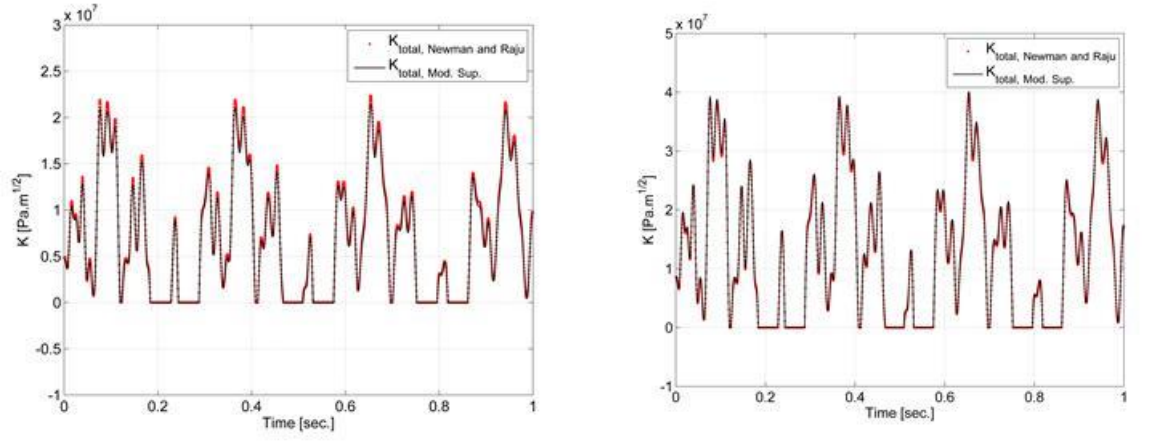

(a) (b)

Figure 5.12 - Results comparison between the novel methodology and the application of the expressions of Newman and Raju: (a) at point A and (b) at point B.

5.3.4.3 Time history of K obtained with model SSM

The SSM model was also analysed using the proposed methodology. In this case, as submodelling was required, the procedure implied the following steps:

- Definition of the boundary nodes of the local model, built with brick elements;
- Static analysis of the global model, built with shell elements; extrapolation of the displacements field from the global model to the boundary nodes of the local model; calculation of the local model response to those imposed displacements and extraction of the correspondent K_{sta} (ANSYS);
- Modal analysis of the global model; for each mode of vibration obtained, extrapolation of the corresponding displacements field to the boundary nodes of the local model and calculation of the response of this latter model to those imposed displacements; extraction, for each mode, of the corresponding K_j from the local model (ANSYS);
- Determination, in MATLAB, of the time histories of the modal coordinates, $Y_j(t)$, using a procedure analogous to the described at section 5.3.4.2;
- Calculation of the time history $K_{total}(t)$ and of the several modal contributions, $K_j \cdot Y_j(t)$.

The response obtained with the SSM model, in terms of $K(t)$ was compared with that obtained with the BRM model (Figure 5.13).

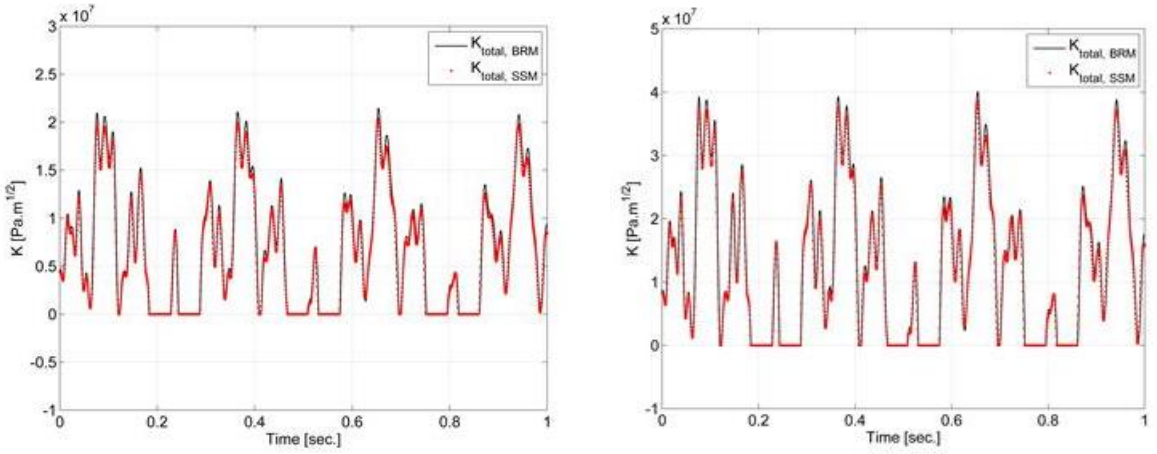

(a) (b)

Figure 5.13 - Results comparison between the BRM and SSM models: (a) at point A and (b) at point B.

As it can be observed, the results are almost identical. The suitability of the application of submodelling techniques in this context is, thus, stressed.

5.4 CONCLUDING REMARKS

The problem of structural fatigue damage, in steel components, can be studied accurately with Fracture Mechanics concepts. Nevertheless, in the Civil Engineering context, this approach is not generally used, due to the different dimensional scales of the structures and of the details prone to fatigue damage. That scale discrepancy is detrimental to the execution of the numerical dynamic analysis required.

The current Chapter presented a methodology that simplifies the application of Fracture Mechanics in the context of dynamic analysis of structures using the modal superposition method. This new approach for obtaining time histories of the stress intensity factor was proposed and validated with a simple example. It drastically reduced the number of calculations involved for obtaining the time history of K, since it implied solving the structure only for the static load and for each one of the modes of vibration associated with it. Moreover, it allows obtaining explicitly the contributes of static loading and of each mode of vibration to the total value of $K(t)$. Finally, the methodology showed to be compatible with the application of submodelling techniques, situation where the different advantages presented are kept or even expanded.

Due to the good results and validation achieved, the methodology was later employed in the fatigue crack propagation analysis of a detail of a real structure. Those results are presented and discussed in Chapter 7.

Chapter 6

FATIGUE DAMAGE MONITORING OF THE BRIDGE OF THE NEW RAILWAY CROSSING OF RIVER SADO

6.1 INTRODUCTION

As already mentioned before, the problem of fatigue is very common in steel and composite bridges and in railway bridges in particular (Cremona et al., 2013, Clubley and Winter, 2003, Cho et al., 2001, Leander et al., 2010). As traffic loads tend to increase and bridges degrade, the problem is even more relevant, becoming one of the main topics of investigation as illustrated by an increasing number of international research projects, such as Details (Chellini et al., 2009), Sustainable Bridges (Cremona et al., 2007), FADLESS (Lippi et al., 2011) and Mainline (Paulsson, 2013).

Since fatigue damage is localised at critical details of the structures, the most usual way for the infrastructure managers to assess it is by periodic or extraordinary bridge inspections (Righiniotis, 2006, Herter, 2012). When fatigue damage is detected, the actual condition of the bridge is often assessed by load tests and short term monitoring (Leander et al., 2010, Lippi et al., 2011, Nagy et al., 2013, Zhou et al., 2013, Caglayan et al., 2009, Brencich and Gambarotta, 2009, Marques et al., 2009, Stamatopoulos, 2013, Srinivas et al., 2013, Fu and Zhang, 2011). In some cases, the short term monitoring is also performed during the subsequent repair, strengthening and/or replacement activities (Rodrigues et al., 2012) or even later, to assess the

improvements resulting from the retrofitting/enhancement measures (Andersson et al., 2013). The data obtained during the short term monitoring of fatigue prone structures is analysed and, commonly, used to extrapolate the results for longer periods of time (Meneghetti et al., 2012, Zhou, 2006).

Nevertheless, it is not economically feasible to perform interventions in all bridges, at the same time. Their advanced assessment (structural health monitoring - SHM), by means of long-term monitoring systems, could help to prioritise and to schedule inspections and interventions (Orcesi and Frangopol, 2011, Wong, 2012). Advances in technology, such as the development of industrial computers, the wireless communication systems (Picozzi et al., 2010, Garcia-Palacios et al., 2012, Meyer et al., 2010) and the enhancement of all types of electronic transducers, helped increasing the number of applications of long-term monitoring systems to critical structures worldwide (Magalhães et al., 2008, Cross et al., 2013). The benefits of structural health monitoring are quantifiable (Orcesi and Frangopol, 2013) and, in some countries, the use of long-term monitoring systems is even being addressed by regulations (Moreu et al., 2012). Most of the long-term monitoring systems are focused on detecting damage events (Cury and Crémona, 2012, Sun and Yan, 2012). As the objectives of the SHM become more ambitious, towards damage localization (Benedettini et al., 2012, Whelan and Janoyan, 2010, Dilena and Morassi, 2011, Yao and Glisic, 2012, Glisic and Inaudi, 2012), damage severity assessment (Santos et al., 2013) and lifetime prediction update, the complexity of the data analysis algorithms also increases.

The long-term monitoring of the global dynamic properties of the structures is one of the most common methods to try to detect the structural damage (He et al., 2012, Rahmatalla et al., 2014, Caglayan et al., 2011, Magalhães et al., 2012b, Ko et al., 2002, Magalhaes et al., 2012). In this context, some attempts were made in the past to replace the installation of sensors in the bridge by the utilization of instrumented test vehicles (Van Bogaert, 2012).

An alternative approach is to use a long-term monitoring system that measures strain at a number of details considered of relevance in order to estimate cumulative damage (Guo and Chen, 2013, Ye et al., 2012, Ni et al., 2012, Guo and Chen, 2011, Liu et al., 2010) or even to detect it (Phares et al., 2013, Yao and Glisic, 2012).

Some structures, as the Tsing Ma Bridge, due to their relevance and scale, have long-term monitoring systems that combine the monitoring of their global dynamic behaviour with the local monitoring of strains (Duan et al., 2011, Ni et al., 2008, Chan et al., 2006, Li et al., 2012).

A structural health monitoring system should not only be able to perform damage quantification, but also to relate the damage with the external actions that originate it. This is the reason why the traffic characterization is a feature of paramount importance in a long-term monitoring system to be implemented either in roadway or railway bridges (Guo et al., 2012). It allows to understand the type of traffic that has the biggest impact on the structural degradation and to forecast traffic evolution (Fu and You, 2011). The measurement of real traffic also allows avoiding the use of conservative standard load models, when assessing damage evolution and planning inspections frequency (Ottosson et al., 2012a).

The Weigh-In-Motion (WIM) systems try to assess the vehicles geometry and loading by interpreting measurements performed directly in the railway track (Meli and Pugi, 2013). Some common WIM technologies are: i) rail shear measurements using shear strain gauges welded or bonded to the neutral axis of the rail (Julián Valerio, 2005); ii) rail shear measurements, achieved by means of a circular slot drilled on the neutral line of the rail (Esveld, 2001); iii) rail bending measurements (Sekuła and Kołakowski, 2012); iv) instrumented rail pads (SensorLine, 2008). An alternative approach, the Bridge Weigh-In-Motion (B-WIM) uses the structural response of the bridge to compute the vehicles geometry and axles load, after a proper calibration process (Karoumi et al., 2005, Liljencrantz et al., 2007, Pimentel et al., 2008, Seo et al., 2013).

As a complement to the SHM systems, in order to forecast the structural behaviour/degradation, due to fatigue, or others, the development of well-calibrated numerical models of the structure is considered a very important step (Vincenzi et al., 2012, Chen et al., 2011). The calibration of a numerical model may be performed with experimental data resulting from the long-term monitoring system (Gomez and Feng, 2012, He et al., 2008) or from a short term one (Ribeiro et al., 2012, Schlune et al., 2009).

As underlined by Guo et al. (2012), the numerical model also plays an important role by allowing to extend the SHM results to the fatigue assessment of non-monitored details. Methodologies based on the influence line concept and that allow achieving those objectives are presented in (Orcesi and Frangopol, 2010) and (Zeng et al., 2012). Other alternative approach explored in the past, was to assume constant relations between the maximum stresses in different

details of the bridge, and use those relations as scale factors to convert the damage measured at instrumented details into damage in the remaining points of the structure (Hakola et al., 2012). Finally, in other cases, the simulation of numerical models with real traffic was performed (He et al., 2008).

The above mentioned methodologies lack, in some cases, accuracy, and in other cases are not computationally efficient. That is the reason why, in the past, tracking fatigue damage in all critical details of long-span railway bridges was not achievable in an efficient and economical way.

This Chapter presents a new methodology for the real time fatigue assessment of railway bridges, combining an affordable long-term monitoring system and minimal computer resources. This methodology overcomes the above mentioned limitations and allows computing the fatigue damage at the critical details of the structure, based on the monitored characteristics of traffic and on a detailed numerical model of the structure, adequately calibrated/validated.

This methodology is applied to the bridge of the new railway crossing of the river Sado, in Portugal. This case study offered the characteristics needed for an adequate validation of the methodology: it is a long span railway bridge with complex structure, with several details prone to fatigue damage and bearing a mix of heavy freight traffic and relatively high speed passenger trains. The bridge is described in the next Section.

6.2 BRIDGE OF THE NEW RAILWAY CROSSING OF RIVER SADO

6.2.1 Context

The bridge of the new railway crossing of river Sado is a composite, bowstring bridge, located at the Lisbon-Algarve railway line, in Portugal (Figure 6.1).

(a) (b)

Figure 6.1 - Bridge of the new railway crossing of the river Sado: (a) location (REFER, 2011) and (b) overview (REFER, 2010).

This structure, a reference in the Portuguese Railway Network, was designed by the companies *GRID – Consultas, Estudos e Projectos de Engenharia* and *Greisch Ingénierie* (Reis and Lopes, 2009) and it is part of a wider investment, named Alcácer Bypass, considered as a priority by the Strategic Framework for the Railway's Sector in Portugal (MOPTC, 2006). It consists of a 29 km long alternate railway path, between the Pinheiro Station and the km 94 of the above mentioned Lisboa-Algarve line (Figure 1.2). Its main objectives are:

- The capacity improvement of the sea port of Sines, by making faster its connection to the logistic hubs of Poceirão and Elvas, to the sea ports of Setúbal and Lisbon and to the future Lisbon-Madrid High Speed Railway line (REFER, 2010);
- The promotion of interoperability of Portuguese railway network with the European transports network, integrating the Sines/Algeciras-Madrid-Paris axis, Priority Project number 16 of the Trans-European Transport Network (EC, 2011, IMTT, 2011);
- The reduction of travel time in the Lisbon-Algarve connection and the corresponding transfer of passengers from road to railways;

- The reduction of railway's operation costs associated with maintenance (Martins, 2009).

The bridge reflects the general requirements of the Alcácer Bypass: it is prepared for freight trains with up to 25 tons per axle and for conventional and tilting passenger trains with speeds of 200 km/h and 220 km/h, respectively. In the future, some adjustments at the track level, will allow the maximum speeds to be 220 km/h for conventional and 250 km/h for tilting passenger trains (Martins, 2009).

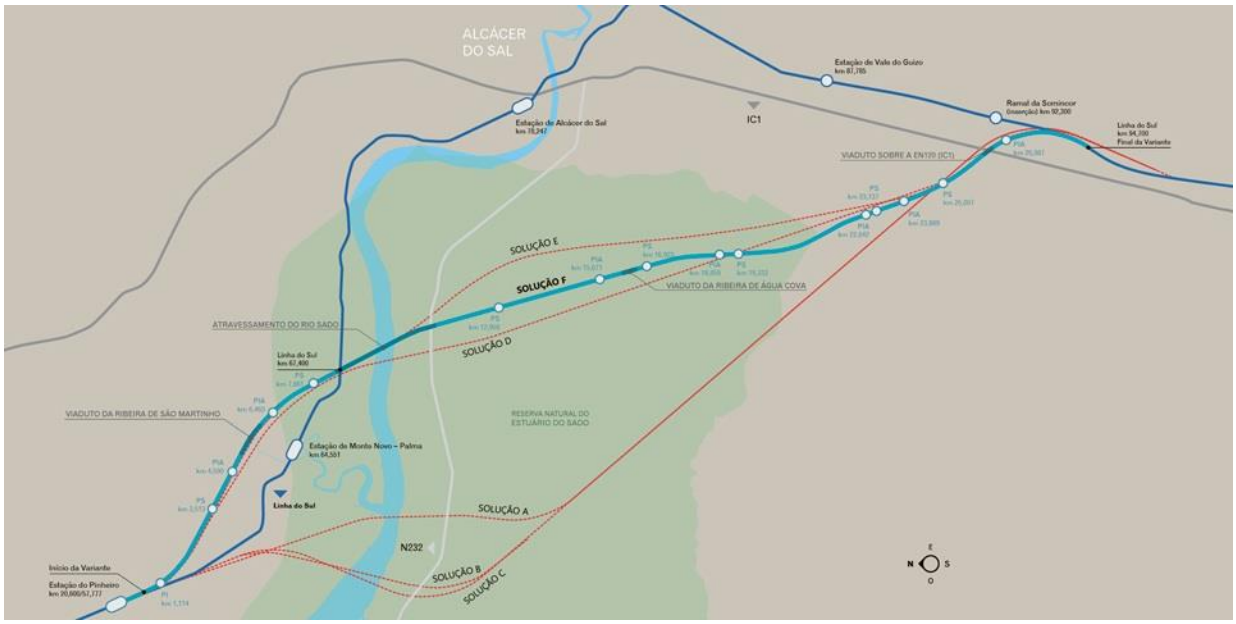

Figure 6.2 - Alcácer Bypass: different routes studied and final commissioned route (solution F) (REFER, 2010)

Still in this context, it is important to underline the continuous and consistent increase in annual throughput in the sea port of Sines (Figure 6.3), over the last years (Porto de Sines, 2013). Official forecasts pointed to the duplication of these values between 2010 and 2015, which indicates that also the traffic over the bridge will increase in the same period, together with the potential for fatigue damage.

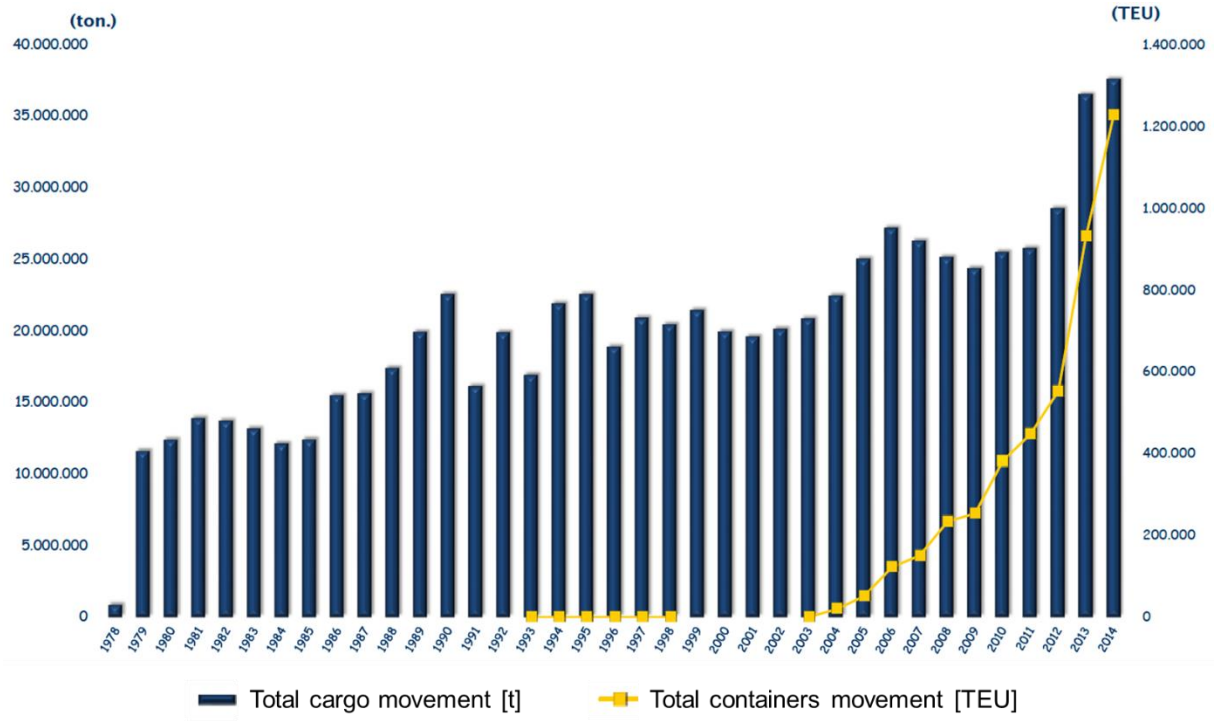

Figure 6.3 - Annual cargo movement in the sea port of Sines (Porto de Sines, 2015)

6.2.2 Description

6.2.2.1 Structure

The bridge has 3 continuous spans (160 m each) and a total length of 480 m. It is part of a longer structure, which includes the North access viaduct (1115 m length) and the South access viaduct (1140 m length). Either the bridge and access viaducts are prepared for hosting 2 tracks.

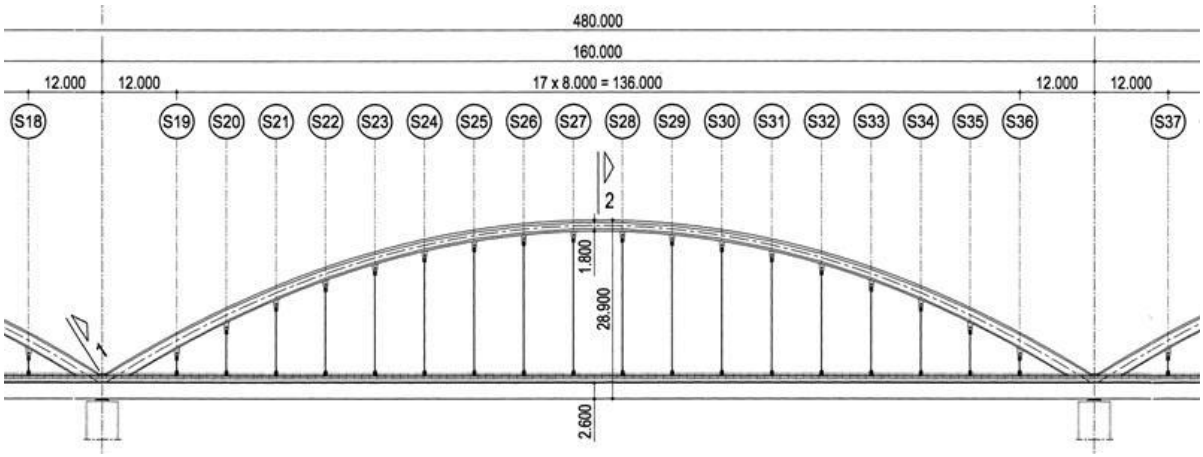

Figure 6.4 - Side elevation of the 2nd span of the bridge (GRID et al., 2006).

The bridge is suspended from 3 arches that are centred with the structure. Each arch connects to the corresponding span of the deck by 18 hangers (Figure 6.4). The hangers have a circular section with 200 mm diameter and are 8 m apart from each other.

The deck is composed by a concrete slab laid over a trapezoidal steel box (Figure 6.5). The concrete slab has a total width of 15.85 m and a maximum thickness of 43 cm (Figure 6.8). The steel box, U-shaped, has tilted webs and a total height of 2.6 m. The bottom flange, 6.2 m wide, varies in thickness from 100 mm over the bearings and 45 mm at the mid spans. Both top lateral flanges have 1.5 m width and 35 mm to 50 mm thickness. The central top flange, 1.5 m wide, has thicknesses ranging from 35 mm to 100 mm. This central flange presents a longitudinal reinforcement, at its bottom (350 mm vs. 35 mm or 350 mm vs. 45 mm). Finally, the tilted webs present constant 30 mm thickness through the entire length of the deck.

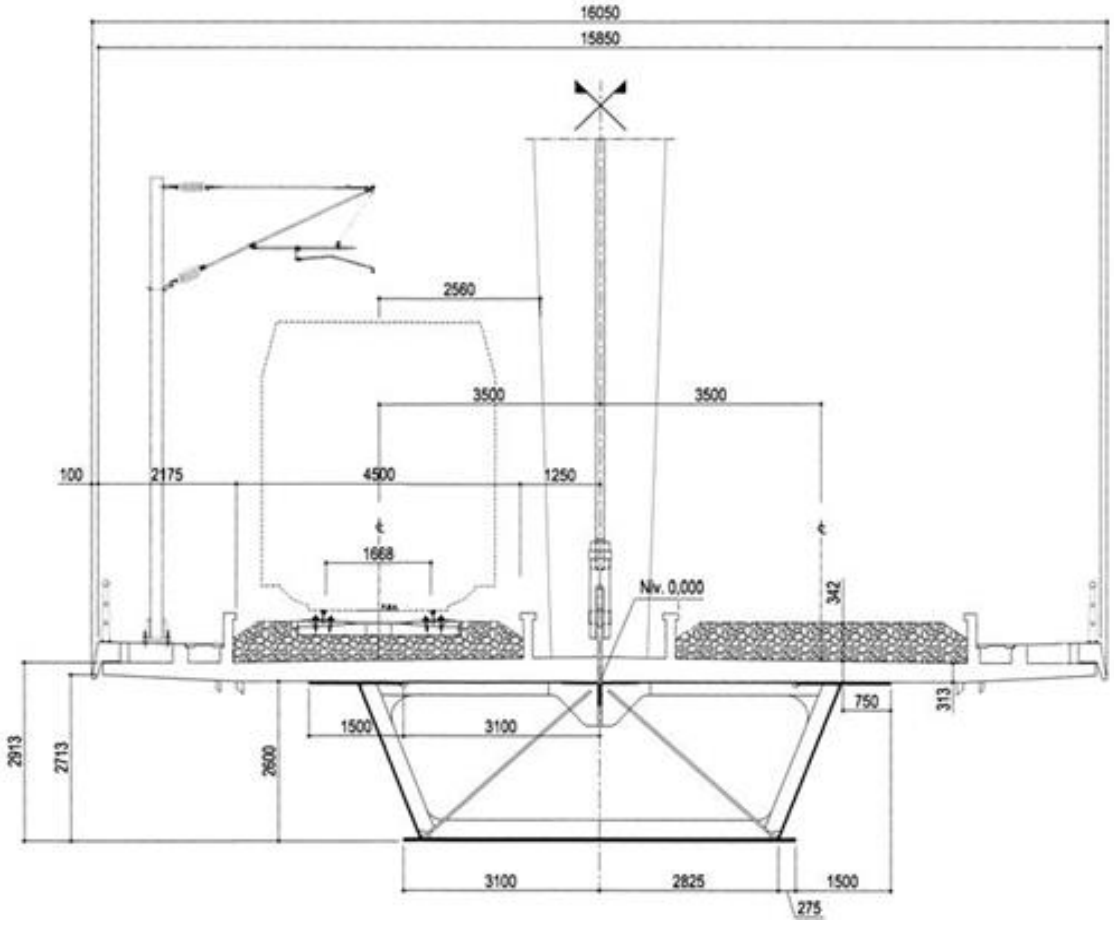

Figure 6.5 - Cross section of the deck (GRID et al., 2006).

At each hanger-to-deck connection, a steel diaphragm and two diagonal strings transfer the suspension loads from the hangers to the deck. Diagonals are 600 mm wide and have a thickness

of 35 mm. In order to enhance its fatigue endurance, the intersection between each diagonal and the bottom flange of the deck is achieved by means of a cast steel special piece (Reis and Lopes, 2009). At its top connection, the diagonal hangs from a special gusset, 40 mm thick (Figure 6.6).

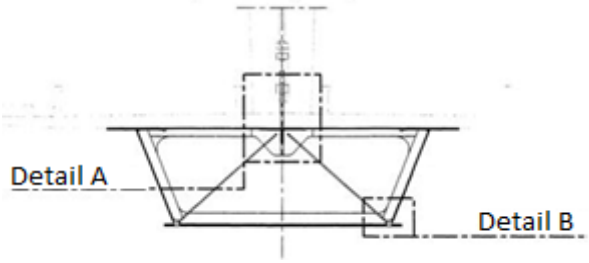

(a) Location of details (GRID et al., 2006)

(b) Diaphragms and diagonals

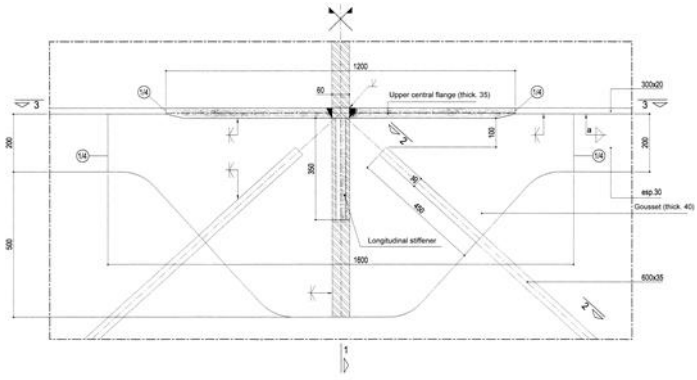

(c) Detail A – Design (GRID et al., 2006)

(d) Detail A - Construction

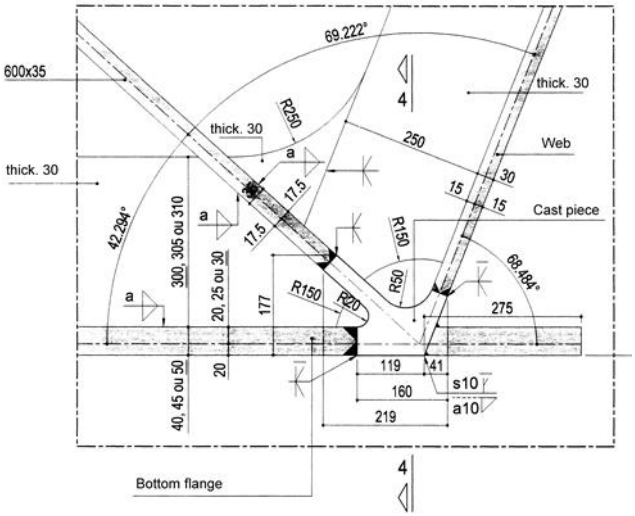

(e) Detail B – Design (GRID et al., 2006)

(f) Detail B - Construction

Figure 6.6 - Diaphragms of the deck: typical details.

Above the concrete slab, the hanger-to-deck connection can be considered a spherical hinge (Figure 6.7). The bottom of each hanger is threaded to a cast steel piece specially conceived for that purpose.

Figure 6.7 - Spherical hinge at hanger to deck connection.

The concrete slab thickness ranges from 0.20 m at the edge and 0.43 m at the bridge's plane of symmetry (Figure 6.8). The inner ballast-guard beams present 0.73 m height whilst the outer ones present 0.8 m height. The footways, edge beams and catenary bearings are all laid over the slab, as well as a triple waterproofing cap.

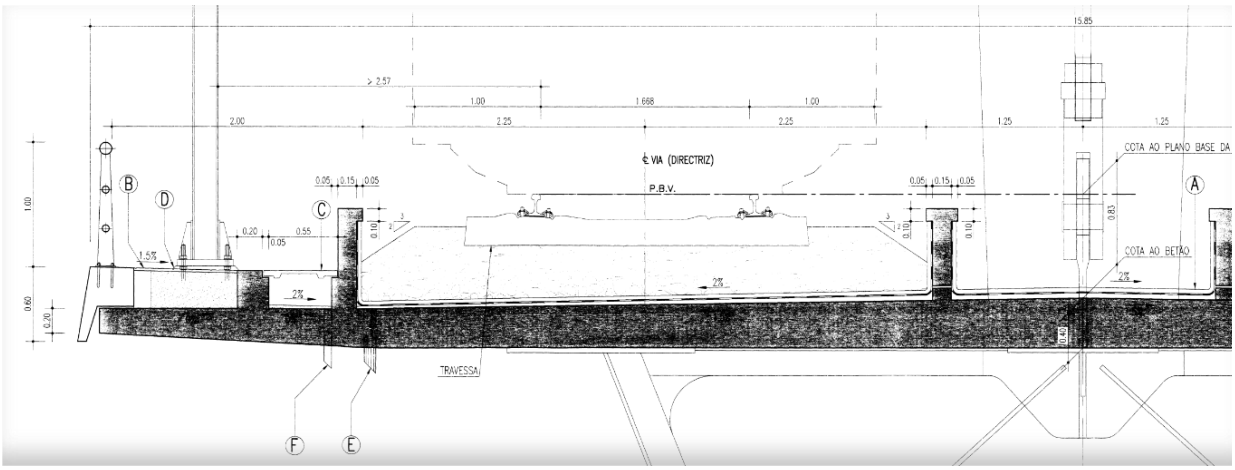

Figure 6.8 - Concrete slab (GRID et al., 2006)

The three parabolic arches have a total height of 25.4 m and hexagonal cross section with variable height-to-width ratio (Figure 6.9). The maximum height (2400 mm) and minimum width (1490 mm) are observed at the arches' ending points, while the minimum height (1800 mm) and maximum width (3200 mm) appear at the higher section.

The arches' top and bottom flanges have 60 mm to 120 mm thicknesses. The arches' webs are 80 mm to 120 mm thick.

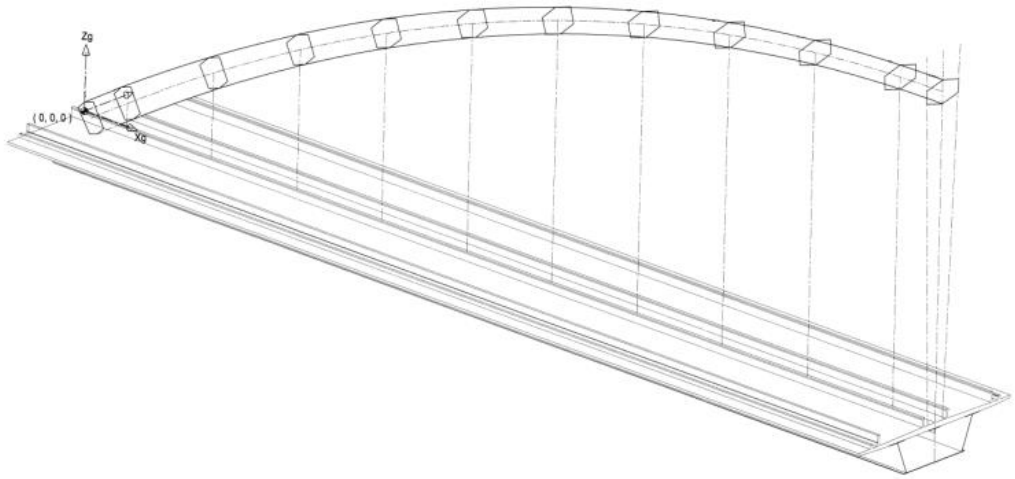

Figure 6.9 - Arches: cross section variation (GRID et al., 2006).

The hanger-to-arch connection is performed by means of an eye-plate with a spherical hinge and a special cast steel piece. At these intersection points, the arches present transverse diaphragms that increase the overall stiffness and limit section distortion (Figure 6.10).

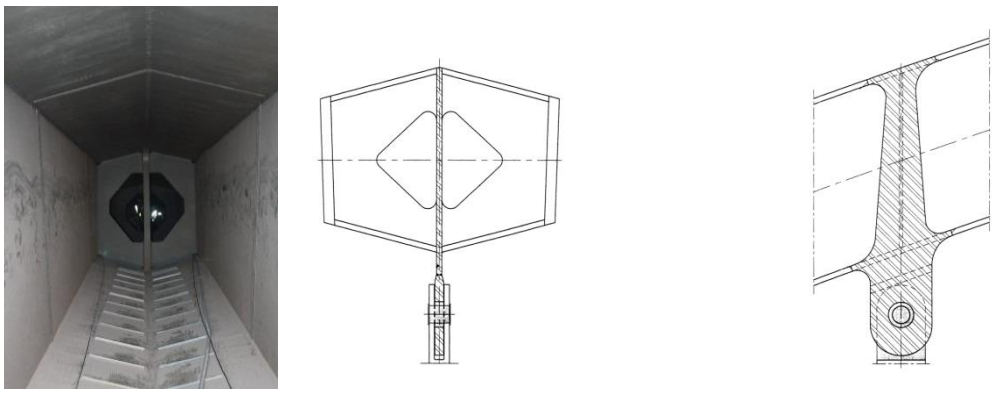

(a) (b)

Figure 6.10 - Arches: (a) inside view and (b) diaphragms and stiffeners (GRID et al., 2006).

Concrete partially fills the extremities of the arches at the bridge entrance points. No concrete is present at the arches extremities over the intermediate piers of the bridge. At those points access to the interior of the 3 arches is provided for maintenance and/or inspection activities (Figure 6.11).

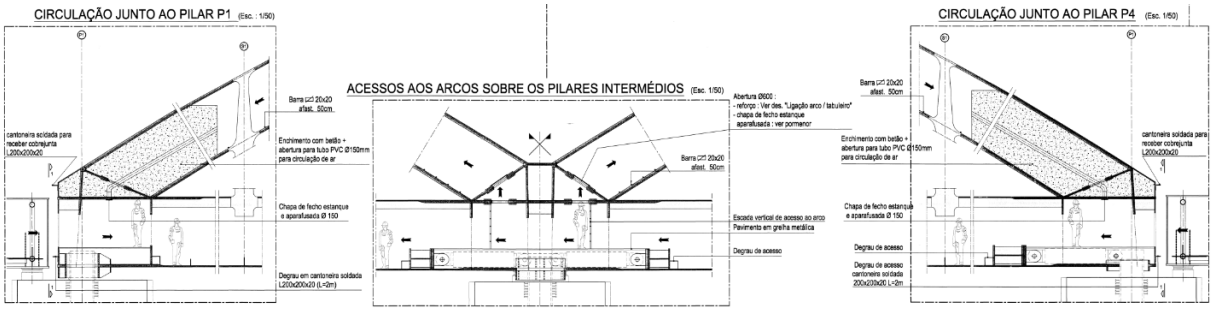

Figure 6.11 - Inspection access to the interior of the arches (GRID et al., 2006).

It should be underlined that under the extremities of the arches the steel deck presents vertical stiffeners with thicknesses up to 120 mm (Figure 6.12).

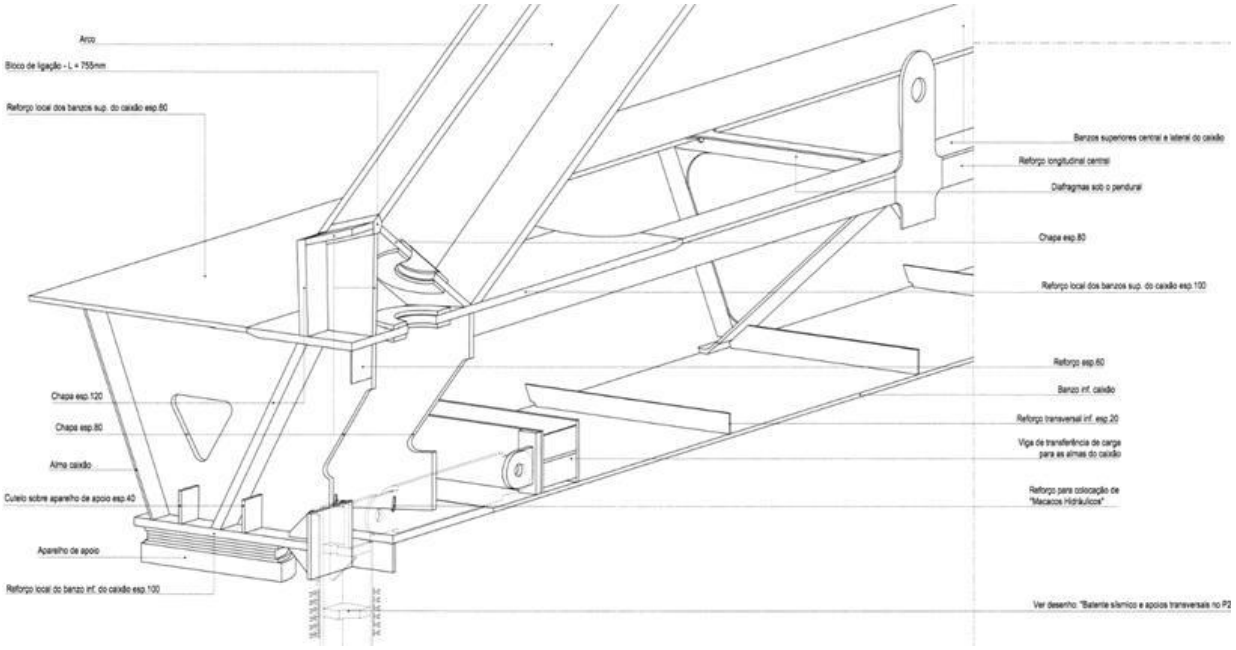

Figure 6.12 - Vertical stiffeners bellow the arches' extremities (GRID et al., 2006).

The hangers have a circular section with 200 mm diameter.

The 4 piers of the bridge, named P1 (at the North), P2, P3 and P4 (at the South), were built in reinforced concrete. They have a hexagonal hollow section with maximum width and height of 8.5 m and 5.2 m, respectively (Figure 6.13).

All piers are 25 m height and bear over blocks of 9 (P1 and P4) or 12 (P2 and P3) reinforced concrete pilings, with diameters of 2 m (Figure 6.14).

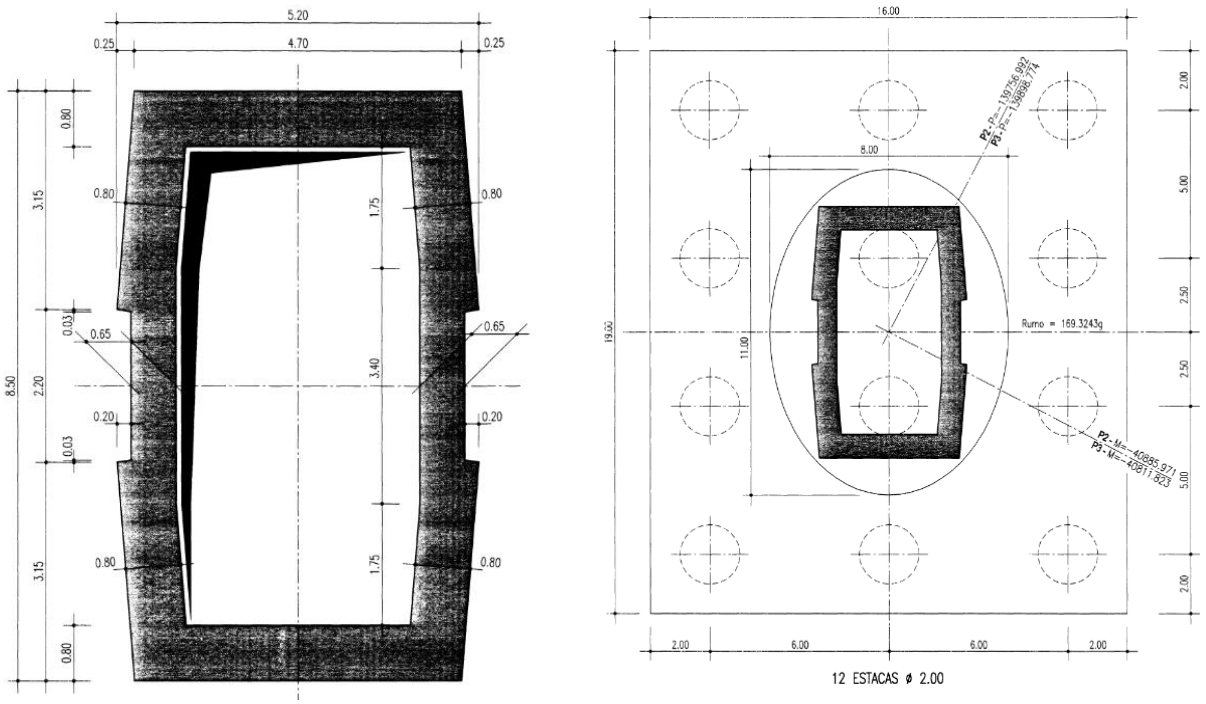

(a) (b)

Figure 6.13 - Cross section of the piers (GRID et al., 2006): (a) floor-plan and (b) floor-plan including foundations.

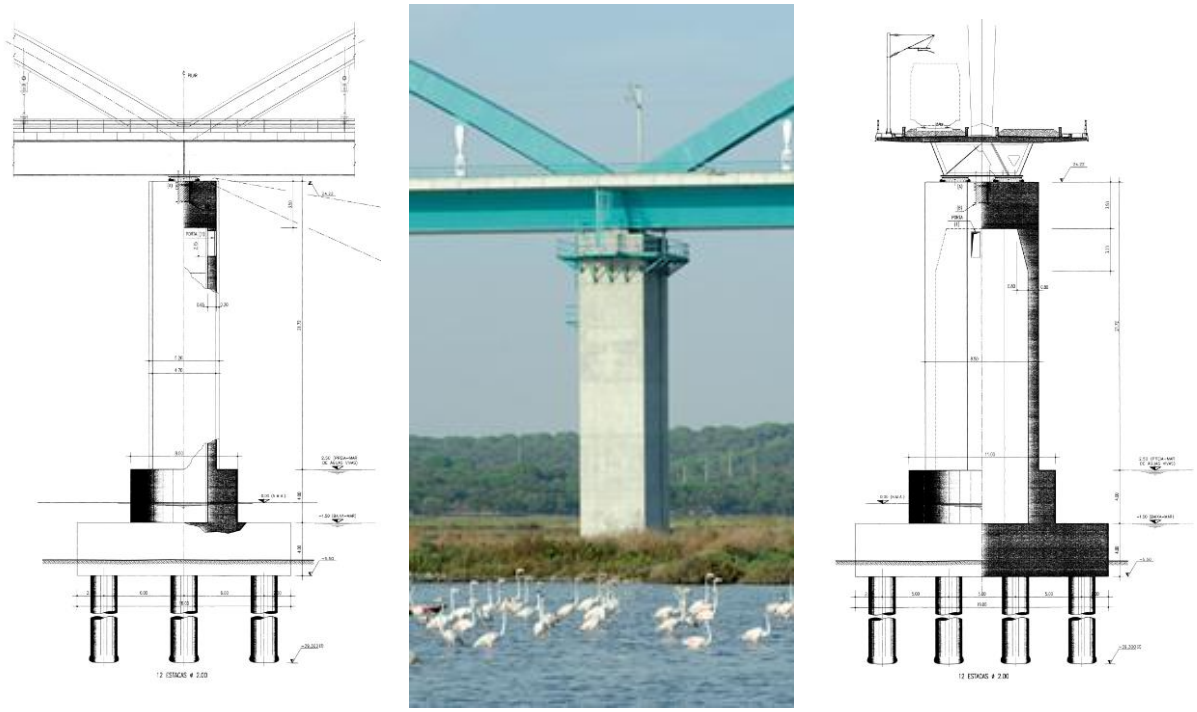

(a) (b) (c)

Figure 6.14 - Pier P2: (a) side elevation (GRID et al., 2006), (b) actual photograph (REFER, 2010) and (c) front elevation (GRID et al., 2006).

Like in the case of the arches, the piers were also provided with access conditions for inspection at their interior, exterior and bearings. Access is provided in different ways: by vertical inspection stairs, by REFER's inspection vehicle and by the interior of the deck (Figure 6.15).

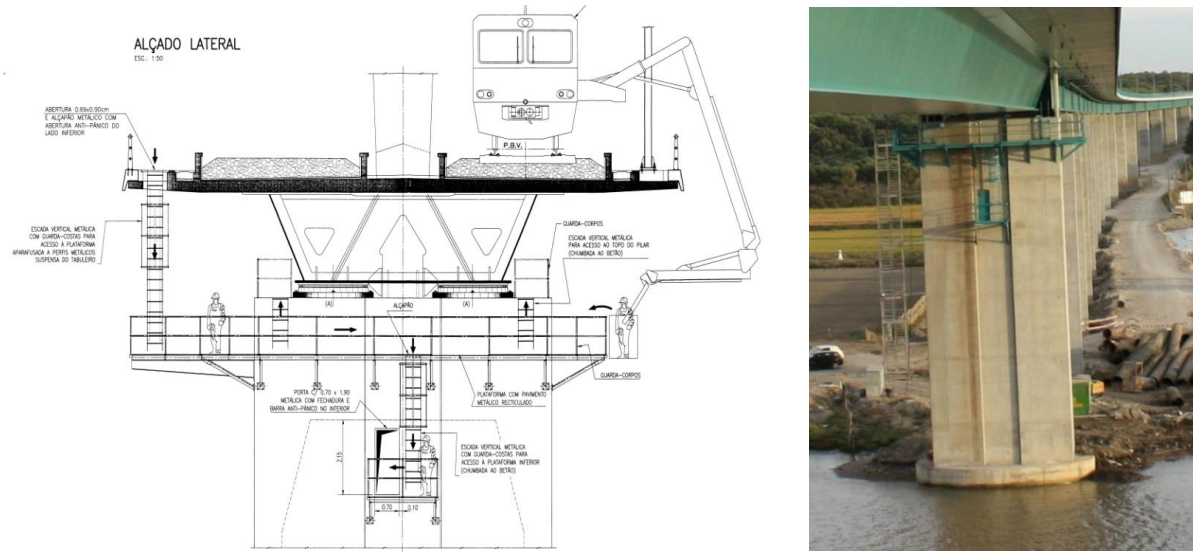

(a) (b)

Figure 6.15 - Platforms for piers inspection: (a) design (GRID et al., 2006) and (b) actual

At each pier, 2 spherical and multidirectional bearings, 4 m apart, are present. The bearings have a circular contact surface, with 920 m diameter at P1 and P4 and 1300 mm diameter at P2 and P3. The transverse movement of the deck is totally restricted at all piers. Longitudinal movement is totally restricted at P1 and conditioned, by seismic dampers, at P2, P3 and P4.

6.2.2.2 Track

The track is built with UIC60E1 rails and monoblock sleepers. Even if the current distance between rails corresponds to Iberian-track gauge, all the sleepers are ready for future migration into Standard-track gauge (Figure 6.16).

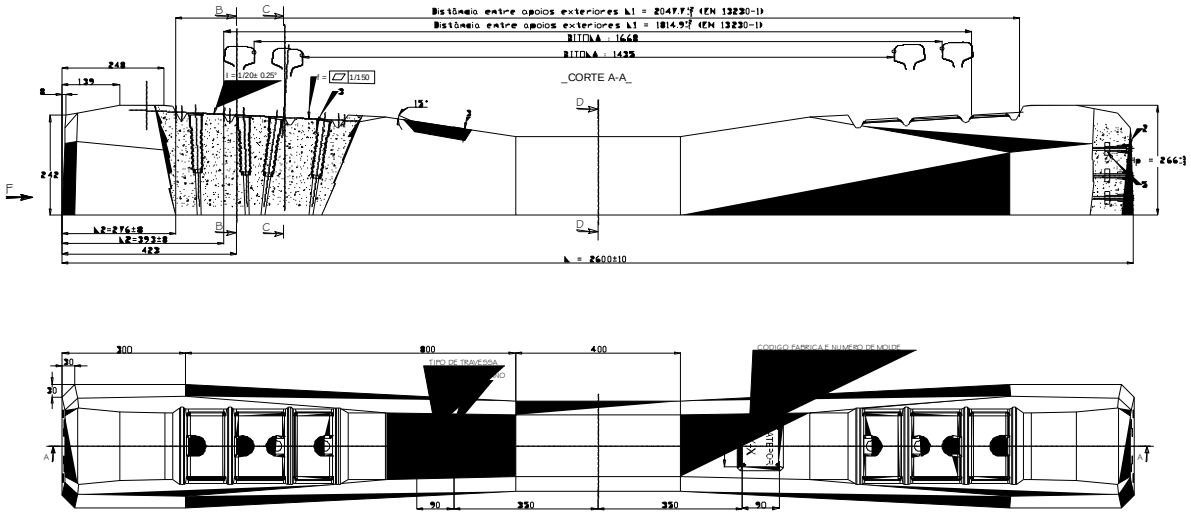

Figure 6.16 - Pre-stressed concrete sleepers (SATEPOR, 2011).

At the upstream side of the bridge, the track is completely operational. At the downstream side, only ballast was put in place, in order to reduce torsion and structural mass asymmetry (Figure 6.17).

Figure 6.17 - Ballasted track located at the upstream side of the bridge.

6.2.2.3 Materials

The steel used in the construction of the bridge (deck, arches, hangers, diaphragms) was mainly of the S355NL grade, a fine grained steel with good characteristics for welding (IPQ, 2009a). The thicknesses involved ranged from 16 mm to 120 mm. Anti-seismic elements were made on S460ML steel (IPQ, 2009b). Finally, the cast steel components (bottom diagonals' connections, hangers' connections) were executed in G20Mn5 grade steel. All the steel plates have a minimum through the thickness quality grade of Z15. In special cases, such as the hangers' connections, a Z35 quality grade was adopted.

Concerning the concrete, different grades were chosen, for each application, on the bridge: C40/50 in the slab, C35/45 in the piers and C30/37 in the foundations. All the reinforcement steel is of A500 NR grade.

6.2.3 Construction process

The construction process of the bridge directly impacts in some mechanical and structural parameters, such as, for example, the extent of concrete cracking on the bridge or the quality of the welding. Due to its complexity, only the main steps are described.

The deck was build up, from several components, over a 180 m platform, sustained on the first 4 piers of the South access viaduct (Figure 6.18). After the conclusion of each 160 m span of the deck, the same span was displaced by a system of incremental pulling (Teixeira Duarte - Engenharia e Construções S.A., 2008).

Figure 6.18 - Span of the bridge being assembled, over the South access viaduct (REFER, 2010).

The elementary units, or dowels, used on the construction of the deck, had 10 m length and were built in 3 parts, in a steel mill, before being transported to the construction site. At the construction site, the 3 different parts of each elementary unit were assembled (Figure 6.19) and painted. An industrial facility, 105 m long and 12 m wide, was specifically developed for that purpose (Figure 6.20).

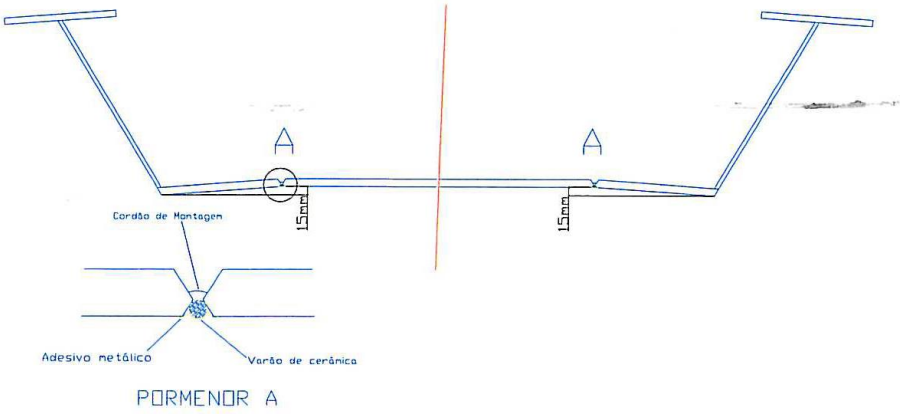

Figure 6.19 - Assembly of the 3 main parts of each elementary unit of the deck (Teixeira Duarte - Engenharia e Construções S.A., 2009).

(a) (b)

Figure 6.20 - Assembly of the parts of the dowels of the deck: (a) webs and bottom flange (Teixeira Duarte - Engenharia e Construções S.A., 2009) and (b) diaphragms and top flanges.

Due to the thicknesses involved, the welding processes were chosen in order to achieve big deployment rates, associated with increased reliability (Nunes and Nicolau, 2009): submerged arc welding, when flat position, and MIG/MAG in the other situations (Figure 6.21). Whenever possible, the MIG/MAG process was complemented by the *Rail Track* system, which allows the semi-automation of the process by aiding the torch movement.

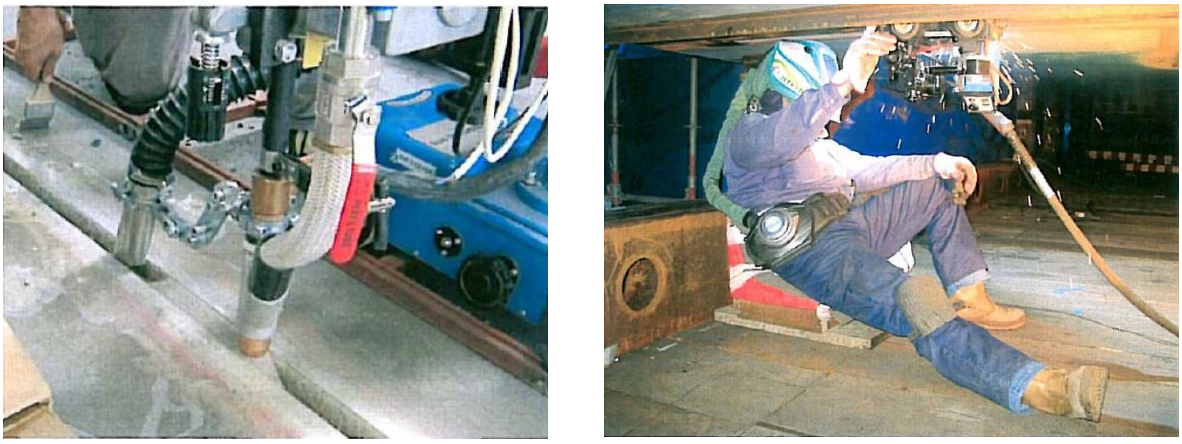

(a) (b)

Figure 6.21 - Welding processes adopted at the construction site (Teixeira Duarte - Engenharia e Construções S.A., 2009): (a) submerged arc welding and (b) MIG/MAG process with *Rail Track*.

The welds shown in Figure 6.21 were always performed after pre-heating the plates to weld. After welding and before painting, all welds were subjected to non-destructive tests (visual

inspection, dye penetrant liquid, magnetoscopy, ultra-sound, X-ray) to assure conformity with the high demanding requirements established.

Levelling (Figure 6.22), positioning (Figure 6.23) and assembly of the different elementary units were performed over the pulling platform.

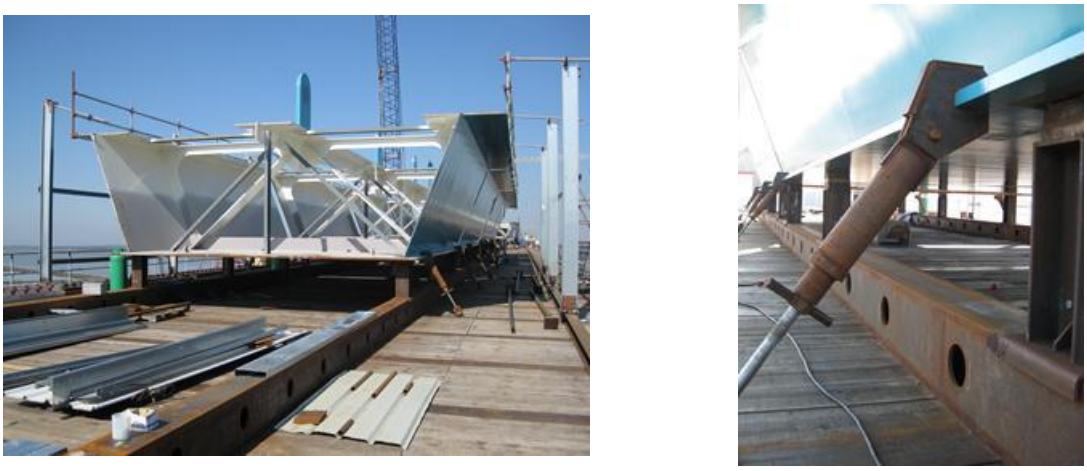

(a) (b)

Figure 6.22 - Dowel's levelling: (a) dowel over the pulling platform and (b) levelling apparatus.

The welds involved in the assemblage of two consecutive dowels were always Z-shaped, avoiding potential single plan weaknesses and/or discontinuities in mechanical properties (Figure 6.23).

(a) (b) (c)

Figure 6.23 - Dowels positioning: (a) complimentary dowels, (b) gap control and (c) apparatus for gap control (Teixeira Duarte - Engenharia e Construções S.A., 2009).

The assemblage of successive dowels was also performed by submerged arch welding and MIG/MAG welding. The protected environment was granted by welding workshops built over the pulling platform (Figure 6.24).

(a) (b)

Figure 6.24 - Welding workshop at the pulling platform: (a) steel box exiting workshop and (b) last dowel.

The incremental pulling system included a hydraulic central, two hydraulic actuators with capacity for 250 tons, each, and a 20 m long launching nose (Figure 6.25).

(a) (b)

Figure 6.25 - Deck's launching: (a) launching platform and (b) launching nose.

To make the deck's launching and posterior arches' erection feasible, 6 temporary piers were built, 2 at each span of the bridge (Figure 6.26). Each temporary pier was composed by 4 external

and 2 central piles of 1.2 m of diameter. The piles were nailed to the river bed and had total heights ranging from 35 m to 50 m.

Each arch was built over the corresponding span of the deck, by assembly of 8 m components, in 3 distinct segments. Hangers were laid horizontally, connected on their top hinge. Consequently, when each arch was elevated, the hangers elevated together with it (Figure 6.27).

Figure 6.26 - Temporary piers.

Figure 6.27 - Elevation of the segments of one arch (REFER, 2010).

The segments of each arch were welded together and the arches' extremities were welded to their springing (Figure 6.28). The hangers could then be nailed to the deck, at their bottom hinges, and their length was adjusted to theoretical design lengths (Figure 6.29).

Figure 6.28 - Springing of one arch (REFER, 2010).

Figure 6.29 - Bottom hinge before nailing (REFER, 2010).

After adjusting the different hangers, vertical reaction on the temporary piers became almost null and they were removed (Figure 6.30). The arches and the steel box were still subjected to a pre-stress, by lowering the bearings of P2 and P3 by 1.3 m.

The next step consisted in concreting the slab of the deck (Figure 6.31). Different concreting stages were adopted in order to minimise cracking due to creep and shrinkage.

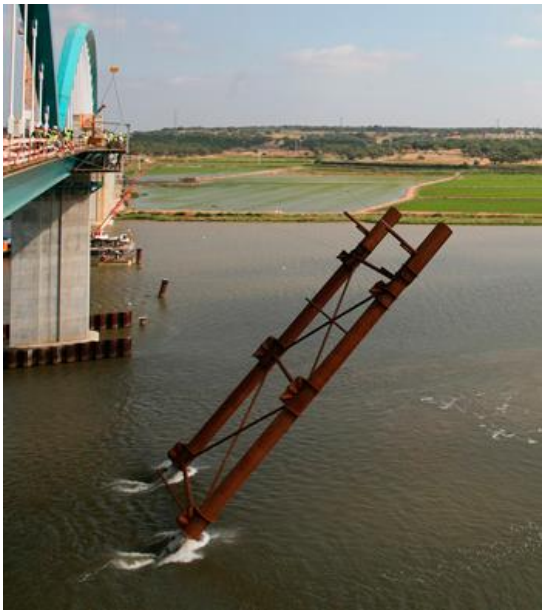

Figure 6.30 - Removal of the temporary piers (REFER, 2010).

Figure 6.31 - Concreting of a ballast-guard.

Once the structure was finished, the construction of the ballasted track started (Figure 6.32), as well as the installation of the catenary and of the communication, signalling and control technological systems (Figure 6.33).

(a)

(b)

(c)

Figure 6.32 - Track's construction: (a) sleepers, (b) expansion joint and (c) downstream vs. upstream tracks.

Figure 6.33 - Catenary and signalling system (REFER, 2010).

6.2.4 Critical details to fatigue

The details potentially prone to fatigue damage were identified from the structural design and from *in situ* observation, during the construction phase. The different details were classified to fatigue strength according to Eurocode 3 (CEN, 2004). Preliminary fatigue analysis on all components was performed, using Eurocode 3 methodology and the numerical model of the structure. Based on that analysis, the bottom connection of the diagonals of each diaphragm and the cope hole at the top connection of the same elements (Figure 6.34) were identified as the critical details for fatigue.

(a) (b)

Figure 6.34 - Details classification according to fatigue: (a) upper (top) extremity and (b) lower (bottom) extremity of the diagonal.

However, it must be stressed that the classification of the critical details based on the Eurocode 3 database is not always straightforward. Analogy between different details with similar structural behaviour was assumed, like in the case of the cope hole at the top connection of the diagonals. SN curve determination tests were conducted, in order to confirm the adopted fatigue strength classification (Silva et al., 2013). Those tests, conducted in small scale reproductions of the detail, revealed higher strength to fatigue than the suggested by the 45 classification. Nevertheless, since the maximum thickness of the diagonal simulated in the tests (12 mm) was lower than the real one (35 mm), and, as the fatigue strength of this type of detail is assumed to decrease with the thickness, the classification (category 45) was kept.

These details were considered to have low structural redundancy and therefore a safe life approach was deemed adequate. As the consequences of failure would be high, a partial safety factor for fatigue strength equal to 1.35 was adopted, according to Table 3.5.

6.3 NUMERICAL MODEL OF THE BRIDGE

6.3.1 Description

A numerical model of the bridge was developed using ANSYS software (Figure 6.35). Both beam and shell elements were employed.

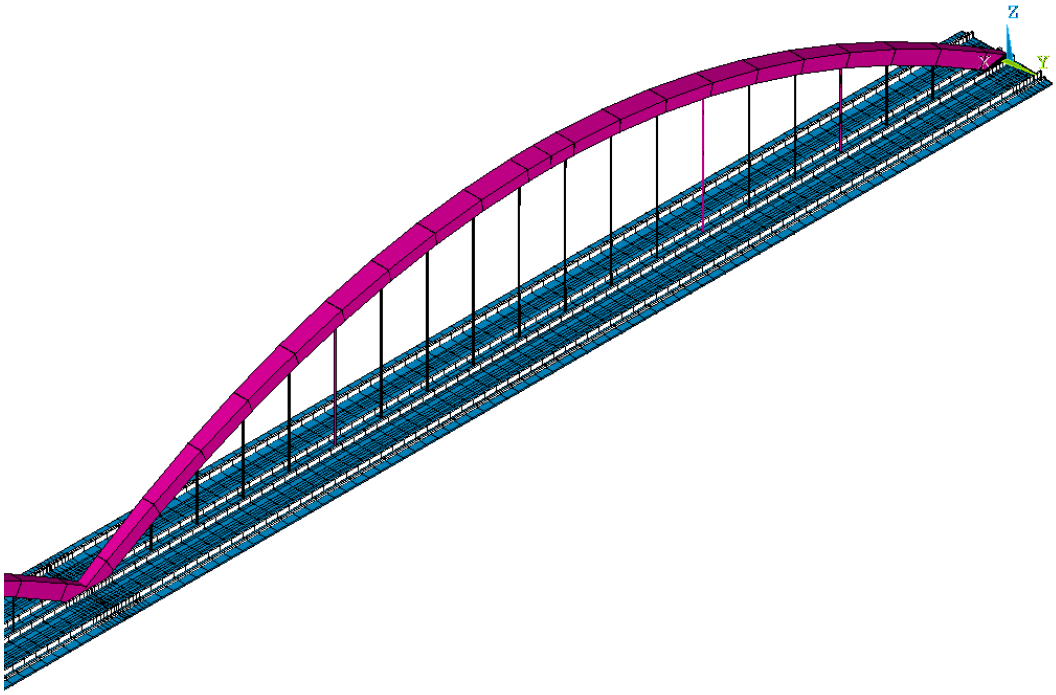

Figure 6.35 – Numerical model of the bridge of the new railway crossing of river Sado (1st span).

Shell elements (SHELL63 of ANSYS library) were used to model the concrete slab and the steel box girder. The beam elements (BEAM44) were employed to model the arches, the hangers, the diaphragms and the diagonals, the transverse stiffeners and the ballast containing beams (Figure 6.36). Nodal mass elements (MASS21) were applied to the structure in order to reproduce the mass of the diaphragms of the arches. Rigid connections (MPC184) were also used to connect the concrete slab to the upper flanges of the steel box.

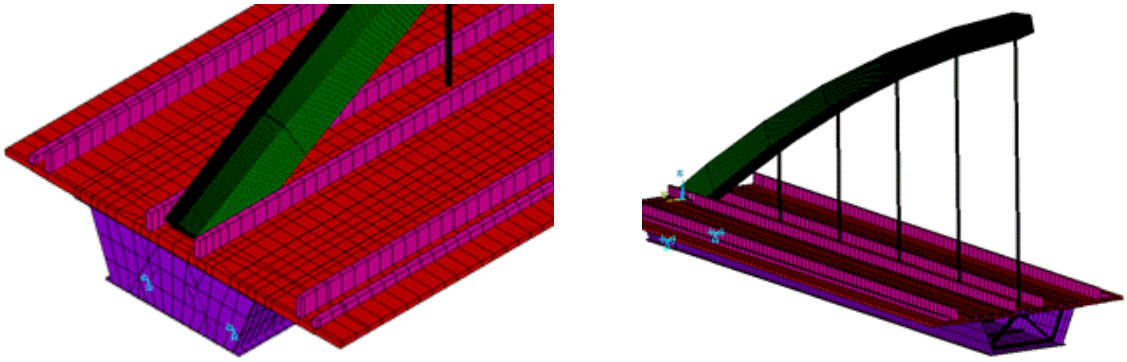

(a) (b)

Figure 6.36 - Numerical model of the bridge: (a) deck and arch's ending point and (b) cut view of the deck and arch.

After performing a sensitivity analysis, a mesh of elements with maximum 2 m of longitudinal length was adopted.

Two different approaches were employed when modelling the diaphragms and diagonals of the bridge. The diaphragms 51 and 54 and corresponding diagonals were modelled with a fine mesh of shell elements, with maximum dimension of 0.1 m (Figure 6.37(a)). This allowed to better capture the stress concentration at the extremities of the diagonals. All other diaphragms and diagonals were modelled using the beam elements (Figure 6.37(b)).

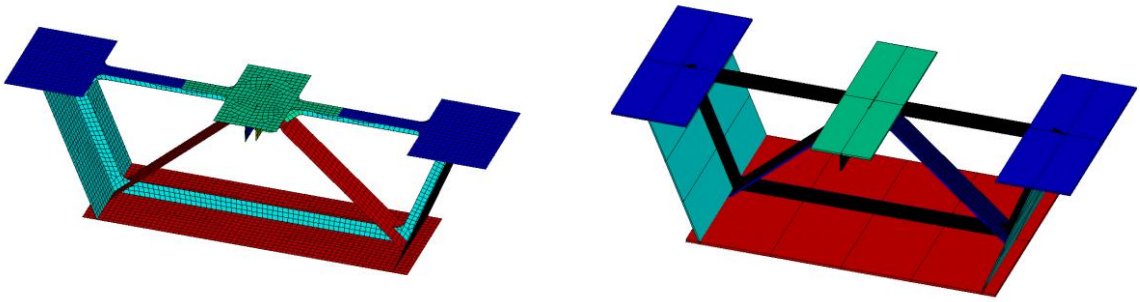

(a) (b)

Figure 6.37 - Modelling of diaphragms and diagonals: (a) refined and (b) not refined.

The track was not modelled explicitly. Nevertheless, its mass was distributed in the concrete slab, between the ballast guards.

The number of elements and nodes employed in the model is 40157 and 32862, respectively. The total number of Degrees of Freedom (DOF) is 197154.

6.3.2 Geometrical and mechanical characteristics

In this section, the geometrical and mechanical characteristics of the elements composing the deck and the arches of the bridge are presented.

6.3.2.1 Deck

The density of the steel employed in the deck was considered equal to 7850 kg/m^3. A Young Modulus of 210 GPa and a Poisson's ratio of 0.3 were adopted.

Concerning the concrete of the concrete slab, a density of 2500 kg/m^3 was employed. The Young Modulus, before the model updating, was assumed to be 35 GPa. This is the secant modulus of elasticity of concrete at 28 days for a C40/50 concrete which is the minimum quality required at design phase (GRID et al., 2006). After the model updating, described in Section 6.3.3.2, a value of 43 GPa was considered. The Poisson's ratio employed was 0.15.

The mass of the track and of the non-structural elements were computed and distributed in the sections of the concrete slab identified in Figure 6.38. Table 6.1 summarises the adopted values.

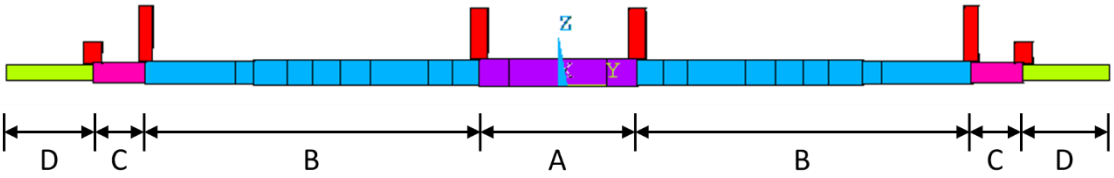

Figure 6.38 – Cross section of the numerical model of the concrete slab.

Table 6.1 – Additional mass associated to the track and non-structural elements of the deck's slab.

Section	Description	Mass
A	Concrete slab covering (waterproofing covering, light concrete and screed)	190 kg/m^2
B	Track (ballast, sleepers, rails) and concrete slab covering (waterproofing covering, light concrete and screed)	1255 kg/m^2
C	Prefabricated concrete slabs	77 kg/m^2
D	Lightweight concrete and metallic bridge-rail	735 kg/m^2

The diagonals located at each diaphragm have a rectangular cross section with 35×600 mm. Their geometric characteristics are summarised in Table 6.2.

Table 6.2 – Geometric characteristics of the diagonals present at the diaphragms.

Location	**Cross section**	**Geometric characteristics**
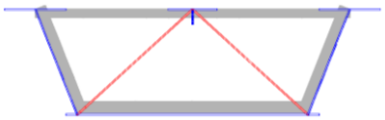	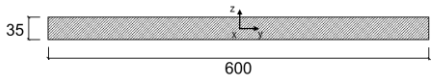	$A = 0.021\ m^2$ $I_y = 0.214E\text{-}05\ m^4$ $I_z = 0.630E\text{-}03\ m^4$ $J = 0.828E\text{-}05\ m^4$

6.3.2.2 Arches and hangers

The arches and hangers were modelled using a steel with characteristics similar to the ones of the steel employed in the deck box girder.

As mentioned before, all the hangers have the same circular cross-section with a diameter of 200 mm. The arches, on the other hand, have variable cross section, due to varying height, width and thickness of flanges and webs. These geometric characteristics were reproduced in the numerical model (Figure 6.39).

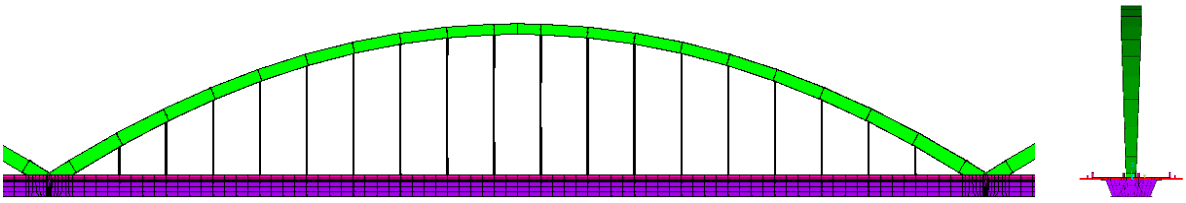

(a) (b)

Figure 6.39 – Modelling of the arch and hangers: (a) side elevation of the 2nd span and (b) front elevation of the bridge.

The corresponding mechanical properties are summarised in Tables 6.3 to 6.6. Furthermore, nodal masses were added to the nodes of the hanger-to-arch connections, in order to replicate the stiffening diaphragms existing at those locations (Tables 6.4 to 6.6).

Table 6.3 – Geometric characteristics of the hangers.

Element	**A [m^2]**	**I_y [m^4]**	**I_z [m^4]**	**J [m^4]**
Hangers	3.14E-2	7.85E-5	7.85E-5	1.57E-4

Table 6.4 – Geometric characteristics of the 1st arch.

Element	Location	A [m^2]	I_y [m^4]	I_z [m^4]	J [m^4]	Additional Nodal Mass [kg]
1st arch	P1	0.841	0.558	0.280	0.637	-
	Diaph. 1	0.904	0.543	0.480	0.876	881
	Diaph. 2	0.861	0.463	0.597	0.906	968
	Diaph. 3	0.699	0.316	0.647	0.732	960
	Diaph. 4	0.701	0.293	0.736	0.737	963
	Diaph. 5	0.702	0.272	0.809	0.728	963
	Diaph. 6	0.759	0.280	0.902	0.773	964
	Diaph. 7	0.656	0.249	0.761	0.674	961
	Diaph. 8	0.660	0.241	0.789	0.665	946
	Diaph. 9	0.663	0.237	0.804	0.659	944
	Diaph. 10	0.663	0.237	0.804	0.659	944
	Diaph. 11	0.660	0.241	0.789	0.665	946
	Diaph. 12	0.656	0.249	0.761	0.674	961
	Diaph. 13	0.650	0.262	0.719	0.685	964
	Diaph. 14	0.641	0.277	0.663	0.693	963
	Diaph. 15	0.701	0.293	0.736	0.737	963
	Diaph. 16	0.699	0.316	0.647	0.732	960
	Diaph. 17	0.697	0.341	0.543	0.706	968
	Diaph. 18	0.764	0.428	0.446	0.741	881
	P2	0.861	0.556	0.337	0.718	-

Table 6.5 – Geometric characteristics of the 2nd arch.

Element	Location	A [m^2]	I_y [m^4]	I_z [m^4]	J [m^4]	Additional Nodal Mass [kg]
2nd arch	P2	0.841	0.558	0.280	0.637	-
	Diaph. 19	0.904	0.543	0.480	0.876	881
	Diaph. 20	0.779	0.404	0.570	0.816	968
	Diaph. 21	0.699	0.316	0.647	0.732	960
	Diaph. 22	0.701	0.293	0.736	0.737	963
	Diaph. 23	0.702	0.272	0.809	0.728	963
	Diaph. 24	0.702	0.255	0.867	0.713	964
	Diaph. 25	0.626	0.238	0.740	0.650	961
	Diaph. 26	0.629	0.230	0.766	0.641	946
	Diaph. 27	0.631	0.226	0.780	0.636	944
	Diaph. 28	0.631	0.226	0.780	0.636	944
	Diaph. 29	0.629	0.230	0.766	0.641	946
	Diaph. 30	0.626	0.238	0.740	0.650	961
	Diaph. 31	0.620	0.250	0.700	0.661	964
	Diaph. 32	0.702	0.272	0.809	0.728	963
	Diaph. 33	0.701	0.293	0.736	0.737	963
	Diaph. 34	0.699	0.316	0.647	0.732	960
	Diaph. 35	0.697	0.341	0.543	0.706	968
	Diaph. 36	0.764	0.428	0.446	0.741	881
	P3	0.861	0.556	0.337	0.718	-

Table 6.6 – Geometric characteristics of the 3rd arch.

Element	Location	A [m^2]	I_y [m^4]	I_z [m^4]	J [m^4]	Additional Nodal Mass [kg]
3rd arch	P3	0.841	0.558	0.280	0.637	-
	Diaph. 37	0.904	0.543	0.480	0.876	881
	Diaph. 38	0.779	0.404	0.570	0.816	968
	Diaph. 39	0.699	0.316	0.647	0.732	960
	Diaph. 40	0.701	0.293	0.736	0.737	963
	Diaph. 41	0.701	0.272	0.809	0.728	963
	Diaph. 42	0.650	0.262	0.719	0.685	964
	Diaph. 43	0.656	0.249	0.761	0.674	961
	Diaph. 44	0.660	0.241	0.789	0.665	946
	Diaph. 45	0.663	0.237	0.804	0.659	944
	Diaph. 46	0.663	0.237	0.804	0.659	944
	Diaph. 47	0.660	0.241	0.789	0.665	946
	Diaph. 48	0.656	0.249	0.761	0.674	961
	Diaph. 49	0.650	0.262	0.719	0.685	964
	Diaph. 50	0.756	0.299	0.840	0.788	963
	Diaph. 51	0.701	0.293	0.736	0.737	963
	Diaph. 52	0.699	0.316	0.647	0.732	960
	Diaph. 53	0.697	0.341	0.543	0.706	968
	Diaph. 54	0.834	0.487	0.463	0.815	881
	P4	0.860	0.556	0.337	0.718	-

6.3.3 Validation with Ambient Vibration Test

6.3.3.1 Test Setup

Ambient Vibration Tests (AVT) are a widely recognised method to characterise the dynamic properties of bridges (Ribeiro et al., 2012, Magalhães et al., 2012a, Brownjohn et al., 2010, Goulet et al., 2014, Gentile and Saisi, 2013, Gentile and Saisi, 2011, Zhang et al., 2013).

An AVT was also performed at the bridge of the new railway crossing of river Sado, covering 33 sections of the deck and 19 sections of the arches (Figure 6.40). The number of sensors available led to the execution of 20 different setups. The link between different setups was achieved by 8 reference points, at 4 sections of the deck. The measurement points and directions are identified at Figure 6.41.

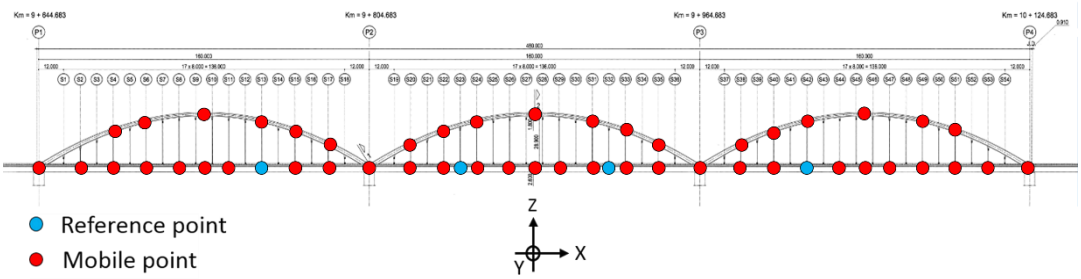

Figure 6.40 - Monitored points.

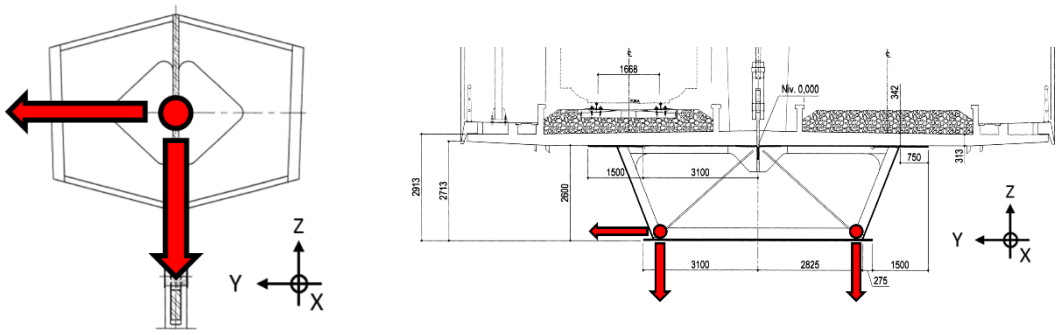

(a) (b)

Figure 6.41 - Measurement directions: (a) arch's section and (b) deck's section.

The data acquisition hardware used was the NI cDAQ-9172 with analog input modules NI 9233 IEPE. Fourteen piezoelectric accelerometers were used (PCB 393A03) with a sensitivity of 1000 mV/g and a measurement range of ±5g. Each setup had a duration of 20 minutes and a sampling rate of 2000 Hz, decimated to 100 Hz.

Due to the length of the structure, coaxial cables up to 250 m were used to connect the sensors to the acquisition system placed at the central span of the bridge.

6.3.3.2 Results

The data of the different setups was processed using two different algorithms available in software ARTEMIS (SVS, 1999-2010): EFDD and SSI-UPC. The modes of vibration identified included bending and torsion vibration modes of the deck and transverse vibration modes of the arches. The SSI-UPC algorithm, in particular, allowed distinguishing different modes of vibration contained in closely spaced frequencies. It revealed high efficiency, condensing all setups in a single Stabilization Diagram (Döhler et al., 2010).

The numerical model was updated in order to better replicate the experimental mode shapes and natural frequencies. The parameter revealing higher influence in the numerical model dynamic properties was the Young Modulus of the concrete (E_c) used in the construction of the deck's slab. Figure 6.42 illustrates the variation of some of the natural frequencies as a function of this parameter. The evolution of the corresponding objective function, which is the sum of the natural frequency absolute differences, is also presented. The values of E_c varied between 35 and 50 GPa. The final adopted value was E_c = 43 GPa.

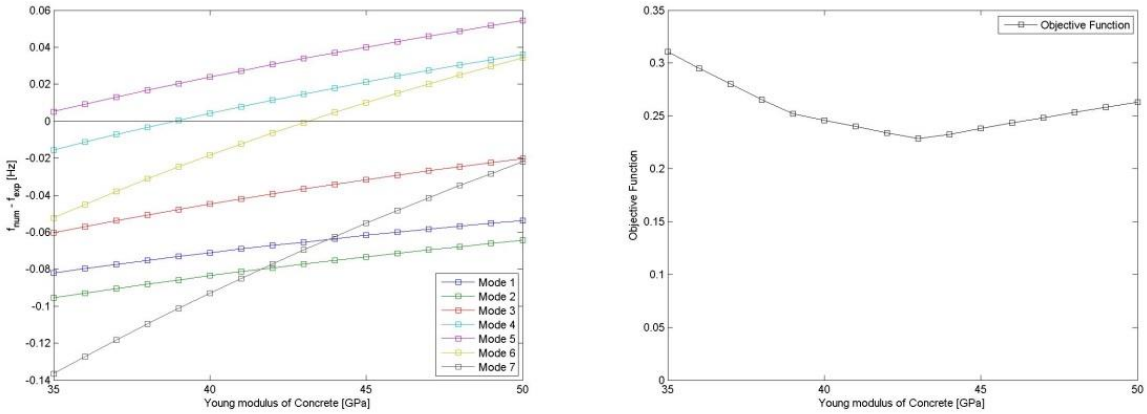

(a) (b)

Figure 6.42 - Model update: (a) difference between f_{num} and f_{exp} and (b) objective function as a function of Young Modulus of concrete.

Some of the modes of vibration identified during the AVT are compared, in Figures 6.43 to 6.46, with the corresponding modes of vibration obtained with the numerical model.

(a) f_{exp} = 0.868 Hz (b) f_{num} = 0.803 Hz

Figure 6.43 - 1st vertical bending mode of vibration.

(a) f_{exp} = 1.000 Hz (b) f_{num} = 0.923 Hz

Figure 6.44 - 2nd vertical bending mode of vibration.

(a) f_{exp} = 1.174 Hz (b) f_{num} = 1.140 Hz

Figure 6.45 - 3rd vertical bending mode of vibration.

(a) f_{exp} = 1.466 Hz (b) f_{num} = 1.481 Hz

Figure 6.46 - 4th vertical bending mode of vibration.

Table 6.7 summarises the results in terms of natural frequencies and modal damping coefficients for the first 7 modes of vibration.

Table 6.7 - Natural frequencies and modal damping coefficients.

Mode number	Natural Frequency (Hz)			Damping (%)		MAC	Description
	Numerical	Experimental					
		SSI	EFDD	SSI	EFDD		
1	0.803	0.868	0.868	1.519	1.239	0.97	Vertical bending mode
2	0.923	1.000	1.001	0.894	1.060	0.93	Vertical bending mode
3	1.140	1.174	1.180	1.099	0.744	0.94	Vertical bending mode
4	1.481	1.466	1.466	0.769	0.546	0.95	Vertical bending mode
5	1.501	1.467	-	1.537	-	0.86	Vertical bending mode
6	2.142	2.145	2.140	3.057	0.345	0.82	Torsion mode
7	3.249	3.322	3.315	4.581	0.463	0.89	Vertical bending mode

As reflected in the high Modal Assurance Criterion (MAC) values, the agreement between the experimental and numerical modes of vibration is good. In addition, the natural frequencies are very similar, with differences typically below 0.08 Hz. Both methods used for modal information extraction showed similar results, which can be considered a cross-check of the analysis. These results support that the numerical model reflects correctly the dynamic behaviour of the real structure.

6.3.4 Validation with Load Tests

The long-term monitoring system that will be described in detail in Section 6.4 was used during the load tests performed at the commissioning phase by the Portuguese National Laboratory for Civil Engineering (LNEC). Three different types of vehicles were used to load the bridge:

- Single power engine machine;
- Short freight train (87.242 m) with 5 double hopper ballast containers;
- Long freight train (130.762 m) with 7 double hopper ballast containers plus 1 single hopper ballast container.

The characteristics of the power engine machine, double hopper ballast container and single hopper ballast container are illustrated in Figures 6.44, 6.45 and 6.46, respectively.

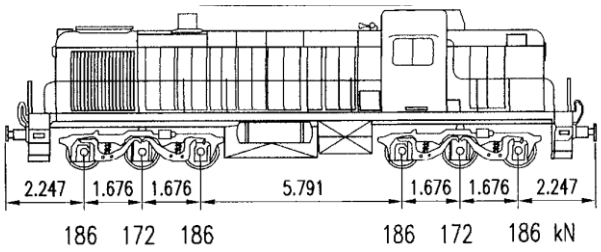

(a)

(b)

Figure 6.47 – Power engine machine (1500 series): (a) distances between axles, average load per axle and (b) overview in the context of the load test performed.

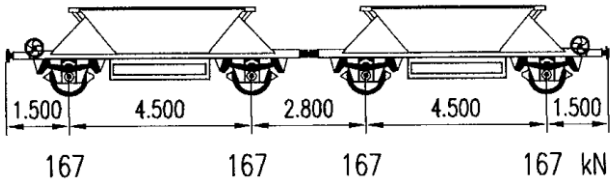

(a)

(b)

Figure 6.48 - Double hopper ballast container: (a) distances between axles, average load per axle and (b) overview in the context of the load test performed.

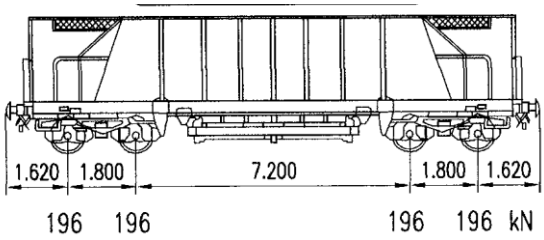

(a)

(b)

Figure 6.49 - Single hopper ballast container: (a) distances between axles, average load per axle and (b) overview in the context of the load test performed.

Since the axle loads of the power engine machine were known with a high degree of accuracy, they were used to calibrate the traffic characterization system, allowing the determination of the factor *C*, in Equation 6.11.

The different loading positions adopted by the long freight train, during the load test, are illustrated in Figure 6.50.

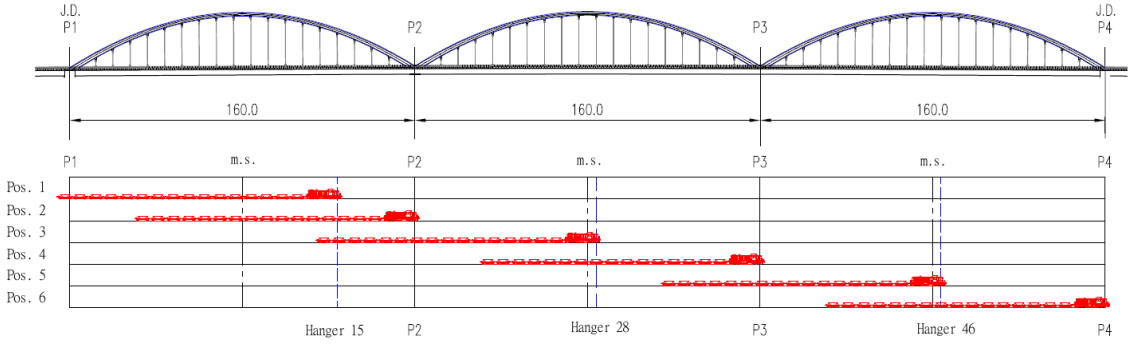

Figure 6.50 - Long freight train loading positions (adapted from LNEC (2011)).

For each loading position, each strain gauge measured the corresponding deformation. A good agreement was achieved between numerical and experimental results. Figure 6.51 compares the numerical and experimental results for strain gauge SG 51-1 (see Figure 6.62).

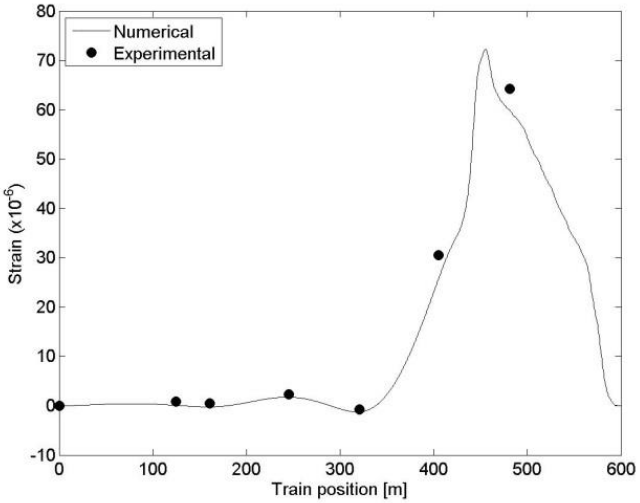

Figure 6.51 - Experimental vs. Numerical strain (at position of SG 51-1) due to long freight train static loading.

Also during the load test, the bridge undertook a quasi-static loading with the power engine machine at 7 km/h. In this case, again, there was a good agreement between the numerical and experimental results (Figure 6.52).

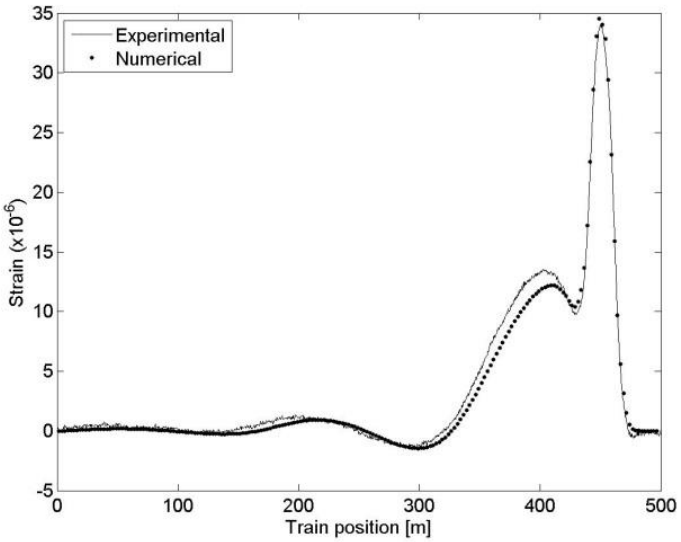

Figure 6.52 - Experimental vs. Numerical strain (at position of SG 51-1) due to power engine machine quasi-static loading.

6.3.5 Extraction of relevant modal parameters

The validated numerical model is used to perform a single modal analysis. The information obtained from the modal analysis can be stored in a very condensed way. For each *j* mode of

vibration, the modal mass, modal frequency and modal damping ratio are stored (m_j, ω_j and ξ_j, respectively). If J is the total number of modes of vibration considered, then the information is stored in three $J \times 1$ vectors: **M**, **ω** and **ξ**.

In the case study, the number of modes of vibration considered in the analysis was 1500 and the natural frequency of the last mode considered was 35 Hz.

When assessing the dynamic response of the structure (Liu et al., 2013) using the modal superposition method, it is generally accepted that it is dependent on the above mentioned vectors and on the modal forces over time:

$$\mathbf{F}(t)=\begin{bmatrix} F_1(t) \\ \vdots \\ F_j(t) \\ \vdots \\ F_J(t) \end{bmatrix} = \begin{bmatrix} \Phi_{1,1} \dots \Phi_{1,k} \dots \Phi_{1,K} \\ \vdots \quad \ddots \quad \vdots \quad \ddots \quad \vdots \\ \Phi_{j,1} \cdots \Phi_{j,k} \cdots \Phi_{j,K} \\ \vdots \quad \ddots \quad \vdots \quad \ddots \quad \vdots \\ \Phi_{J,1} \cdots \Phi_{J,k} \cdots \Phi_{J,K} \end{bmatrix} \cdot \begin{bmatrix} F_1(t) \\ \vdots \\ F_k(t) \\ \vdots \\ F_K(t) \end{bmatrix} \tag{6.1}$$

where $\Phi_{j,k}$ is the modal displacement of the degree of freedom k, for the mode of vibration j and $F_k(t)$ is the loading history (Clough and Penzien, 1975).

In the case of a railway bridge loaded by a train, the loads can be considered as applied in the vertical direction, at the nodes that correspond to the rail. All other degrees of freedom have a null applied load. So, for that case, only the vertical nodal displacements of the nodes that define the rails, for each j mode of vibration, $\mathbf{\Phi_{rail}}$, need to be stored. If the total number of nodes defining the rails is L, the information fits a matrix with $J \times L$ elements and then, Equation (6.1) can be restricted to the non-null terms:

$$\mathbf{F}(t)=\begin{bmatrix} F_1(t) \\ \vdots \\ F_j(t) \\ \vdots \\ F_J(t) \end{bmatrix} = \begin{bmatrix} \Phi_{1,1} \dots \Phi_{1,l} \dots \Phi_{1,L} \\ \vdots \quad \ddots \quad \vdots \quad \ddots \quad \vdots \\ \Phi_{j,1} \cdots \Phi_{j,l} \cdots \Phi_{j,L} \\ \vdots \quad \ddots \quad \vdots \quad \ddots \quad \vdots \\ \Phi_{J,1} \cdots \Phi_{J,l} \cdots \Phi_{J,L} \end{bmatrix} \cdot \begin{bmatrix} F_1(t) \\ \vdots \\ F_l(t) \\ \vdots \\ F_L(t) \end{bmatrix} \tag{6.2}$$

In the case of the numerical model of the bridge of the new railway crossing of river Sado, the number of nodes representing the rails is 620, so, the matrix to be stored, $\mathbf{\Phi_{rail}}$, has a dimension of 1500×620. This is a very condensed format when compared with storing the modal displacements for all the degrees of freedom of the model, which would generate a 1500×197154 matrix.

Finally, the modal stresses for each j mode of vibration, at each critical detail m, $\sigma_{j,m}$, are also recorded. If a total of M critical details are considered, the info fits in a $J \times M$ matrix, $\boldsymbol{\sigma}$.

$$\boldsymbol{\sigma} = \begin{bmatrix} \sigma_{1,1} \cdots \sigma_{1,m} \cdots \sigma_{1,M} \\ \vdots \quad \ddots \quad \vdots \quad \ddots \quad \vdots \\ \sigma_{j,1} \cdots \sigma_{j,m} \cdots \sigma_{j,M} \\ \vdots \quad \ddots \quad \vdots \quad \ddots \quad \vdots \\ \sigma_{J,1} \cdots \sigma_{J,m} \cdots \sigma_{J,M} \end{bmatrix} \tag{6.3}$$

Considering as fatigue critical details the 2 diagonals of each one of the 54 diaphragms of the bridge, only 108 nodal stresses per mode of vibration are required (1500 × 108 matrix).

Once the above mentioned matrices are stored, the numerical model of the bridge is no longer needed for the subsequent steps of the fatigue assessment.

6.4 LONG-TERM MONITORING SYSTEM

6.4.1 Introduction

A monitoring system was developed in order to characterise railway traffic and its effects on critical points of the structure. Consequently, the system includes traffic and structural response characterization modules. A trigger allows start storing the data when a traffic event occurs. The acquisition system allows managing the information that, after some preliminary processing, is sent to a server, via 3G connection. The different components of the system are distributed along the bridge as illustrated in Figure 6.53.

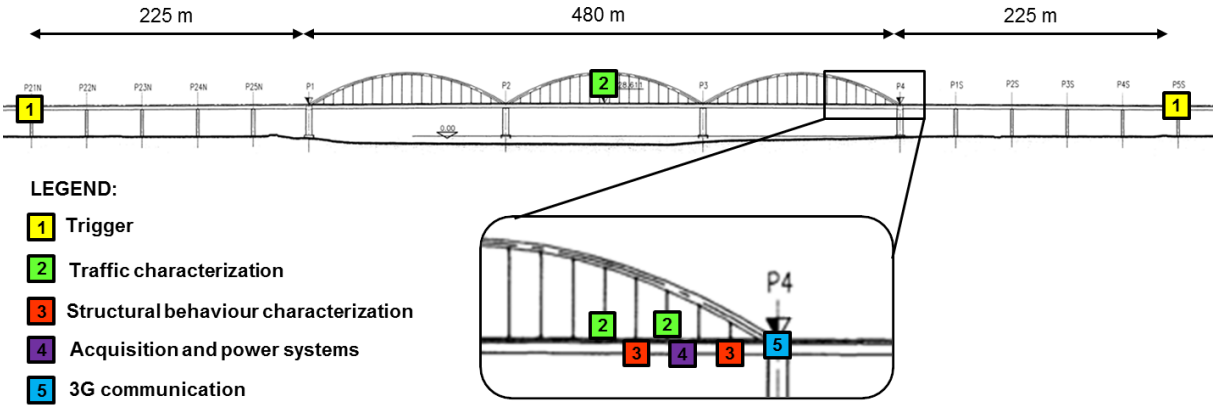

Figure 6.53 - Location of the different components of the system.

6.4.2 Traffic Characterization Module

The traffic is characterised both quantitatively and qualitatively. The quantitative evaluation is performed using 2 different types of sensors:

- Fibre optic rail pad sensors, Sensor Line FORPS-UIC60-1-20;
- Strain gauges in full Wheatstone bridges configuration.

The qualitative information is provided by an IP Camera placed at one hanger of the bridge.

6.4.2.1 Qualitative evaluation

The IP camera, model Vivotek IP 7330, was installed in the hanger number 28 (Figure 6.54). The camera trigger is activated by movement detection. Train passage is recorded by photograph and video, and this info is appended to the data of each traffic event. In Figure 6.55, the photographic record of the passage of 3 different types of trains is presented.

Figure 6.54 - IP camera installed in a hanger.

(a) (b) (c)

Figure 6.55 - IP camera recorded images: (a) Alfa Pendular passengers train, (b) intercity passengers train and (c) freight train.

6.4.2.2 Quantitative evaluation

Four instrumented rail pad sensors, Sensor Line FORPS-UIC60-1-20 (Figure 6.56), were installed at two different sleepers, 16 m apart from each other, at the same bridge's sections as hangers 50 and 52 (Figure 6.57).

(a) (b)

Figure 6.56 - Fibre optic rail pad sensors (FORPS): (a) overview and (b) in place.

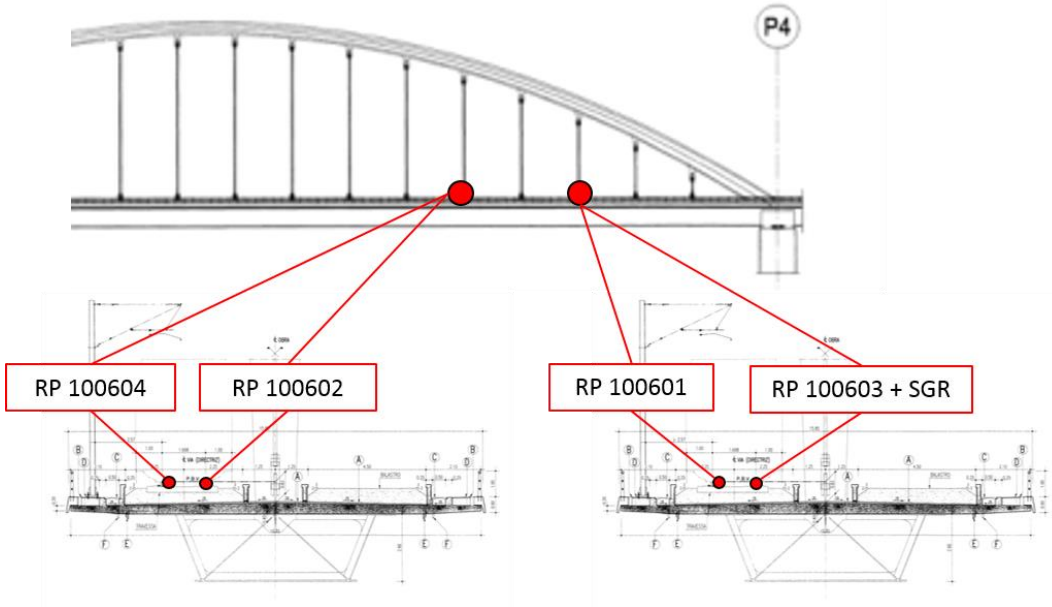

Figure 6.57 - Location and labelling of the instrumented rail pads and strain gauges in the rails.

The instrumented rail pads are used to compute the speed of the train and the axles spacing. This is achieved by analysing the time duration from each train axle to go from one rail pad section to another rail pad section, 16 m apart.

Each rail pad has a fibre optic embedded in its elastomeric material (Figure 6.58).

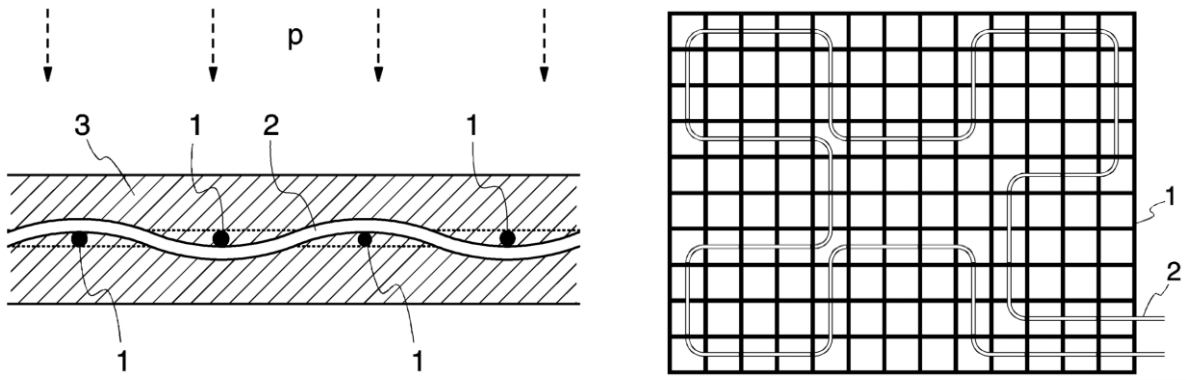

Figure 6.58 - Instrumented rail pad sensors structure (1 – interference grid (*grating*), 2 – fibre optic, 3 – elastomer) (SensorLine, 2008)

The fibre optic is plugged to a transducer that inputs a certain amount of light in one of its extremities and measures the amount of light coming out on the other extremity, converting it into an electrical signal. When one rail pad is loaded, it produces a reduction in the amount of light transmitted through the fibre optic and, consequently, a variation in the electrical sign measured (Figure 6.59).

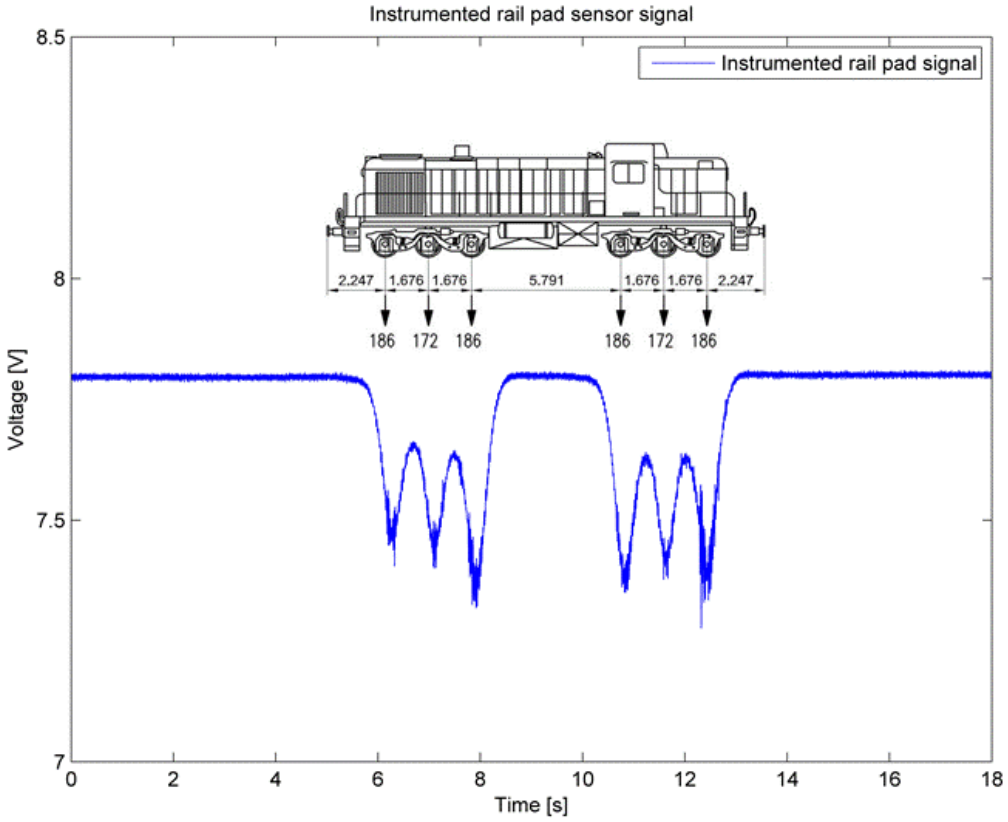

Figure 6.59 - Instrumented rail pad sensor signal.

The timing of the peaks of the electrical sign is used to define the above mentioned train speed and axis spacing. The process is described in Section 6.4.7.

In order to characterise the axle loads, three full Wheatstone bridges were installed at three different rail sections, near hanger 52 (Figure 6.57).

Each full Wheatstone bridge results from welding 4 shear strain gauges, VISHAY LEA-06-W125F-350/3R, at the neutral axis of the rail. Both sensors and cables were protected against potentially harmful maintenance operations, to be performed later, on the track (Figure 6.60).

(a) (b) (c)

Figure 6.60 - Strain gauges in the rails: (a) location, (b) welding and (c) protection.

The adopted configuration makes the full Wheatstone bridge sensitive almost exclusively to the shear stresses in the vertical plan parallel to the axis of the rail. In each moment, the shear strain is measured at 2 consecutive sections, τ_{S2} and τ_{S3} (Figure 6.61a)). The difference between these two measurements, $\Delta\tau = \tau_{S3} - \tau_{S2}$, is proportional to the vertical load applied to the rail between those sections (Figure 6.61(b)).

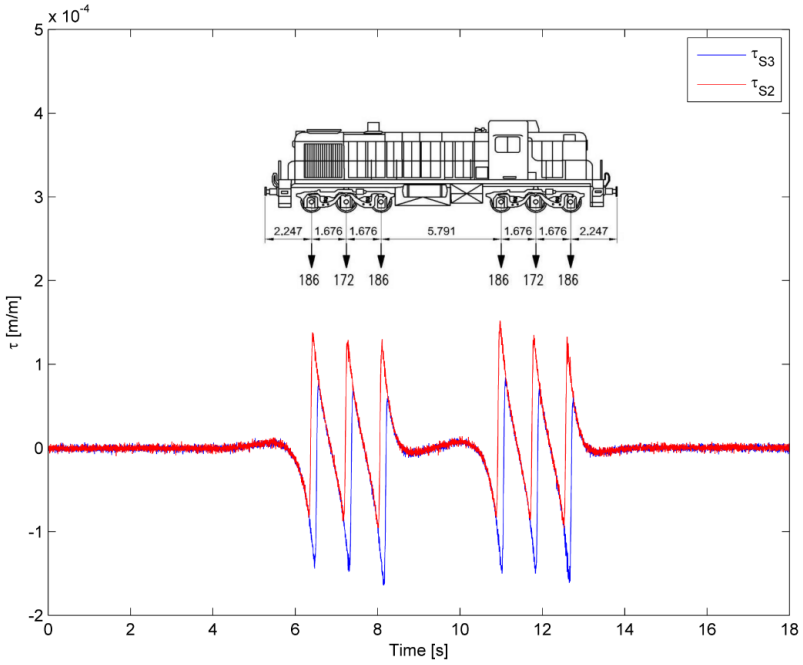

(a)

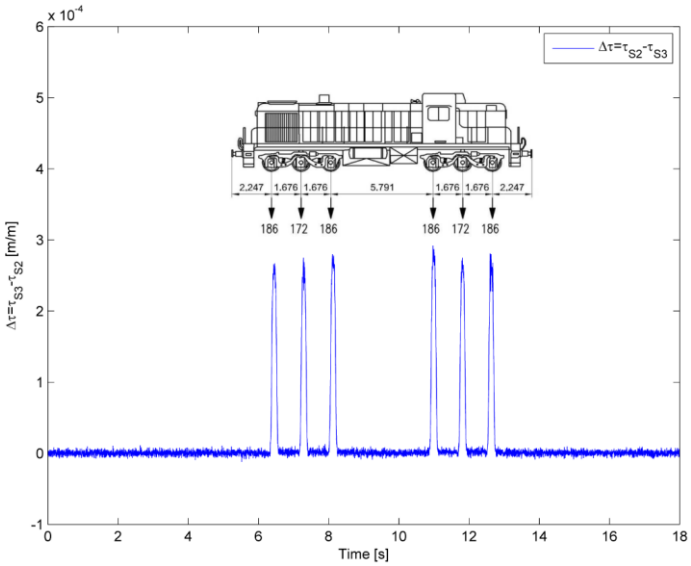

(b)

Figure 6.61 - Signal of full Wheatstone bridges at S2 and S3: (a) τ_{S2} and τ_{S3} and (b) $\Delta\tau = \tau_{S3} - \tau_{S2}$.

As discussed in (Julián Valerio, 2005), this is the principle used to measure the axle loads of the different trains passing over the bridge.

6.4.3 Structural Response Characterization Module

A total of 32 strain gauges, VISHAY CEA-06-125UN-350/P2, were installed in the structure. The location of the 4 strain gauges relevant for this study is illustrated at Figure 6.62.

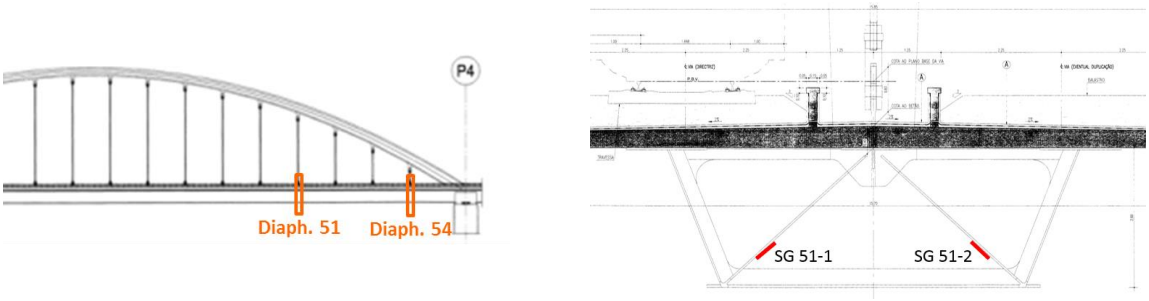

(a) (b)

Figure 6.62 - Location of strain gauges: (a) instrumented sections and (b) nomenclature of strain gauges at Diaphragm 51.

6.4.4 Trigger module

To start the data recording at each traffic event, two uniaxial accelerometers are placed on the access viaducts, at a distance of 225 m from each extremity of the bridge. Every time an arbitrary level of acceleration is reached, the shunt calibration of all bridges of strain gauges installed in the structure is performed and the acquisition system starts recording.

6.4.5 Data acquisition and control module

The data acquisition and control system adopted was the National Instruments cRIO-9024 with a NI 9116 chassis. The cRIO-9024 incorporates a PAC industrial computer and the chassis supports multiple modules for interface with sensors and other devices (Figure 6.63).

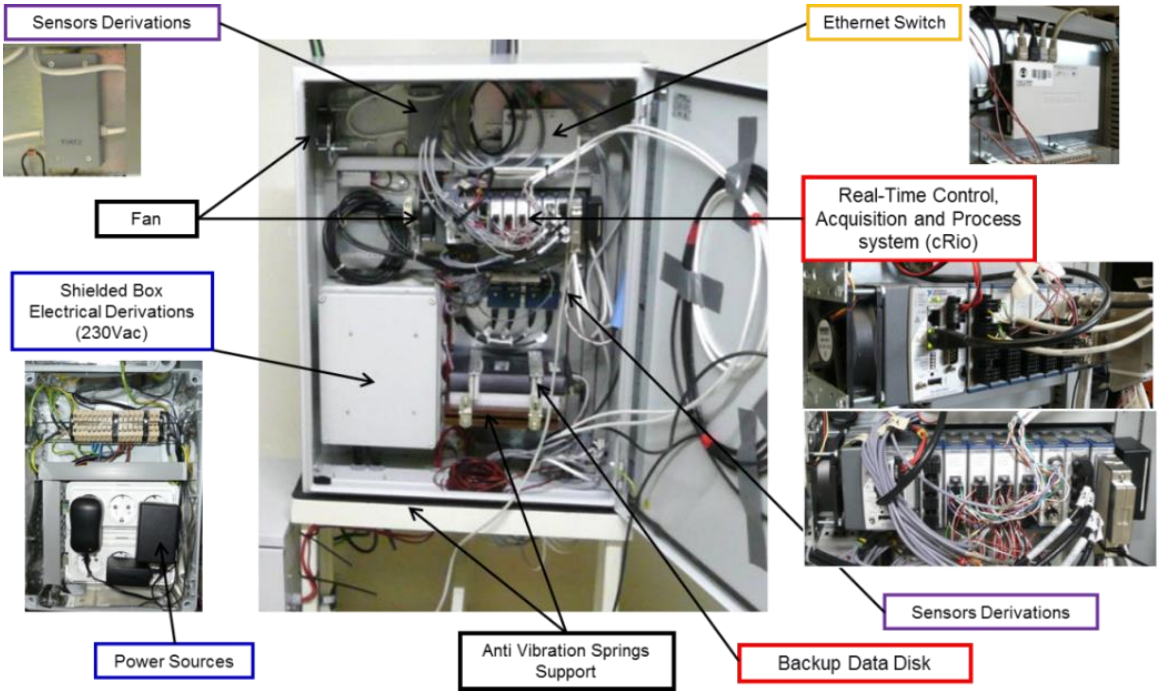

Figure 6.63 - Data acquisition and control module.

The strain gauges installed in the deck are connected to a National Instruments module NI 9236 (1/4 Wheatstone bridges), while the strain gauges installed in the rail are connected to the NI 9237 module (Full Wheatstone bridges). Finally, the instrumented rail pad transducers are connected to the NI 9205 analog input module.

6.4.6 Communication module

A router manages the communication between the cRIO and the 3G connection. The acquired data is sent, via a 3G connection, to a remote location and saved in a network hard drive installed at the bridge.

6.4.7 Database

The monitoring system logs the relevant information about the traffic and the structural response into a database. A MATLAB routine was developed for this purpose. When a train approaches the bridge, it induces vibration on the access viaduct, which is detected at the corresponding trigger. The date and hour of the trigger is recorded, in the format "YYYY_MM_DD_HH_mm", and composes the univocal index number identifying that traffic event. The data from all sensors is recorded during 120 seconds after the trigger.

6.4.7.1 Determination of Train Speed, Direction and Axles Spacing

As mentioned before, the determination of train speed, direction and axles spacing is obtained using the information provided by the instrumented rail pads. The raw analog signal of the rail pad sensors is sampled at 2048 Hz. For each instrumented rail pad, the light transmittance of the attached fibre optic sensor is computed by comparing the Sensor Line (SL) Transducer Output Voltage (V_{out}) with the SL Transducer Input Voltage (V_{in}=10 V), according to (SensorLine, 2008) (Equation (6.4)):

$$T(t)=\frac{1}{\frac{10}{V_{out}(t)}-1} \tag{6.4}$$

The reference value of the light transmittance, T_{ref}, is the average value of the light transmittance during the short undisturbed period, after the trigger event (Equation (6.5)).

$$T_{ref}=\overline{T}(t) \tag{6.5}$$

The relative variation of light transmittance during the traffic event, $\delta T(t)$, can then be computed:

$$\delta T(t)=\frac{T_{ref}-T(t)}{T_{ref}} \tag{6.6}$$

A Chebyshev Type II low-pass filter, of order 8, and with a cut-off frequency of 80 Hz is applied to the $\delta T(t)$ signal. An example of the consequent filtered transmittance relative variation signal is illustrated at Figure 6.64.

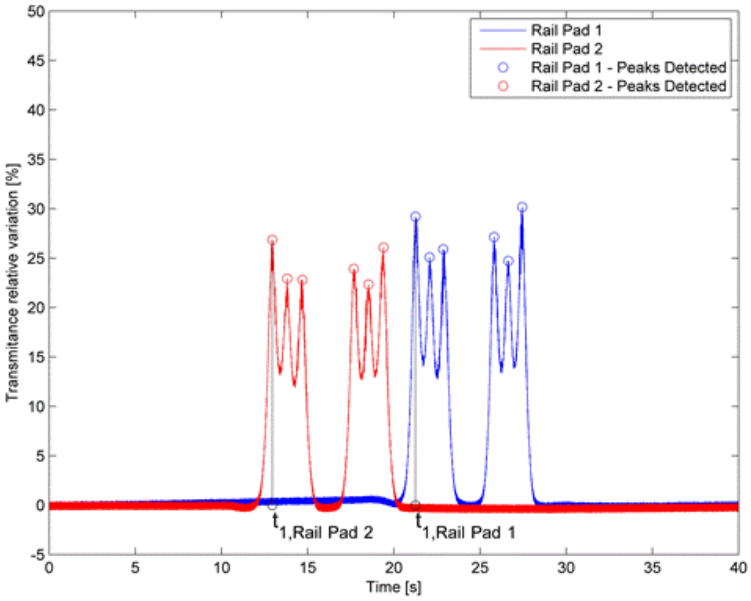

Figure 6.64 - Filtered transmittance relative variation.

The processed signals of two of the instrumented rail pads Rail Pad 1 and Rail Pad 2 are then used to compute the speed and direction of the train. When the axle number i crosses the bridge, it originates a peak on the signal of the rail pad sensors, at instants of time $t_{i,\ Rail\ Pad\ 1}$ and $t_{i,\ Rail\ Pad\ 2}$. As the distance between the rail pad sensors is well defined (16 m) the train speed can be computed:

$$v_i\ [\text{m/s}] = \frac{16}{t_{i,\ Rail\ Pad\ 1} - t_{i,Rail\ Pad\ 2}} \tag{6.7}$$

The signal of the computed speed indicates, automatically, the direction of the traffic: positive for North-South, negative for South-North.

Once the train speed is determined, the spacing between axle i and axle i+1, D_i, can be computed using the following equation:

$$D_i = v_i \cdot (t_{i,\ Rail\ Pad\ 1} - t_{i+1,Rail\ Pad\ 1}) \tag{6.8}$$

If the train has I number of axles, their different spacing values are stored in a (I-1)×1 vector, **D**.

Finally, considering the longitudinal origin of the bridge at pier P1 (x = 0 m), the positioning of the Rail Pad 1 is x = 436 m. With this information, and assuming constant train speed over the bridge, v, the location of the first axle of the train over time, can be obtained from the following equation:

$$x(t) = 436 + v \times (t - t_{1,\ Rail\ Pad\ 1}) \tag{6.9}$$

Equation (6.9) is particularly useful when analysing structural response as a function of the position of the train over the bridge.

6.4.7.2 Determination of Train Axle Loads

The train axle loads are determined using the information provided by the strain gauges welded to the rail.

The raw signal of each full Wheatstone bridge, $\tau(t)$, is sampled at 2048 Hz and then detrended using the average values of the raw signal during the periods of stabilised response at the beginning and end of the traffic event, $\tau_d(t)$. From the detrended signal the filtered signal is computed by application of a Chebyshev Type II low-pass filter, of order 8 and with a cut-off frequency of 250 Hz, $\tau_f(t)$.

The main input parameters needed to determine the axle loads are the differential between the detrended and filtered shear strains measured in the full Wheatstone bridges at sections 2 and 3:

$$\Delta\tau(t) = \tau_{f,\ S3}(t) - \tau_{f,\ S2}(t) \tag{6.10}$$

The instants of time corresponding to the peaks of the $\Delta\tau(t)$ signal are recorded. For the axle number i of the train, the corresponding instant of time is t_i. The peak values in the differential shear strains (Figure 6.65) are then extracted from $\Delta\tau(t)$:

$$\Delta\tau_i = \Delta\tau(t_i) \tag{6.11}$$

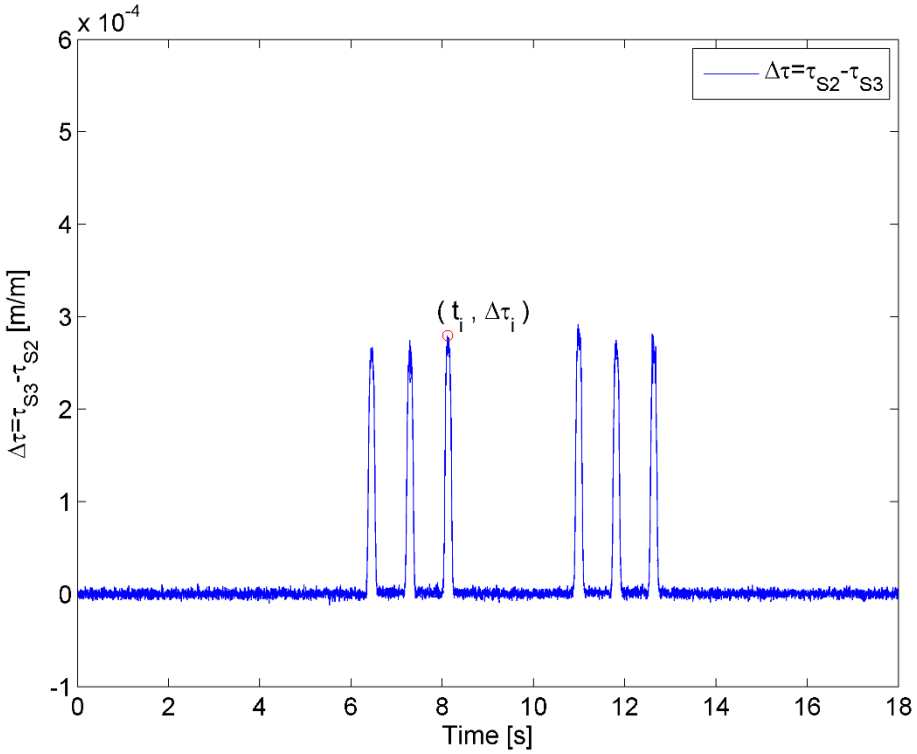

Figure 6.65 - Detection of peaks of differential shear strain.

As demonstrated in (Julián Valerio, 2005), the peaks in the shear strain can be related with the axle loads, **F**, by a constant of proportionality, *C*:

$$\mathbf{F} = [\Delta\tau] \cdot C \tag{6.12}$$

C can be determined by calibration with known axle loads from reference vehicles. That was performed at the Load Test described in Section 6.3.3. For **F** in [kN] and $[\Delta\tau]$ in [10^{-6} m/m], a value of $C = 0.707$ was adopted.

6.4.7.3 Train carriages identification

For each traffic event, the carriages, wagons and locomotives composing the train are automatically identified. This is performed in two steps, by means of a sub-routine, developed in MATLAB, that analyses the number of axles and corresponding distances, **D**, of the train:

- the vehicles composing the train (carriages and/or wagons and locomotives) are isolated, based on a minimum allowable distance between bogies;

- each vehicle is compared with a database of carriages, wagons and locomotives, which was built based on information available from the Operating Companies, and is labelled accordingly.

The sequence of vehicles, for each train, is then stored in the database.

6.4.7.4 Stress Histories at Instrumented Locations

The raw signal of the strain gauges installed in the deck, $\varepsilon(t)$, is first detrended and then filtered with a Chebyshev Type II low-pass filter, of order 8 and with a cut-off frequency of 35 Hz. The treated signal is $\varepsilon_f(t)$.

The filtered signal, $\varepsilon_f(t)$, is subsequently decimated to 20 samples per second, $\varepsilon_d(t)$. Then the stress, $\sigma(t)$, is computed, according to the equation:

$$\sigma(t) = \varepsilon_d(t) \cdot E \tag{6.13}$$

where E is the Young module of the steel. Finally, the rainflow method for counting of cycles is applied (Fryba, 1996), using a subroutine developed in MATLAB. With the stress cycles identified, the corresponding histogram of stress ranges is computed.

6.5 ASSESSMENT OF THE FATIGUE BEHAVIOUR

6.5.1 Methodology

Since the database built with the monitoring system stores all the relevant information concerning the traffic events on the bridge, the fatigue damage assessment can be performed in a very efficient way, according to the procedures described in this section. The information needed is:

- The characteristics of each traffic event, **F**, **D** and v, stored at the long-term monitoring system database;
- The modal characteristics of the representative numerical model of the bridge, stored once, in a very condensed way:
    - Modal mass vector, **M**;
    - Natural frequencies vector, **ω**;
    - Modal damping ratios vector, **ξ**;

- Modal displacements at the rails, $\mathbf{\Phi_{rail}}$;
- Modal stresses at the critical details, $\boldsymbol{\sigma}$.

With this information, the stress history at each detail *m*, for a traffic event, $\sigma_m(t)$, can be computed by application of the Modal Superposition Method (Clough and Penzien, 1975). The modal coordinates time history, for all modes of vibration considered in the analysis, $\mathbf{Y}(t)$ can be calculated from the modal characteristics of the structure and the loading history. The time integration is performed using the HHT method (Chung and Hulbert, 1993).

The stress history at the details is obtained by combining $\mathbf{Y}(t)$ with $\boldsymbol{\sigma}$:

$$\sigma_m(t) = \begin{bmatrix} \sigma_{1,m} \\ \vdots \\ \sigma_{j,m} \\ \vdots \\ \sigma_{J,m} \end{bmatrix}^T \cdot \begin{bmatrix} Y_1(t) \\ \vdots \\ Y_j(t) \\ \vdots \\ Y_J(t) \end{bmatrix} \tag{6.14}$$

Finally, the computation of fatigue damage, from the stress history, is performed by the application of Rainflow Method (Fryba, 1996). The process is schematically represented in Figure 6.66.

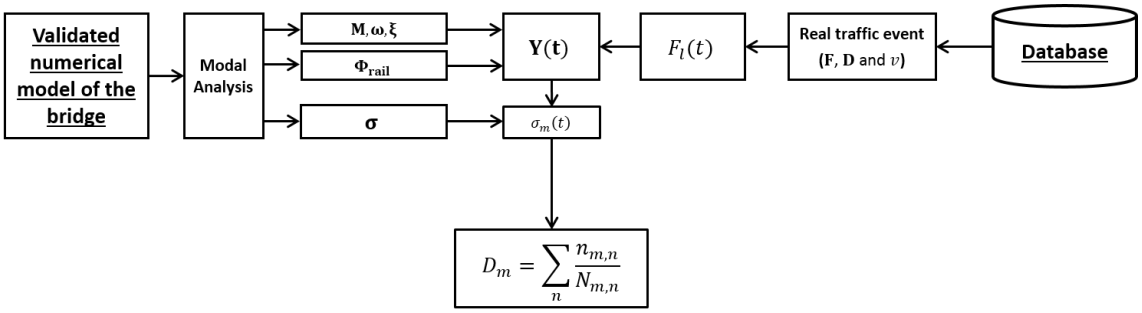

Figure 6.66 - Workflow for fatigue damage computation.

The entire workflow described was implemented in MATLAB® version 2010b and can be calculated in 3 minutes per traffic event (average time, in a personal computer with a Dual Core Intel T9600 2.8 GHz processor and 6 GB RAM memory).

6.5.2 Traffic characteristics

The traffic log database allowed characterizing the traffic over the bridge. The traffic characteristics, together with the stress influence line length of the critical details, are well

recognised as very relevant for fatigue damage (Ottosson et al., 2012b). The real traffic can then be compared with standard traffic.

Concerning the train speed histogram, 3 main groups of trains can be identified (Figure 6.67):

- Alfa Pendular passenger trains, circulating at speeds from 200 km/h to 212 km/h;
- Intercity passenger trains, circulating at speeds between 145 km/h and 160 km/h;
- Freight trains, at speeds between 75 km/h and 95 km/h.

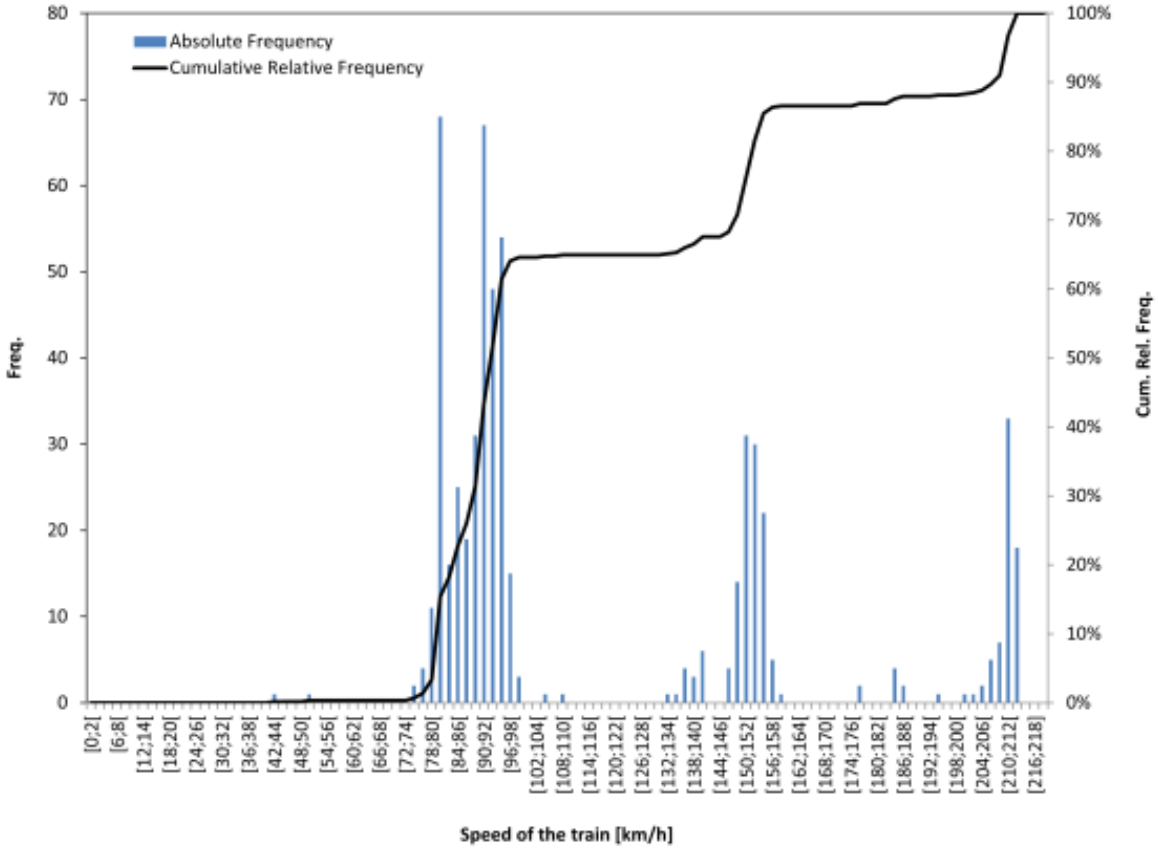

Figure 6.67 - Histogram of trains' speed.

The train's most frequent lengths correspond to the Alfa Pendular and Intercity passenger trains (Figure 6.68). Freight trains have lengths typically higher than 300 m. Maximum train length observed in the period was 520 m.

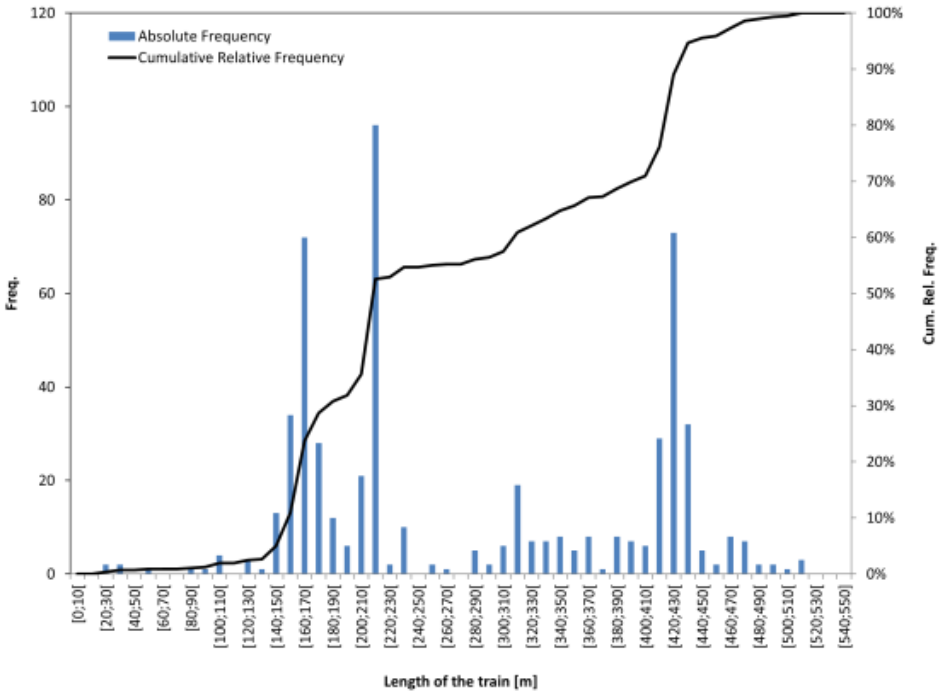

Figure 6.68 - Histogram of trains' length.

The most typical axle loads range is the 180 kN to 230 kN. Less than 1% of the axles exceed the 250 kN load (Figure 6.69), which is the maximum axle load allowed at the standard fatigue load models of Eurocode 1 (CEN, 2002).

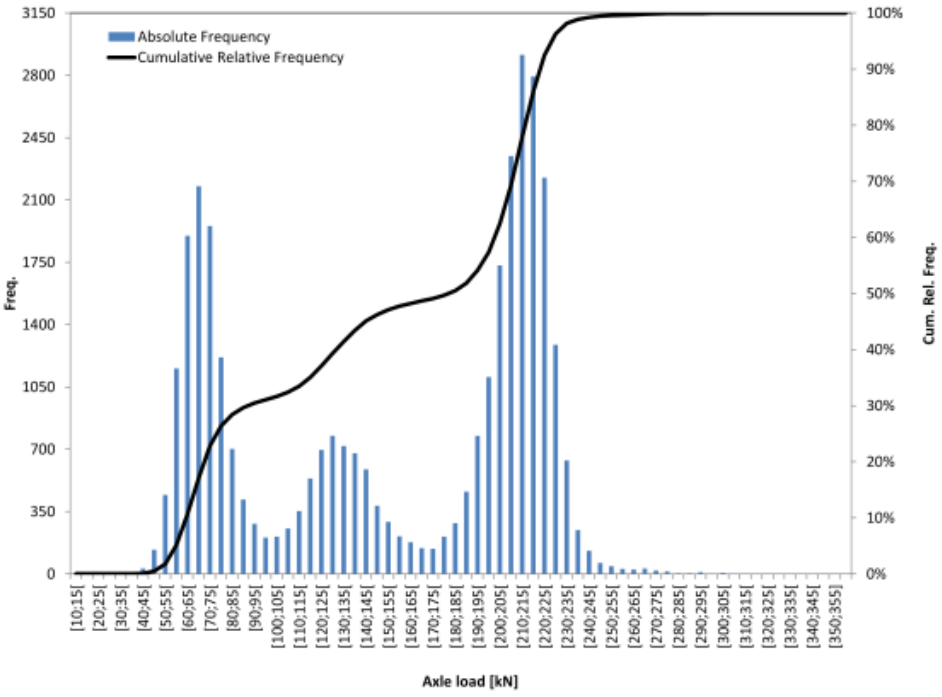

Figure 6.69 - Histogram of axle loads.

The total load per unit length can reach values up to 74 kN/m (Figure 6.70), lower than the 80 kN/m defined by the LM71 of Eurocode 1 (CEN, 2002).

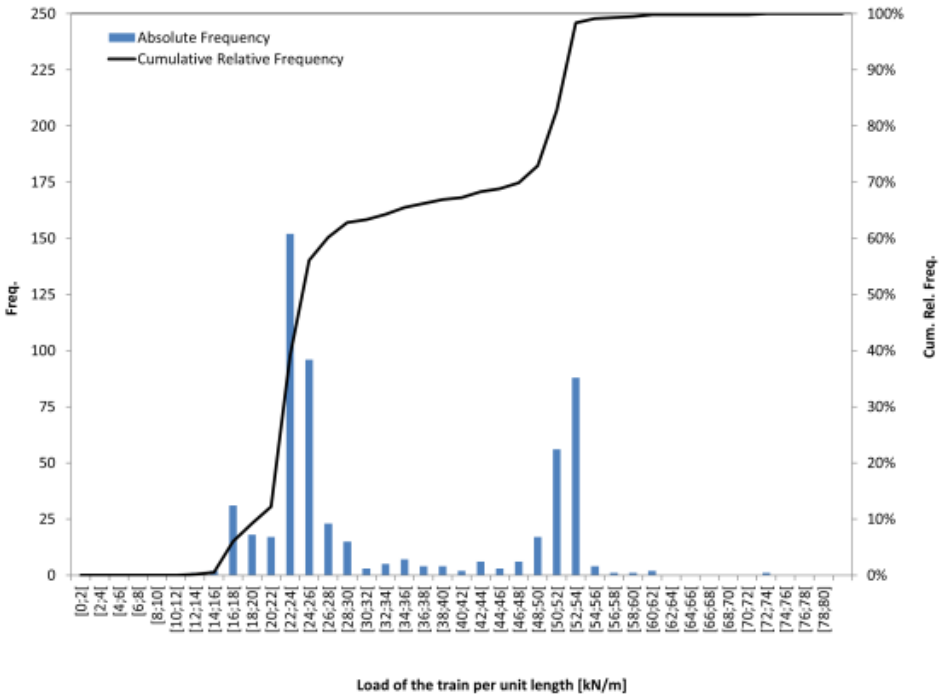

Figure 6.70 - Histogram of the load of the trains per unit length.

Finally, the trains have a maximum number of axles typically below 102 (Figure 6.71).

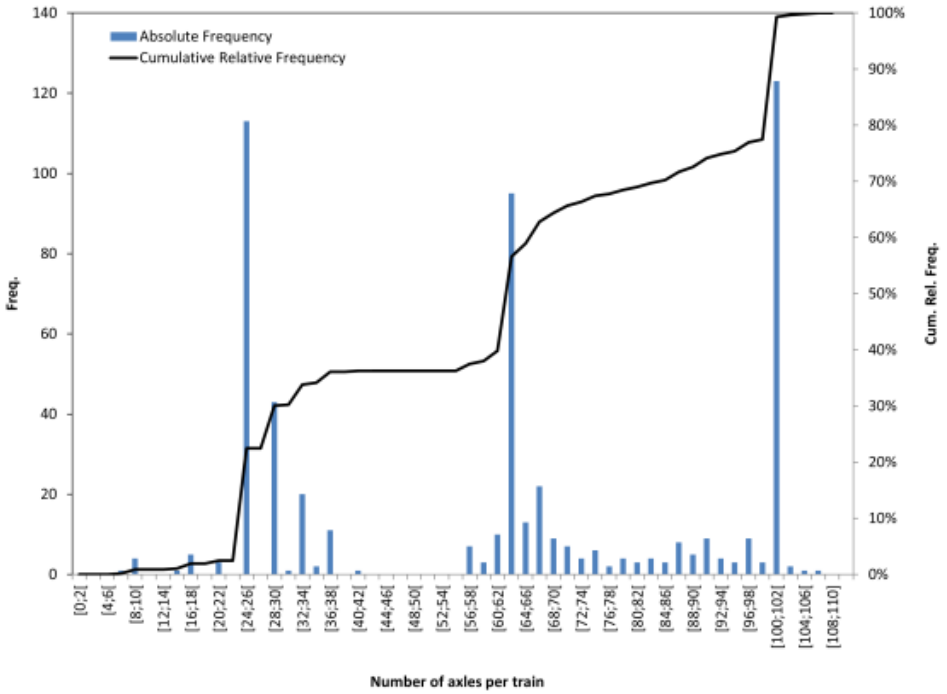

Figure 6.71 - Histogram of the number of axles per train.

6.5.3 Fatigue Damage

6.5.3.1 Monitored details

In the case study, the measured stress histories at the instrumented details (diagonals of diaphragms 51 and 54), for each traffic event, are recorded and available in the database. Those stress histories are obtained from sensors SG 51-1 and SG 54-1 (see Figure 6.62) and can be used to validate the accuracy and efficiency of the proposed methodology.

The first step for that validation consists in comparing the measured stress history with the stress history computed using the proposed methodology, implemented in MATLAB. Figure 6.72 presents three examples of experimental and numerical stress histories, at both strain gauges, showing a good agreement. In that Figure, the traffic event 1 corresponds to a Alfa Pendular passenger train, while traffic events 2 and 3 correspond to freight trains.

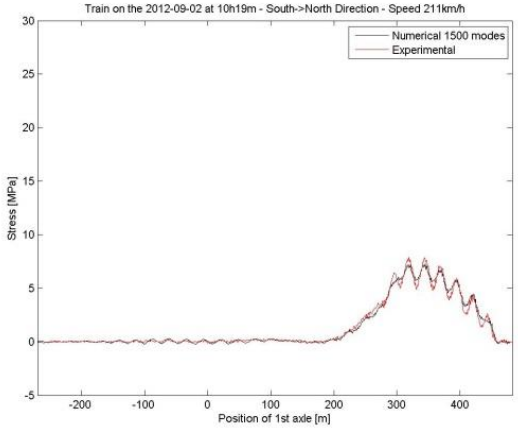

(a) Traffic event 1 - SG 51-1

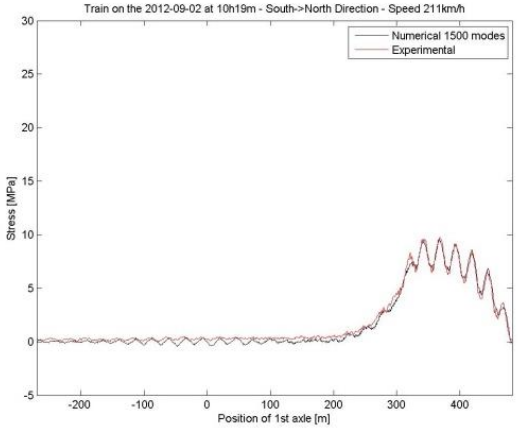

(b) Traffic event 1 - SG 54-1

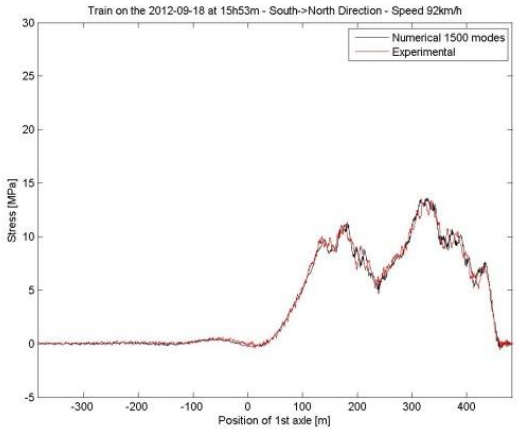

(c) Traffic event 2 - SG 51-1

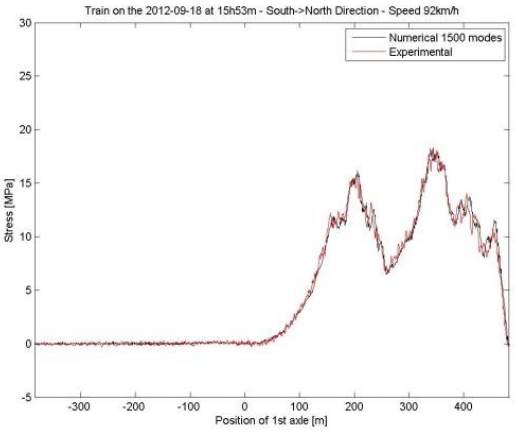

(d) Traffic event 2 - SG 54-1

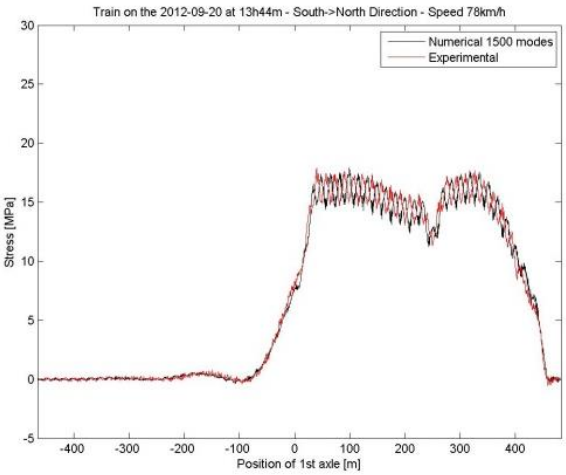

(e) Traffic event 3 - SG 51-1

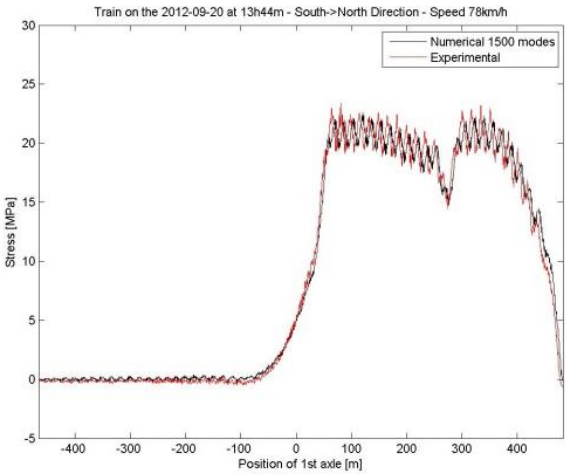

(f) Traffic event 3 - SG 54-1

Figure 6.72 - Experimental and numerical stresses for 3 different traffic events stored at the database.

It was observed that for the same type of trains crossing the bridge, the dispersion on the axle loads does not reflect into a big dispersion on the numerical response obtained. This is particularly evident when analysing several passages of the Alfa Pendular tilting train, at speeds over 200 km/h (Figure 6.73 and Figure 6.74). This characteristic of the long-term monitoring system is of paramount importance, as highlighted by Kolakowski et al. (2011).

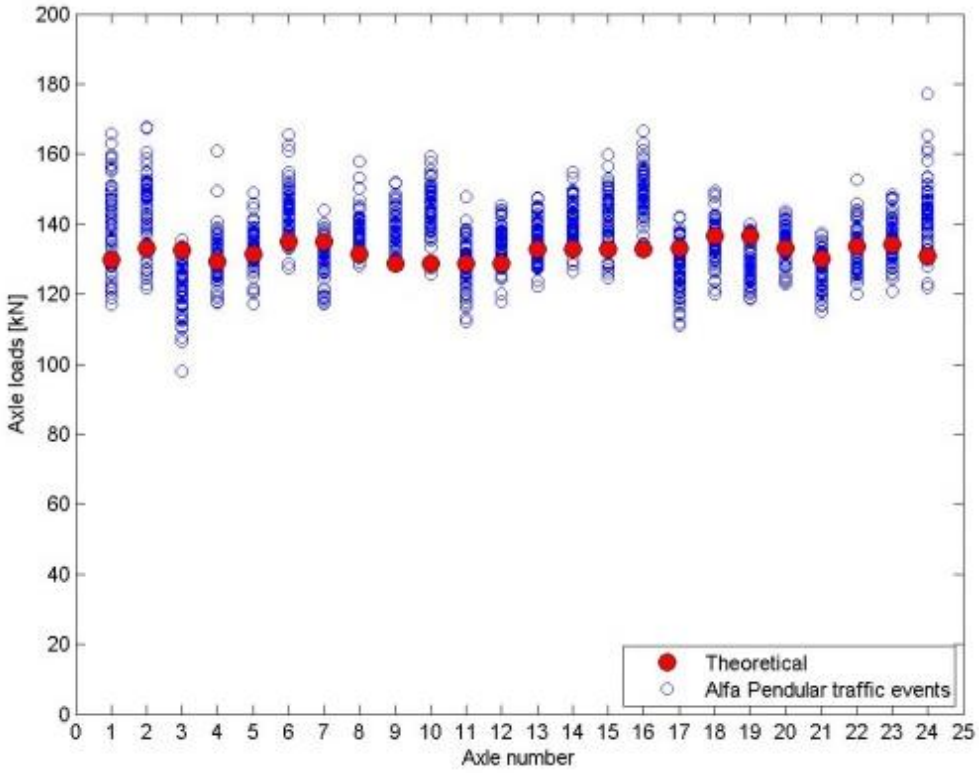

Figure 6.73 - Dispersion of Alfa Pendular axle load measurements.

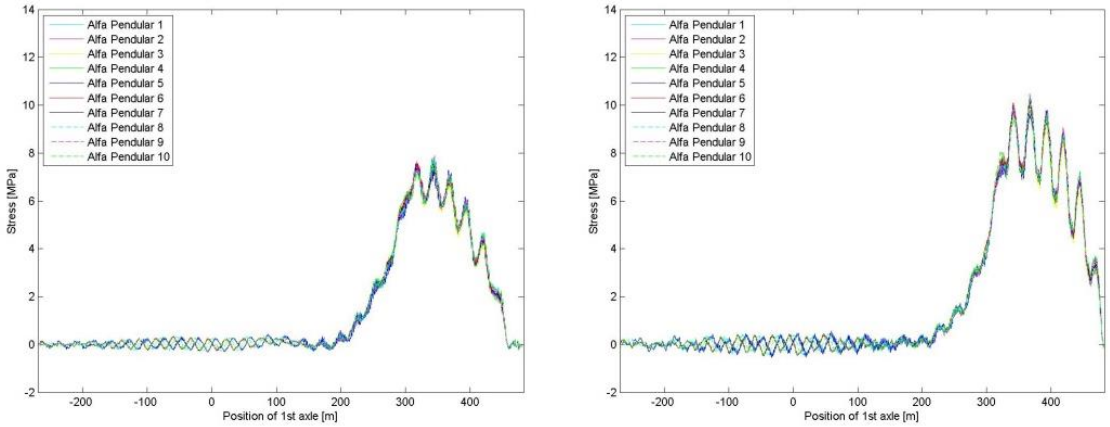

(a) (b)

Figure 6.74 - Dispersion of Alfa Pendular numerical simulation results: (a) SG 51-1 and (b) SG 54-1.

The influence of using an adequate number of modes of vibration in the analysis is illustrated in Figure 6.75:

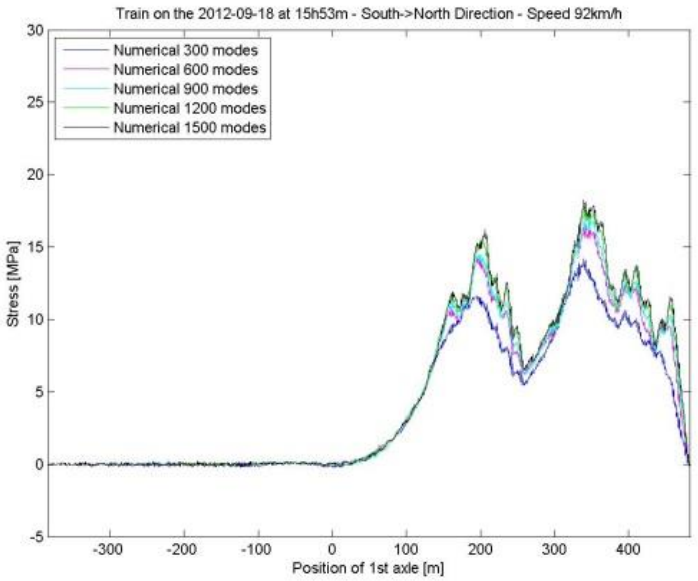

Figure 6.75 - Example of numerical simulation of response at SG 54-1, with increasing number of modes of vibration.

The fatigue damage for those details and for all the traffic events is computed, using the two alternatives: real and numerical stress histories. When plotting the corresponding cumulative damage versus number of traffic events (Figure 6.76) it can be observed that the results obtained using the real and the numerical stress histories are similar. After 565 traffic events, the cumulative fatigue damages obtained by numerical simulations, at the bottom of the diagonals, are only 5% higher and 8% lower than the experimental, for Diaphragm 51 and Diaphragm 54, respectively. In the case of the top of the diagonals, the computed fatigue damage is 5% higher and 10% lower than the experimental, for the same diaphragms.

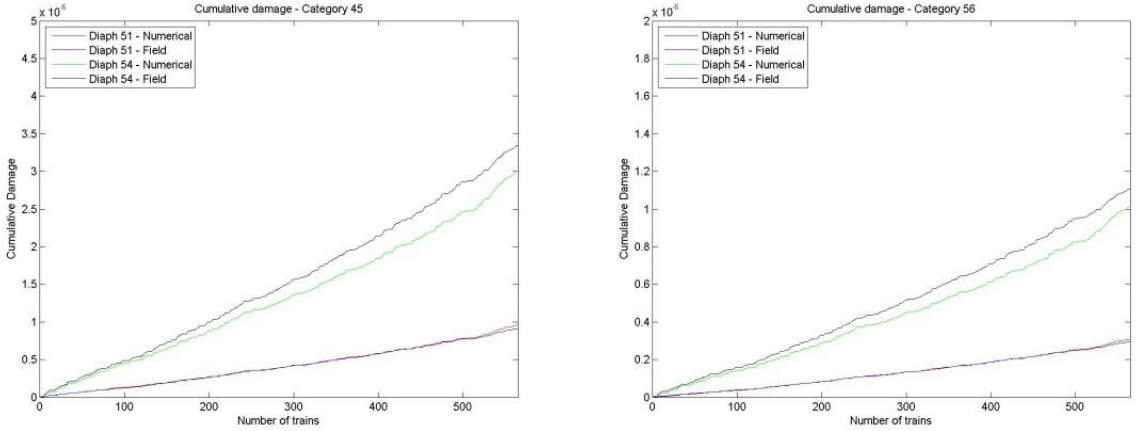

(a) (b)

Figure 6.76 - Cumulative damage at diagonals 51 and 54: (a) detail at the top of the diagonal and (b) detail at the bottom of the diagonal.

The validity of the proposed methodology is then demonstrated. It is important to stress that the higher differences observed at diaphragm 54, between the cumulative damage obtained by numerical simulation and by field measurements are justified by an increased frequency of high stress ranges in the field measurements (Figure 6.77).

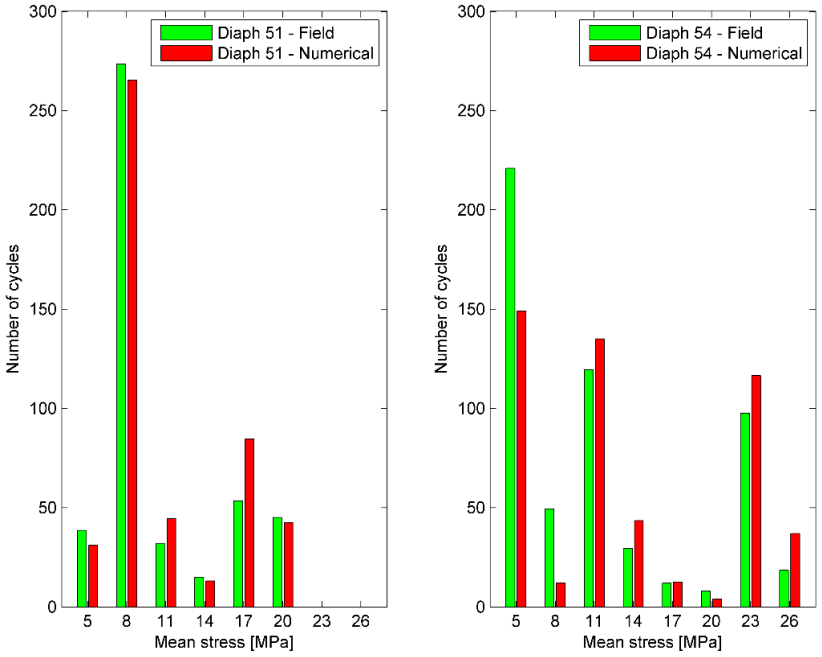

Figure 6.77 - Histograms of stress ranges for numerical and field records at the diagonals of Diaphragms 51 and Diaphragm 54.

6.5.3.2 Extrapolation for non-monitored details

The methodology presented was validated and, consequently, the workflow can then be applied, with a high degree of confidence, to non-monitored details. The only additional information required is the modal stresses at those details (matrix **σ**).

The diagonals of the diaphragms represented on Figure 6.78 were considered as the most critical non-monitored details.

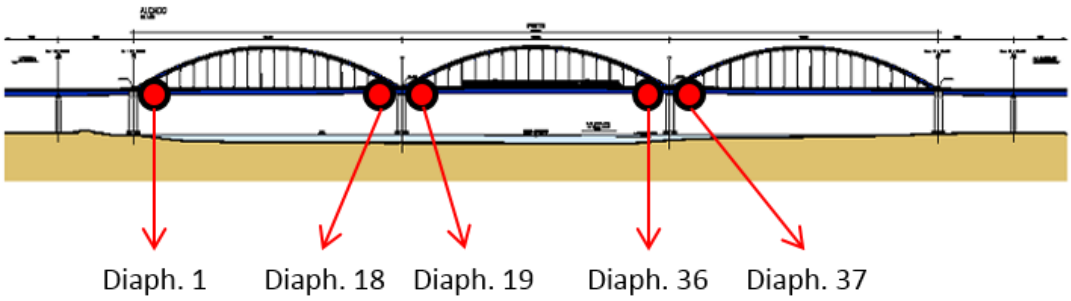

Figure 6.78 - Diaphragms with the most critical non-monitored diagonals.

The result of the numerical simulation of the structural response, at those details and for 2 arbitrary traffic events, is presented in Figure 6.79.

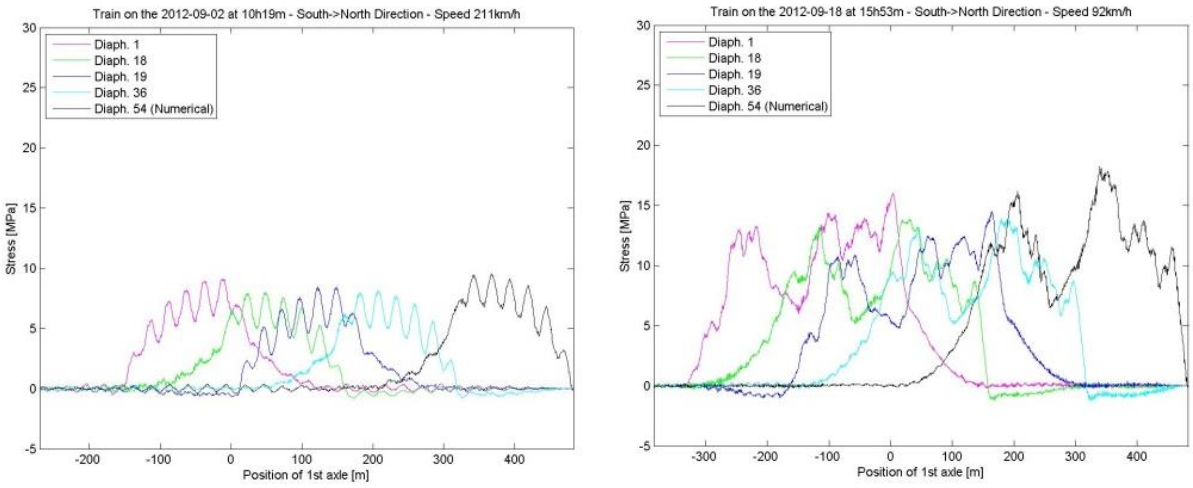

(a) (b)

Figure 6.79 - Simulated stress history at non-instrumented details of the bridge: (a) traffic event 1 and (b) traffic event 2.

The cumulative damage at the identified details, for the traffic events in the period, is represented in Figure 6.80. It can be understood that even if these are the most critical details,

concerning fatigue damage, the total fatigue damage observed in the period is very low, indicating a high lifespan for the bridge.

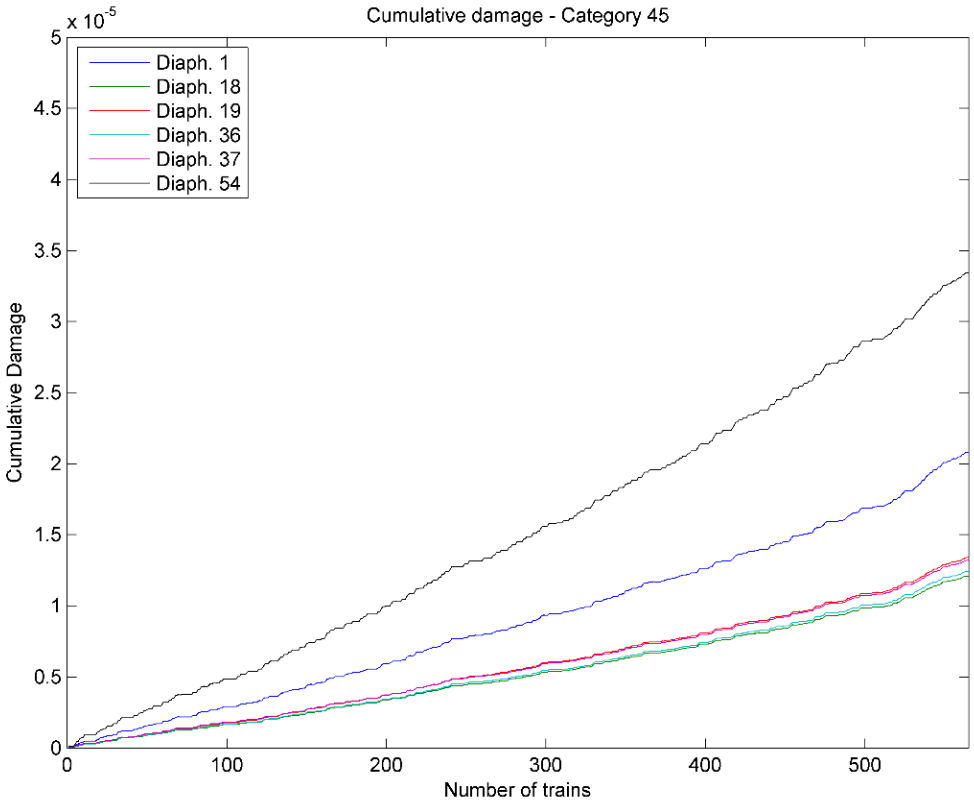

Figure 6.80 - Cumulative damage for non-instrumented details of the bridge – Category 45.

Also, from the analysis of the cumulative fatigue damage for all the diagonals of all diaphragms, Figure 6.81, it can be confirmed that the critical details, concerning fatigue damage, are the diagonals at the extremities of each span. This is justified by the shorter and therefore stiffer hangers at those locations. The diagonals of the diaphragms at the entrance and exit of the bridge, in particular, present higher damage because of the higher dynamic impact observed.

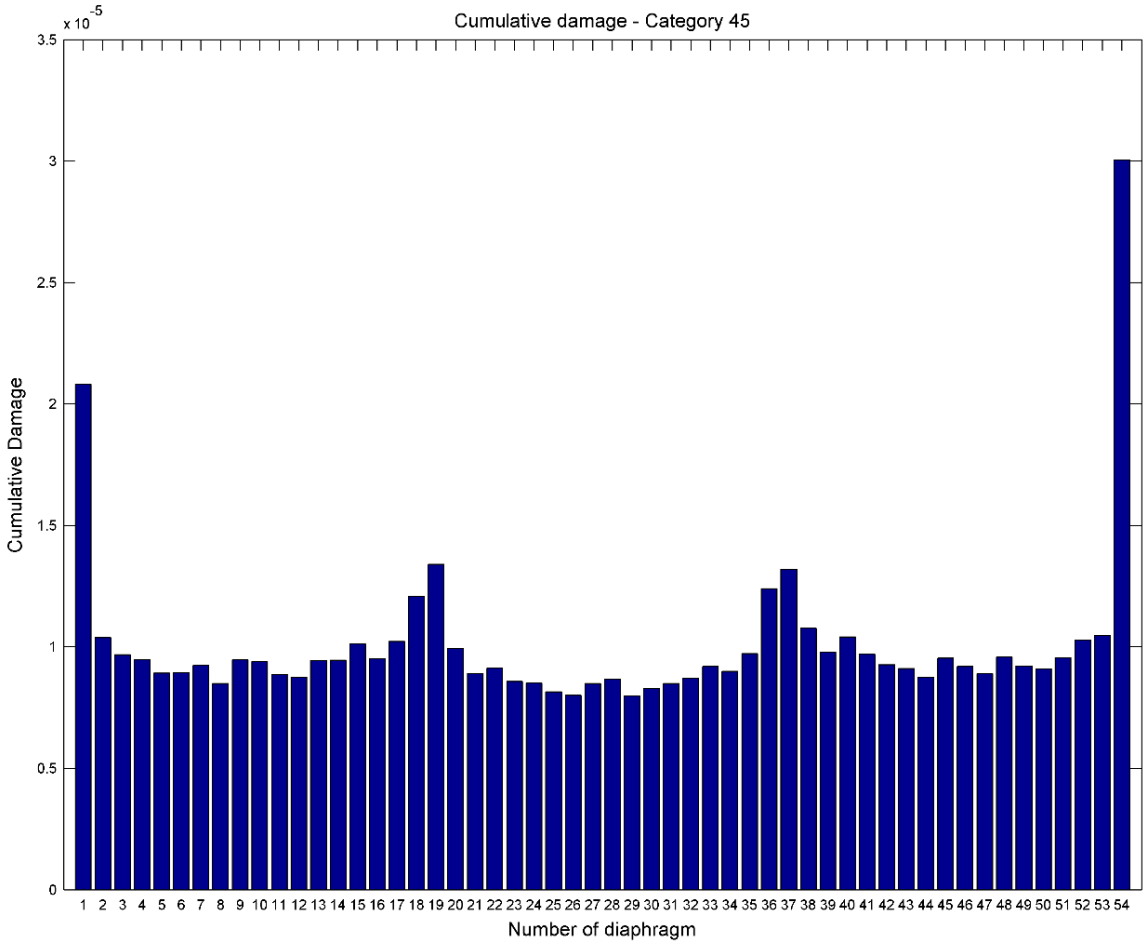

Figure 6.81 - Cumulative fatigue damage after 565 traffic events – Category 45.

6.5.4 Fatigue Damage vs Traffic Characteristics

It can be observed that most of the fatigue damage at the top connection of the diagonals is originated from heavy freight trains (>35 kN/m) circulating at speeds between 70 km/h and 100 km/h (Figure 6.82 and Figure 6.83).

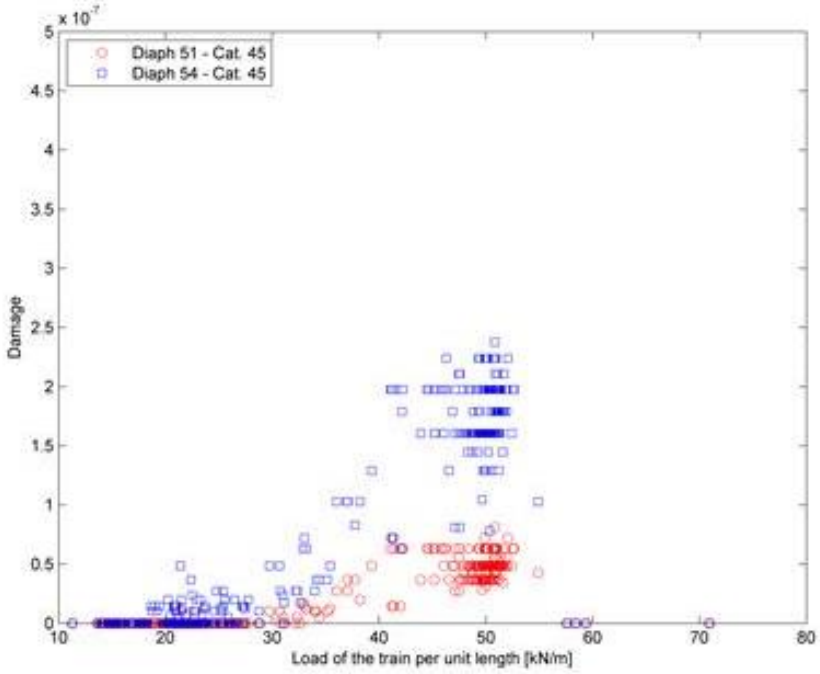

Figure 6.82 - Damage (Diaph. 51 and 54, Cat. 45) *vs.* Train load per unit length.

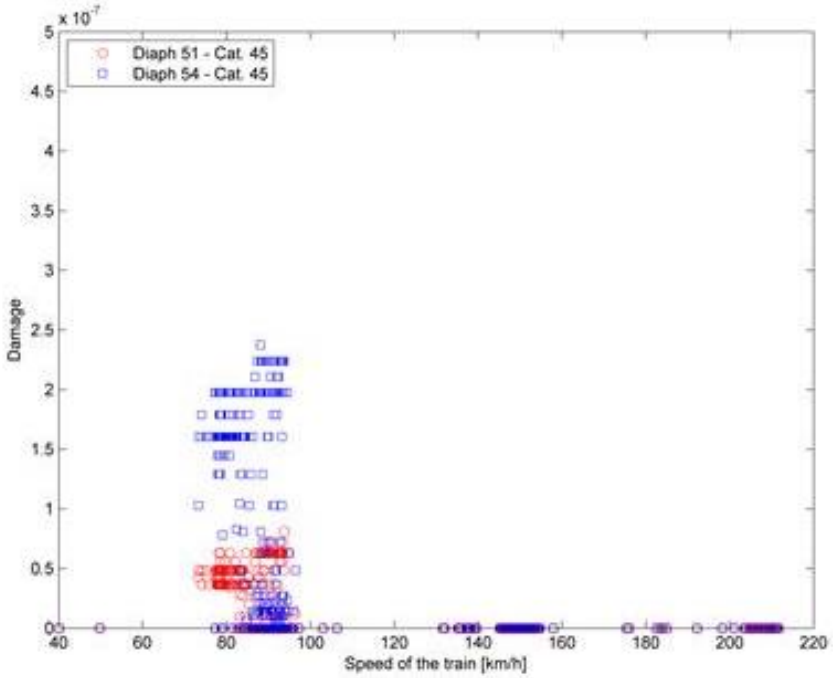

Figure 6.83 - Damage (Diaph. 51 and 54, Cat. 45) vs. Speed of the train.

Two major groups of freight trains contribute to the fatigue damage (Figure 6.84, Figure 6.85 and Figure 6.86):

- Freight trains with total length around 200 m and a total load of 10 500 kN distributed through 62 axles;

- Freight trains with total length around 415 m, total load higher than 20 000 kN and 100 axles.

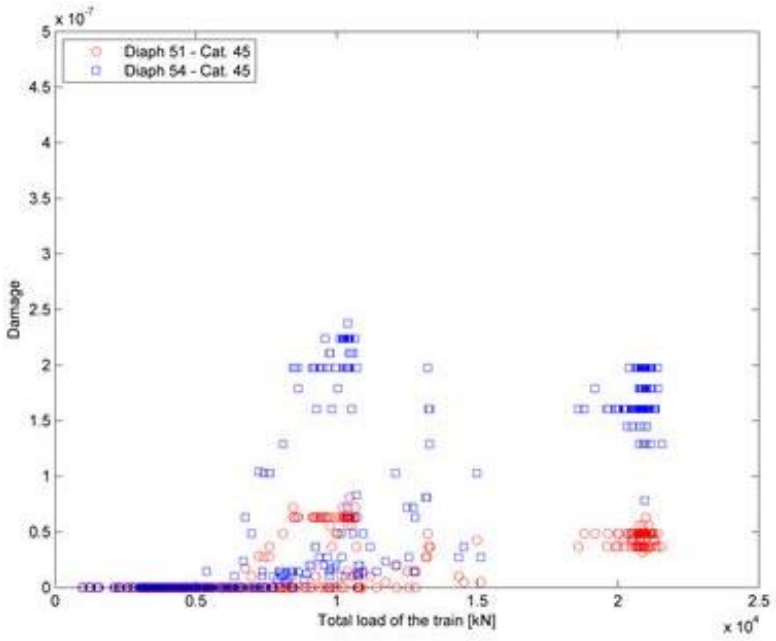

Figure 6.84 - Damage (Diaph. 51 and 54, Cat. 45) vs. Total load of the train.

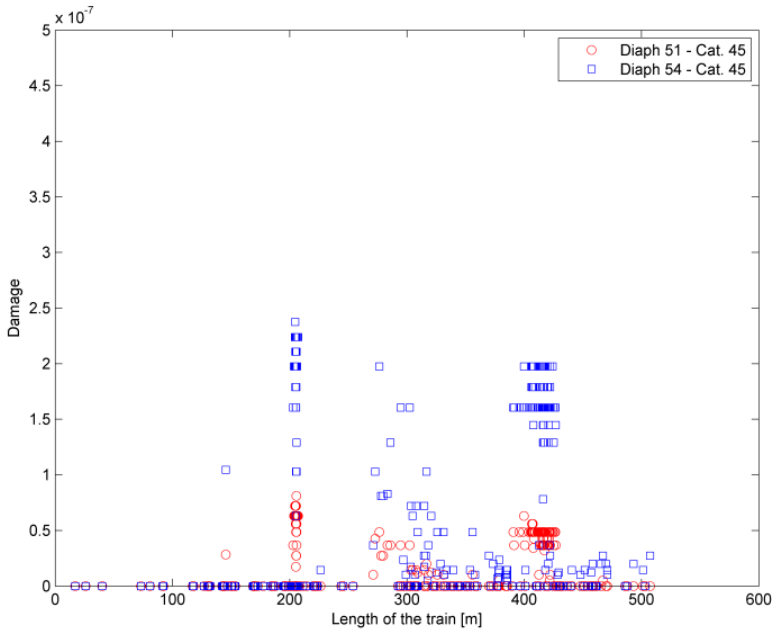

Figure 6.85 - Damage (Diaph. 51 and 54, Cat. 45) vs. Length of the train.

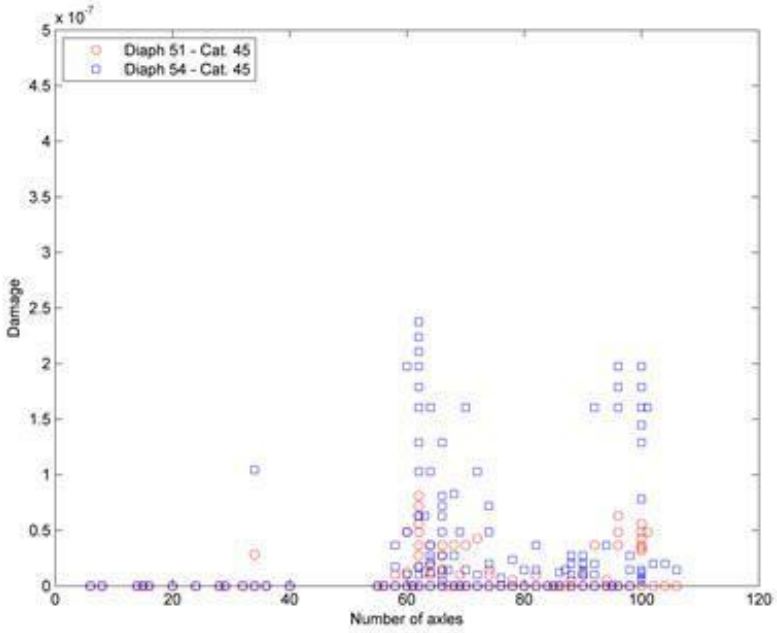

Figure 6.86 - Damage (Diaph. 51 and 54, Cat. 45) vs. Number of axles of the train.

It can then be concluded that the bridge is more vulnerable to distortions/deformations imposed by heavy freight trains, circulating at low speed, than to vibrations induced by passenger trains, circulating at high speed.

The identification and analysis of this correlation between fatigue damage and the type of traffic can be particularly useful for the infrastructure managers.

6.6 CONCLUDING REMARKS

In this Chapter, an innovative methodology for the real time fatigue assessment of long-span railway bridges, combining an affordable long-term monitoring system and minimal computer resources, was presented. The bridge of the new railway crossing of river Sado was used as case study for the validation of the methodology.

The main conclusion concerning the design and implementation of long-term monitoring systems is that the inclusion of a traffic characterization system is of paramount importance for data validation and results extrapolation. The use of shear strain gauges in the rails showed to be a very appropriate technique for axle loads quantification.

Referring to the new method developed and presented in this Chapter, it showed to be very efficient, in order to compute in real time the fatigue damage in the critical details of railway

bridges. Only a very limited set of modal parameters of the numerical model needed to be extracted once, stored in a condensed matrix format (less than 10 MB) and incorporated in the long-term monitoring workflow (with local processing). That limited set of modal parameters allows accurate simulations of the real response of the structure with a very limited computational effort. Another advantage of the current methodology is that the real traffic characteristics are considered. The stress history and corresponding damage at all critical details of the structure can then be computed. In the details where strain gauges are installed, the comparison between the numerical simulation and the measurements allows confirming the adequacy and robustness of this approach.

The proposed method also allowed to identify the type of traffic that contributes the most to the fatigue damage at the critical details of the bridge, an information that can be particularly useful for the infrastructure managers.

In the specific case of the bridge of the new railway crossing the river Sado, the most critical details to fatigue are the diagonals of the diaphragms, namely those at the extremities of each span of the bridge. The trains that may contribute the most for fatigue damage are the freight trains. Nevertheless, the estimated cumulative damage at those details, after 565 traffic events, is very low. Passenger trains led to almost null fatigue damage, according to the assessment performed.

In this Chapter, the fatigue analysis of the case study bridge was performed based on S-N curves and nominal stresses. In Chapter 7, the new methodology described in Chapter 5 is employed in the simulation of fatigue crack propagation in one of the critical details of the same bridge.

Chapter 7

ADVANCED FATIGUE ASSESSMENT OF THE BRIDGE OF THE NEW RAILWAY CROSSING OF RIVER SADO

7.1 INTRODUCTION

In Chapter 5, a new methodology for the efficient crack analysis of dynamically loaded structures was presented and validated with a simple example. Chapter 6, on the other hand, showed how a long-term monitoring system, when combined with modal information retrieved from a calibrated numerical model, can be used to compute the fatigue damage at critical details of a railway bridge, in real time. It was highlighted that such a long-term monitoring system would need to be able to both monitor structural behaviour and characterise traffic.

In Chapter 7, the methodology described in Chapter 5 is combined with the workflow described in Chapter 6, in order to achieve the real time simulation of fatigue crack propagation in a detail of the case study bridge, due to real traffic, in a computationally efficient way (Albuquerque et al., 2015b). The bridge is an example of a composite structure with both steel and concrete combined to form a box girder deck. As demonstrated in Chapter 6, most of the connections between the steel elements are performed by welding and as discussed in Chapter 2, weldments are typical locations for fatigue crack initiation. The length and direction of each fatigue crack increment is determined in the simulation according to Fracture Mechanics principles. The local time-history data needed for the fatigue damage assessment is generated

using the new concept of modal stress intensity factors and the modal superposition method, as per Chapter 5 (Albuquerque et al., 2012a). The loading considered in the simulation is composed by the traffic events obtained with the long-term monitoring system and stored in the database, as described in Chapter 6 (Albuquerque et al., 2015a). To illustrate the efficiency of the proposed method, a hypothetical scenario of fatigue residual life assessment is presented herein.

In addition, if we refer to the previous Figure 4.25 in Section 4.5.5, and as mentioned before, any fatigue crack propagation analysis requires the adequate crack propagation law to be defined. In the case of the bridge of the new railway crossing over river Sado, these crack propagation laws were characterised experimentally through tests performed on Compact Tension (CT) specimens and following well-established procedures such as ASTM E647 (Albuquerque et al., 2012b). This experimental work is described in Section 7.2.

The tests investigated crack propagation through base material (BM), weld metal (WM) and heat affected zone (HAZ). The specimens are of the same steel grade and weldments followed the same welding process as in the construction of the critical details (diaphragm's diagonals) of the real structure. It was also intended to perform the fatigue crack growth rate (FCG) testing using CT specimens with the thickness of the structural details of interest, as it is recognised that thickness has an influence on fracture behaviour. Since the origins of crack opening displacement testing, it has been specified that testing should be done using specimens with the same thickness of the construction or structural detail of interest, *e.g.* (BSI, 1979). Nevertheless, the final thickness adopted for the specimens is slightly lower than the thickness of the welded plates from which the specimens were extracted, since due to the distortion associated with the welding process it would be impossible to have specimens containing weld and flat surfaces keeping the original plates thickness. However, the difference between thicknesses (32 mm in the specimens *versus* 35 mm in the original welded plate) is considered to have little impact on the obtained results.

Furthermore, although these tests have been the object of standards for a long time, they still pose challenges, particularly in cases where the specimens' material is not homogeneous and when there are internal stresses in the specimen, such as residual stress fields originated from the manufacturing process. These two situations are commonly found when testing specimens that include weldments. The behaviour of such specimens may be slightly influenced by residual stress when their dimensions are small and unable to retain the residual stress state of the original

structure. However, considering larger specimens, the effects of residual stresses may be significant, and the interpretation of the tests becomes more challenging. That is the case of the tests undertaken and described in Section 7.2.

Finally, it should be referred that since the fractographic analysis of the failure surfaces of structural components is considered an important method to interpret the causes of fatigue failures, two of the fatigue tested CT specimens were the object of Scanning Electron Microscopy (SEM) analysis, namely, one BM specimen and one HAZ specimen. Observed striations are assumed to be a product of fatigue, with each striation corresponding to a load cycle. However, not all the load cycles seem to produce striations and not all the striations have an orientation perpendicular to the direction of the macroscopic crack growth. Moreover, there are divergent opinions regarding the influence of existing residual stresses on the striations spacing. These discussions are also addressed in next Section.

7.2 ASSESSMENT OF THE FATIGUE CRACK PROPAGATION STRENGTH

7.2.1 Fatigue crack growth tests

7.2.1.1 Experimental details

CT specimens according to the ASTM E647 (ASTM, 2000) were machined from welded plates approximately 1 m long and 230 mm wide. A butt weld with a double V preparation joined the plates along their longer side. According to the welding procedure qualification followed for the bridge, the welding process was the flux-cored wire metal-arc welding with active gas shield (welding process 136, according to EN ISO 15614-1:2004), with a 100ºC preheating and an inter-run temperature lower than 250ºC. The welding sequence included multi-run welding on alternate sides of the plate and the filler metal was the MEGAFIL 710 M. The preparation dimensions were a thickness of root face of 2 mm, a gap of 3 mm and a bevel angle of 60º. The welds were ground flushed during the machining process. As mentioned above, the CT specimens were extracted from three different locations, sampling base material (BM), weld metal (WM) and heat affected zone (HAZ), always with the initial notch (and cracking plane) parallel to the weld line. The dimensions were a thickness (B) of 32 mm, a width (W) of 132 mm, an overall width of 165 mm and an overall height of 158.4 mm. The double V preparation of the original plates implied that the specimens identified as HAZ actually sample the heat affected zone close to the original plate's free surfaces and base metal in the mid thickness. The specimen

geometry used is presented in Figure 7.1, whereas Figure 7.2 schematically shows the location of the WM and HAZ specimens.

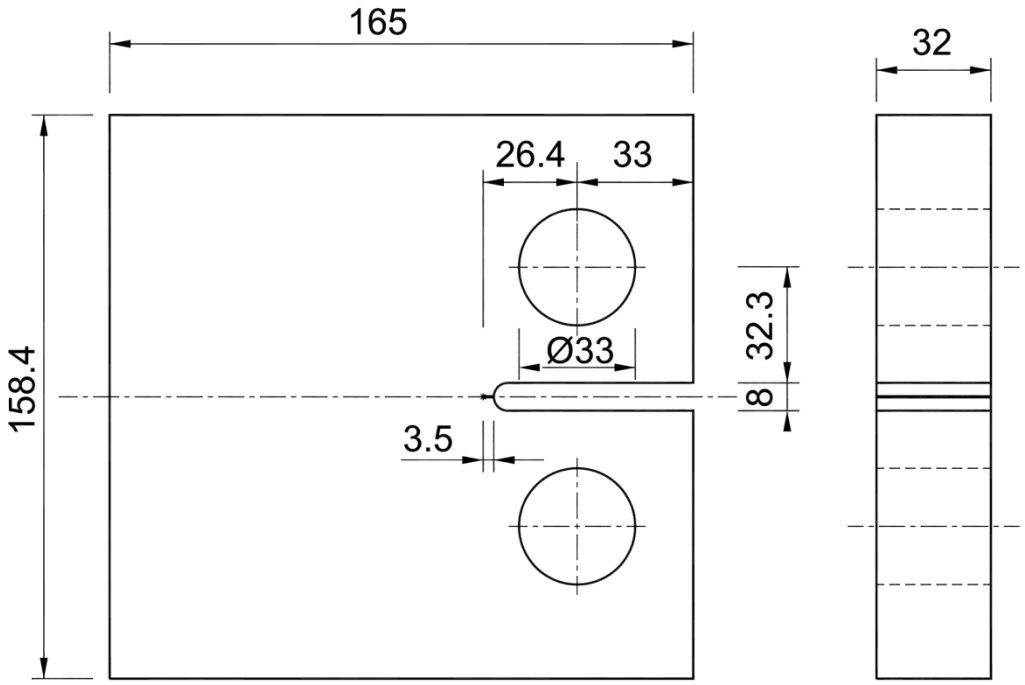

Figure 7.1 - CT specimen.

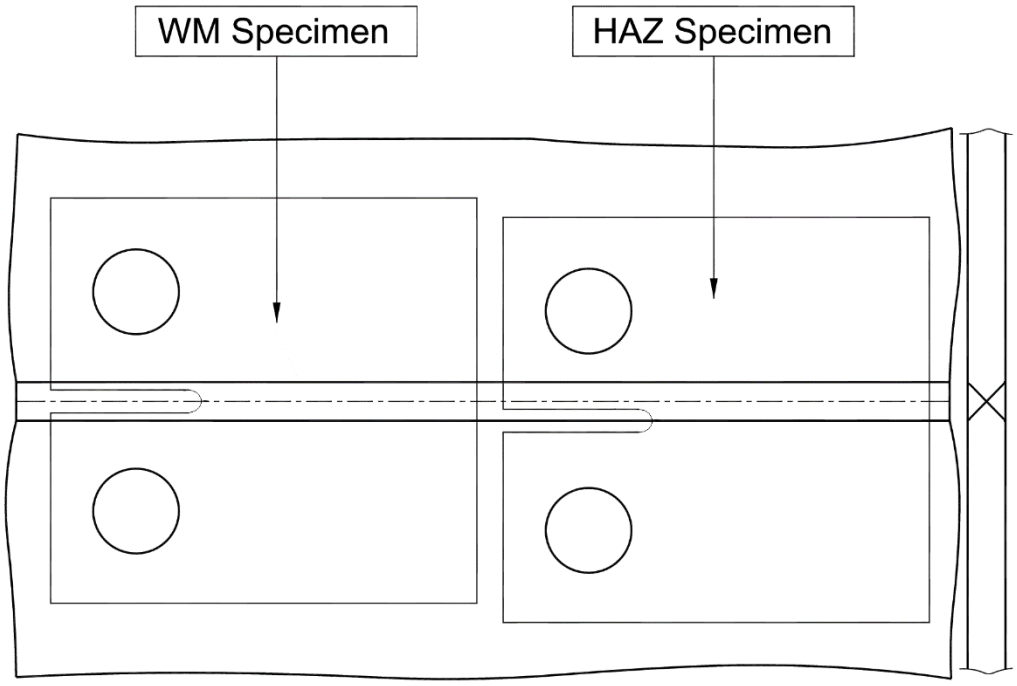

Figure 7.2 - Schematic representation of the location of specimens containing weldments.

The notch used was obtained through two different techniques; up to a certain distance from the load line the notch was machined by simple milling with a tool perpendicular to the specimen face, and the last 3.5 mm of the initial notch were obtained using a wire electrical discharge machining (EDM) equipment leaving a final notch tip radius of 0.15 mm. A fatigue pre-crack was grown starting from this EDM notch, making sure that the maximum loads were low enough in order to limit plastic deformation at the crack tip, in accordance with (ASTM, 2000). Pre-cracking was performed under $R = P_{min}/P_{max} = 0.1$, where P is the applied load.

The servo-hydraulic MTS testing machine used had a 250 kN load capacity, and the testing frequency was chosen to be between 6 and 10 Hz depending on the actual load of each specimen. Travelling microscopes (20x magnification) were used on each side of the specimen to make periodic readings of current crack length a as a function of number of cycles N.

The base material used was the steel grade S355NL according to EN 10025, EN 10029 and EN 10163, with the chemical composition presented in Table 7.1. Some basic mechanical proprieties are given in Table 7.2. Both the chemical composition and the mechanical properties were provided by the material supplier.

Table 7.1 - Chemical composition of the S355NL steel (base material).

Steel grade	Sample	C (%)	Si (%)	Mn (%)	P (%)	S (%)	Al (%)
S355NL	A	0.14	0.28	1.23	0.013	0.004	0.027
	B	0.13	0.24	1.11	0.011	0.005	0.022

Steel grade	Sample	N (%)	Cr (%)	Cu (%)	Ni (%)	Ti (%)	V (%)	Nb (%)
S355NL	A	0.007	0.008	0.31	0.29	0.016	0.044	0.001
	B	0.007	0.006	0.25	0.27	0.013	0.043	0.001

Table 7.2 - Some mechanical proprieties of the base material.

Steel grade	Sample	R_{eh} (N/mm^2)	R_m (N/mm^2)	Elongation (%)	Charpy (J) at T= -50º
S355NL	A	400	557	27.7	176
	B	405	516	30.2	118

Measurements of the Vickers hardness (HV) were carried out in the weld metal, using a 20 kgf weight (Figure 7.3). The variation of hardness through the thickness, in the weld metal zone, revealed some dispersion of results, with the higher values present at the weld root (HV≈260) and the lower values at the surface (HV≈180). This variation is explained by the deposition

sequence of the weld metal, which led to two different types of microstructures: a columnar microstructure (dendritic) due to solidification and a recrystallised microstructure, in the inter-run zones, that resulted from the thermal cycle (heating and cooling) of the subsequent run. At the weld root, higher cooling rates during the welding process led to the higher hardness. In spite of that, different authors refer that variations in the microstructure have low influence in the fatigue crack propagation rate, in the region where the Paris' law apply (Ritchie, 1977). Furthermore, the fatigue crack propagation rates in the WM or HAZ are usually equal to or less than the fatigue crack propagation rates in base material (Barsom and Rolfe, 1999). Therefore little consequences of the microstructure heterogeneity of weld metal are expected in the test results.

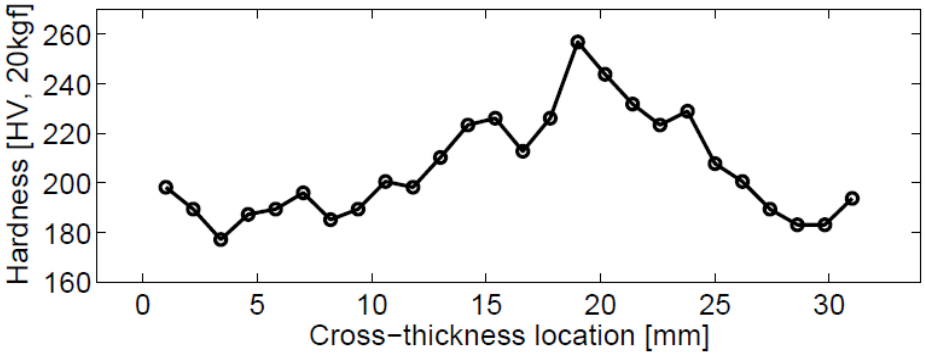

(a)

(b)

Figure 7.3 - Vickers hardness measurements: (a) hardness and (b) macrostructure.

In order to characterise the fatigue crack propagation of the base material, welded material and heat affected zone, a test matrix of nine cases was adopted, with three different *R* ratios: 0.1, 0.4 and 0.7.

As mentioned before, in the absence of residual stresses, the characterization of fatigue crack propagation of base material is generally simple, since the tests usually have straightforward interpretation (ASTM, 2000). The results obtained for the base material, tested under the three

values of *R*, are presented in Figure 7.4, where each straight line corresponds to the best fit of the Paris' Law to the data of the type presented in Figure 7.5, consisting of an example of base material specimen tested under $R = 0.1$. The data was determined according to the ASTM E647 standard (ASTM, 2000).

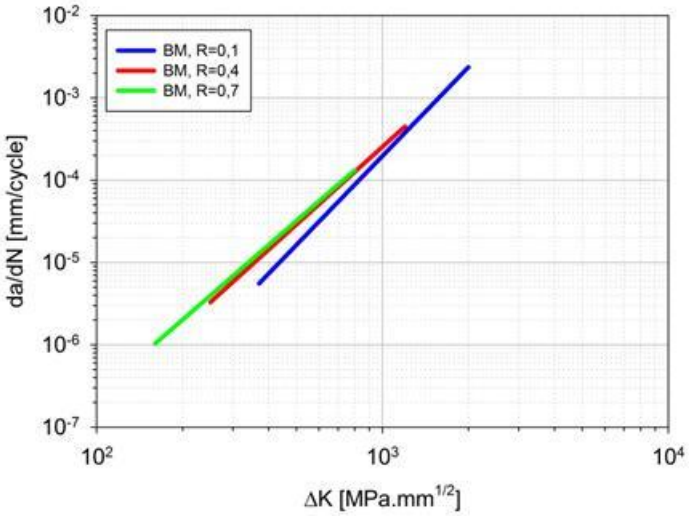

Figure 7.4 - Base material da/dN vs. ΔK data for the three R values tested.

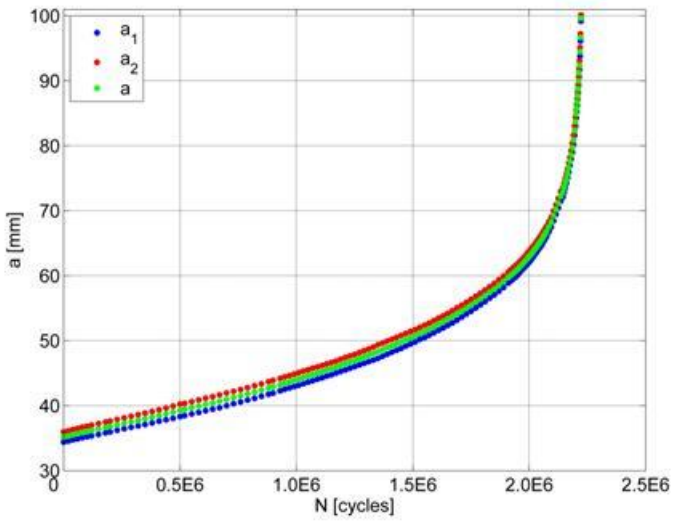

Figure 7.5 - Example of *a vs. N* data obtained – case of a BM specimen tested under $R = 0.1$, showing crack lengths on both sides (a_1 and a_2) and average crack value *a*.

However, when testing specimens containing welds (either WM or HAZ specimens), a rather more complex behaviour was found. Firstly, pre-cracking implied the use of load levels substantially higher than those used for the base material specimens. Secondly, at the start of the

actual tests, a decreasing crack growth rate with increasing crack length was found, under constant amplitude loading.

This behaviour was attributed to residual stress and consequent crack closure effects. Higher loads had to be used for pre-cracking. The first of these specimens was completely opened revealing the fracture surface, and an unusual crack pattern was found, as depicted in Figure 7.6. The interpretation of this figure is coherent with the unexpected behaviour of decreasing da/dN with increasing a (and N) that was found and mentioned above. In its early stages, which lasted an unusually long number of cycles, the crack was not a through crack; during those initial stages, the mid thickness part of the specimen did not present crack growth and the crack was just growing at the two surfaces of the specimen; the existence of an uncracked central region would therefore delay the propagation.

Figure 7.6 - Fracture surface in the end of the test (HAZ, R = 0.1).

7.2.1.2 Discussion of the results

In order to provide an explanation for the observed surface crack behaviour (also reported in an early work by Mills and James (1987)), an attempt was made to model this particular situation using a 3D finite element model and the commercial ABAQUS software package. The purpose was to determine the stress values on the free surfaces of the specimen, in the direction normal to the crack plane, for two representative cases depicted in Figure 7.7, and to try to explain the unexpected deceleration of the crack propagation rate. This figure shows two schematic representations of two stages of the crack propagation that led to the actual fracture surface

photographed in Figure 7.6. In the left diagram, the situation corresponding to a visible fatigue crack with tip at point A is shown, whereas the right diagram shows a subsequent moment where the visible crack tip is at point B. There is no claim of precise correspondence of the geometry shown in Figure 7.7 and actual crack scenarios in the specimen; the aim of this exercise is to evaluate if, for a crack growth pattern of the same type as that experimentally observed, stress at region A would be higher or lower than at region B, for identical loads applied to the specimen. The stress values obtained near the tip of the visible cracks, for the two situations considered in the model, are approximately 40% lower for the longer crack (point B) than for the shorter crack (point A), justifying the deceleration in the crack propagation rate observed in the early stages of the FCG test of this HAZ specimen.

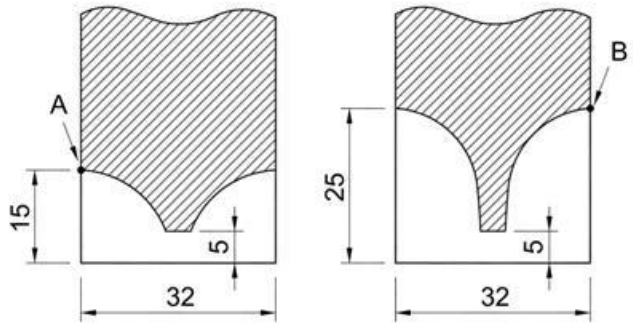

Figure 7.7 - Representation of the two exemplary cases studied for determination of the influence of the not-cracked zone on different crack lengths.

The initial test presenting the features mentioned above raised the need for a measurement of residual stresses and closure effects. Such complementary studies were performed by other authors that had identified similar behaviours earlier. Beghini and Bertini (1990) used the sectioning technique, based on strain gauges bonded to the surface of the specimen close to the crack line, to identify compressive stresses near the crack tip of welded steel specimens, albeit with a different thickness and material. These authors also adopted the back face strain gauge technique to identify the crack opening load P_{op}, and therefore the effective amplitude of the stress intensity factor range, $\Delta K_{eff,}$ which is a function of (P_{max}-P_{op}), as ΔK is a function of (P_{max}-P_{min}). This procedure was also adopted by Kitsunai (1983a, 1983b), whereas in Kitsunai et al. (1998) it was used the X-ray diffraction with the $\sin^2\psi$ method, with a parallel-beam diffractometer. However, both the sectioning and X-ray diffraction methods only provide information on residual stresses close to surface and, therefore, do not provide all the required information for the current case.

While the back face strain gauge is an established technique to deal with the opening load effect, the sectioning method for residual stress evaluation cannot provide enough insight into the peculiar crack front behaviour mentioned above (see Figure 7.6). This clearly requires full field measurement of residual stress along the crack plane, not just information on the residual stress state near the surface.

The contour method (Prime, 2001) was chosen for residual stress measurement. A full map of residual stresses perpendicular to the surface of interest may be obtained using this technique. The contour method is a relaxation-based technique. First, a wire EDM cut is performed through the specimen, revealing the section of interest. In a second step, the displacement of the new free surfaces is measured precisely using a coordinate measuring machine and in the third and fourth steps the obtained data are treated and applied to a finite element method model for stress calculation based on the measured displacement. Only the stresses on, and perpendicular to, the free surface are retrieved from the model. These stresses represent the relaxed residual stresses when the straight cut was performed. Figure 7.8 shows the measured residual stresses for a specimen with the notch in the middle of the weld nugget. Details concerning this residual stress measurement are available in (Richter-Trummer and de Castro, 2011). Rading (2005) presents residual stress measurements for a different welded steel CT specimen, with different thickness, using neutron diffraction. No full field measurement is provided in that work; nevertheless, in the regions where a comparison could be made, the trend of the residual stress data of (Rading, 2005) is similar to the one presented here. Mochizuki (2007) presents the through thickness variation of residual stress, obtained with the inherent strain method, for a X-shaped groove with a lower thickness and a different welding sequence. The pattern of residual stress distribution was also similar to the one presented for the observed specimens.

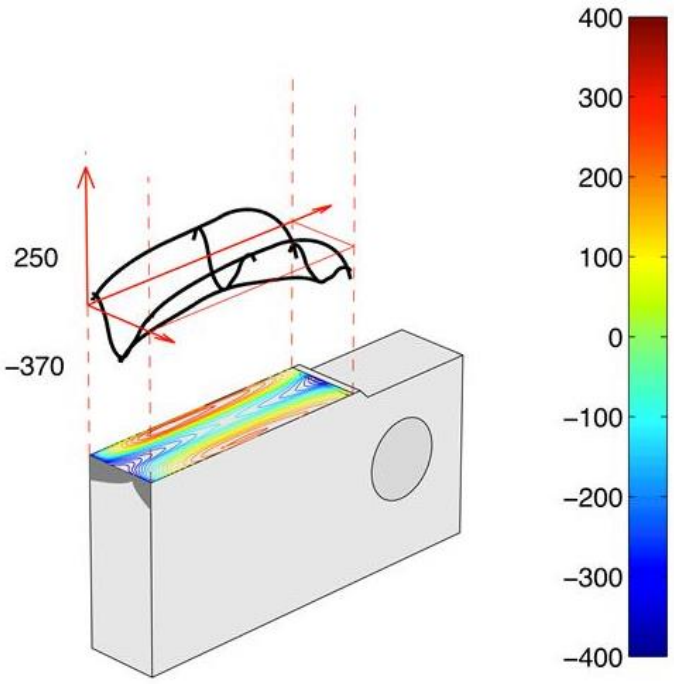

Figure 7.8 - Residual stress perpendicular to the surface where the crack is expected to grow (Richter-Trummer and de Castro, 2011); the max. and min. residual stress values (MPa) are indicated in the vertical axis.

In the mid-thickness of the specimen, compressive residual stresses are found, and the highest values appear in the middle of the EDM notch front. This may explain the observed crack growth behaviour in the case of these thick welded specimens. Furthermore the crack front shown in Figure 7.6 may be better understood based on this residual stress distribution.

It was shown that in situations where there is an important variation of the residual stress state through the thickness, the measurement techniques providing information on residual stress only near the surface (*e.g.* sectioning technique), or the techniques averaging residual stress effects (*e.g.* cut compliance method used by Lados and Apelian (2006)), will not provide adequate interpretation of the specimens' behaviour. However, thinner specimens, where no significant variation of residual stress through the thickness is expected, may be analysed successfully using such techniques.

The difference between fatigue crack growth tests using base material and welded material has been identified by several authors. In the present work, the measured *da/dN vs.* nominal ΔK data displays a strong influence of the weldments on the FCG rates, with the base material presenting higher *da/dN* values. An evaluation of opening load behaviour was therefore carried out, and it showed extensive closure caused by residual stresses in the HAZ and WM specimens.

This evaluation was achieved by bonding strain gauges to the face opposite to the crack front of each HAZ and WM specimen. The inflection points in the measurements performed with the strain gauges allowed to identify the opening load (P_{op}) and to compute the effective stress intensity factors ΔK_{eff}, as mentioned before. Higher test loads were considered after the understanding of the crack closure effects present in the first HAZ specimen tested. For these higher loads, the cracks in the specimens were always through cracks and consequently, their length was computed according to standard procedures.

Having discussed the special circumstances of the specimens used in the present FCG tests, the results obtained will now be presented. The results for base material specimens were already shown in Figure 7.4 above. The *da/dN vs.* ΔK data for weld material and HAZ specimens are represented in Figure 7.9 and Figure 7.10 respectively.

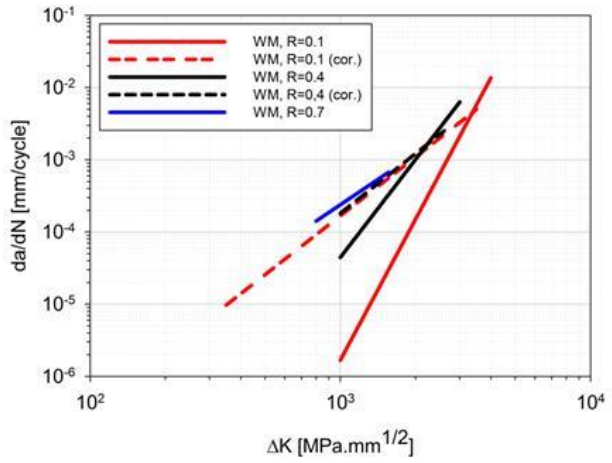

Figure 7.9 - Weld material *da/dN vs.* ΔK data for the three R values tested ('cor' - ΔK_{eff}).

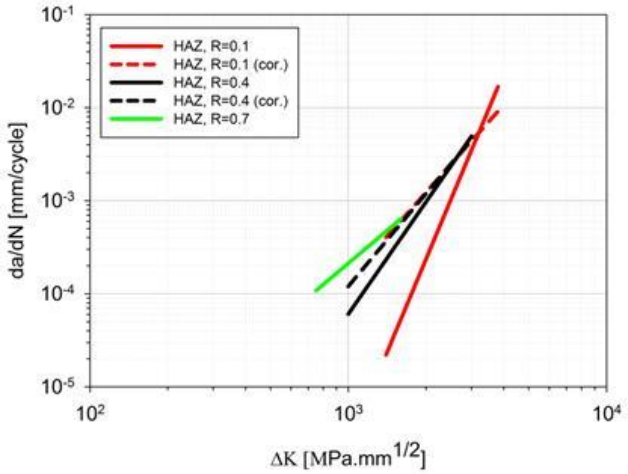

Figure 7.10 - Heat affected zone material *da/dN vs.* ΔK data for the three R values tested ('cor' - ΔK_{eff}).

Constants C and m of the Paris law (Equation (7.1)) for the three types of specimen (BM, WM and HAZ) and for the three nominal load ratios considered (0.1, 0.4 and 0.7) are shown in Table 7.3, where data obtained is presented together with the respective R^2 values (coefficient of determination).

$$da/dN = C\,(\Delta K)^m \tag{7.1}$$

When the opening load effect was taken into consideration, it was found that the *da/dN vs.* ΔK_{eff} of the BM, HAZ and WM specimens is approximately identical. If opening load effects are considered, the difference between the FCG rates for the three *R* values is small, even if, as expected, higher *R* values correspond to higher FCG rates.

Table 7.3 - C, m and R^2 for the several specimens.

	Load ratio R	*C* [a]	*m* [a]	R^2
BM	0.1	6.83E-15	3.48	0.99
	0.4	9.93E-14	3.14	0.99
	0.7	3.47E-13	2.95	0.96
HAZ	0.1 [b]	5.72E-14	3.13	0.99
	0.1 [b]	5.53E-15	3.43	0.98
	0.4 [b]	1.31E-14	3.31	0.97
	0.7	6.20E-13	2.83	0.92
WM	0.1 [b]	2.85E-13	2.91	0.97
	0.4 [b]	1.02E-12	2.75	0.98
	0.7	1.39E-12	2.73	0.94

[a] for *da*/*dN* in mm/cycle and *ΔK* in MPa·$mm^{1/2}$;
[b] data corrected for closure effects induced by residual stresses.

7.2.2 Fractographic analysis

7.2.2.1 Experimental details

In order to complement the information that was gathered, a fractographic analysis was performed at CEMUP (*Centro de Materiais da Universidade do Porto*), with key contributions from Miranda, R.M.C., Richter-Trummer, V. and Figueiredo, M.A.V., co-authors of (Albuquerque et al., 2012b).

Fracture surface samples of CT fatigue tested specimens were observed using an high resolution (Schottky) environmental scanning electron microscope with X-ray microanalysis and backscattered electron diffraction pattern analysis: FEG-ESEM / EDS / EBSD : FEI Quanta 400 FEG ESEM / EDAX PEGASUS X4M. The dimensions of the specimens were compatible with the SEM equipment (surface area of approximately 32mm x 100mm). The analysed specimens were one BM specimen tested under load ratio R = 0.4 (specimen CT3), and one HAZ specimen tested under R = 0.1 (specimen CT2). 40 micrographs were obtained for the BM specimen (CT3) and 123 micrographs were obtained for the HAZ specimen (CT2), sampling the area of crack growth; in the case of the HAZ, the higher density of micrographs was taken at the initial fatigue crack growth region, ahead of the initial wire electro discharge machining (w-EDM) notch.

Figure 7.11 shows the crack plane, the w-EDM notch front, and a region where, in the case of the HAZ specimen, the higher number of observations was made. Several micrographs of the region of initial fatigue crack propagation were obtained, and assembled together in order to provide a complete imaging of the region of interest, as depicted in Figure 7.12.

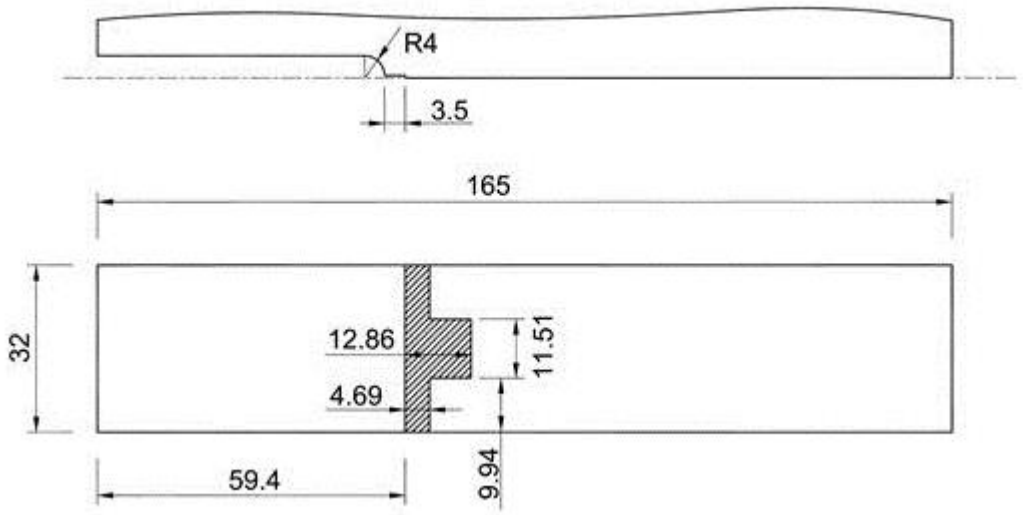

Figure 7.11 - Partial representation of the specimen half where micrographs have been taken for analysis of the initial crack growth region.

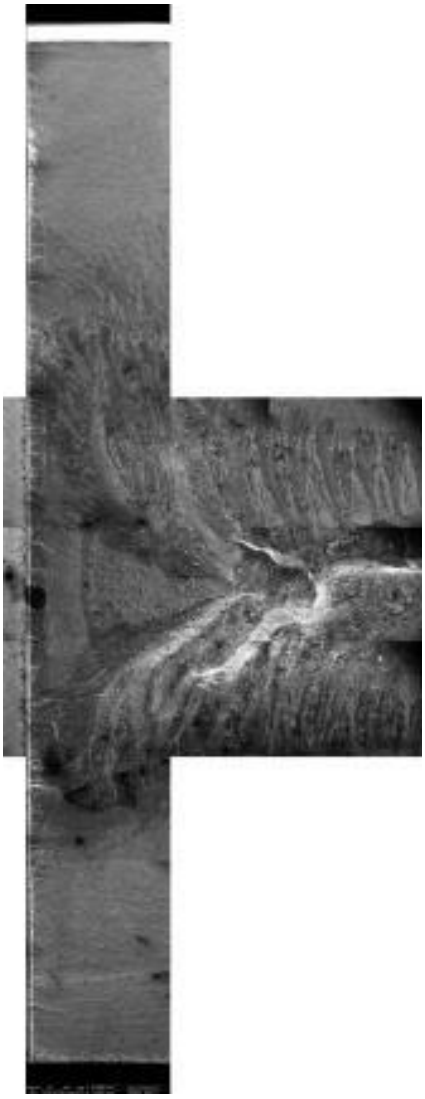

Figure 7.12 - Assembly of the micrographs taken in the initial crack growth zone (HAZ, R = 0.1, CT2).

From the various observations carried out, those presenting greater evidence of striation were selected. In those micrographs, the striation spacing, s, was estimated according to the procedure illustrated in Figure 7.13. The procedure consists of identifying one or more straight lines of length l encompassing the striations patch and approximately perpendicular to the striations, Equation (7.2).

$$s = l \,/\, number\ of\ striations \tag{7.2}$$

Considering the direction of the propagation as being normal to the striations, it was observed that, in most of the SEM observations carried out, the orientation of the striations had no discernible pattern or relation with the macroscopic propagation direction.

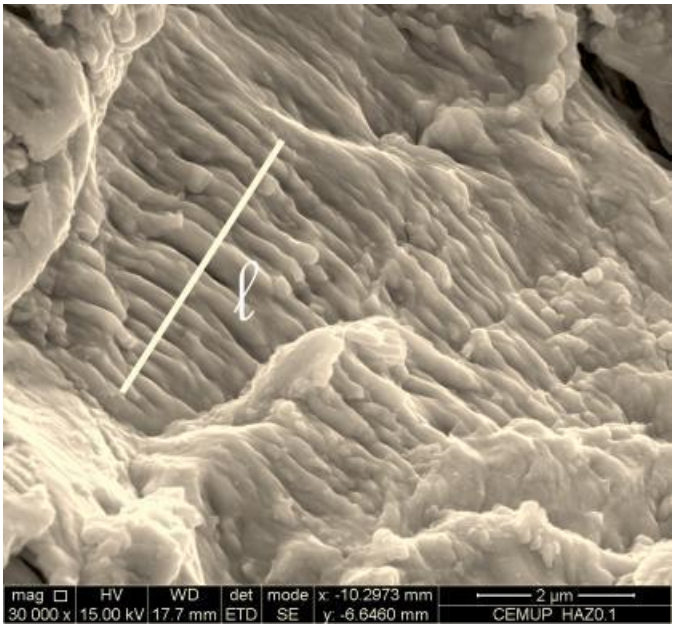

Figure 7.13 - Example representation of measurements performed for striation spacing determination (HAZ, R = 0.1, CT2).

Figure 7.14 and Figure 7.15 show two examples of micrographs without striations. Figure 7.14 corresponds to the final unstable region of the crack propagation, displaying typical ductile fracture appearance. Figure 7.15 presents a featureless fracture, corresponding to an intermediate point of the fatigue crack propagation, which could be described as ropey (Griebel, 2009).

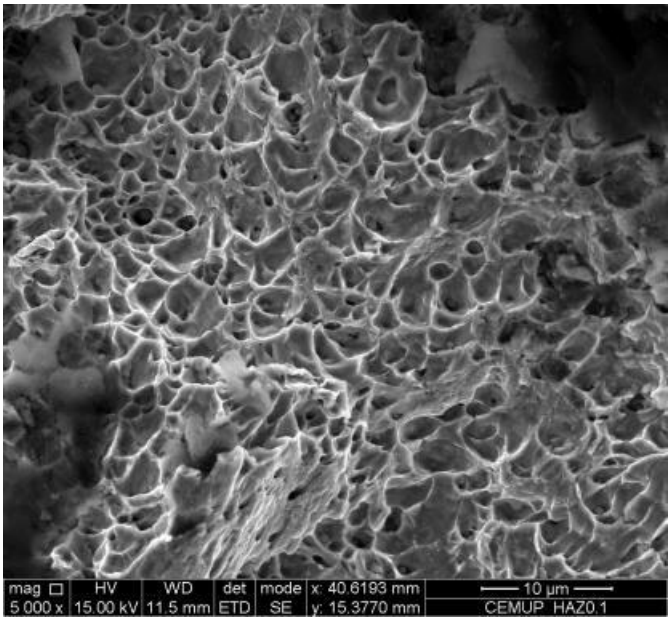

Figure 7.14 - Micrograph of the end zone of propagation, showing a typical ductile rupture (HAZ, R = 0.1, CT2).

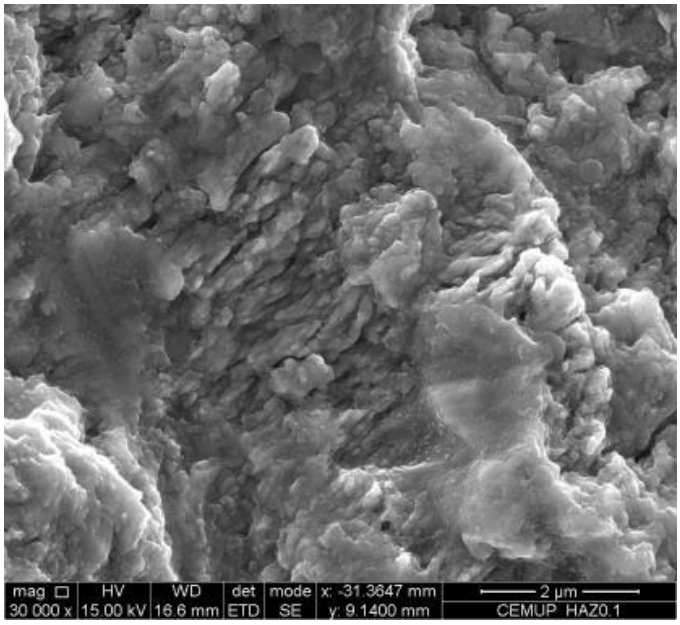

Figure 7.15 - Micrograph of a zone of propagation where neither striations nor ductile rupture were found (HAZ, R = 0.1, CT2).

For each micrograph where it was possible to identify striations, one or more determinations of s were carried out. Figure 7.16 and Figure 7.17 show the mean average (dots) and the dispersion band (from minimum to maximum s) of the results at a given location, for the HAZ and BM specimens respectively.

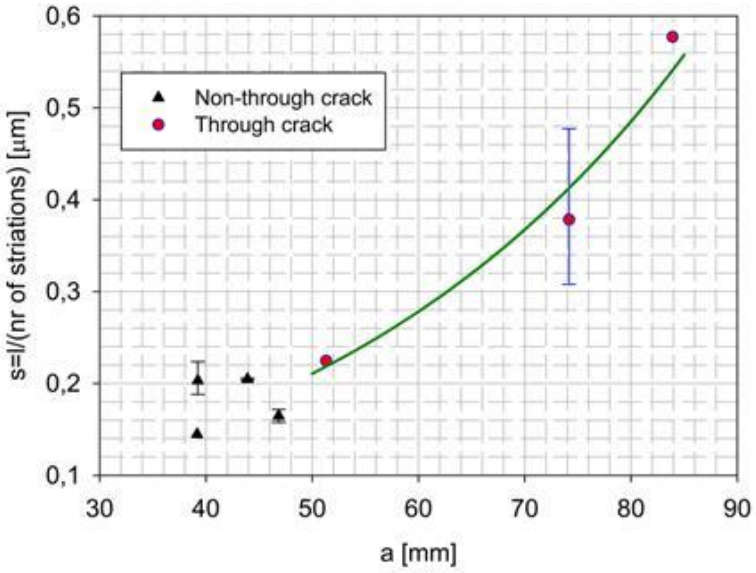

Figure 7.16 - Striation spacing (s) versus crack length (a) for specimen CT2.

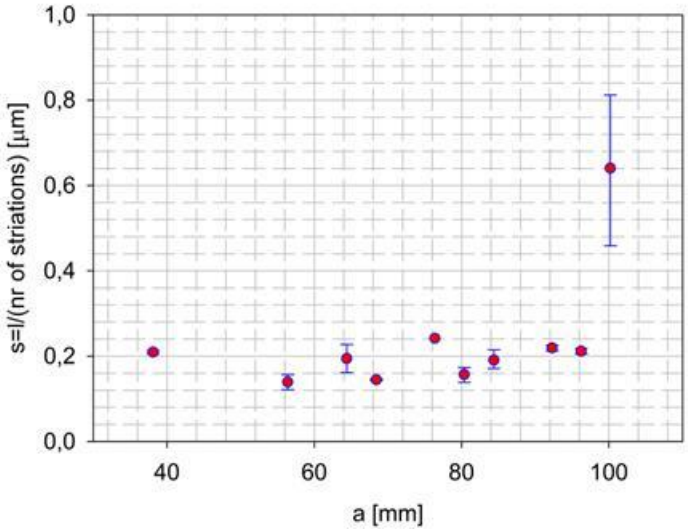

Figure 7.17 - Striation spacing (*s*) versus crack length (*a*) for specimen CT3.

These figures show, for each specimen, the microscopic crack growth rate. The crack length, *a*, was measured from the loading line, *i.e.*, the line of the centres of the loading pins used. It is possible to observe that *s* - the microscopic FCG rate - increases as the fatigue crack grows.

Figure 7.18 shows a comparison of the macroscopic FCG rates (*da*/*dN*) obtained from the tests performed on the CT specimens (Miranda et al., 2011, Miranda, 2011) with the microscopic FCG rates (*s*) obtained through striation spacing measurements using SEM micrographs. The red line in the figure corresponds to the situation *s*/(*da*/*dN*) = 1, which would imply that the macroscopic FCG rate coincides with the striation spacing measured using SEM. That would indicate the possibility of inferring macroscopic FCG rates from microscopic observations. When possible, this is of great practical interest in the context of failure analyses.

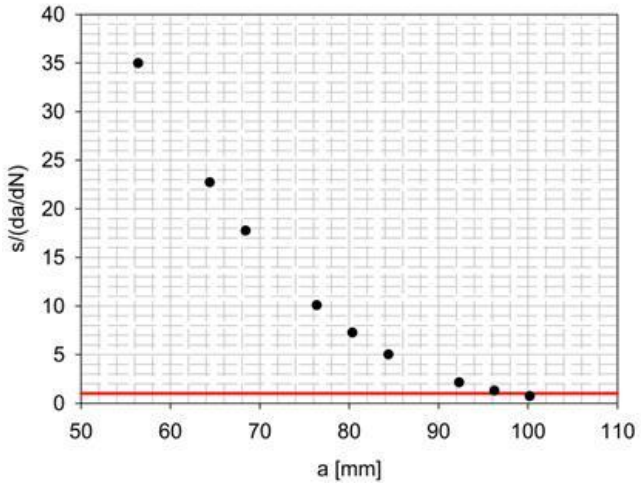

Figure 7.18 - Relation between results obtained by macroscopic and microscopic measurements for specimen CT3.

The quasi random orientation of the striation patches, the occurrence of regions with a featureless appearance, mixed with regions with striations, and the inherent difficulty of observation and counting striations, lead in general to a ratio $s/(da/dN)$ with values above unity, which, as mentioned before, only approached the macroscopic value towards the end of the FCG test.

7.2.2.2 Discussion of the results

It is generally accepted that each striation is a result of a load cycle; however, not all load cycles lead to striations.

Past experience indicates that it is in general easier to find striations in Al alloys than in steel. That situation is stated, for example, in (Hubbard, 2003), where the behaviour of Al 7075 and steel 4340 are compared from this standpoint. Schijve (2003) discusses the progress of the state of the art concerning fatigue striations, since these were identified in the middle of past century.

Lynch and Moutsos (2006) discuss the influence of the ΔK value in the striation phenomenon, and show that differences in behaviour for low or high ΔK values are to be expected. The fatigue fracture surface may present situations where striation patches or regions coexist with other facies, including dimples - characteristic of ductile rupture - or cleavage appearance. Those situations lead, necessarily, to the absence of a direct relationsh between da/dN and s, as it was the case in the present work.

In fatigue, as the crack grows, the striation spacing *s* tends to increase; the methodology of striation counting should take this fact into account, in order to aim at a constant precision of counting in the various regions of the crack path.

The measurement should be performed through a flat surface, perpendicular to the electrons' beam (DeVries et al., 2010). This may be difficult to achieve when the fracture surface is clearly irregular, as it was also the case in the observed specimens.

The present work identifies the relative independence of *s* with ΔK, up to substantial values of ΔK. Situations similar to this are described in the literature, albeit the opposite phenomena can also be found. Grundy (1994), for example, found constant values of *s* and decreasing values of *s*/(*da/dN*) as the crack length increases, concluding that in that case no relation existed between *s* and *da*/*dN*. On the other hand, Hershko et al. (2008) found close values between *s* and *da*/*dN* for an aluminium alloy (AA2024-T3) and also steel (AISI-4130). In that work, it was underlined the need for adequate observation techniques, allowing for the identification of small distances between striations.

The problem of striation creation during fatigue crack propagation is a topic of persistent interest, *e.g.* (Moreira and de Castro, 2010). The reason for this interest is namely the contribution of striation measurements to the analysis and interpretation of failure: the existence of striations is an evidence of fatigue processes; and if $s = da/dN$, the measurement of *s* would allow making quantitative interpretations on the rupture process, including an estimation of the loads acting on the damaged component.

Recently, Bulloch and Callagy (2010) have found evidences that, in phase II of the crack propagation process, the value of *s* allows for the prediction of the macroscopic crack growth rate, *da*/*dN*, with small errors. The results presented in this work describe a different situation, *i.e.*, independence between the values of *s* and ΔK up to high values of ΔK.

The behaviour found in the present work has similarities with the behaviour of a ferritic steel described by Roven and Nes (1991), where a plot is presented with the horizontal axis corresponding to macroscopic crack propagation in the range 10^{-11} up to 10^{-6} m/cycle, and the vertical axis corresponding to *s*, in the range 10^{-8} up to 10^{-6} m/cycle. In this type of representation, microscopic *s* values, resulting from the analyses of SEM micrographs, are plotted against the corresponding macroscopic values of *da*/*dN* in the same location.

Davidson and Lankford (1992) obtained results with the same trend, when analysing a stainless steel 16-13, although the measured striation spacing was one order of magnitude higher than that referred by Roven and Nes (1991) for a ferritic steel.

Following this representation format, Figure 7.19 shows the results obtained in the present experimental work, for the BM specimen tested under R = 0.4 and for the HAZ specimen tested under R = 0.1, together with those of (Roven and Nes, 1991). A very substantial coincidence is found between the results. The results presented in (Davidson and Lankford, 1992) are also plotted in Figure 7.19 for comparison.

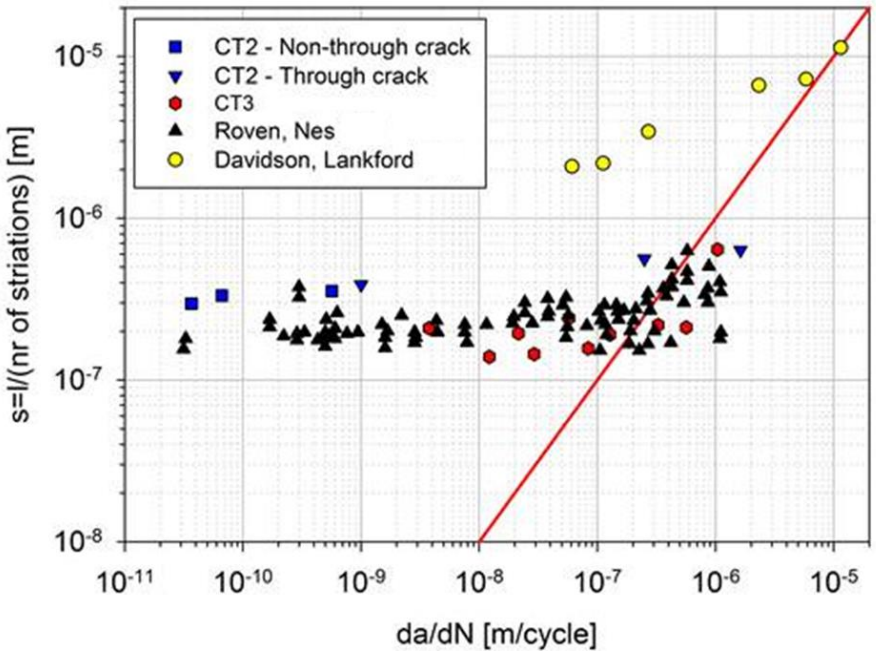

Figure 7.19 - Distance between striations *s vs. da/dN* for both tested specimens compared to literature data (CT2 - HAZ, R = 0.1 and CT3 - base material, R = 0.4).

Furthermore, the HAZ specimen (CT2) contained very high residual stresses, (Richter-Trummer and de Castro, 2011), specifically in the direction perpendicular to the crack plane, which caused the marked crack closure effect observed during the fatigue tests. The present results show a situation where the striation spacing proved to be insensitive to the presence of important residual stresses.

Figure 7.19 also shows that, for the ferritic steels examined, FCG rates below 2 to 3 x10^{-7} m/cycle decrease while *s* values maintain an approximately constant value. This threshold is over the transition between Region I and II of the FCG process and this fact must be taken into account when performing failure analyses involving measurements of *s* using SEM.

In the present case, the value of *s* may be used as a conservative upper bound of the real crack growth rate.

7.3 SIMULATION OF FATIGUE CRACK PROPAGATION

7.3.1 Theoretical background

Most of the theoretical background associated with the methodology employed was already addressed in Chapter 5, more specifically at Sections 5.2.1 to 5.2.3. Nevertheless, due to the higher complexity of the application presented in the current Chapter, some additional considerations must be highlighted.

The proposed methodology is applied with a fatigue model in order to track the evolution of the damage at the investigated detail (welded detail). Since initial cracks are normally present in welded joints, their fatigue behaviour is usually well characterised by Fracture Mechanics principles (Radaj et al., 2009). Therefore, the initiation phase is disregarded in this work. Nevertheless, the proposed methodology can also be extended to elastic local/notch approaches to fatigue that are usually adopted to model fatigue crack initiation. Moreover, when the dimension of the plastic zone at the crack tip is small when compared with the crack length, Linear Elastic Fracture Mechanics (LEFM) can be assumed.

As demonstrated in Chapter 4, in the linear elastic domain, the stress fields around the crack tip are controlled by the stress intensity factor (SIF), *K* (Broek, 1987). The fatigue crack propagation rate, on the other hand, is related to the range of *K*, which is commonly represented as ΔK. In the current work, the previously mentioned Paris law (Equation (7.5)) is adopted (Paris et al., 1961) to characterise that relation:

$$\frac{da}{dN} = C \cdot \Delta K^m \tag{7.3}$$

In spite of its known limitations, Paris law has been widely used due to its simplicity. It should be remembered that this relation is only valid for the fatigue crack propagation in Region II (see Figure 4.24, in Section 4.5.5). Near threshold (Region I) and near unstable crack propagation (Region III) regimes are not accounted by the Paris relation.

Complex structures, such as railway bridges, under complex loading, such as railway traffic, can be subjected to mixed mode (I+II) crack growth conditions. Mixed mode crack propagation was therefore assumed in the current work. This is a major increase in complexity when

comparing to the simple example presented in Chapter 5. Mode I (opening mode) is originated by stresses normal to the crack plane (see Figure 7.20a)). Mode 2 (shear or sliding mode) results from in-plane shear with the displacement between the crack faces being in the plane of the crack and perpendicular to the crack front (see Figure 7.20b)).

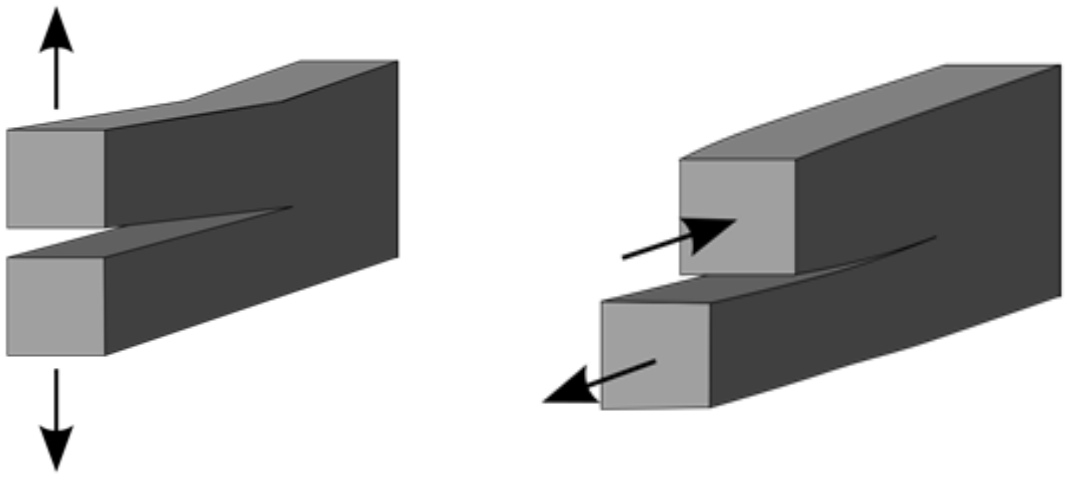

(a) (b)

Figure 7.20 - Crack loading modes intervening in mixed mode (I+II) crack propagation: (a) Mode I (opening mode) and (b) Mode II (sliding mode).

In the case of mixed mode fatigue crack propagation, the Paris relation may be applied with an equivalent stress intensity factor range. For the computation of the equivalent stress intensity factor, the relation proposed by Tanaka (1974) was selected:

$$K_{eq}(t)=\sqrt[4]{K_{\mathrm{I}}^4(t)+8\cdot K_{\mathrm{II}}^4(t)} \tag{7.4}$$

where K_{I} is the stress intensity factor component originated by mode I and K_{II} is the stress intensity factor component originated by mode II loading conditions.

For a variable amplitude loading, the rainflow method (Matsuishi and Endo, 1968) can be applied in order to extract the histogram of equivalent stress intensity factor ranges ($\Delta K_{eq,i}$, n_i). The fatigue crack propagation corresponding to that histogram can be computed by the direct integration of the Paris law:

$$\Delta a = \sum_i n_i \cdot C \cdot \Delta K_{eq,i}^{\ m} \tag{7.5}$$

In order to reproduce the crack propagation path, a crack branching criterion was adopted. The first step consisted in the computation of the kink angle time history, $\theta(t)$, using the Maximum Tangential Stress (MTS) criterion (Erdogan and Sih, 1963):

$$\theta(t)=\cos^{-1}\left(\frac{3\cdot K_{II}^2(t)+\sqrt{K_I^4(t)+8\cdot K_I^2(t)\cdot K_{II}^2(t)}}{K_I^2(t)\cdot 9\cdot K_{II}^2(t)}\right) \tag{7.6}$$

For an histogram of stress intensity factors, e.g. corresponding to the passage of a train, an equivalent kink angle is computed using the weighted average function described by (Fracture Analysis Consultants, 2011):

$$\overline{\theta}=\frac{\sum_{i=1}^{n}\frac{da}{dN}(\Delta K_{eq,i})\cdot\theta_i(K_I,K_{II})}{\sum_{i=1}^{n}\frac{da}{dN}(\Delta K_{eq,i})} \tag{7.7}$$

As described in Chapter 5, the use of the modal superposition method allows the computation of stress intensity factor time histories, $K_{total}(t)$, with a low computational cost. If mixed mode crack propagation is assumed, besides K_I also K_{II} needs to be computed. That can be achieved, in a similar way, by applying Equation (7.8):

$$K_{II}(t) = K_{II,\,sta}+\sum_j K_{II,\,j}\cdot Y_j(t) \tag{7.8}$$

In the case of Mode II, negative values of stress intensity factor are allowed, as they do not represent overlapping of crack faces. On the contrary, symmetrical values of K_{II} correspond to opposite directions of relative movement between the faces of the crack.

Moreover, as discussed in Chapter 5, in order to obtain the time histories of stress intensity factors (Mode I and/or Mode II), the requirement is to compute the modal stress intensity factors for an adequate number of vibration modes, K_j, plus the stress intensity factor regarding to the static load (e.g. self-weight), K_{sta}.

7.3.2 Proposed workflow for residual fatigue life assessment of bridge details

Based on the fatigue model and on the methodology described in the previous section, a workflow was developed, in order to assess the fatigue crack propagation behaviour in critical details of bridges. The workflow is divided in two main steps.

The first step (Figure 7.21) consists in some pre-processing and requires the following inputs:

- global numerical model of the bridge;

- numerical model of the detail(s) under analysis;
- traffic information, such as axle loads, axle's spacing and trains' speed. The traffic scenario may be obtained from monitoring systems or from other sources such as standards.

The modal analysis performed on the global numerical model of the structure allows the computation of the modal displacement fields, Φ_j, and dynamic properties, ω_j and m_j. The modal damping ratios, ξ_j, can be estimated based on standards or on field measurements. On the other hand, the displacement field originated by the static loading, Φ_{sta}, is obtained after a static analysis of the same model.

The above mentioned displacement fields are then extrapolated to the boundary nodes of the numerical model of the detail, through a submodelling process. The boundary nodal displacements associated with the static loading are stored in the $BDCO_{sta}$ file. Additionally, the displacements associated with each j^{th} mode of vibration are stored in the $BDCO_j$ file.

Finally, the traffic data available in the monitoring system database (trains' speed, axle loads and axles spacing) is combined with the dynamic properties (Φ_j, ξ_j, ω_j and m_j) of the global model in order to obtain the time histories of the modal coordinates, $Y_j(t)$. That is achieved by solving Equation (5.2) – see Section 5.2.1 - for each traffic event and for each mode of vibration.

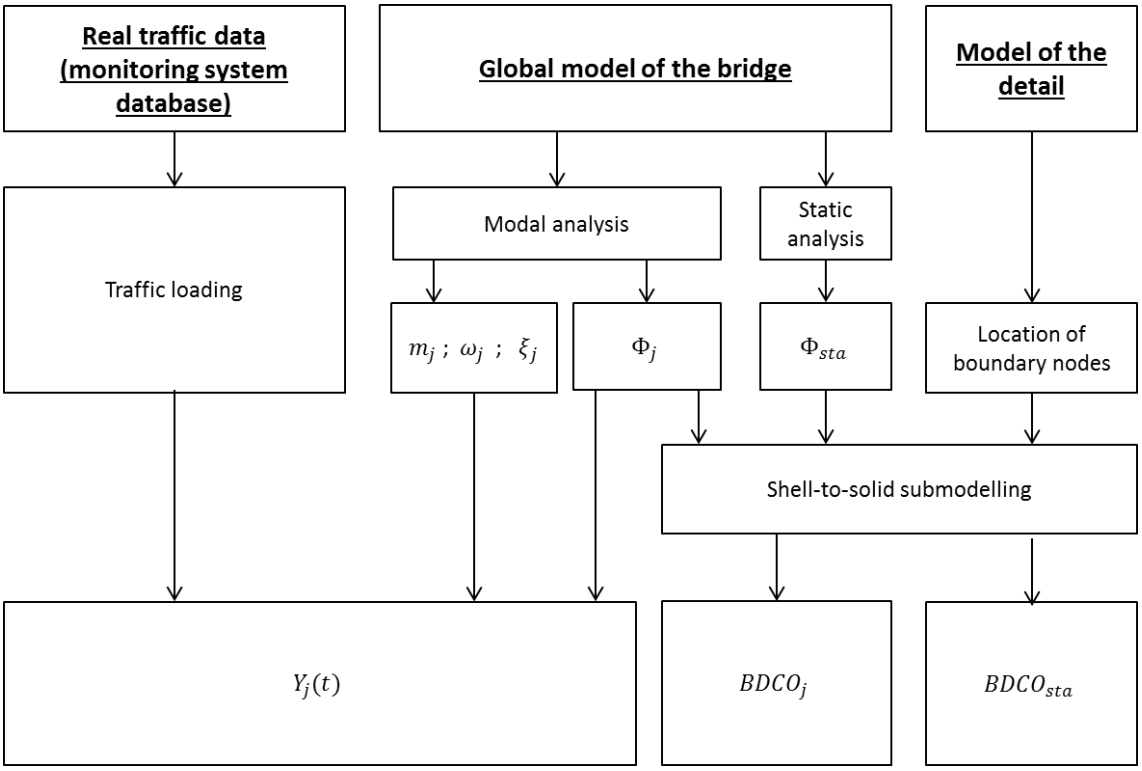

Figure 7.21 - Workflow 1st step: pre-processing of the input data.

Therefore, the outputs of the first step of the workflow are:

- the time histories of the modal coordinates for each mode of vibration of the structure and for each traffic event considered, $Y_j(t)$;
- the nodal displacements to be applied to the boundaries of the local model of the detail in order to replicate the static and modal displacement fields, $BDCO_{sta}$ and $BDCO_j$.

One of the major advantages of the proposed method is that these outputs only need to be computed once. Then, they become the only input needed for the second step of the workflow (see Figure 7.22), which consists of the crack propagation simulation.

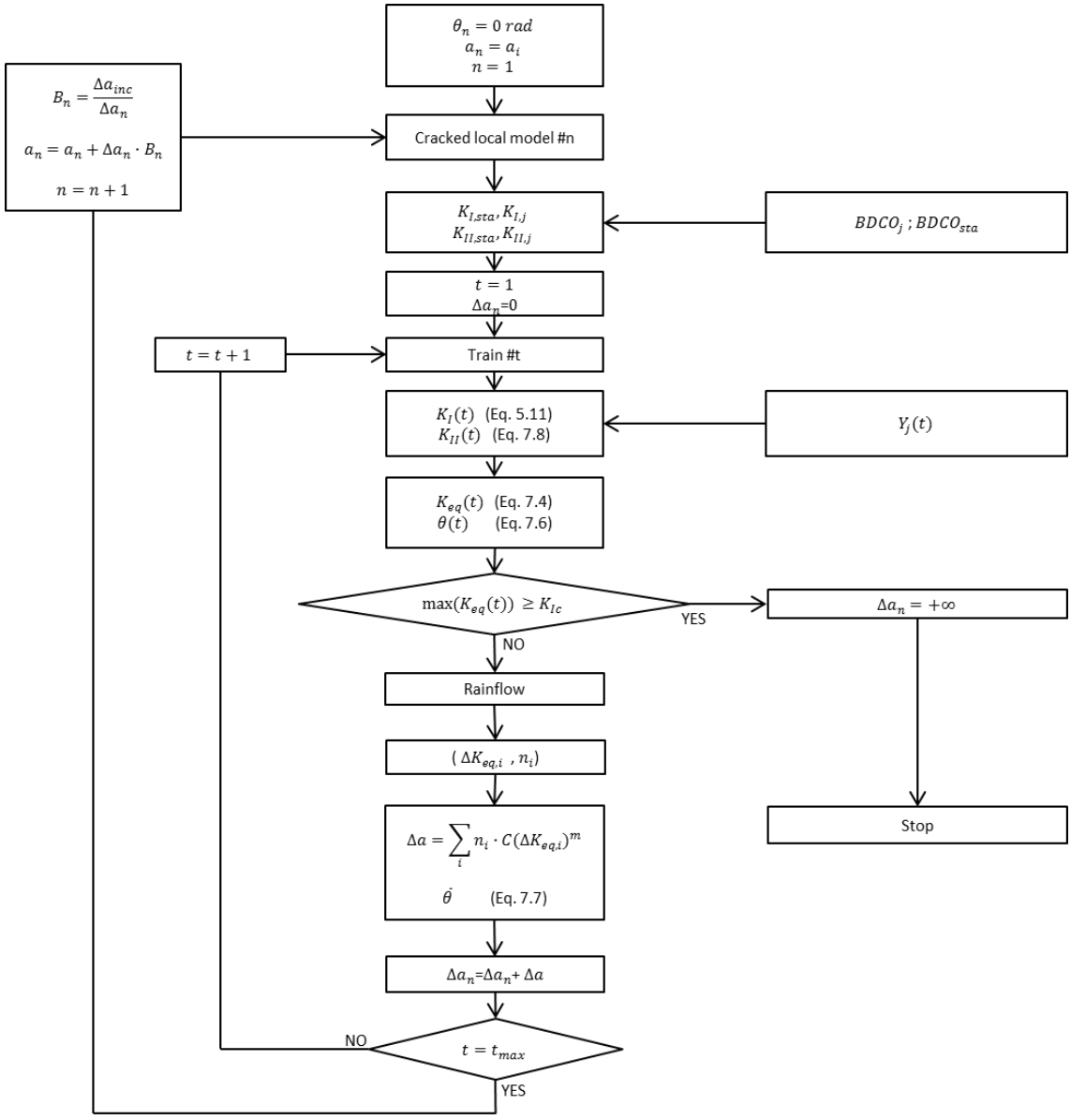

Figure 7.22 - Workflow 2nd step: crack propagation simulation.

The simulation starts with an initial crack in the local model of the detail. Applying the previously stored boundary conditions ($BDCO_{sta}$ and $BDCO_j$), the static and modal stress intensity factors, K_{sta} and K_j are computed, using an appropriate numerical method (such as Virtual Crack Closure Technique (VCCT) (Krueger, 2002), J-integral (Rice, 1968) or Displacements Extrapolation (DE) (Silva et al., 2013)).

For each train stored in the monitoring system database the corresponding modal coordinates are loaded allowing to compute $K_I(t)$ and $K_{II}(t)$, by application of Equation (5.11) and Equation (7.8), respectively. Equivalent stress intensity factor, $K_{eq}(t)$ (Equation (7.4)), and the kink angle θ (Equation (7.6)) are subsequently computed. At this point, if the maximum observed value of

$K_{eq}(t)$ exceeds the material toughness, K_{Ic}, that means the crack would propagate in unstable way. Therefore, the simulation stops and current crack length is considered the final crack length before failure of the detail. Otherwise, if the maximum observed value of $K_{eq}(t)$ does not exceed the adopted material toughness, the crack propagation associated with the train passage is computed. The rainflow method is applied to the $K_{eq}(t)$ time history, to obtain the histogram of stress intensity factor ranges. Then, Equations (7.5) and (7.7) are applied to compute the fatigue crack growth length and direction corresponding to that train passage, Δa. The contribution of all trains is summed up to obtain a final crack increment, Δa_n. For computational reasons, it is useful to adopt constant crack length increments, Δa_{inc}, between iterations. In that case, the crack increment corresponding to a loading block needs to be scaled by $B_n = \Delta a_{inc}/\Delta a_n$, where B_n represents the number of loading blocks needed, in order to achieve the Δa_{inc} increment.

After computing the crack increment for all the trains in the monitoring system database, the total crack length and direction is updated in the local model and the process is repeated.

In the next section, the application of the proposed workflow to the case study is described.

7.3.3 Application of the proposed methodology to the case study

7.3.3.1 Identification of the critical detail

The case study used to apply and validate the proposed methodology is the bridge of the new railway crossing of river Sado, described in Chapter 6.

The application of the standard fatigue assessment methods present in Eurocode 3 is not straightforward for a bridge with such characteristics. The equivalent constant amplitude stress range method, suggested in the same standard, is only applicable to structures with simple structural arrangements such as simply supported or continuous beams, which is not the case of this composite bowstring bridge. Moreover, it is only applicable to spans up to 100m. Finally, the equivalent constant amplitude stress range method requires the adoption of one of three different standard traffic mixes. In this case, the bridge is loaded by both heavy freight trains and passenger trains, which constitute a variety of train types that is not well captured by any of those standard traffic mixes.

Even the application of the linear damage accumulation method, also foreseen in Eurocode 3, rises important challenges. Some of the bridge's most critical details, concerning fatigue damage, are not well captured in the detail categories present in that standard. That is the case of the top

connection of the diagonals present at each hanger-to-deck connection (Figure 7.23). The classification of this welded detail according to Eurocode 3 is ambiguous, since the local weld features of this detail (Figure 7.24(a)) are not well captured in any of the fatigue detail categories. The Eurocode 3 suggests that the fillet weld should finish 10mm from the plate end (see Figure 7.24(b)). However, the investigated weld connection of the bridge does not end 10mm from the plate end. Instead, it continues its path passing through the hole at the top of the diagonal plate (Figure 7.24(a)). The structural detail shown below (Figure 7.23) was the one chosen to apply the proposed methodology. In particular, the analysed diaphragm was the Diaphragm 51.

(a) (b)

Figure 7.23 - Critical detail to fatigue damage: (a) cross-section of the deck and (b) critical detail.

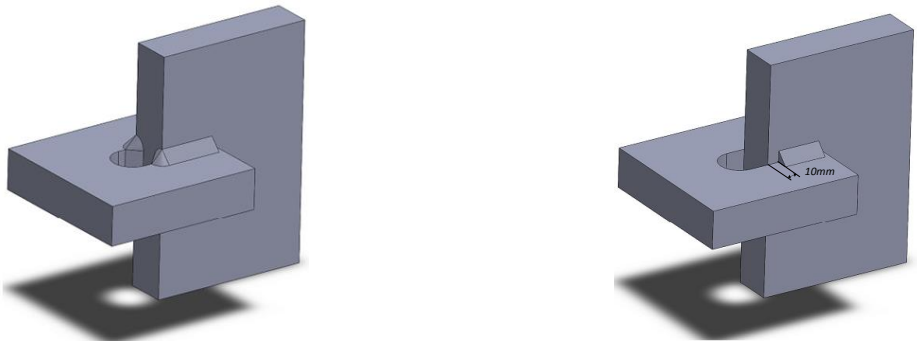

(a) (b)

Figure 7.24 - Schematic representation of the local weld features of the critical detail: (a) actual weld connection and (b) Eurocode 3 detail category.

7.3.3.2 Local monitoring of the critical detail

Due to the paramount relevance of this structure, a long-term monitoring system was installed on it, as per description in Chapter 6. This monitoring system allowed the real time traffic characterization and structural behaviour evaluation (Albuquerque et al., 2015a).

The structural behaviour was assessed by means of strain gauges installed at the diagonals of diaphragm 51 and 54 (Figure 6.47, in Section 6.4.3). At Diaphragm 51, in particular, 5 local strain gauges were installed at the top of the diagonal in order to better assess the stress field near the detail (Figure 7.25).

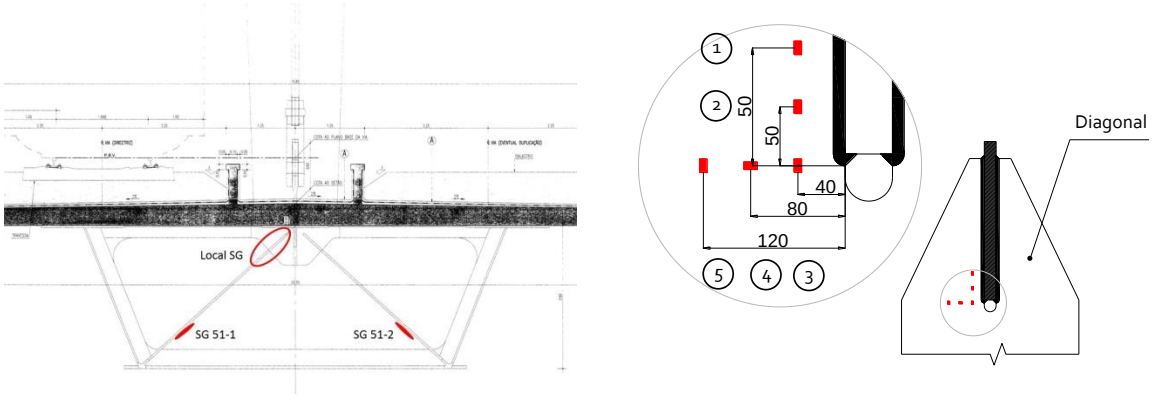

(a) (b)

Figure 7.25 - Location of strain gauges at diaphragm 51: (a) global and local strain gauges - schematics and (b) local strain gauges – location and labelling (dimensions in mm).

The traffic was characterised using shear strain gauges welded to the rails and instrumented rail pad sensors, as described in Chapter 6. As described earlier, each train crossing the bridge is totally characterised (train speed and direction, axle loads and axles spacing), through routines developed for that purpose, in MATLAB, and the corresponding information stored in a database also in MATLAB format. The information is sent, through a 3G connection, to a server at the Faculty of Engineering of University of Porto. Therefore, an extensive database, including real strain measurements and trains characteristics is available and was used in the present work.

7.3.3.3 The global numerical model of the bridge

The global numerical model of the bridge was developed using the ANSYS software and its *Parametric Design Language* (APDL), according to the description in Section 6.3.

As previously mentioned, the numerical model was calibrated, based on the results of an Ambient Vibration Test and a load test performed in the bridge (Albuquerque et al., 2011). After calibration of the global numerical model, a modal analysis was performed and the corresponding modal properties (Φ_j, ξ_j, ω_j and m_j) were computed and exported to MATLAB. In MATLAB, those modal properties are combined with the traffic information already stored in the database, $F(t)$, and the dynamic response of the structure is simulated, using the modal superposition

technique (Equation (7.4)) and adopting a total of 1500 modes of vibration. At this stage, the modal coordinates, $Y_j(t)$, are computed and stored.

7.3.3.4 The numerical model of the critical detail and shell-to-solid sub-modelling

A local finite element model of the investigated welded detail was also developed. Its geometry was defined using the commercial software SOLIDWORKS and then exported to the finite element software ANSYS®. All the properties of the finite element model are defined in a parametric format, using ANSYS APDL language. The parametric code allows the inclusion of a fatigue crack. If a crack is considered, the code allows the definition of its geometry, i.e., the crack path. Both the local finite element model and the above mentioned parametric code were developed by António L.L. Silva, co-author of the paper (Albuquerque et al., 2015b).

An uncracked geometry was first modelled aiming the validation of the submodelling process and the submodel itself, comparing numerical results with experimental data from the local strain gauges placed near the welded joint (see Figure 7.25). Furthermore, the uncracked finite element model allowed the detection of potential fatigue cracking hot spots.

Once the potential crack location is defined, the APDL routine developed allows the implementation of the initial crack explicitly in the finite element model of the welded detail. Moreover, the APDL routine was also used to update the fatigue crack path after each iteration of the workflow.

Figure 7.26 shows the local finite element model with an initial crack. The bulk of the welded detail was modelled using tetrahedral quadratic finite elements. However, at the crack tip, a refined region was modelled with hexahedral quadratic finite elements, in order to enable the accurate assessment of the stress intensity factors. The transition between the refined and coarse regions is achieved by means of pyramidal finite elements.

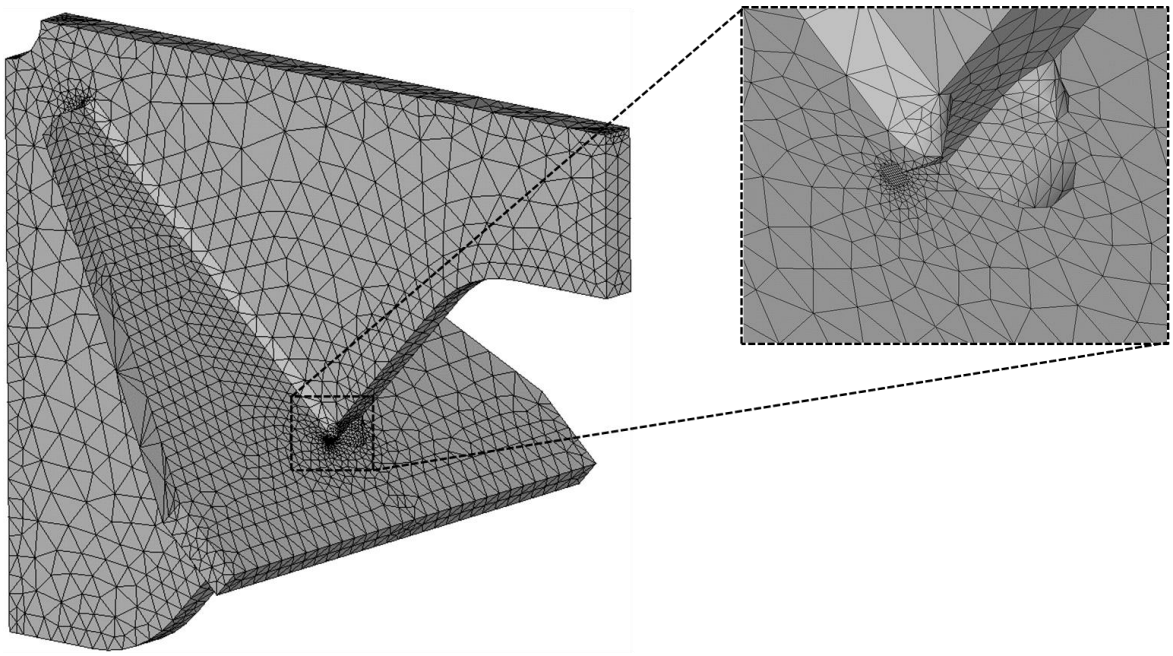

Figure 7.26 - Local finite element model.

In order to accurately compute the stress/strain at the local finite element model of the detail, the boundary conditions resulting from the global finite element model of the bridge must be interpolated to the whole set of boundary nodes of the local finite element model. This is achieved using the shell-to-solid submodeling procedure available in ANSYS (2009a). In order to allow this procedure to work properly, the shell planes of the global model should fit the mid thickness of the plates of the local model. That was achieved in this case as illustrated in Figure 7.27.

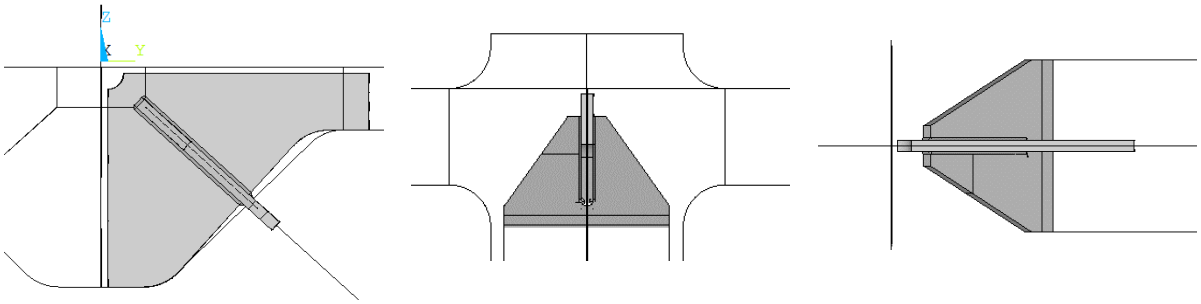

(a) Front view (b) Side view (c) Top view

Figure 7.27 - Shell-to-solid sub-modelling: fit of the local model (in grey) on the global model.

By applying the shell-to-solid submodeling procedure, the computation of the static and modal stress intensity factors in the fine numerical models of the critical details, built with volume elements, can be uncoupled from the analysis of the global numerical model of the structure, which reduces the total computation effort (Albuquerque et al., 2012a).

The virtual crack closure technique (VCCT), described by Krueger (2002), as well as the Displacement Extrapolation (DE) method were implemented in APDL for stress intensity factors computation.

7.3.3.5 Fatigue model assumptions

The implementation of the adopted fatigue model required the definition of the appropriate Fracture Mechanics parameters. The Paris law material constants, *C* and *m*, were determined by the fatigue crack propagation tests described in Section 7.2.

In order to establish the fatigue crack propagation domain, the material toughness was considered K_c = 1434 MPa$\sqrt{\text{mm}}$. This value was based on the maximum stress intensity factors measured at failure, during a set of fatigue tests performed on CT specimens of the same material (Carvalho et al., 2014). Fatigue crack propagation was simulated until K_{eq} reached K_C.

The adopted initial crack length, a_i, was 15mm. At the end of each iteration, the crack length is incremented by 5mm (Δa_{inc}). As the traffic loading block originates a much lower crack progression, Δa_n, the equivalent number of traffic loading blocks, B_n, needs to be computed. Table 7.4 summarises the Fracture Mechanics parameters considered in the analysis.

Table 7.4 - Adopted parameters for fatigue analysis.

C	m	K_{Ic}	a_i	Δa_{inc}
*	*	MPa$\sqrt{\text{mm}}$	mm	mm
9.93E-14	3.14	1434 (Carvalho et al., 2014)	15	5

*Paris law parameters set for da/dN in mm/cycle and stress intensity factors in $MPa\sqrt{mm}$

7.3.4 Analysis and discussion of results

7.3.4.1 Experimental Validation

In order to validate the adopted submodeling procedure, the experimental strain gauge data available was compared with the numerical simulation results obtained at the same locations, in the uncracked submodel. The numerical simulation was performed in MATLAB using the modal superposition technique. An example of that comparison, for a freight train (Figure 6.55(c), in Section 6.4.2), is shown in Figure 7.28. The strains are plotted as a function of the position of the 1st axle of the train.

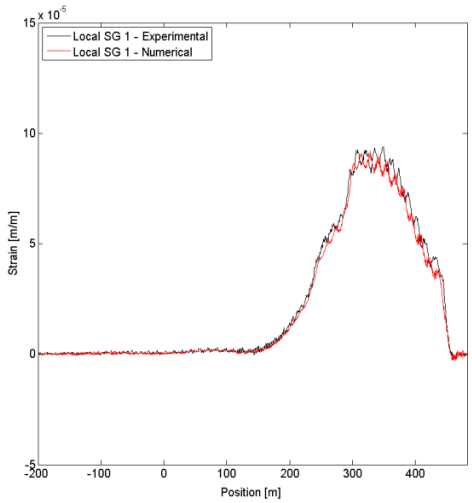

(a) Local SG 1

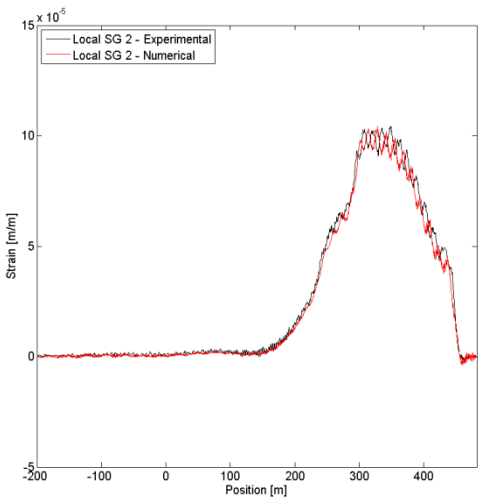

(b) Local SG 2

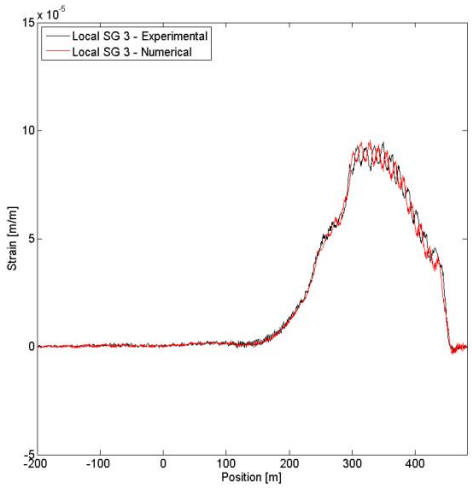

(c) Local SG 3

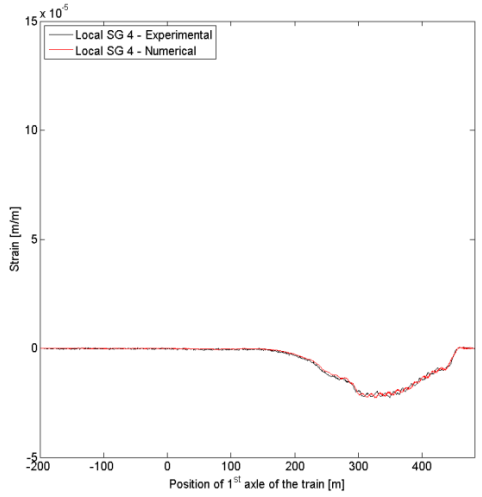

(d) Local SG 4

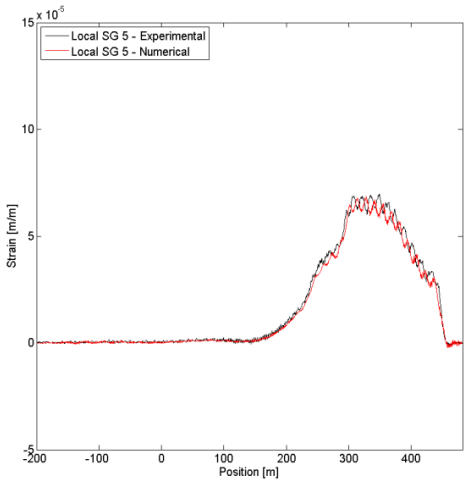

(e) Local SG 5

Figure 7.28 - Strains at the location of the local SG: Experimental vs Numerical.

A very good agreement can be observed between the experimental and the numerical results, which confirms the adequacy of the applied submodeling techniques.

After validation of the submodelling procedure, the uncracked local model was used to determine the most probable crack initiation spot. For several train passage simulations, the maximum normal stresses at the diagonal were observed at the same location (Figure 7.29(a)). This location was coincident with the crack initiation location observed in the experimental tests performed in small-scale replicas of this welded joint (Silva et al., 2013) (Figure 7.29(b)).

This location was then adopted for the initial crack in the local model. It must be stressed that even if experimental observations pointed to the formation of 2 symmetrical fatigue cracks (Figure 7.29(b)), only one fatigue crack was modelled. That allowed reducing the complexity of the model without jeopardizing the validation of the proposed methodology.

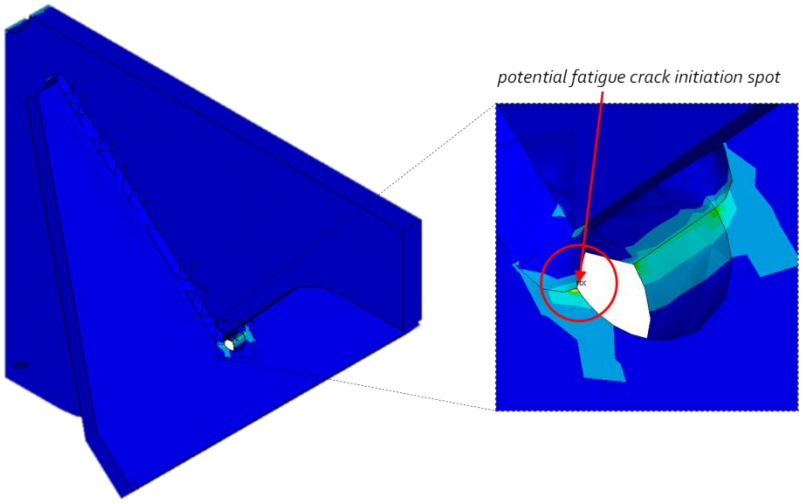

(a)

(b)

Figure 7.29 - Fatigue crack initiation spot: (a) numerical simulation vs. (b) tested experimental joints (Silva et al., 2013).

7.3.4.2 Comparison of stress intensity factor's computation techniques

Different numerical methods are available for the numerical computation of stress intensity factors. In the current work, two different methods were used for cross-validation: the virtual crack closure technique (VCCT) (Krueger, 2002) and the displacements extrapolation (DE) method (ANSYS, 2009b). The stress intensity factors were computed in ANSYS using both methods for the same freight train presented before and for an initial crack dimension of 15 mm. The results are presented in Figure 7.30. The difference between both methods is less than 10%. Therefore, the DE method was adopted as the reference and is the basis for the numerical results presented in the rest of this Chapter. From the results presented in Figure 7.30, it can also be observed that for the initial crack, Mode I stress intensity factor, K_I, is one order of magnitude higher than Mode II stress intensity factor, K_{II}.

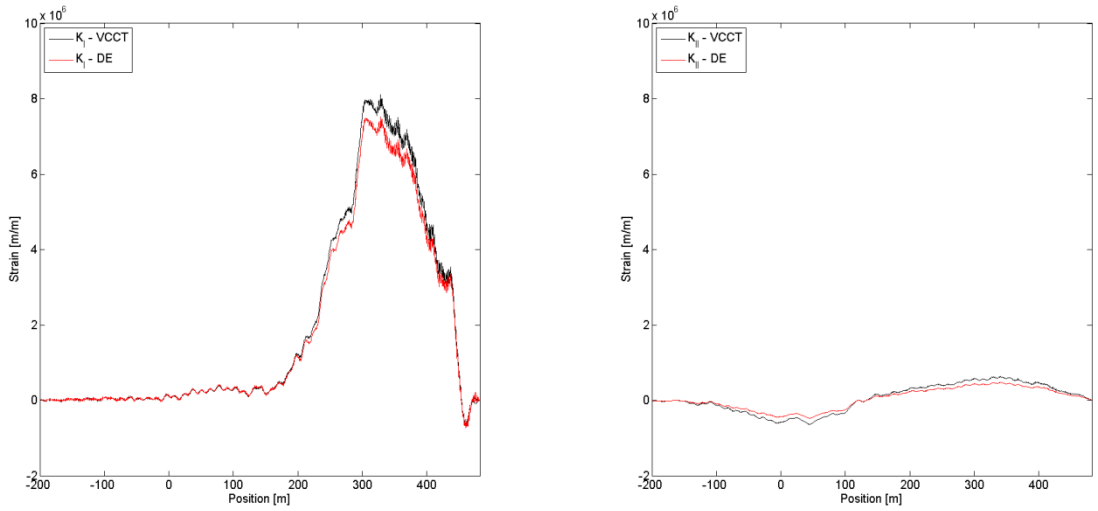

(a) (b)

Figure 7.30 - Computation of K(t): VCCT vs. DE methods: (a) $K_I(t)$ and (b) $K_{II}(t)$.

7.3.4.3 Computation of residual fatigue life

Once all the different techniques employed were validated, the entire workflow presented in Section 7.3.2 was run (Figure 7.21 and Figure 7.22), in order to assess the residual fatigue life of the structure, taking into account a postulated initial defect of 15 mm.

The crack propagation occurred, as expected, in the direction perpendicular to the principal stresses, which underlined the importance of considering a crack branching criteria. The crack propagation stopped at iteration number 33, when the maximum computed stress intensity factor

reached the adopted material toughness, K_{Ic} = 1434 MPa$\sqrt{\text{mm}}$. The entire crack propagation path (a = 175 mm) is illustrated in Figure 7.31.

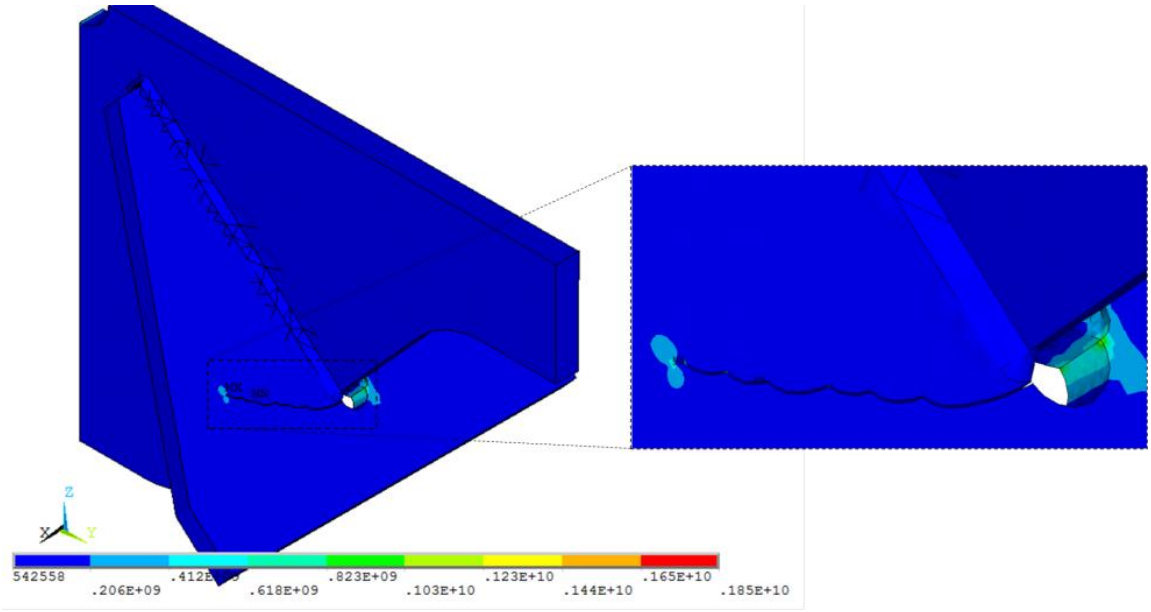

Figure 7.31 - Fatigue crack propagation path.

The crack propagation simulation workflow, comprising blocks of 565 trains, 33 crack increments and 1500 modes of vibration, was completed in approximately 3.5 days, confirming the high computational efficiency of the proposed methodology. A personal computer with a 3.2 GHz i7 processor and 24 GB RAM memory was used.

Each traffic load block includes 565 trains corresponding to a total traffic load of 0.52 million t. The equivalent annual traffic volume is 3.1 million t/year. The trains are freight and passenger trains (Figure 6.49), with a variety of weights, speeds and lengths, as illustrated in Figures 6.61 to 6.65.

The evolution of the total crack length as a function of the cumulative traffic volume is shown in Figure 7.32. It should be noted that the changes in crack propagation rate and in the crack path observed over time are affected by the length of the finite crack increments adopted in the workflow (Δa_{inc} = 5 mm). Smaller crack increments would provide more accurate results, but with associated costs in terms of computation time.

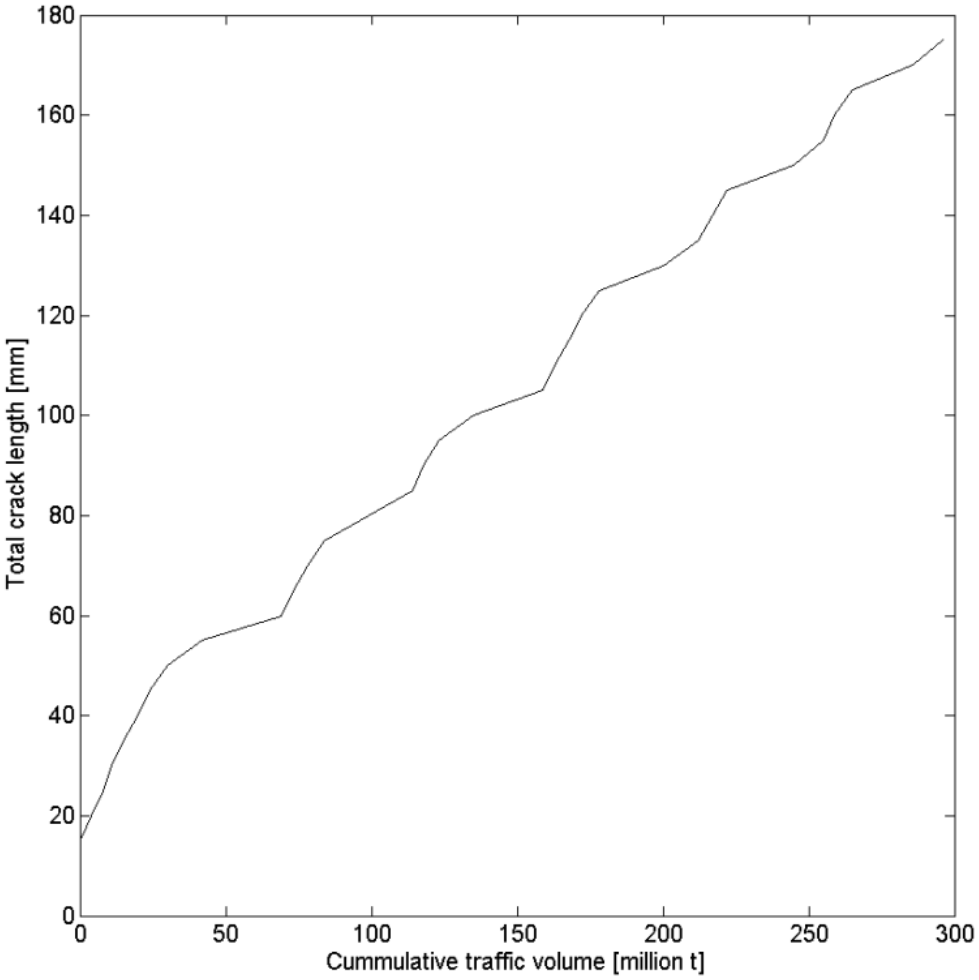

Figure 7.32 - Crack propagation length as a function of cumulative traffic.

If the current traffic volumes on the bridge were kept stable in the remaining life of the bridge, the hypothetical crack would propagate during approximately 95 years (Figure 7.33). Nevertheless, it should be noted that the fatigue traffic mixes present in the standards usually assume higher traffic volumes. In the Eurocodes, for instance, an annual traffic volume of 25 MM t is considered as reference.

As long as the selected block of 565 trains remains representative of the type of trains running on the bridge, the relationship between fatigue crack length and cumulative traffic volume remains unchanged and equal to the one represented in Figure 7.32. Therefore, under this condition, the assessment of fatigue crack propagation for higher traffic volumes does not require repeating the simulation: an increased annual traffic volume will only accelerate in time the crack propagation. As an example, if the annual traffic volume doubles, the time required to achieve the collapse of the element halves.

Based on the above mentioned assumptions, 3 additional scenarios were analysed:

- a scenario of 25 million t per year;
- a scenario where the traffic volume has an initial value of 3.1 million t in the first year but increases 5% per year in the subsequent years;
- a scenario where the traffic volume has an initial value of 3.1 million t in the first year but increases 1% per year in the subsequent years.

In the first case, the simulated crack would take approximately 12 years to propagate, while in the second and third cases the same crack propagation would take 35 and 67 years, respectively (Figure 7.33).

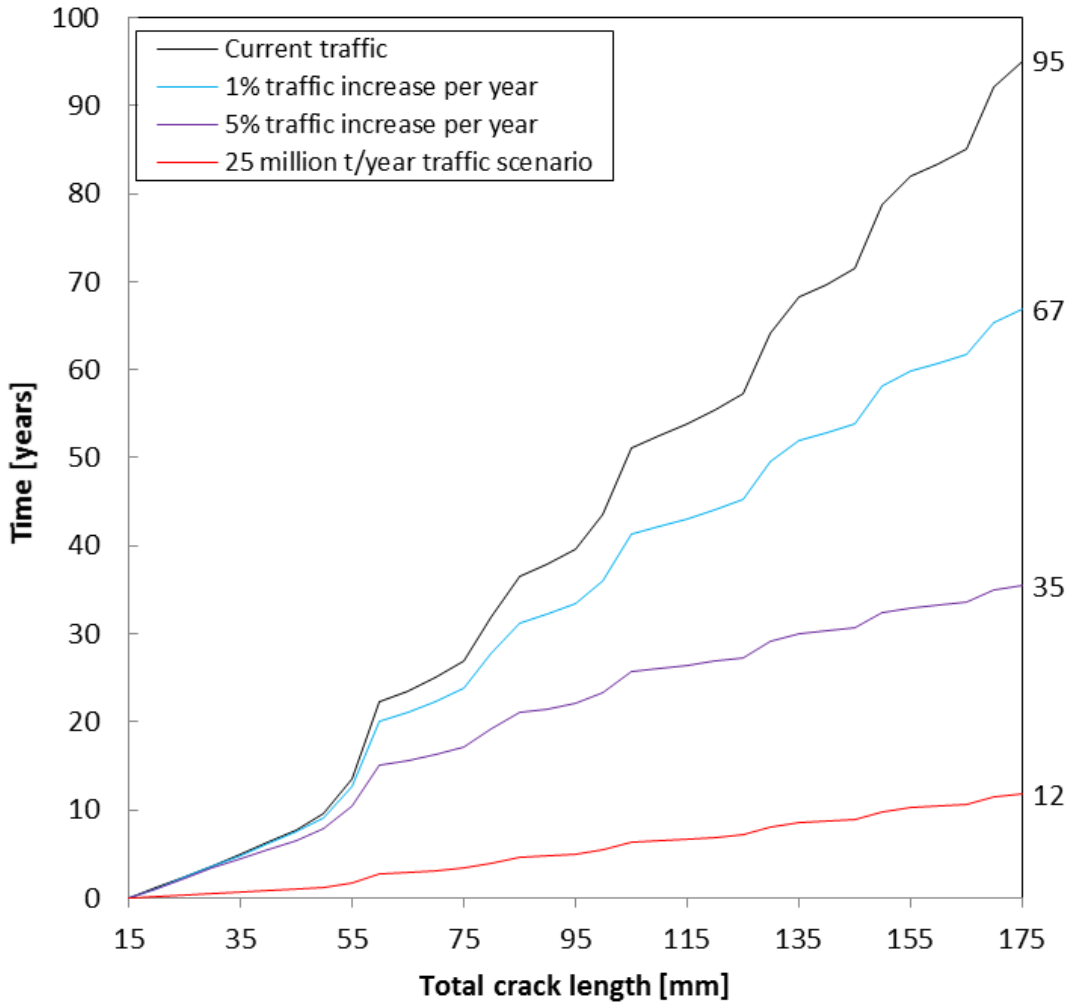

Figure 7.33 - Crack propagation length vs Time.

It should also be noted that these results were achieved with a highly conservative assumption on the initial crack dimension (15 mm). The hypothetical crack initiation period and/or propagation period up to that 15 mm crack dimension are therefore disregarded, in this conservative scenario.

The use of the Paris law is also considered a conservative assumption for the range of stress intensity factors observed in this analysis, since no crack propagation threshold ΔK_{th} was adopted.

Finally, it should be stressed that the current analysis focused only in one of the details of the bridge (a diagonal of diaphragm 51) because its main objective was to validate the proposed methodology. In spite of that, extending the analysis to other details would follow the same workflow. The only requirement would be building a new submodel for each additional detail considered.

7.4 CONCLUDING REMARKS

In this Chapter, the application of the modal superposition of stress intensity factors to the simulation of the fatigue crack propagation in a detail of the bridge of the new railway crossing over river Sado is presented. Before the numerical simulation, fatigue crack propagation laws were established based on proper tests in CT specimens reproducing the characteristics of the steel and weldments used on the bridge's construction.

Base material CT specimens were tested for fatigue crack propagation at $R = 0.1$, $R = 0.4$ and $R = 0.7$. Base material fatigue crack propagation rates at $R = 0.4$ and $R = 0.7$ present considerable overlap. Exceptionally slow crack propagation rates were observed on the surfaces at the initial stages while testing WM and HAZ specimens, with decreasing da/dN as the surface a increased. These specimens revealed an unusual crack pattern, displaying growth just at the free surfaces. These phenomena were justified by the residual stress field, measured in detail using the contour method, in the cracking plane.

Raw da/dN versus ΔK data for WM and HAZ specimens presents considerably lower FCG rates than BM specimens tested at the same R values. An approximate measurement of the crack closure effect was performed using back face strain gauges. The consideration of the closure loads made it possible to estimate ΔK_{eff}. When ΔK_{eff} is considered, the FCG rates for all types of

specimen become approximately similar, even if, as expected, slightly higher FCG rates are found for higher *R* values.

The fracture surfaces of two specimens were analysed using SEM, revealing striation regions or patches coexisting with regions without striations.

In each region presenting striations, it was possible to identify a dominant direction of propagation, normal to the striations. However, this direction varied from region to region, and a relation with the macroscopic FCG direction was not deemed feasible. Fatigue striations were found to be irregular and hard to identify.

The relation *s*/*(da/dN)* presented values decreasing up to unity as *a*/*W* increased; for low *a*/*W* values, *s* is one or two orders of magnitude greater than *da*/*dN*. FCG rates below approximately 2 to 3 x10^{-7} m/cycle were associated with approximately constant *s* values. This limit exceeds the transition between Regions I and II of the FCG process. This fact must be taken into account when performing failure analyses involving measurements of *s* using SEM. Striation spacing proved to be insensitive to residual stress.

The FCG laws obtained were included in the second step of this application, which was the numerical simulation of the fatigue crack growth at the critical detail under analysis, the top connection of a diagonal located at diaphragm 51. This step was achieved using minimal computational resources: the entire crack propagation simulation workflow was completed in approximately 3.5 days, using a personal computer with a 3.2 GHz i7 processor and 24 GB RAM memory. The crack propagation simulation stopped when the maximum simulated stress intensity factor achieved the toughness of the material, which happened at a crack length of 175 mm. Once the toughness of the material is achieved, the fatigue crack is expected to propagate on a sudden and unstable way and, therefore, the structural detail is considered to be collapsed.

Shell-to-solid submodelling proved to be an effective way to address multiple-scale structural problems, such as localised fatigue crack propagation in large structures. The structural response simulated using the submodel was compared with the record of 5 strain gauges installed at the detail under analysis, with a very good agreement being observed for the set of traffic events considered.

Modal superposition of stress intensity factors confirmed to be an adequate and efficient method when multiple and complex load histories are considered, such as multiple traffic events on bridges. In addition, for the current case study and critical detail considered, the assumption

of mixed mode fatigue crack propagation had impact on crack propagation path, allowing the crack to align with the principal stresses acting on the element.

For the simulation an initial crack length of 15 mm was considered. The crack initiation phase and the propagation up to that length was therefore disregarded. This can therefore be considered as a highly conservative case. The adopted location of that initial crack was the same where fatigue cracks initiated during experimental tests performed in small-scale replicas of this welded joint (Silva et al., 2013). Numerical simulations of train passages confirmed that this location is the one where maximum normal stresses are observed. No threshold value of stress intensity factor was adopted.

The fatigue crack simulation under the above mentioned conservative assumptions and for the current traffic volumes (3.1 million t/year) indicates a remaining fatigue life for the detail of approximately 95 years.

Additionally, the proposed methodology allowed the quick assessment of the impact of different traffic scenarios: 1% yearly increase of traffic volume; 5% yearly increase of traffic volume; a higher constant traffic volume (25 million t/year). In these 3 scenarios, the remaining fatigue life of the detail would be 67, 35 and 12 years, respectively.

Because the main objective of this analysis was to validate the proposed methodology, only one of the details of the bridge was assessed. Nevertheless, extending the analysis to other details would follow the same workflow.

Moreover, it was demonstrated that the computation of modal stress intensity factors can be embedded in a long-term monitoring system, allowing the real time assessment of fatigue cracks propagation.

Finally, it should be underlined that the simulation can be optimised, in the future, by the implementation of parallel computing, further increasing the computational efficiency.

Chapter 8

CONCLUSIONS

8.1 GENERAL CONCLUSIONS

The main objective of this thesis was to develop and implement new numerical and experimental methodologies to achieve a more accurate and efficient fatigue assessment of railway bridges.

In Chapter 2, a bibliographic review on structural failures caused by fatigue made clear that this is a common phenomenon to several areas of Engineering. Moreover, an historical overview on the main milestones related to the understanding of fatigue demonstrated that explaining fatigue requires inputs from different disciplines, from metallurgy to structural engineering and materials science. It is demonstrated, also, that one of the main difficulties when assessing fatigue is its multi-scale nature. The dimensional scale of the problem may span several orders of magnitude: it starts usually, at the dislocations level (order of nanometres) and may extend to the dimension of the structural elements (order of meters).

Still in Chapter 2, the typical causes for fatigue damage observed in steel and composite bridges were identified as being: the existence of defects on welds; the adoption of details with poor fatigue behaviour; the occurrence of unattended stresses and deformations at some of the connections (secondary distortions and tensions); excessive vibrations; the presence of aggressive environments (corrosion-induced fatigue).

The bibliographic review allowed also to identify the most common locations for fatigue damage in bridges. Many of the fatigue cracks observed are initiated at some sort of structural discontinuity, either induced by secondary distortions or by stresses concentration: connections of transverse members to main longitudinal members; diaphragms; coped-hole or cut-short beam ends; eyebars; cover plates; flange gusset plates. Others initiate at welding defects, in both longitudinal and transverse welds. The examples of bridges evidencing fatigue cracks that were presented at end of Chapter 2 illustrate this aspect.

In Chapter 3, some structural design standards were analysed, in terms of their fatigue assessment procedures and recommendations. Since in the European Union the Eurocodes are the reference standards, special emphasis was given to them. Other codes considered were the BS5400, the AASHTO Bridge Design Specifications and the IIW Fatigue Design Recommendations.

All those codes use simple fatigue assessment methodologies, based on S-N curves and on the Palmgren-Miner rule. Therefore, their applicability is limited in fit-for-purpose assessments, e.g. in situations where fatigue damage is found in a structure and its remaining fatigue life needs to be assessed. Moreover, the limited number of detail categories presented in the standards does not cover the entire range of structural details identified in real structures. That was the case of the critical detail identified in the case of the bridge of the new railway crossing of river Sado. That detail, which is the top connection of the diagonals located at each diaphragm, does not fit any of the detail categories present in the Eurocode. The classification process, in that case, becomes ambiguous and highly dependent on the assumptions of the engineer classifying it. Obtaining a fit-for-purpose S-N curve is not usually feasible, as the tests need to be performed in numerous real-scale replicas of the investigated detail and testing each specimen is highly time consuming.

Only the IIW Fatigue Design Recommendations suggest more advanced fatigue assessment approaches, namely those based on the effective notch stresses and those based on Fracture Mechanics.

The more advanced methodologies for the fatigue assessment of structures, addressed in Chapter 4, are usually local approaches, less dependent on the global geometry of the details. Therefore, in these methodologies, the same strength curve normally applies to several different details.

The approaches based on the analysis of structural stresses and strains are adequate for modelling fatigue when structural discontinuities are present. Structural stress strength curves are not as common as nominal stresses strength curves, but can still be found on a variety of standards, including Eurocode 3 and IIW.

The approaches based on notch stresses and strains are useful when analysing fatigue caused by notch induced stress concentrations. The severity of the notch is usually related to the notch radius. In the case of the computed notch stresses, they can be assessed using the nominal stresses strength curves. In the case of the notch strains, strength curves are usually obtained by testing small scale specimens. This fact makes it easier, faster and less resources consuming to obtain these strength curves than the nominal and structural stress strength curves. Nevertheless, computing fatigue life of structures that already evidence fatigue cracks is not possible with these approaches.

Finally, the Fracture Mechanics concepts allow the use of crack propagation laws which are useful to analyse how fatigue cracks propagate through time, as a function of loading.

Fatigue crack propagation laws can be characterised experimentally, through standard experiments conducted on small scale specimens. Typical strength curves express the crack propagation rate as a function of the stress intensity factor range, which controls the stress field around the crack front, in the linear elastic domain. Those curves are material dependent and not dependent on the type of the detail and therefore much easier to obtain on a fit-for-purpose basis.

Obtaining the stress intensity factor time histories in cracks located at complex details and under complex loading may be a challenge. It was shown that finite element models of the details, with very fine meshes, are often required, which contrasts with the coarse meshes that must be used when modelling the remaining structure. It was also shown that, over the last years, the development of XFEM is allowing to overcome one main drawback of this approach which is the re-meshing required after each crack propagation increment. Nevertheless, the challenge of applying Fracture Mechanics in the context of fatigue analysis of large Civil Engineering structures, under complex loading, remains.

After reviewing the advantages and limitations of the different fatigue assessment methods discussed in Chapter 4, it was understood that the new methodology to be developed in the current work should focus on facilitating the application of Fracture Mechanics to the fatigue assessment of railway bridges.

Among all the above mentioned local approaches, those using Fracture Mechanics were considered the most appropriate for aiding Infrastructure Managers planning inspections and scheduling retrofitting actions. When fatigue cracks are found in the structures, e.g. during inspection activities, the remaining fatigue life of the component can be computed using these approaches.

A new methodology was therefore developed, as described in Chapter 5. The methodology is based on the concept of modal stress intensity factors, which means the stress intensity factor obtained with the configuration of a certain mode shape. One of the most important points raised by the methodology, was that modal stress intensity factors could have a negative sign, which occurs every time the mode shape originates an overlapping of the crack faces. Only the total response, obtained by summing up the contributions (both negative and positive) of all the considered modes of vibration, has a physical meaning. Therefore, the negative values of the stress intensity factor must be disregarded only when looking at that total response.

The advantage of the proposed method is that the stress intensity factor has to be computed only for the static loading and for each of the modes of vibration considered in the dynamic analysis. This corresponds to a very low computational effort when compared with the alternative approaches found in literature, which would require the stress intensity factor to be computed for all time steps of the dynamic analysis, typically thousands of times for each traffic event.

Initially, the method was validated using a simple example: a simply supported beam, with a semi-elliptical crack, under dynamic loading. The dynamic analysis covered a 5 seconds period. A total of 50 000 time steps were used, corresponding to a time step of 0.0001s. The dynamic response of the beam was characterised using the first 5 modes of vibration and the self-weight of the beam was the only static loading considered in the analysis. Therefore, the application of the new methodology allowed to obtain the entire stress intensity factor time history from only 6 computational runs, instead of the 50 000 required by conventional methods found in literature.

The methodology proved to be fully compatible with the application of submodeling techniques. The results obtained using a submodel of the cracked zone were equal to the results obtained in an integral model of the bridge, containing the cracked zone.

Finally, it is worth mention that the computation of the stress intensity factors was performed using the Virtual Crack Closure Technique (VCCT), which was programmed in ANSYS using its specific Parametric Design Language (APDL).

After the development of the new numerical methodology for the fatigue assessment of railway bridges, the work focused on the development of new experimental assessment methods. That objective was pursued using the bridge of the new railway crossing of river Sado as a case study. This work was described in Chapter 6.

The details of the bridge, potentially prone to fatigue damage, were identified from the structural design and from *in situ* observation, during the construction phase. The different details were classified for fatigue strength according to Eurocode 3. Preliminary fatigue analysis was performed on all components, using Eurocode 3 methodology and the numerical model of the structure. Based on that analysis, the bottom connection of the diagonals of each diaphragm and the cope hole at the top connection of the same elements were identified as the critical details for fatigue. Those details were classified, according to the Eurocodes, with Detail Categories 56 and 45, respectively.

The numerical model of the structure was also developed using ANSYS software. Shell elements were used to model the concrete slab and the steel box girder. Beam elements were used to model the arches, the hangers, the diaphragms and the diagonals, the transverse stiffeners and the beams containing the ballast layer. Nodal mass elements were applied to the structure in order to reproduce the mass of the diaphragms of the arches. Rigid connections were also used to connect the concrete slab to the upper flanges of the steel box.

The diaphragms 51 and 54 and corresponding diagonals were modelled with a finer mesh of shell elements. This allowed to better capture the stress concentration at the extremities of the diagonals. All other diaphragms and diagonals were modelled using beam elements.

An Ambient Vibration Test was performed in order to calibrate the numerical model that was developed. It covered 33 sections of the deck and 19 sections of the arches. The number of sensors available required the execution of 20 different test setups.

The data of the different setups was processed using software ARTeMIS. The Enhanced Frequency Domain Decomposition (EFDD) and the Stochastic Subspace Identification - Unweighted Principal Component (SSI-UPC) algorithms were used and allowed identifying the first 7 modes of vibration of the bridge. Those modes of vibration were used as the reference to update of the numerical model.

The Young Modulus of the concrete used on the construction of the slab of the bridge's deck, E_c, was identified as the most influencing parameter in the modal properties of the numerical

model. After fine tuning this parameter, the Modal Assurance Criterion (MAC) values of the 6 vertical bending modes of vibration were all above 0.86. The torsion mode of vibration had a MAC value of 0.82. Concerning the natural frequencies, the difference between the numerical and experimental ones was typically below 0.08Hz. In the end of the calibration process, the adopted value of E_c was 43 GPa.

A monitoring system was developed and installed on the bridge, intending to characterise the railway traffic and its effects on the critical points of the structure that were identified before.

Concerning the traffic characterization, trains' axles spacing and speed are characterised through fibre optic rail pad sensors that were installed on sleepers 16 m apart of each other (side by side with hangers 50 and 52). The instrumented rail pads proved to be very effective on accomplishing this objective.

The axle loads were determined through strain gauges at the neutral axis of the rail. The strain gauges were mounted on full Wheatstone arrangement and welded in 2 sections between 2 successive rail sleepers, side by side to hanger 52. When each axle of the train crosses the bridge, the difference between shear strains in the 2 sections is proportional to the vertical axle load. The adopted procedure showed to provide adequate accuracy to estimate axle loads.

An IP camera was installed in hanger number 28 and it provided complementary qualitative information, allowing e.g. to obtain images of all trains crossing the bridge, which can be useful when analysing special events such as trains whose weight is outside typical ranges.

The traffic characterization system allowed to build a database with the characterization of each traffic event on the bridge. Three main groups of trains could be identified: Alfa Pendular passenger trains circulating at speeds between 200 km/h and 212 km/h; Intercity passenger trains circulating at speed between 145 km/h and 160 km/h; freight trains, circulating at speed between 75 km/h and 95 km/h.

The structural response was characterised through a total of 32 strain gauges installed at different points of the structure. The 4 strain gauges relevant for this study were located at the diagonals of Diaphragms 51 and 54.

At each traffic event, the strain measurements allowed to compute the stress and the corresponding fatigue damage. The trains contributing the most to the fatigue damage are freight trains with loads ranging from 40 kN/m to 55 kN/m and with lengths around 200 m and 400 m.

The capability of the system to characterise the traffic allowed to compare the measured strains with the strains simulated using the modal characteristics of the numerical model of the bridge. That comparison showed very similar responses, thus providing further validation of the numerical model of the bridge. The passages of the Alfa Pendular train, which has constant length and almost constant axle loads, helped to demonstrate that in spite of the slight oscillations of train axle load measurements, across different traffic events, the corresponding response of the structure is kept almost constant.

The modal characteristics of the numerical model of the bridge, combined with the traffic database that was assembled, allowed also computing the damage at the diagonals that were not monitored directly through strain gauges. The diagonals at the North and South entrances of the bridge, close to piers P1 and P4, respectively, showed the highest values of strains and fatigue damage, followed by the diagonals located at the end of each span of the bridge, close to piers P2 and P3. This is due to the higher dynamic impact observed at these locations and also due to the shorter and, therefore, stiffer hangers existing in these points.

It must be stressed that the new developed method, presented in Chapter 6, showed to be very efficient and able to compute the fatigue damage of the critical details of railway bridges in real-time. Only a very limited set of modal parameters of the numerical model needed to be extracted, stored in a condensed matrix format (less than 10 MB) and incorporated in the monitoring system workflow. That limited set of modal parameters allowed accurate simulations of the real response of the structure with a reduced computational effort. Another advantage of that methodology is that the real traffic characteristics are considered.

At the commissioning phase of the bridge, load tests were performed by LNEC. The load tests consisted of positioning 2 types of freight trains, containing 11 and 15 ballast containers, respectively, at specific loading positions and measuring the corresponding deformations, deflections and strains at specific points of the structure. The monitoring system developed in this work was used during those tests, so that the measured response of the bridge could be compared with that of the numerical model. In addition, the commissioning phase also allowed the calibration of the axle loads measurement system.

In Chapter 7, it was described the application of the new numerical method (presented in Chapter 5) to the simulation of the fatigue crack propagation on a detail of the same bridge under study.

First of all, the fatigue crack propagation strength of the steel and weldments of the bridge was characterised. The crack propagation tests were performed on compact tension (CT) specimens according to ASTM E647. CT specimens were machined in order to study the crack propagation through base material, heat affected zone (HAZ) and weld metal (WM). The specimens had a thickness close (32 mm) to the thickness of the diagonals (35 mm) that were identified as the critical details of the bridge, concerning fatigue. In the case of the specimens testing HAZ and WM, crack closure effects were observed due to the residual stresses contained in the welds. A strain gauge enabled to measure strains in the back face of those specimens, therefore allowing to quantify and account for those effects. The tests allowed determining the *C* and *m* values of the Paris law, for the steel used in the construction of the bridge. For the base material, the value of C ranged from 6.83E-15, for a load ratio of 0.1, to 3.47E-13, for a load ratio of 0.7. The values of *m* ranged from 3.48 to 2.95 for the same load ratios.

The top connection of one of the diagonals of the diaphragm 51 was the detail of the bridge selected for the simulation. A model of the detail was developed in ANSYS. This local model fitted totally on the global model of the structure, so that ANSYS shell-to-solid submodeling technique could be used. In addition, 5 strain gauges were bounded to the detail, on the bridge, and connected to the monitoring system, so that the strains simulated using the submodel could be compared with the measured ones. The results were very similar, therefore confirming the adequacy of the numerical submodeling technique that was used.

The crack path was input in the numerical model of the detail through ANSYS APDL language. The stress intensity factor at the crack front was computed using VCCT and Displacements Extrapolation (DE) methods, which were also programmed in APDL. An initial crack with 15 mm was assumed, on the location where the stress concentration was higher: at the cope hole, close to the root of the weld. Because the detail undergoes complex loading, the methodology described in Chapter 5 had to be extended to mixed mode condition. This was achieved with success, with the equivalent stress intensity factor being computed using Tanaka's expression and the kink angle time history using the Maximum Tangential Stress criterion.

The simulation of the fatigue crack propagation was performed for load blocks of 565 trains, corresponding to a total traffic load of 0.52 million t. 1500 modes of vibration were considered and 5 mm crack increments were adopted in the workflow. The simulation stopped after 33 iterations, when the total crack length reached 175 mm. At that moment, the maximum stress

intensity factor achieved a value equal to the adopted toughness of the material (1434 MPa$\sqrt{\text{mm}}$). This corresponded to a remaining fatigue life, after the crack of 15 mm was observed, of 95 years. The total fatigue life, including the initiation phase and the crack propagation up to the first 15 mm would be higher. The simulation took 3.5 days therefore confirming the high computational efficiency of the new proposed methodology, compared to other approaches.

In summary, the initial objective of this Thesis, which was to provide new numerical and experimental methodologies for the accurate and efficient fatigue assessment of railway bridges was achieved.

Concerning the numerical component of the work, a new methodology for the computation of stress intensity factors time histories was developed. For that, the concept of modal stress intensity factors was introduced, allowing the application of the modal superposition technique in the context of Fracture Mechanics. The methodology was first tested and validated with a simple example and later applied to the simulation of a fatigue crack propagation on a detail of the bridge of the new railway crossing of river Sado. The new methodology showed to be highly efficient computationally and made it feasible to use Fracture Mechanics concepts and crack propagation laws when analysing railway bridges subject to a wide range of traffic scenarios. It also proved to be possible to embed the new methodology on a monitoring system in order to perform real-time estimations of fatigue cracks' propagation.

Referring to the experimental component of the work, an integrated monitoring system was designed and implemented in the bridge of the new railway crossing of river Sado, allowing the traffic characterization, the real time fatigue damage quantification in monitored details and, using the compiled traffic data, the fatigue damage estimation in non-monitored details. Load tests and Ambient Vibration Tests were performed on the bridge allowing the subsequent calibration of the numerical model of the structure. Additionally, fatigue crack propagation tests were performed on CT specimens made of the steel and welds employed on the construction of the bridge. This allowed to characterise the crack propagation laws that were required for the employment of fatigue assessment methodologies based on Fracture Mechanics.

8.2 FUTURE DEVELOPMENTS

The two main achievements in current thesis were the development of a new numerical methodology for the simulation of fatigue crack propagation in critical bridge details and the

design and implementation of a monitoring system focused on fatigue damage monitoring. These two tools also constitute the main areas selected for further research and development.

Concerning the numerical methodology, its application to the simulation of fatigue crack propagation in the case study used a local numerical model of the detail to analyse, where the fatigue crack was modelled explicitly. Over the last years, meshless methods have been developed simplifying the implementation of successive crack increments in the local models. The most widely accepted method is X-FEM, already discussed in Chapter 4. As a future enhancement of the proposed workflow, X-FEM should be implemented as the default method for modelling the crack in the local model of the detail. This would increase the flexibility of crack modelling.

Another step towards the improvement of this tool is to consider the impact that the reduction in stiffness of the damaged components has on the global response of the structure. The workflow presented in the present thesis assumed that the modal properties of the structure are not modified by the presence and increasing length of the fatigue cracks. That is a fair approximation when the fatigue cracks are relatively small when compared with the section of the structural detail. However, as the crack's length increases towards the failure of the structural component, it may start affecting the global response of the structure, with the forces being redistributed to other structural components. In order to take this effect into account, in the future, the workflow presented in this work must be improved as follows:

- Firstly, the local model of the detail must be converted into a superelement, a feature already available in commercial finite elements software such as ANSYS. A superelement is a group of previously assembled elements that is treated as a single element. The superelement, once generated, may be included in any ANSYS model, such as the global model of the bridge, and be used in any analysis type for which it is applicable. Therefore, the superelement is a possible way to reflect the mass and stiffness of the local model in the global model. It does not intend, though, to replace submodeling but only to replicate, in the global modal, the damage level of the local detail.
- During the simulation of the crack propagation, every time the crack length is incremented in the local detail, a new version of the superelement is generated. If the difference in stiffness between the new version of the superelement and the previous

version exceeds a certain threshold value, the new superelement is considered as the reference and updated in the global model of the bridge;

- In that case, the modal analysis of the global model is performed again. The modal coordinates are re-computed for all the modes of vibration considered and for each traffic event. The mode shapes of each mode of vibration are converted to boundary conditions of the local detail, through the shell-to-solid submodeling technique already applied before. After this update, the simulation of the crack propagation continues as per the workflow described in Chapter 7.

Another way for the improvement of the computational efficiency of the numerical workflow is to adapt the code to parallel computing, taking advantage of MATLAB potential on this field. Further improvement in the MATLAB code is also possible benefiting from Graphic Processing Unit (GPU) technology.

The monitoring system allowed building a database of traffic events on the bridge. The fatigue damage, computed by the linear damage accumulation method is also stored in the same database. In the future, the monitoring system can also be improved to allow the real-time estimation of fatigue cracks propagation, through the method described in Chapter 7. In order to do so, the modal stress intensity factors need to be stored and embedded in the monitoring system. The modal stress intensity factors would be computed for real fatigue cracks found previously or for hypothetical fatigue cracks assumed to be present in the most critical locations. For each traffic event, the traffic characteristics and corresponding modal coordinates are computed by the monitoring system. Combining the modal coordinates with the modal stress intensity factors allows obtaining the stress intensity factor time histories. The corresponding fatigue crack increment can then be computed using the methodology described in Chapter 7.

Finally, still concerning the monitoring system, a graphic interface can be developed in the future, allowing an easier and more interactive access to the database, by the users.

REFERENCES

AASHTO (2012) LRFD Bridge Design Specifications. Washington, D.C., AASHTO.

ABS (2014) Guide for Fatigue Assessment of Offshore Structures. Houston, USA, American Bureau of Shipping.

ADIB-RAMEZANI, H. & JEONG, J. (2007) Advanced volumetric method for fatigue life prediction using stress gradient effects at notch roots. *Computational Materials Science,* 39**,** 649-663.

ADIB, H. & PLUVINAGE, G. (2003) Theoretical and numerical aspects of the volumetric approach for fatigue life prediction in notched components. *International Journal of Fatigue,* 25**,** 67-76.

AL-EMRANI, M. & KLIGER, R. (2009) Fatigue prone details in steel bridges. *NSCC2009.*

ALBUQUERQUE, C., DE CASTRO, P. M. S. T. & CALÇADA, R. (2012a) Efficient crack analysis of dynamically loaded structures using a modal superposition of stress intensity factors. *Engineering Fracture Mechanics,* 93**,** 75-91.

ALBUQUERQUE, C., PINTO, N. M. P., CALÇADA, R., GABRIEL, J. & DE CASTRO, P. M. S. T. (2015a) Efficient fatigue damage monitoring method for critical details of railway bridges. *Journal of Constructional Steel Research,* (Under revision).

ALBUQUERQUE, C., SILVA, L., DE JESUS, A. & CALÇADA, R. (2015b) An efficient methodology for fatigue damage assessment of bridge details using modal superposition of stress intensity factors. *International Journal of Fatigue,* 81, 61-77.

ALBUQUERQUE, C. M. C., MIRANDA, R. M. C., RICHTER-TRUMMER, V., FIGUEIREDO, M. A. V. D., CALÇADA, R. & CASTRO, P. M. S. T. D. (2012b) Fatigue crack propagation behaviour in thick steel weldments. *International Journal of Structural Integrity,* 3**,** 184-203.

ALBUQUERQUE, C. M. C., PINTO, N. M. P., CALÇADA, R. A. B. & GABRIEL, J. (2011) Experimental characterization of the dynamic behaviour of the new railway bridge over the river

Sado. IN L'AQUILA, U. O. & MILANO, P. D. (Eds.) *EVACES 2011*. Varenna, Italy, University of L'Aquila, Politecnico di Milano.

ALIABADI, M. H. & ROOKE, D. P. (1991) *Numerical fracture mechanics,* Southampton Dordrecht, Computational Mechanics Publications Kluwer Academic Publishers.

ANDERSSON, A., LEANDER, J. & KAROUMI, R. (2013) Extending the fatigue service life of a railway bridge by local approaches. *International IABSE Conference - Assessment, Upgrading and Refurbishment of Infrastructures.* Rotterdam.

ANSYS (2009a) Advanced Analysis Techniques Guide. *Release 12.0 Documentation for ANSYS.* ANSYS, Inc.

ANSYS (2009b) Theory Reference. *Release 12.0 Documentation for ANSYS.* ANSYS, Inc.

API (2014) Planning, Designing and Constructing Fixed Offshore Platforms-Working Stress Design. API.

ASTM (2000) E647 - Standard Test Method for Measurement of Fatigue Crack Growth Rates. USA, ASTM International.

ASTM (2012) E606 - Standard Test Method for Strain-Controlled Fatigue Testing. USA, ASTM International.

ATZORI, B. & MENEGHETTI, G. (2001) Fatigue strength of fillet welded structural steels: finite elements, strain gauges and reality. *International Journal of Fatigue,* 23**,** 713-721.

AWS (2010) Structural Welding Code -Steel. AWS.

AYALA-URAGA, E. & MOAN, T. (2007) Fatigue reliability-based assessment of welded joints applying consistent fracture mechanics formulations. *International Journal of Fatigue,* 29**,** 444-456.

BABUŠKA, I. & MELENK, J. M. (1997) THE PARTITION OF UNITY METHOD. *International Journal for Numerical Methods in Engineering,* 40**,** 727-758.

BARSOM, J. M. & ROLFE, S. T. (1999) *Fracture and Fatigue Control in Structures,* Butterworth-Heinemann.

BARSOUM, R. S. (1977) Triangular quarter-point elements as elastic and perfectly-plastic crack tip elements. *International Journal for Numerical Methods in Engineering,* 11**,** 85-98.

BATHE, K. J. (1996) *Finite element procedures,* Prentice Hall.

BAUSCHINGER, J. (1886) On the change of the elastic limit and the strength of iron and steel, by drawing out, by heating and cooling, and by repetition of loading. *Minutes of Proceedings of the Institution of Civil Engineers with Other Selected and Abstracted Papers,* 87**,** 463-465.

BEGHINI, M. & BERTINI, L. (1990) Fatigue crack propagation through residual stress fields with closure phenomena. *Engineering Fracture Mechanics,* 36**,** 379-387.

BELLETT, D., TAYLOR, D., MARCO, S., MAZZEO, E., GUILLOIS, J. & PIRCHER, T. (2005) The fatigue behaviour of three-dimensional stress concentrations. *International Journal of Fatigue,* 27**,** 207-221.

BENEDETTINI, F., MORASSI, A. & VESTRONI, F. (2012) *Structural assessment of bridges and health monitoring programs based on dynamical tests,* Boca Raton, CRC Press-Taylor & Francis Group.

BENNETT, J. & MINDLIN, H. (1973) Metallurgical Aspects of the Failure of the Point Pleasant Bridge. *Journal of Testing and Evaluation,* 1.

BRANCO, C. A. G. D. M., FERNANDES, A. A. & DE CASTRO, P. M. S. T. (1999) *Fadiga de estruturas soldadas,* Lisboa, Fundação Calouste Gulbenkian.

BRENCICH, A. & GAMBAROTTA, L. (2009) Assessment procedure and rehabilitation of riveted railway girders: The Campasso Bridge. *Engineering Structures,* 31**,** 224-239.

BROEK, D. (1987) *Elementary engineering fracture mechanics,* Dordrecht, Martinus Nijhoff Publishers.

BROWNJOHN, J. M. W., MAGALHAES, F., CAETANO, E. & CUNHA, A. (2010) Ambient vibration re-testing and operational modal analysis of the Humber Bridge. *Engineering Structures,* 32**,** 2003-2018.

BSI (1979) BS 5762 - Methods for crack opening displacement (COD) testing. BSI.

BSI (1980) BS5400: Steel, concrete and composite bridges. *Part 10: Code of practice for fatigue.* BSI.

BUCIUMEANU, M., PALAGHIAN, L., MIRANDA, A. S. & SILVA, F. S. (2011) Fatigue life predictions including the Bauschinger effect. *International Journal of Fatigue,* 33**,** 145-152.

BULLOCH, J. H. & CALLAGY, A. G. (2010) A detailed study of the relationship between fatigue crack growth rate and striation spacing in a range of low alloy ferritic steels. *Engineering Failure Analysis,* 17**,** 168-178.

BYERS, W. G., MARLEY, M. J., MOHAMMADI, J., NIELSEN, R. J. & SARKANI, S. (1997) *Fatigue Reliability Reassessment Applications: State-of-the-Art Paper,* ASCE.

CAGLAYAN, B. O., OZAKGUL, K. & TEZER, O. (2009) Fatigue life evaluation of a through-girder steel railway bridge. *Engineering Failure Analysis,* 16**,** 765-774.

CAGLAYAN, O., OZAKGUL, K., TEZER, O. & UZGIDER, E. (2011) Evaluation of a steel railway bridge for dynamic and seismic loads. *Journal of Constructional Steel Research,* 67**,** 1198-1211.

CARVALHO, D., SILVA, A. L. L., JESUS, A. M. P. & FERNANDES, A. A. (2014) Fatigue behaviour of stuctural steels. Comparison of strain-life and fatigue crack propagation data. *9º Congresso Nacional de Mecânica Experimental.* Aveiro, Portugal.

CASAVOLA, C. & PAPPALETTERE, C. (2009) Discussion on local approaches for the fatigue design of welded joints. *International Journal of Fatigue,* 31**,** 41-49.

CEN (2002) Eurocode 1: Actions on structures. *Part 1-1: General actions - Densities, self-weight, imposed loads for buildings.* Brussels, Belgium, CEN.

CEN (2003) Eurocode 1: Actions on structures. *Part 2: Traffic loads on bridges.* Brussels, CEN.

CEN (2004) Eurocode 3: Design of steel structures. *Part 1-9: Fatigue.* CEN.

CEN (2006) Eurocode 3: Design of steel structures. Part 2: Steel Bridges. Brussels, CEN.

CHAN, T. H. T., GUO, L. & LI, Z. X. (2003) Finite element modelling for fatigue stress analysis of large suspension bridges. *Journal of Sound and Vibration,* 261**,** 443-464.

CHAN, T. H. T., YU, L., TAM, H. Y., NI, Y. Q., LIU, S. Y., CHUNG, W. H. & CHENG, L. K. (2006) Fiber Bragg grating sensors for structural health monitoring of Tsing Ma bridge: Background and experimental observation. *Engineering Structures,* 28**,** 648-659.

CHELLINI, G., LIPPI, F. V., SALVATORE, W. & TSCHUMI, M. (2009) Fatigue assessment of Sesia high-speed railway viaduct. IN BURCHI, S., LIPPI, F. V. & SALVATORE, W. (Eds.) *DETAILS European Research Project - Final Workshop.* Lucca, Italy.

CHEN, Z., XU, Y. & WANG, X. (2012) SHMS-based fatigue reliability analysis of multiloading suspension bridges. *Journal of Structural Engineering,* 138**,** 299-307.

CHEN, Z. W., XU, Y. L., XIA, Y., LI, Q. & WONG, K. Y. (2011) Fatigue analysis of long-span suspension bridges under multiple loading: Case study. *Engineering Structures,* 33**,** 3246-3256.

CHO, H.-N., LIM, J.-K. & CHOI, H.-H. (2001) Reliability-based fatigue failure analysis for causes assessment of a collapsed steel truss bridge. *Engineering Failure Analysis,* 8**,** 311-324.

CHUNG, J. & HULBERT, G. M. (1993) A time integration algorithm for Structural Dynamics with improved numerical dissipation: the Generalized-alpha Method. *Journal of Applied Mechanics,* 60**,** 371-375.

CLOUGH, R. W. & PENZIEN, J. (1975) *Dynamics of structures,* McGraw-Hill.

CLUBLEY, S. K. & WINTER, S. N. (2003) On the fatigue and fracture of site splice welds at the River Mardle Viaduct. *Engineering Failure Analysis,* 10**,** 593-604.

CORMIER, N. G., SMALLWOOD, B. S., SINCLAIR, G. B. & MEDA, G. (1999) Aggressive submodelling of stress concentrations. *International Journal for Numerical Methods in Engineering,* 46**,** 889-909.

COSTA, B. J. A. & FIGUEIRAS, J. A. (2012) Fiber optic based monitoring system applied to a centenary metallic arch bridge: Design and installation. *Engineering Structures,* 44**,** 271-280.

CREMONA, C., EICHLER, B., JOHANSSON, B. & LARSSON, T. (2013) Improved assessment methods for static and fatigue resistance of old metallic railway bridges. *Journal of Bridge Engineering,* 18**,** 1164-1173.

CREMONA, C., PATRON, A., JOHANSSON, B., LARSSON, T., EICHLER, B., HÖHLER, S. & KÜHN, B. (2007) Inproved Assessment Methods for Static and Fatigue Resistance of Old Steel Railway Bridges. *Sustainable Bridges - Assessment for Future Traffic Demands and Longer Lives.*

CROSS, E. J., KOO, K. Y., BROWNJOHN, J. M. W. & WORDEN, K. (2013) Long-term monitoring and data analysis of the Tamar Bridge. *Mechanical Systems and Signal Processing,* 35**,** 16-34.

CRUPI, G., CRUPI, V., GUGLIELMINO, E. & TAYLOR, D. (2005) Fatigue assessment of welded joints using critical distance and other methods. *Engineering Failure Analysis,* 12**,** 129-142.

CURY, A. & CRÉMONA, C. (2012) Assignment of structural behaviours in long-term monitoring: Application to a strengthened railway bridge. *Structural Health Monitoring,* 11**,** 422-441.

DAVIDSON, D. L. & LANKFORD, J. (1992) Fatigue crack growth in metals and alloys: mechanisms and micromechanics. *International Materials Reviews,* 37**,** 45-76.

DE CASTRO, J. T. P. & MEGGIOLARO, M. A. (2009a) *Fadiga - Técnicas e Práticas de Dimensionamento Estrutural sob Cargas Reais de Serviço: Volume I - Iniciação de Trincas*, CreateSpace.

DE CASTRO, J. T. P. & MEGGIOLARO, M. A. (2009b) *Fadiga - Técnicas e Práticas de Dimensionamento Estrutural sob Cargas Reais de Serviço: Volume II - Propagação de Trincas, Efeitos Térmicos e Estocásticos*, CreateSpace.

DE CASTRO, P. M. S. T. (2008) Notas sobre a Análise Linear Elástica do Estado de Tensão e Deformação de Sólidos Contendo Fendas. Porto, FEUP - Faculdade de Engenharia da Universidade do Porto.

DE MORAIS, A. B. (2007) Calculation of stress intensity factors by the force method. *Engineering Fracture Mechanics,* 74**,** 739-750.

DEMERS, C. E. & FISHER, J. W. (1989) *A survey of localized cracking in steel bridges: 1981 to 1988*, Center for Advanced Technology for Large Structural Systems (ATLSS), Lehigh University.

DEVRIES, P. H., RUTH, K. T. & DENNIES, D. P. (2010) Counting on fatigue: Striations and their measure. *Journal of Failure Analysis and Prevention,* 10**,** 120-137.

DILENA, M. & MORASSI, A. (2011) Dynamic testing of a damaged bridge. *Mechanical Systems and Signal Processing,* 25**,** 1485-1507.

DÖHLER, M., ANDERSEN, P. & MEVEL, L. (2010) Data Merging for Multi-Setup Operational Modal Analysis with Data-Driven SSI. *28th International Modal Analysis Conference (IMAC).* Jacksonville, USA.

DONG, P. (2001) A structural stress definition and numerical implementation for fatigue analysis of welded joints. *International Journal of Fatigue,* 23**,** 865-876.

DONG, P. (2005) A Robust Structural Stress Method for Fatigue Analysis of Offshore/Marine Structures. *Journal of Offshore Mechanics and Arctic Engineering,* 127**,** 68-74.

DOWLING, N. E. (2007) *Mechanical behavior of materials: engineering methods for deformation, fracture, and fatigue*, Prentice Hall.

DUAN, Y. F., XU, Y. L., FEI, Q. G., WONG, K. Y., CHAN, K. W. Y., NI, Y. Q. & NG, C. L. (2011) Advanced finite element model of Tsing Ma Bridge for structural health monitoring. *International Journal of Structural Stability & Dynamics,* 11**,** 313-344.

EC (2010) High-Speed Europe: A sustainable link between citizens. Luxembourg, European Commission.

EC (2011) Priority Project 16: Freight railway axis Sines/Algeciras-Madrid-Paris. European Comission.

EC (2013) The Core Network Corridors: Trans European Transport Network 2013. European Commission.

EL HADDAD, M. H., SMITH, K. N. & TOPPER, T. H. (1979a) Fatigue Crack Propagation of Short Cracks. *Journal of Engineering Materials and Technology,* 101**,** 42-46.

EL HADDAD, M. H., TOPPER, T. H. & SMITH, K. N. (1979b) Prediction of non propagating cracks. *Engineering Fracture Mechanics,* 11**,** 573-584.

ELBER, W. (1971) The significance of fatigue crack closure. *Damage Tolerance in Aircraft Structures,* ASTM STP 486**,** 230-242.

ERDOGAN, F. & SIH, G. C. (1963) On the Crack Extension in Plates Under Plane Loading and Transverse Shear. *Journal of Fluids Engineering,* 85**,** 519-525.

ESDEP (1996) *Fatigue,* Berkshire, The Steel Construction Institute.

ESVELD, C. (2001) *Modern railway track,* MRT-Productions.

EWALDS, H. L. & WANHILL, R. J. H. (1985) *Fracture mechanics,* London, Edward Arnold/DUM.

EWING, J. A. & HUMPHREY, J. C. (1903) The Fracture of Metals under Repeated Alternations of Stress. *Philosophical Transactions of the Royal Society of London A: Mathematical, Physical and Engineering Sciences,* 200**,** 241-250.

EWING, J. A. & ROSENHAIN, W. (1900) The Crystalline Structure of Metals. *Philosophical Transactions of the Royal Society of London A: Mathematical, Physical and Engineering Sciences,* 195**,** 279-301.

FETT, T. & MUNZ, D. (1997) *Stress intensity factors and weight functions,* Southampton, Computational Mechanics Publications.

FISHER, J. W. (1984) *Fatigue and fracture in steel bridges case studies,* New York, John Wiley & Sons.

FORMAN, R. G., KEARNEY, V. E. & ENGLE, R. M. (1967) Numerical analysis of crack propagation in cyclic-loaded structures. *Transactions of ASME, Journal of Basic Engineering,* 89**,** 459-464.

FORMAN, R. G., SHIVAKUMAR, V., METTU, S. R. & NEWMAN, J. C. (2000) Fatigue Crack Growth Computer Program NASGRO Version 3.0 - Reference Manual. IN NASA (Ed., NASA.

FORSYTH, P. J. E. & RYDER, D. A. (1960) Fatigue Fracture: Some Results Derived from the Microscopic Examination of Crack Surfaces. *Aircraft Engineering and Aerospace Technology,* 32**,** 96-99.

FRACTURE ANALYSIS CONSULTANTS, I. (2011) Franc3D Reference Manual. v6 ed. New York.

FRICKE, W. (2012) *IIW Recommendations for the fatigue assessment of welded structures by notch stress analysis: IIW 2006-09,* Woodhead Publishing Limited.

FRICKE, W. & PAETZOLD, H. (2010) Full-scale fatigue tests of ship structures to validate the S-N approaches for fatigue strength assessment. *Marine Structures,* 23**,** 115-130.

FRIES, T.-P. & BELYTSCHKO, T. (2010) The extended/generalized finite element method: An overview of the method and its applications. *International Journal for Numerical Methods in Engineering,* 84**,** 253-304.

FRYBA, L. (1996) *Dynamics of railway bridges,* T. Telford.

FU, C. & ZHANG, N. (2011) Investigation of bridge expansion joint failure using field strain measurement. *Journal of Performance of Constructed Facilities,* 25**,** 309-316.

FU, G. & YOU, J. (2011) Extrapolation for Future Maximum Load Statistics. *Journal of Bridge Engineering,* 16**,** 527-535.

FURUKAWA, K. & MURAKAMI, Y. (1999) Method for Estimating Service Load from Striation Width and Height. IN BICEGO, V., NITTA, A., PRICE, J. W. H. & VISWANATHAN, R. (Eds.) *Case Histories on Integrity and Failures in Industry.* Milan, Italy.

GARCIA-PALACIOS, J., ARAUJO, A., NIETO-TALADRIZ, O., SAMARTIN, A., REYNDERS, E. & DE ROECK, G. (2012) *Low cost dynamic structural identification system for extensive bridge monitoring,* Boca Raton, CRC Press-Taylor & Francis Group.

GENTILE, C. & SAISI, A. (2011) Ambient vibration testing and condition assessment of the Paderno iron arch bridge (1889). *Construction and Building Materials,* 25**,** 3709-3720.

GENTILE, C. & SAISI, A. (2013) Operational modal testing of historic structures at different levels of excitation. *Construction and Building Materials,* 48**,** 1273-1285.

GERBER, W. (1874) Bestimmung der Zulossigen Spannungen in Eisen Constructionen. *Z. Bayer Arch. Ing. Ver.,* 6.

GINER, E., SUKUMAR, N., TARANCÓN, J. E. & FUENMAYOR, F. J. (2009) An Abaqus implementation of the extended finite element method. *Engineering Fracture Mechanics,* 76**,** 347-368.

GLISIC, B. & INAUDI, D. (2012) Development of method for in-service crack detection based on distributed fiber optic sensors. *Structural Health Monitoring-an International Journal,* 11**,** 161-171.

GOMEZ, H. C. & FENG, M. Q. (2012) *Bridge condition assessment based on long-term monitoring data and finite element model updating,* Boca Raton, CRC Press-Taylor & Francis Group.

GOODMAN, J. (1899) *Mechanics applied to engineering,* London, Longmans, Green & Co.

GOULET, J., TEXIER, M., MICHEL, C., SMITH, I. & CHOUINARD, L. (2014) Quantifying the Effects of Modeling Simplifications for Structural Identification of Bridges. *Journal of Bridge Engineering,* 19**,** 59-71.

GRID, GREISH, BEG & FERBRITAS (2006) Variante de Alcácer: Projecto de Execução do Atravessamento do Rio Sado. IN REFER (Ed.

GRIEBEL, A. (2009) Technical Brief: Fatigue Dimples. *Journal of Failure Analysis & Prevention,* 9**,** 193-196.

GRIFFITH, A. A. (1921) The Phenomena of Rupture and Flow in Solids. *Philosophical Transactions of the Royal Society of London A: Mathematical, Physical and Engineering Sciences,* 221**,** 163-198.

GRUNDY, D. C. (1994) Fatigue and fracture of a railway wheel steel. Massachusetts Institute of Technology.

GUINEA, G. V., PLANAS, J. & ELICES, M. (2000) KI evaluation by the displacement extrapolation technique. *Engineering Fracture Mechanics,* 66**,** 243-255.

GUO, T. & CHEN, Y.-W. (2011) Field stress/displacement monitoring and fatigue reliability assessment of retrofitted steel bridge details. *Engineering Failure Analysis,* 18**,** 354-363.

GUO, T. & CHEN, Y. W. (2013) Fatigue reliability analysis of steel bridge details based on field-monitored data and linear elastic fracture mechanics. *Structure and Infrastructure Engineering,* 9**,** 496-505.

GUO, T., FRANGOPOL, D. M. & CHEN, Y. (2012) Fatigue reliability assessment of steel bridge details integrating weigh-in-motion data and probabilistic finite element analysis. *Computers & Structures,* 112–113**,** 245-257.

HAGHANI, R., AL-EMRANI, M. & HESHMATI, M. (2012) Fatigue-prone details in steel bridges. *Buildings,* 2**,** 456-476.

HAI, D. T. (2006) Current status of existing railway bridges in Vietnam: An overview of steel deficiencies. *Journal of Constructional Steel Research,* 62**,** 987-994.

HAKOLA, I., HRADIL, P. & HALONEN, M. (2012) *Bridge testing, monitoring and condition assessment in Finland,* Boca Raton, CRC Press-Taylor & Francis Group.

HAOJIE, S., WEIXING, Y. & YITAO, W. (2014) Synergistic Damage Mechanic Model for Stiffness Properties of Early Fatigue Damage in Composite Laminates. *Procedia Engineering,* 74**,** 199-209.

HAYES, B. (1996) Classic brittle failures in large welded structures. *Engineering Failure Analysis,* 3**,** 115-127.

HE, L. Q., QIN, S. Q., BUI, T. T., REYNDERS, E., CUADRADO, M., MUSEROS, P. & DE ROECK, G. (2012) *Operational modal analysis of a high-speed railway bridge: the Jalon viaduct,* Heverlee, Katholieke Univ Leuven, Dept Werktuigkunde.

HE, X. H., YU, Z. W. & CHEN, Z. Q. (2008) Finite element model updating of existing steel bridge based on structural health monitoring. *Journal of Central South University of Technology,* 15**,** 399-403.

HERSHKO, E., MANDELKER, N., GHEORGHIU, G., SHEINKOPF, H., COHEN, I. & LEVY, O. (2008) Assessment of fatigue striation counting accuracy using high resolution scanning electron microscope. *Engineering Failure Analysis,* 15**,** 20-27.

HERTER, J. (2012) *Inspection Strategies to prevent Fatigue Failure of Gusset Plates in Steel Truss Bridges,* Boca Raton, CRC Press-Taylor & Francis Group.

HUBBARD, J. L. (2003) Comparison of transmission and scanning electron fractography. *Practical Failure Analysis,* 3**,** 55-61.

IIW (2008) Recommendations for Fatigue Design of Welded Joints and Components. Paris, France, IIW.

IMTT (2011) Rede Trans-Europeia de Transportes. Instituto da Mobilidade e dos Transportes Terrestres.

INGLIS, C. E. (1913) Stresses in Plates Due to the Presence of Cracks and Sharp Corners. *Transactions of the Institute of Naval Architects,* 55**,** 219-241.

IPQ (2009a) NP EN 10025: Produtos laminados a quente de aços de construção - Parte 3: Condições técnicas de fornecimento de aços de construção soldáveis de grão fino no estado normalizado/laminado normalizado. Portugal, IPQ.

IPQ (2009b) NP EN 10025: Produtos laminados a quente de aços de construção - Parte 4: Condições técnicas de fornecimento de aços de construção soldáveis de grão fino obtidos por laminagem termomecânica. Portugal, IPQ.

IRWIN, G. R. (1957) Analysis of Stresses and Strains Near the End of a Crack Traversing a Plate. *Journal of Applied Mechanics,* 79**,** 361-364.

JOHANNESSON, P., SVENSSON, T. & DE MARÉ, J. (2005) Fatigue life prediction based on variable amplitude tests--methodology. *International Journal of Fatigue,* 27**,** 954-965.

JULIÁN VALERIO, E. A., ANTONIO SANTOS, VICENTE CUÉLLAR (2005) SUPERTRACK Final Report: Instrumentation, monitoring and physical modelling of high-speed lines. CEDEX, ADIF.

KAROUMI, R., WIBERG, J. & LILJENCRANTZ, A. (2005) Monitoring traffic loads and dynamic effects using an instrumented railway bridge. *Engineering Structures,* 27**,** 1813-1819.

KING, L. W. (1898) The Code of Hammurabi. *The Avalon Project.* Yale Law School.

KISS, K. & DUNAI, L. (2000) Stress history generation for truss bridges using multi-level models. *Computers & Structures,* 78**,** 329-339.

KISS, K. & DUNAI, L. (2002) Fracture mechanics based fatigue analysis of steel bridge decks by two-level cracked models. *Computers & Structures,* 80**,** 2321-2331.

KITSUNAI, Y. (1983a) Effect of specimen size and configuration on fatigue crack growth behavior of mild steel butt welded joints. *Journal of the Society of Materials Science,* 32**,** 304-309.

KITSUNAI, Y. (1983b) Effect of specimen size and configuration on fatigue crack growth behavior of welded joints. IN PRESS, S. (Ed. *ICF International Symposium on Fracture Mechanics.* Beijing, Beijing and VNU Science Press.

KITSUNAI, Y., TANAKA, M. & YOSHIHISA, E. (1998) Influence of residual stresses and loading frequencies on corrosion fatigue crack growth behavior of weldments. *Metallurgical and Materials Transactions A: Physical Metallurgy and Materials Science,* 29**,** 1289-1298.

KO, J. M., SUN, Z. G. & NI, Y. Q. (2002) Multi-stage identification scheme for detecting damage in cable-stayed Kap Shui Mun Bridge. *Engineering Structures,* 24**,** 857-868.

KOLAKOWSKI, P., SZELAZEK, J., SEKULA, K., SWIERCZ, A., MIZERSKI, K. & GUTKIEWICZ, P. (2011) Structural health monitoring of a railway truss bridge using vibration-based and ultrasonic methods. *Smart Materials & Structures,* 20.

KÖTTGEN, V. B., OLIVIER, R. & SEEGER, T. (1987) *The influence of plate thickness on fatigue strength of welded joints, a comparison of experiments with prediction by fatigue notch factors,* Delft, Elsevier Science.

KRUEGER, R. (2002) The Virtual Crack Closure Technique: History, Approach and Applications. Hampton, Virginia, USA, NASA.

KUGUEL, R. (1961) A relation between theoretical stress concentration factor and fatigue notch factor deduced from the concept of highly stressed volume. *ASTM Proceeding 1961.* ASTM.

KÜHN, B., LUKIĆ, M., NUSSBAUMER, A., GÜNTHER, H.-P., HELMERICH, R., HERION, S., KOLSTEIN, M. H., WALBRIDGE, S., ANDROIC, B., DIJKSTRA, O. & BUCAK, Ö. (2008)

Assessment of Existing Steel Structures: Recommendations for Estimation of Remaining Fatigue Life. IN SEDLACEK, G., BIJLAARD, F., GÉRADIN, M., PINTO, A. & DIMOVA, S. (Eds.) *JRC Scientific and Technical Reports.* European Commission, Joint Research Centre.

LADOS, D. A. & APELIAN, D. (2006) The effect of residual stress on the fatigue crack growth behavior of Al-Si-Mg cast alloys - mechanisms and corrective mathematical models. *Metallurgical and Materials Transactions A (Physical Metallurgy and Materials Science),* 37A**,** 133-45.

LAWRENCE, F. V., HO, N. J. & MAZUMDAR, P. K. (1981) Predicting the Fatigue Resistance of Welds. *Annual Review of Materials Science,* 11**,** 401-425.

LEANDER, J., ANDERSSON, A. & KAROUMI, R. (2010) Monitoring and enhanced fatigue evaluation of a steel railway bridge. *Engineering Structures,* 32**,** 854-863.

LI, S. L., ZHU, S. Y., XU, Y. L., CHEN, Z. W. & LI, H. (2012) Long-term condition assessment of suspenders under traffic loads based on structural monitoring system: Application to the Tsing Ma Bridge. *Structural Control & Health Monitoring,* 19**,** 82-101.

LI, Z. X., ZHOU, T. Q., CHAN, T. H. T. & YU, Y. (2007) Multi-scale numerical analysis on dynamic response and local damage in long-span bridges. *Engineering Structures,* 29**,** 1507-1524.

LILJENCRANTZ, A., KAROUMI, R. & OLOFSSON, P. (2007) Implementing bridge weigh-in-motion for railway traffic. *Computers & Structures,* 85**,** 80-88.

LIN, X. B. & SMITH, R. A. (1999) Finite element modelling of fatigue crack growth of surface cracked plates: Part I: The numerical technique. *Engineering Fracture Mechanics,* 63**,** 503-522.

LINDBERG, A. Y. & SCHULTZ, A. E. (1997) Incorporation of Fatigue Detail Classification of Steel Bridges into the Minnesota Department of Transportation Database.

LING, J. & PAN, J. (1997) A maximum likelihood method for estimating P-S-N curves. *International Journal of Fatigue,* 19**,** 415-419.

LIPPI, F. V., ORLANDO, M. & SALVATORE, W. (2011) Assessment of the dynamic and fatigue behaviour of the Panaro railway steel bridge. *Structure and Infrastructure Engineering,* 9**,** 834-848.

LIU, K., ZHOU, H., SHI, G., WANG, Y. Q., SHI, Y. J. & DE ROECK, G. (2013) Fatigue assessment of a composite railway bridge for high speed trains. Part II: Conditions for which a dynamic analysis is needed. *Journal of Constructional Steel Research,* 82**,** 246-254.

LIU, M., FRANGOPOL, D. M. & KWON, K. (2010) Fatigue reliability assessment of retrofitted steel bridges integrating monitored data. *Structural Safety,* 32**,** 77-89.

LNEC (2011) Ensaio de carga do novo atravessamento ferroviário do rio Sado na Variante de Alcácer do Sal. Laboratório Nacional de Engenharia Civil.

LOTSBERG, I. & LANDET, E. (2005) Fatigue capacity of side longitudinals in floating structures. *Marine Structures,* 18**,** 25-42.

LYNCH, S. P. & MOUTSOS, S. (2006) A brief history of fractography. *Journal of Failure Analysis and Prevention,* 6**,** 54-69.

MAGALHAES, F., AMADOR, S., CUNHA, A. & CAETANO, E. (2012) *DynaMo - Software for vibration based Structural Health Monitoring,* Boca Raton, CRC Press-Taylor & Francis Group.

MAGALHÃES, F., CAETANO, E., CUNHA, Á., FLAMAND, O. & GRILLAUD, G. (2012a) Ambient and free vibration tests of the Millau Viaduct: Evaluation of alternative processing strategies. *Engineering Structures,* 45**,** 372-384.

MAGALHÃES, F., CUNHA, A. & CAETANO, E. (2012b) Vibration based structural health monitoring of an arch bridge: From automated OMA to damage detection. *Mechanical Systems and Signal Processing,* 28**,** 212-228.

MAGALHÃES, F., CUNHA, Á. & CAETANO, E. (2008) Dynamic monitoring of a long span arch bridge. *Engineering Structures,* 30**,** 3034-3044.

MAGEL, E., SROBA, P., SAWLEY, K. & KALOUSEK, J. (2004) Control of Rolling Contact Fatigue of Rails. *AREMA 2004 Annual Conference.* Nashville, Tennessee, USA, AREMA.

MAHDAVI SHAHRI, M. & SANDSTRÖM, R. (2012) Effective notch stress and critical distance method to estimate the fatigue life of T and overlap friction stir welded joints. *Engineering Failure Analysis,* 25**,** 250-260.

MAKINO, H., KUBO, T., SHIWAKU, T., ENDO, S., INOUE, T., KAWAGUCHI, Y., MATSUMOTO, Y. & MACHIDA, S. (2001) Prediction for Crack Propagation and Arrest of Shear Fracture in Ultra-high Pressure Natural Gas Pipelines. *ISIJ International,* 41**,** 381-388.

MANSON, S. S. (1965) Fatigue: A complex subject—Some simple approximations. *Experimental Mechanics,* 5**,** 193-226.

MARQUES, F., CUNHA, Á., FERNANDES, A. A., CAETANO, E. & MAGALHÃES, F. (2009) Evaluation of dynamic effects and fatigue assessment of a metallic railway bridge. *Structure and Infrastructure Engineering,* 6**,** 635-646.

MARTINS, F. (2009) *Variante de Alcácer e Atravessamento Ferroviário sobre o rio Sado: Enquadramento e Definição Geral da Obra,* Lisboa, Associaçao Portuguesa de Construçao Metálica e Mista.

MATSUISHI, M. & ENDO, T. (1968) Fatigue of metals subjected to varying stress. *Japan Society of Mechanical Engineers.* Fukuoka, Japan.

MCEVILY, A. J. & RITCHIE, R. O. (1998) Crack closure and the fatigue-crack propagation threshold as a function of load ratio. *Fatigue & Fracture of Engineering Materials & Structures,* 21**,** 847-855.

MELI, E. & PUGI, L. (2013) Preliminary development, simulation and validation of a weigh in motion system for railway vehicles. *Meccanica,* 48**,** 2541-2565.

MENANDRO, F. C. M., MOYER, E. T. & LIEBOWITZ, H. A methodology for crack tip mesh design. *Engineering Fracture Mechanics,* 50**,** 713-726.

MENEGHETTI, L. C., TEIXEIRA, R. M., OLIVEIRA, R., BITTENCOURT, T. N. & NETO, A. P. C. (2012) *Fatigue damage assessment of railway steel bridges based on short-term monitoring data,* Boca Raton, CRC Press-Taylor & Francis Group.

METKAR, R., SUNNAPWAR, V. & HIWASE, S. D. (2011) Prediction of fatigue failure in Engineering component by using critical distance approach. *International Review of Mechanical Engineering,* 5**,** 1254-1257.

MEYER, J., BISCHOFF, R., FELTRIN, G. & MOTAVALLI, M. (2010) Wireless sensor networks for long-term structural health monitoring. *Smart Structures and Systems,* 6**,** 263-275.

MIKI, C. (2007) Retrofitting Engineering for Steel Bridge Structures. International Institute of Welding, Japanese Delegation.

MIKI, C. (2010) Retrofitting Engineering for Fatigue Damaged Steel Structures. International Institute of Welding.

MILLS, W. J. & JAMES, L. A. (1987) Residual Stress Effects on Fatigue Crack Growth Behavior in Stainless Steel Welds. *Journal of Pressure Vessel Technology,* 109**,** 336-339.

MINER, M. A. (1945) Cumulative damage in fatigue. *Journal of Applied Mechanics,* 67**,** A159-A164.

MIRANDA, R. M. C. (2011) Study of Fatigue Crack Propagation in Metallic Structures. *Department of Mechanical Engineering.* Porto, Faculty of Engineering of the University of Porto.

MIRANDA, R. M. C., ALBUQUERQUE, C. M. C., RICHTER-TRUMMER, V., FIGUEIREDO, M. A. V., CALÇADA, R. & DE CASTRO, P. M. S. T. (2011) Fatigue crack propagation behavior of the welded steel of a railway bridge. *VI International Materials Symposium Materiais 2011.* Guimarães, Portugal, SPM.

MOCHIZUKI, M. (2007) Control of welding residual stress for ensuring integrity against fatigue and stress-corrosion cracking. *Nuclear Engineering and Design,* 237**,** 107-123.

MOËS, N. & BELYTSCHKO, T. (2002) Extended finite element method for cohesive crack growth. *Engineering Fracture Mechanics,* 69**,** 813-833.

MOPTC (2006) Orientações Estratégicas para o Sector Ferroviário. Ministério das Obras Públicas Transportes e Comunicações.

MOREIRA, P. M. G. P. & DE CASTRO, P. M. S. T. (2010) Fractographic analysis of fatigue crack growth in lightweight integral stiffened panels. *International Journal of Structural Integrity,* 1**,** 233-258.

MOREL, F. & FLACELIÈRE, L. (2005) Data scatter in multiaxial fatigue: from the infinite to the finite fatigue life regime. *International Journal of Fatigue,* 27**,** 1089-1101.

MOREU, F., LAFAVE, J. M. & SPENCER, B. F. (2012) New regulations on railroad bridge safety: opportunities and challenges for railroad bridge monitoring. *Sensors and Smart Structures Technologies for Civil, Mechanical, and Aerospace Systems 2012.*

MURAKAMI, Y. (1987) *Stress intensity factors handbook,* Oxford, Pergamon Press.

NAGY, W., SCHOTTE, K., STAEL, D., BACKER, H. D. & BOGAERT, P. V. (2013) Structural monitoring of the Irish railway viaduct in Belgium. *International IABSE Conference - Assessment, Upgrading and Refurbishment of Infrastructures.* Rotterdam.

NDTRC (2014) NDT Education Resource Center. https://www.nde-ed.org.

NEUBER, H. (1961) Theory of Stress Concentration for Shear-Strained Prismatical Bodies With Arbitrary Nonlinear Stress-Strain Law. *Journal of Applied Mechanics,* 28**,** 544-550.

NEWMAN, J. C., JR. (1984) A crack opening stress equation for fatigue crack growth. *International Journal of Fracture,* 24**,** R131-R135.

NEWMAN JR., J. C. & RAJU, I. S. (1981) An empirical stress-intensity factor equation for the surface crack. *Engineering Fracture Mechanics,* 15.

NI, Y. Q., XIA, H. W. & KO, J. M. (2008) Structural performance evaluation of Tsing Ma Bridge deck using long-term monitoring data. *Modern Physics Letters B,* 22**,** 875-880.

NI, Y. Q., XIA, H. W., WONG, K. Y. & KO, J. M. (2012) In-Service Condition Assessment of Bridge Deck Using Long-Term Monitoring Data of Strain Response. *Journal of Bridge Engineering,* 17**,** 876-885.

NTSB (1989) Aloha Airlines, Flight 243, April 28, 1988. *Aircraft Accident Report.* Washington, USA, National Transportation Safety Board.

NUNES, J. P. & NICOLAU, H. P. (2009) *Variante de Alcácer do Sal - 2ª Fase - Atravessamento Ferroviário sobre o rio Sado: Construção das Estruturas Metálicas da Ponte e Viadutos de Acesso,* Lisboa, Associaçao Portuguesa de Construçao Metálica e Mista.

O'CONNOR, B. (2007) Eschede Train Disaster. *Leadership ViTS Meeting.* NASA Safety Center.

OEHME, P. (1989) Damage Analysis of Steel Structures. *IABSE 89.*

ORCESI, A. & FRANGOPOL, D. (2010) Inclusion of Crawl Tests and Long-Term Health Monitoring in Bridge Serviceability Analysis. *Journal of Bridge Engineering,* 15**,** 312-326.

ORCESI, A. & FRANGOPOL, D. (2013) Bridge performance monitoring based on traffic data. *Journal of Engineering Mechanics,* 139**,** 1508-1520.

ORCESI, A. D. & FRANGOPOL, D. M. (2011) Optimization of bridge maintenance strategies based on structural health monitoring information. *Structural Safety,* 33**,** 26-41.

OTTOSSON, A., PEDERSEN, C. & O'CONNOR, A. J. (2012a) *Fatigue assessment of bridges using realistic train models,* Boca Raton, CRC Press-Taylor & Francis Group.

OTTOSSON, A., PEDERSEN, C. & O'CONNOR, A. (2012b) Employing Train Weigh in Motion Data in Comparison of Cumulative Fatigue Damage on Bridges. *Procedia - Social and Behavioral Sciences,* 48**,** 3338-3347.

PALMGREN, A. Z. (1924) Die Lebensdauer von Kugellagern. *Zeitschrift des Vereines Deutscher Ingenieure,* 68**,** 339-341.

PARIS, P. C., GOMEZ, M. P. & ANDERSON, W. E. (1961) A Rational Theory of Fatigue. *The Trend in Engineering,* 13**,** 9-14.

PARKER, A. P. (1981) *The Mechanics of Fracture and Fatigue - An Introduction,* London, E & F N Spon.

PAULSSON, B. (2013) Assessment methodos for elderly rail infrastructure. *MAINLINE Project.* UIC, COWI, SKM, TWI, Universidade do Minho, Lulea Tekniska Universitet, DB Netz AG, MÁV

Magyar Államvasutak Zrt, Universitat Politècnica de Catalunya, Graz University of Technology, TCDD, Damill AB, COMSA EMTE, Trafikverket, SETRA, ARTTIC, Skanska A.S.

PEDERSEN, M. M., MOURITSEN, O. Ø., HANSEN, M. R., ANDERSEN, J. G. & WENDERBY, J. (2010) Re-analysis of fatigue data for welded joints using the notch stress approach. *International Journal of Fatigue,* 32**,** 1620-1626.

PETERSON, R. E. (1959) Notch sensitivity. IN SINES, G. & WAISMAN, J. L. (Eds.) *Metal fatigue.* New York, McGraw Hill.

PETERSON, R. E. (1963) *Fatigue of metals in engineering and design,* American Society for Testing and Materials.

PETERSON, R. E. (1974) *Stress concentration factors : charts and relations useful in making strength calculations for machine parts and structural elements*.

PHARES, B., LU, P., WIPF, T., GREIMANN, L. & SEO, J. (2013) Field validation of a statistical-based bridge damage-detection algorithm. *Journal of Bridge Engineering,* 18**,** 1227-1238.

PICOZZI, M., MILKEREIT, C., ZULFIKAR, C., FLEMING, K., DITOMMASO, R., ERDIK, M., ZSCHAU, J., FISCHER, J., ŞAFAK, E., ÖZEL, O. & APAYDIN, N. (2010) Wireless technologies for the monitoring of strategic civil infrastructures: an ambient vibration test on the Fatih Sultan Mehmet Suspension Bridge in Istanbul, Turkey. *Bulletin of Earthquake Engineering,* 8**,** 671-691.

PIMENTEL, R. M. C. M., BARBOSA, M. C. B., COSTA, N. M. S., RIBEIRO, D. R. F., FERREIRA, L. A. A., ARAUJO, F. M. M. & CALÇADA, R. A. B. (2008) Hybrid Fiber-Optic/Electrical Measurement System for Characterization of Railway Traffic and Its Effects on a Short Span Bridge. *Sensors Journal, IEEE,* 8**,** 1243-1249.

PORTO DE SINES (2013) Relatório de Gestão e Contas 2013. Porto de Sines.

PORTO DE SINES (2015) Estatísticas - Movimento de Mercadorias 1978/2014. Porto de Sines.

PRIME, M. B. (2001) Cross-Sectional Mapping of Residual Stresses by Measuring the Surface Contour After a Cut. *Journal of Engineering Materials and Technology,* 123**,** 162-168.

RADAJ, D. (1990) *Design & Analysis of Fatigue Resistant Welded Structures,* Abington Publishing.

RADAJ, D. (1997) Fatigue notch factor of gaps in welded joints reconsidered. *Engineering Fracture Mechanics,* 57**,** 405-407.

RADAJ, D., SONSINO, C. M. & FRICKE, W. (2006) *Fatigue assessment of welded joints by local approaches,* Cambridge, Woodhead Publishing, Ltd.

RADAJ, D., SONSINO, C. M. & FRICKE, W. (2009) Recent developments in local concepts of fatigue assessment of welded joints. *International Journal of Fatigue,* 31**,** 2-11.

RADING, G. (2005) An evaluation of residual stress distribution in welded compact tension specimens using neutron diffraction. *The Journal of Strain Analysis for Engineering Design,* 40**,** 211-216.

RAHMATALLA, S., HUDSON, K., LIU, Y. & EUN, H.-C. (2014) Finite element modal analysis and vibration-waveforms in health inspection of old bridges. *Finite Elements in Analysis and Design,* 78**,** 40-46.

RANNOU, J., LIMODIN, N., RÉTHORÉ, J., GRAVOUIL, A., LUDWIG, W., BAÏETTO-DUBOURG, M.-C., BUFFIÈRE, J.-Y., COMBESCURE, A., HILD, F. & ROUX, S. (2010) Three dimensional experimental and numerical multiscale analysis of a fatigue crack. *Computer Methods in Applied Mechanics and Engineering,* 199**,** 1307-1325.

REFER (2010) *Variante de Alcácer,* Lisboa, REFER.

REFER (2011) Mapa da Rede. REFER.

REIS, A. J. & LOPES, N. T. (2009) *Variante de Alcácer do Sal - Atravessamento Ferroviário sobre o rio Sado: Projecto de Obras de Arte,* Lisboa, Associaçao Portuguesa de Construçao Metálica e Mista.

RIBEIRO, D., CALÇADA, R., DELGADO, R., BREHM, M. & ZABEL, V. (2012) Finite element model updating of a bowstring-arch railway bridge based on experimental modal parameters. *Engineering Structures,* 40**,** 413-435.

RICE, J. R. (1968) A Path Independent Integral and the Approximate Analysis of Strain Concentration by Notches and Cracks. *Journal of Applied Mechanics,* 35**,** 379-386.

RICHTER-TRUMMER, V. & DE CASTRO, P. M. S. T. (2011) Through the thickness measurement of residual stress in a thick welded steel CT specimen by the contour method. *Journal of Strain Analysis for Engineering Design,* 46**,** 315-322.

RICHTER-TRUMMER, V., MIRANDA, R. M. C., ALBUQUERQUE, C. & CASTRO, P. M. S. T. D. (2011) Fatigue Crack Striation Spacing for Welded and Base Material CT Steel Specimens *VI International Materials Symposium MATERIAIS 2011.* Guimarães, Portugal.

RIGHINIOTIS, T. D. (2006) A comparative study of fatigue inspection methods. *Journal of Constructional Steel Research,* 62**,** 352-358.

RIGHINIOTIS, T. D., IMAM, B. M. & CHRYSSANTHOPOULOS, M. K. (2008) Fatigue analysis of riveted railway bridge connections using the theory of critical distances. *Engineering Structures,* 30**,** 2707-2715.

RITCHIE, R. O. (1977) Influence of microstructure on near-threshold fatigue-crack propagation in ultra-high strength steel. *Metal Science,* 11**,** 368-381.

RODRIGUES, C., CAVADAS, F., FÉLIX, C. & FIGUEIRAS, J. (2012) FBG based strain monitoring in the rehabilitation of a centenary metallic bridge. *Engineering Structures,* 44**,** 281-290.

ROOKE, D. P. & CARTWRIGHT, D. J. (1976) *Compendium of stress intensity factors,* London, Her Majesty's Stationery Office.

ROVEN, H. J. & NES, E. (1991) Cyclic deformation of ferritic steel--II. Stage II crack propagation. *Acta Metallurgica et Materialia,* 39**,** 1735-1754.

ROYLANCE, D. (2001) Fatigue. Department of Materials Science and Engineering, Massachussets Institute of Technology, Cambridge, USA.

SAKAMOTO, K., MIKI, C., ICHIKAWA, A. & ABE, M. (1990) Vibration Fatigue of Steel Bridges of the Bullet Train System. *IABSE Workshop - Remaining Fatigue Life of Steel Structures.* Lausanne, Switzerland.

SANTOS, J. P. (2014) Smart Structural Health Monitoring Techniques for Novely Identification in Civil Engineering Structures. *PhD Thesis.* Universidade de Lisboa - Instituto Superior Técnico.

SANTOS, J. P., CRÉMONA, C., ORCESI, A. D. & SILVEIRA, P. (2013) Multivariate statistical analysis for early damage detection. *Engineering Structures,* 56**,** 273-285.

SATEPOR (2011) Materiais de via: travessa de betão monobloco polivalente. REFER.

SAXENA, A. (1998) *Nonlinear fracture mechanics for engineers,* Boca Raton, CRC.

SCHIJVE, J. (2003) Fatigue of structures and materials in the 20th century and the state of the art. *International Journal of Fatigue,* 25**,** 679-702.

SCHIJVE, J. (2009) *Fatigue of Structures and Materials*, Springer.

SCHLUNE, H., PLOS, M. & GYLLTOFT, K. (2009) Improved bridge evaluation through finite element model updating using static and dynamic measurements. *Engineering Structures,* 31**,** 1477-1485.

SCHÜTZ, W. (1996) A history of fatigue. *Engineering Fracture Mechanics,* 54**,** 263-300.

SEKUŁA, K. & KOŁAKOWSKI, P. (2012) Piezo-based weigh-in-motion system for the railway transport. *Structural Control and Health Monitoring,* 19**,** 199-215.

SENSORLINE (2008) FORPS Fiber Optic Rail Pad Sensor Datasheet. SensorLine.

SEO, J., PHARES, B., LU, P., WIPF, T. & DAHLBERG, J. (2013) Bridge rating protocol using ambient trucks through structural health monitoring system. *Engineering Structures,* 46**,** 569-580.

SHI, J., CHOPP, D., LUA, J., SUKUMAR, N. & BELYTSCHKO, T. (2010) Abaqus implementation of extended finite element method using a level set representation for three-dimensional fatigue crack growth and life predictions. *Engineering Fracture Mechanics,* 77**,** 2840-2863.

SILVA, A., JESUS, A., FERNANDES, A. A., FIGUEIREDO, M. & CALÇADA, R. (2013) Análise do comportamento à fadiga de ligações soldadas com base no conceito das tensões estruturais. *3º Congresso Nacional sobre Segurança e Conservação de Pontes - ASCP'2013.* Porto.

SKORUPA, M. (1998) Load interaction effects during fatigue crack growth under variable amplitude loading—a literature review. Part I: empirical trends. *Fatigue & Fracture of Engineering Materials & Structures,* 21**,** 987-1006.

SKORUPA, M. (1999) Load interaction effects during fatigue crack growth under variable amplitude loading—a literature review. Part II: qualitative interpretation. *Fatigue & Fracture of Engineering Materials & Structures,* 22**,** 905-926.

SONSINO, C. M. (1995) Multiaxial fatigue of welded joints under in-phase and out-of-phase local strains and stresses. *International Journal of Fatigue,* 17**,** 55-70.

SONSINO, C. M. (2007) Course of SN-curves especially in the high-cycle fatigue regime with regard to component design and safety. *International Journal of Fatigue,* 29**,** 2246-2258.

SPAGGIARI, A., CASTAGNETTI, D., DRAGONI, E. & BULLERI, S. (2011) Fatigue life prediction of notched components: a comparison between the theory of critical distance and the classical stress-gradient approach. *Procedia Engineering,* 10**,** 2755-2767.

SRINIVAS, V., SASMAL, S., BANJARA, N., RAMANJANEYULU, K. & IYER, N. (2013) Health assessment of a plate girder railway bridge under increased axle loads. *Journal of Bridge Engineering,* 18**,** 969-979.

STAMATOPOULOS, G. N. (2013) Fatigue assessment and strengthening measures to upgrade a steel railway bridge. *Journal of Constructional Steel Research,* 80**,** 346-354.

SULLOWAY, M., KONCZA, L., WOLGEMUTH, T. L., BRESCIA, D. & HORN, W. G. (1979) Final Report on Causes of Fractures in Bent Nos. 24, 25 and 26 of Dan Ryan Rapid Transit Structure. Federal Highway Administration.

SUN, Z. & YAN, T. (2012) *First Year Data Mining for Vibration Based Condition Monitoring of a Cable Stayed Bridge,* Boca Raton, CRC Press-Taylor & Francis Group.

SURESH, S. (2001) *Fatigue of materials,* Cambridge, Cambridge University Press.

SUSMEL, L. (2008) The theory of critical distances: a review of its applications in fatigue. *Engineering Fracture Mechanics,* 75**,** 1706-1724.

SUSMEL, L. (2014) Four stress analysis strategies to use the Modified Wöhler Curve Method to perform the fatigue assessment of weldments subjected to constant and variable amplitude multiaxial fatigue loading. *International Journal of Fatigue,* 67**,** 38-54.

SVS (1999-2010) ARTeMIS Extractor Pro. 5.3 ed. Aalborg, SVS - Structural Vibration Solutions.

TADA, H., PARIS, P. C. & IRWIN, G. R. (2000) *The stress analysis of cracks handbook,* New York, ASME Press Professional Engineering Publishing.

TANAKA, K. (1974) Fatigue crack propagation from a crack inclined to the cyclic tensile axis. *Engineering Fracture Mechanics,* 6**,** 493-507.

TAYLOR, D. (1999) Geometrical effects in fatigue: a unifying theoretical model. *International Journal of Fatigue,* 21**,** 413-420.

TAYLOR, D., BARRETT, N. & LUCANO, G. (2002) Some new methods for predicting fatigue in welded joints. *International Journal of Fatigue,* 24**,** 509-518.

TAYLOR, D. & WANG, G. (2000) The validation of some methods of notch fatigue analysis. *Fatigue & Fracture of Engineering Materials & Structures,* 23**,** 387-394.

TECCHIO, G., DONA, M., CASARIN, F., ISLAMI, K., ZANINI, M. A., PELLEGRINO, C. & MODENA, C. (2013) Monitoring fatigue effects in an orthotropic steel bridge deck. *International IABSE Conference - Assessment, Upgrading and Refurbishment of Infrastructures.* Rotterdam.

TEIXEIRA DUARTE - ENGENHARIA E CONSTRUÇÕES S.A. (2008) Nota técnica 11: Verificação da segurança do tabuleiro na fase do lançamento inscremental e na fase de construção dos arcos e pendurais sobre o tabuleiro. *Variante de Alcácer.*

TEIXEIRA DUARTE - ENGENHARIA E CONSTRUÇÕES S.A. (2009) Travessia Ferroviária do rio Sado - Ponte Metálica e Viadutos de Acesso - Processos de Soldadura Utilizados em Obra.

TOPPER, T. H., WETZEL, R. M. & J.MORROW (1967) Neuber's rule applied to fatigue of notched specimens. U.S Naval Air Engineering Center. Philadelphia, USA.

VAN BOGAERT, P. (2012) *Inspection and evaluation of steel bridges from a high-speed railway network,* Boca Raton, CRC Press-Taylor & Francis Group.

VINCENZI, L., SAVOIA, M. & SALVATORE, W. (2012) *Experimental modal analysis and fatigue assessment on the Lagoscuro viaduct,* Boca Raton, CRC Press-Taylor & Francis Group.

WALKER, W. H., CASSITY, P. A. & HOLBROOK, D. (1992) Three Case Histories of Cracking Problems Associated with Steel Bridge Floor Beams. University of Illinois.

WANG, C., YAN, S. & HAO, L. (2012) *Fatigue safety assessment of existing railway steel bridges based on in-situ monitoring data,* Boca Raton, CRC Press-Taylor & Francis Group.

WHEELER, O. E. (1972) Spectrum loading and crack growth. *Journal of Basic Engineering,* 94**,** 181-&.

WHELAN, M. & JANOYAN, K. (2010) In-service diagnostics of a highway bridge from a progressive damage case study. *Journal of Bridge Engineering,* 15**,** 597-607.

WILLENBORG, J., ENGLE, R. M. & WOOD, H. A. (1971) A crack growth retardation model using an effective stress concept. Dayton, Air Force Flight Dynamic Laboratory.

WONG, K. Y. (2012) *System Design and Implementation of Structural Health Monitoring and Maintenance Management System for Marine Viaduct Bridges,* Boca Raton, CRC Press-Taylor & Francis Group.

XIAO, Z.-G. & YAMADA, K. (2004) A method of determining geometric stress for fatigue strength evaluation of steel welded joints. *International Journal of Fatigue,* 26**,** 1277-1293.

XU, Y.-L., CHEN, Z.-W. & XIA, Y. (2012) Fatigue assessment of multi-loading suspension bridges using continuum damage model. *International Journal of Fatigue,* 40**,** 27-35.

YAO, Y. & GLISIC, B. (2012) *Reliable damage detection and localization using direct strain sensing,* Boca Raton, CRC Press-Taylor & Francis Group.

YE, X. W., NI, Y. Q., WONG, K. Y. & KO, J. M. (2012) Statistical analysis of stress spectra for fatigue life assessment of steel bridges with structural health monitoring data. *Engineering Structures,* 45**,** 166-176.

YIN, T., TYAS, A., PLEKHOV, O., TEREKHINA, A. & SUSMEL, L. (2015) A novel reformulation of the Theory of Critical Distances to design notched metals against dynamic loading. *Materials & Design,* 69**,** 197-212.

ZAPFFE, C. A. & WORDEN, C. O. (1951) Fractographic Registrations of Fatigue. *Transactions of ASM,* 43**,** 959-969.

ZEHSAZ, M., HASSANIFARD, S. & ESMAEILI, F. (2010) Fatigue life estimation for different notched specimens based on the volumetric approach. *14th International Conference on Experimental Mechanics.* Poitiers, France.

ZENG, Y., TAN, H., LI, X., XIANG, Z. & YU, F. (2012) *Fatigue Analysis of Steel Box Stiffening Girders for Large-span Suspension Bridge in its Lifetime,* Boca Raton, CRC Press-Taylor & Francis Group.

ZERBST, U. (2007) *Fitness-for-service fracture assessment of structures containing cracks a workbook based on the European SINTAP/FITNET Procedure,* Amsterdam, Elsevier.

ZHANG, J., PRADER, J., GRIMMELSMAN, K., MOON, F., AKTAN, A. & SHAMA, A. (2013) Experimental Vibration Analysis for Structural Identification of a Long-Span Suspension Bridge. *Journal of Engineering Mechanics,* 139**,** 748-759.

ZHOU, H., LIU, K., SHI, G., WANG, Y. Q., SHI, Y. J. & DE ROECK, G. (2013) Fatigue assessment of a composite railway bridge for high speed trains. Part I: Modeling and fatigue critical details. *Journal of Constructional Steel Research,* 82**,** 234-245.

ZHOU, Y. (2006) Assessment of bridge remaining fatigue life through field strain measurement. *Journal of Bridge Engineering,* 11**,** 737-744.

ZUBILLAGA, L., TURON, A., MAIMÍ, P., COSTA, J., MAHDI, S. & LINDE, P. (2014) An energy based failure criterion for matrix crack induced delamination in laminated composite structures. *Composite Structures,* 112**,** 339-344.